Transverse Cracking of Micro-alloyed Steel Slabs during Continuous Casting, Handling and Charging into the Hot Strip Mill

D o c t o r a l T h e s i s
(D i s s e r t a t i o n)

to be awarded the degree
Doctor of Engineering (Dr.-Ing.)

submitted by

Hossam Shafy
from Giza, Egypt

approved by the Faculty of
Natural and Materials Science,
Clausthal University of Technology,

Date of oral examination
16.12.2020

Bibliografische Information der Deutschen Nationalbibliothek

Die Deutsche Nationalbibliothek verzeichnet diese Publikation in der Deutschen Nationalbibliografie; detaillierte bibliografische Daten sind im Internet über http://dnb.dnb.de abrufbar.

Bibliographic information published by the Deutsche Nationalbibliothek

The Deutsche Nationalbibliothek lists this publication in the Deutsche Nationalbibliografie; detailed bibliographic data are available in the Internet at http://dnb.dnb.de.

Dean:	Prof. Dr.-Ing. Karl-Heinz Spitzer
Chairperson of the Board of Examiners:	Prof. Dr.-Ing. Dieter Meiners
Supervising tutor:	Prof. Dr.-Ing. Heinz Palkowski
Reviewers:	Prof. Dr.-Ing. Roland Krengel Prof. Dr.-Ing. Goran Kugler

Dissertation Technische Universität Clausthal 2020

D 104

1. Auflage, 2021

ISBN 978-3-86948-806-6

This work is dedicated to my father and role model, Dr. Ahmed Shafy, who taught me faith, humanity and engineering.

You will always be my hero …

Acknowledgments

To my dear parents, many thanks for your love, patience and support throughout my entire life. You mean everything to me and I simply owe it all to you! I am grateful to my brothers Mohamed and Amr, who have provided me with moral support and motivation. I am also grateful to all of my family members and friends who have encouraged me along the way.

A very special gratitude goes out to my advisor Prof. Dr.-Ing. Heinz Palkowski for his faithful support and advice over many working years and for supervising my PhD. I really appreciate the time I spend at the Institute of Metallurgy under his supervision and for him I am truly thankful. Special thanks to Prof. Dr.-Ing. Roland Krengel and Prof. Dr.-Ing. Goran Kugler as well for taking the time to review my thesis and join the board of examiners. I thank Prof. Dr.-Ing. Karl-Heinz Spitzer, the faculty dean and Prof. Dr.-Ing. Dieter Meiners, chairperson of the board of examiners, for the smooth examination process.

Many thanks to all my colleagues from Salzgitter Flachstahl GmbH and Salzgitter Mannesmann Forschung GmbH, who helped me through this journey during my internship and PhD times. Special thanks to Dipl.-Ing. Karsten Matthies, director of the hot strip mill of SZFG, Dipl.-Ing. Nils Reuther, department of continuous casting, SZFG, and Dipl.-Ing. Andre Hasenhütl, group leader of material testing, SZMF. This thesis would not have been possible without the support and advice of Dipl.-Ing. Claus-Peter Antoine, senior manager of hot strip development at SZFG, to whom I am very thankful and grateful for the great chance to work with him.

With a special mention to my dear friends Dr.-Ing. Peter Sieczkarek and Dr.-Ing. Sherif El-Shahid for their continuous motivation and support.

Finally, last but by no means least, I would like to express my gratitude to all the staff of Clausthal University of Technology, especially all my dear colleagues at the Institute of Metallurgy. A very special thanks goes to Dr.-Ing. Stephanie Duwe and Mr. Sebastian Fischer. Additionally, I would like to thank all my students and trainees for their helping hands, hard work and friendly behavior.

Thanks for all your encouragement!

Table of contents

Acknowledgments ..... **I**

Table of contents **1**

Nomenclature **5**

Abstract **7**

Zusammenfassung **9**

Chapter 1: Transverse cracking of slabs **11**

1.1 Thesis layout 12

Chapter 2: Big picture and objectives **13**

2.1 SZFG Steelmaking plant 13
2.2 Statistical analysis 14
2.2.1 Cracking risk 14
2.2.2 Grades 14
2.2.3 Slab history and potential cracking reasons 15
2.3 Objectives 18

Chapter 3: Literature survey **20**

3.1 Continuous casting process 20
3.1.1 Process 20
3.1.2 Solidification 21
3.1.3 Oscillation marks and hooks 22
3.1.4 Segregation 24
3.1.5 Defects 24
3.1.6 Transverse cracking 25
3.2 Hot ductility of micro-alloyed steels 27
3.2.1 Hot ductility curve 28
3.2.2 Embrittlement mechanisms 31
3.2.3 Relevance of hot tensile testing to crack sensitivity 33
3.3 Factors affecting the hot ductility 34
3.3.1 Effect of the chemical composition 34

3.3.1.1 Carbon 34
3.3.1.2 Nitrogen 34
3.3.1.3 Titanium 35
3.3.1.4 Niobium 35
3.3.1.5 Vanadium 35
3.3.1.6 Other elements 36
3.3.2 Microstructural effects 36
3.3.2.1 Grain size 36
3.3.2.2 Precipitation 36
3.3.2.3 Parallel effects: Grain size vs precipitates 38
3.3.2.4 Ferrite formation 39
3.3.3 Effect of the casting process 39
3.3.3.1 Mold heat transfer 39
3.3.3.2 Mold oscillation 39
3.3.3.3 Casting temperature 40
3.3.3.4 Casting speed 40
3.3.3.5 Cooling history 40
3.3.3.6 Strain rate 41
3.3.3.7 Thermal stresses 41
3.4 Cracking by transportation and charging 42
3.4.1 Air cooling before charging 42
3.4.2 Effect of volume change 42
3.4.3 Charging in reheating furnace and rolling 43

Chapter 4: Tools and materials characterization 45

4.1 Materials 45
4.2 Instrumentation 46
4.2.1 Dilatometry thermomechanical simulator: Baehr Dil805A/D/T 46
4.2.2 Metallographic preparation 49
4.2.3 Light optical microscope (LOM) 49
4.2.4 Scanning electron microscope (SEM) 49
4.2.5 Hardness testing: Wolpert Dia-Testor 50
4.3 Software 50
4.3.1 MatCalc simulation package 50
4.3.2 Abaqus CAE: Finite element modelling program 51
4.3.3 PXF Workbench Point Count software 51
4.4 Alloy characterization 52
4.4.1 As-cast microstructure analysis 52
4.4.2 Grain size measurement/calculation 58
4.4.3 Austenite to ferrite phase transformation – Dilatometer Dil805A 59
4.4.4 MatCalc Scheil solidification model 60
4.4.5 Measurement of Nil-strength temperature (NST) 61
4.5 Summary and Conclusions 63

Chapter 5: Continuous casting process 65

5.1 Different casting conditions 65
5.2 Evaluation of hot ductility and precipitation kinetics 70
5.2.1 Effect of cooling cycle 72
5.2.1.1 Hot ductility: Alloy-0 (no alloying elements) 73
5.2.1.2 Fracture surface analysis: Alloy-0 73
5.2.1.3 Hot ductility: Alloy-1 (micro-alloyed) 76
5.2.1.4 Fracture surface analysis: Alloy-1 77
5.2.1.5 MatCalc precipitation simulation: Alloy-1 79
5.2.2 Effect of strain rate in Alloy-1 85
5.2.2.1 Hot ductility 85
5.2.2.2 Fracture analysis 86
5.2.3 Simultaneous optimization of cooling rate and strain rate in Alloy-1 91
5.2.4 Comparison between Alloy-0 and Alloy-1 at lower temperatures 93
5.2.4.1 Hot ductility 93
5.2.4.2 Fracture surface analysis 94
5.3 Discussion 96
5.4 Summary and conclusions 99

Chapter 6: Slab handling process 101

6.1 Handling procedures and routes 101
6.2 FEM temperature model 101
6.2.1 FEM model: features / data 101
6.2.2 Single slab model (Route-1) 102
6.2.3 Stack/pile 15 slabs model (Route-3) 103
6.2.4 Four slabs model (Route-1) 106
6.2.5 FEM model validation 107
6.2.6 Evaluation of slab surface cooling rates 108
6.3 Evaluation of slab properties before charging 110
6.3.1 Alloy-1 (micro-alloyed): single slab 110
6.3.2 Alloy-1: pile slabs 112
6.3.3 Alloy-1: MatCalc precipitation modelling 117
6.3.4 Alloy-1: SEM evaluation 120
6.3.5 Alloy-0 (no micro-alloying elements): single and pile slabs 121
6.4 Summary and conclusions 123
6.5 Slab ranking system, Alloy-1 125

Chapter 7: Summary and outlook 128

Chapter 8: Zusammenfassung und Ausblick 130

Bibliography 133

List of figures **143**

List of tables **147**

Publications and projects **148**

Nomenclature

Greek symbols

Symbols	Term
α-ferrite	Alpha-ferrite
γ-Austenite	Gamma, austenite
δ-ferrite	Delta-ferrite
ΔL	Elongation or change in length ΔL = L - L0

Latin symbols and abbreviations

Symbols/Acronym	Term
Ae_3	Equilibrium start temperature of austenite-to-ferrite transformation
Al	Aluminium
Ar_1	End temperature of austenite-to-ferrite transformation during slow cooling
Ar_3	Start temperature of austenite-to-ferrite transformation during slow cooling
C	Carbon
CC	Continuous casting
CS	Casting shop
CSG	Crack sensitive grades
dln	Dislocations
EDX	Energy dispersive X-ray spectroscopy
ER	Elongation to rupture
Fe	Iron
FEM	Finite element method
gb	Grain boundaries
GBS	Grain boundary sliding

HSM	Hot strip mill
HV 20	Vickers hardness, 20 kg load
L	Sample gauge length after test
L_0	Sample gauge length before test
LOM	Light optical microscope
Mn	Manganese
N	Nitrogen
Nb	Niobium
NST	Nil-strength temperature
OM	Oscillation marks
PFZ	Precipitate free zone
Ppt.	Precipitates
R of A	Reduction of area
RT	Room temperature
S	Sulfur
SEM	Scanning electron microscope
SZFG	Salzgitter Flachstahl GmbH
TEM	Transmission electron microscope
Ti	Titanium
V	Vanadium
ZDT	Zero ductility temperature
ZST	Zero strength temperature

Abstract

Steel is still one of the most important materials worldwide in terms of demand and economic impact and considered irreplaceable in many applications. Products/parts made of steel can be found mainly in the automotive and transport areas, construction as well as household appliances. Material defects during steel production and downstream cause interruptions to the nonstop production process resulting in reduced production efficiency or even material loss and machinery damage. In a world production scale; energy, time and material loses due to steel slab cracking costs the steel industry hundreds of millions of euros every year.

One of the serious defects facing slab quality and continuity of the planned rolling schedule is surface transverse cracking during continuous casting (CC), transportation/storage or hot rolling. Micro-alloyed steel grades are one of the most susceptible grades prone to this kind of failure due to precipitation of fine particles in critical sizes and distribution. The defect possibility is higher after ferrite formation at lower temperature ranges. Other critical effects during slab cooling emerge later on in the slab storage area or by reheating in the hot strip mill (HSM). Understanding the conditions leading to cracking and perusing its prevention/prediction is in the focus of interest as crack avoidance has an enormous monetary impact by reducing the energy consumption as well as from environmental aspects.

The main objective of this work is to understand and evaluate the potential cracking reasons of steel slabs of the crack sensitive grades (CSG) through an industrial approach in a steel plant. This is considered the base for a prediction model for slab cracking behaviour based on both industrial and laboratorial results. CSG follow a special casting and handling set of regulations in terms of casting speed, secondary cooling, stockyard handling and temperature for charging into the reheating furnaces. The statistical analysis of the defected/cracked slabs enlightened the slab temperature and deformation histories and possible deviations from ideal/set production instructions. Critical failure parameters were defined, classified and ranked according to their influence on the cracking risk.

The effect of process variations and disturbances on surface cracking for the two steel grades; **Alloy-1** (0.08% C, 0.12% Ti and 0.05% Nb) and **Alloy-0** (0.08% C and 0.001% Ti) was evaluated. The defects during the CC process were studied by hot tensile testing (Baehr DIL805 A/T), microstructure investigation, and simulation of precipitation kinetics of Ti- and Nb-carbonitrides using MatCalc software. Furthermore, a FEM (finite element method) temperature model (by Abaqus CAE) was developed to evaluate temperature profiles on different slab regions during slab cooling at different handling routes. The validated

temperature prediction helped to study the effect of different routes - according to the planned charging temperature into the HSM - on phase transformation and material properties before furnace charging. Finally, the critical situations during production that possibly lead to cracking were defined, explained and confirmed by industrial analyses. The cracking mechanisms of these types of steel grades could be predicted and will be used as a base for the extension to further critical grades.

Zusammenfassung

Stahl ist einer der weltweit wichtigsten Werkstoffe in Bezug auf Nachfrage und wirtschaftliche Auswirkungen und wird in vielen Anwendungen als unersetzlich angesehen. Materialfehler während der Stahlproduktion führt zu Unterbrechungen des Nonstop-Produktionsprozesses, was zu einer verringerten Produktionseffizienz oder sogar zu Materialverlust und Anlagenschäden führt. In einem Weltproduktionsmaßstab; Energie-, Zeit- und Materialverluste durch Risse an Stahlbrammen kosten die Stahlindustrie jedes Jahr Hunderte Millionen Euro.

Einer der gravierenden Defekte bei der Brammenqualität und Kontinuität des geplanten Walzprogramms ist die Oberflächenquerrissbildung beim Stranggießen, Transport/Lagerung oder Warmwalzen. Mikrolegierte Stahlsorten sind eine der anfälligsten Sorten, die aufgrund der Ausscheidung feiner Partikeln in kritischen Größen und Verteilungen für diese Art von Versagen anfällig sind. Die Defektmöglichkeit ist nach Ferritbildung in niedrigen Temperaturbereichen höher. Weitere kritische Effekte beim Abkühlen einer Bramme treten später im Brammenlager oder durch Wiedererwärmung in der Warmbandstraße auf. Das Verständnis der Bedingungen, die zu Rissen führen, und die Durchsicht ihrer Verhinderung/Vorhersage stehen im Fokus des Interesses, da die Vermeidung von Rissen enorme finanzielle Auswirkungen hat, indem sie den Energieverbrauch sowie unter Umweltaspekten reduziert.

Das Hauptziel dieser Arbeit war es, die möglichen Ursachen für die Querrissentstehung in Stahlbrammen ausgesuchter rissempfindlicher Sorten durch einen industriellen Ansatz in einem integrierten Hüttenwerk zu analysieren und zu bewerten, um diesen als Grundlage für ein Vorhersagemodell zur Rissentstehung in Brammen zu nutzen. Basis dazu waren neben der Analyse von Betriebsdaten auch Laboruntersuchungen an diesen kritischen Sorten.

Rissempfindliche Sorten unterliegen im betrieblichen Ablauf speziellen Vorschriften für das Stranggießen (Gießgeschwindigkeit, Sekundärabkühlung) und das Handling im Brammenlager und der Lagerung bis zum Einstoß in die Wiedererwärmöfen im Warmwalzwerk. Die statistische Analyse der über mehrere Jahre defekten/gerissenen Brammen ermöglichte die Erfassung der Temperatur- und Umformungshistorie der Bramme und mögliche Abweichungen von den für diese Sorten geltenden Vorgaben. Kritische Parameter konnten definiert, klassifiziert und nach ihrem Einfluss auf das Rissrisiko eingestuft werden.

Die Auswirkung von (erkannt kritischen) Prozessschwankungen/-störungen auf die Querrissbildung wurde untersucht und bewertet für die zwei Stahlsorten Alloy-1 (0,08% C, 0,12% Ti und 0,05% Nb) und Alloy-0 (0,08% C und 0,001% Ti). Die während des Stranggießens auftretenden Defekte wurden durch Warmzugversuche, die im Umform-dilatometer DIL805 A/T durchgeführt wurden, Mikrostrukturuntersuchungen und Simulation der Ausscheidungskinetik von Ti- und Nb-Karbonitride mit MatCalc Software untersucht. Darüber hinaus wurde ein FEM-Temperaturmodell (Finite Elemente Methode) mit Abaqus CAE entwickelt, um die Temperaturprofile auf verschiedenen Brammenbereichen während der Brammenabkühlung auf verschiedenen Erzeugungsrouten zu berechnen. Die validierte Temperaturvorhersage half dabei, die Auswirkung verschiedener Routen - entsprechend der geplanten Einstoßtemperatur in die Warmbandstraße - auf die Phasenumwandlung und die Materialeigenschaften vor dem Ofeneinsatz zu beschreiben. Schließlich wurden die kritischen Situationen während der Produktion - die möglicherweise zu Rissen führen - definiert, erklärt und durch die industrielle Analyse bestätigt. Die Rissmechanismen dieser Stahlsorten können vorhergesagt und als Grundlage für die Erweiterung auf weitere kritische Sorten genutzt werden.

Chapter 1: Transverse cracking of slabs

The worldwide steel production (approximately 1870 million tons crude steel in 2019 - according to World Steel Association) contributes to a huge part of the global trade and economy. Securing safe, environmentally friendly and uninterrupted steel production processes assures high production efficiency and market stability. Nowadays, more than 90% of the worldwide steel production is produced by continuous casting (CC). The defect of only 0.5% of CC production costs the industry hundreds of millions € every year in a worldwide scale. Besides, the cost of process interruption duration and the extra operational and energy costs have to be added.

This thesis deals with the potential transverse cracking that might appear during the production and handling of micro-alloyed steel slabs, in particular in the process chain starting from CC followed by handling and logistics in the slab storage area and ends by charging into the reheating furnace of the hot strip mill (HSM). It represents an industrial and scientific approach investigating the problem of transverse cracking of slabs through defined production routes. This thesis tries to give reasonable answers to questions like: Why does surface transverse cracking take place and how? Is it possible to define the cracking situations/critical conditions for some grades? And how to ensure a nonstop process and bypass any potential interruptions by optimizing the processing routes and charging schedules of slabs with critical conditions?

This is an approach in trying to understand the cracking phenomena in terms of reasons and mechanisms in both, research and industrial contexts. The big aim is offering a practical solution to avoid material damage and process disturbance. The scope of this work is focusing on defining and studying the critical situations - deviation from ideal practice - that might lead to slab cracking during CC, slab transportation or yard storage up to feeding into the reheating furnace. Applying the findings of this work to planning of slab logistics and rolling schedules is believed to enhance securing a smooth and uninterrupted production process.

In this regard, it is important to note that in this context, a safe process permanence is the first priority. This means, in the HSM for example, that eliminating/sacrificing a slab with high cracking probability from the rolling schedule due to a high possibility of surface or internal material damage in order to save the process is to be much appreciated than to risk the hot rolling mill efficiency and process continuity. Trouble in the reheating furnace by a cracked slab will strongly influence production efficiency and might last for hours or even days. Changing the slab's processing route or its charging schedule - according to its casting conditions and current temperature -, could be a solution in many cases to avoid both, risking the HSM and wasting energy costs. Slab cracking/breakage in the reheating furnace or by early roughing passes is considered to be the worst-case scenario for the HSM and removing such a 'critical' slab from the rolling schedule in advance or adjusting its handling process, would be the highly acknowledged solution. The question here is

which slabs are more sensitive/subjected to cracking than others, how to rank those sensitive grades, and how to handle them in a safe way.

Scientific research approaching solutions for current industrial problems, developing ideas for real industrial challenges and building models for process optimization, is - in my opinion - one of the most reasonable investment of scientific studies into practice. This work is a result of a cooperation and mutual reach project between the Department of Metal Forming and Processing in the Institute of Metallurgy, Clausthal University of Technology, and Salzgitter Flachstahl GmbH (SZFG), Department of HSM.

1.1 Thesis layout

This dissertation is composed of eight chapters followed by listing of the bibliography and lists of the presented figures and tables. **Chapter 1** gives a short overview about the steel industry. **Chapter 2** explains the risk of slab transverse cracking problems, the results of a statistical analysis using SZFG data, and the plan of the experimental work and objectives. In **Chapter 3**, the state of the art is explained in a detailed literature survey. **Chapter 4** illustrates the materials, instrumentations, devices and software used to produce the experimental work. The CC process and the effect of deviation from ideal process parameters on crack sensitivity is analyzed in **Chapter 5**. In **Chapter 6**, the effect of slab handling and transportation routes on cooling and the corresponding microstructure development are studied. **Chapter 7 and 8** are summarizing the results of the thesis and recommendation for further work is given in English and German, respectively.

Chapter 2: Big picture and objectives

This chapter gives an overview of a common production and handling process from casting to charging into the reheating furnaces of a hot strip mill (HSM). The key parameters for the experimental work and thesis objectives and outlines are described.

2.1 SZFG Steelmaking plant

Steel slabs of different grades with dimensions mostly (10 – 12 m) in length, (220 – 350 mm) in thickness and up to 2500 mm in width are cast in the casting shop (CS), which includes four continuous casting (CC) machines. In normal cases, slabs of crack sensitive grades (CSG) - according to handling requirements - have to follow one of three designed transportation roots after casting. The slab route is planed based on which class of material the slab belongs to and the schedule of the HSM.

Route-1 is the fastest route designed for direct hot charging into the HSM, Route-2 represents very slow cooling in an isolated closed box for later warm charging, while Route-3 is stack cooling down to an ambient or room temperature (RT) in the slab storage area and later cold charging into the HSM according to the rolling schedule. Slabs taking Route-1 will follow a slow cooling schedule, but faster than Route-2 slabs (box cooling). Slabs from most of CSG are - in general - not allowed to cool down below 250 °C or 150 °C. Those slabs are scheduled for hot and warm charging with charging temperatures > 250 °C or 150 °C, according to the charging instructions. **Fig. 2.1** shows a sketch of the handling process.

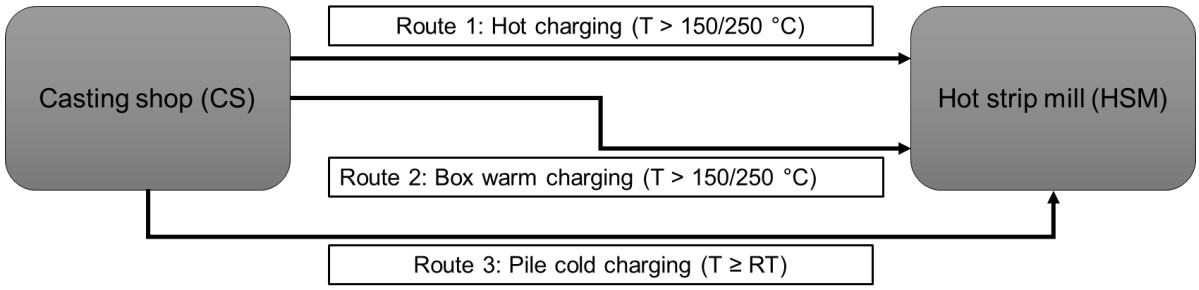

Fig. 2.1: Transportation routes of CSG from CS to HSM

CSG differ in their chemical compositions and handling guidelines and are often prone to surface cracking. Surface cracking might take place during/by the end of casting process, during transportation and storage or even in the reheating furnace of the HSM. The work will be classified into two parts: part one, analysis of the CC process (**Chapter 5**) and part two transportation, handling and charging (**Chapter 6**). First, a complete statistical analysis of cracked slabs over a period of four years was carried out to investigate the history of damaged material and get familiar with grades having higher cracking risk.

2.2 Statistical analysis

Based on plant analyses, this part is giving answers to some basic and critical questions like: which grades are sensitive to surface cracking? Under which (abnormal) production condition might cracking occur? Is it possible to repair a cracked slab? And what damage does a cracked slab represent to the HSM process beside the material loss?

To give an answer to these questions, the process mentioned above was observed and analyzed in terms of production and handling histories over four years. The purpose is understanding the course of ideal/set process and how far a (small) deviation from ideal process can lead to defects. The plant analysis and statistics are meant to be presented as the first step in the problem analysis, as it is the base for the work structure before literature overview and experimental work. Based on the plant analysis, the objectives are to be defined and the experimental work is to be planned.

2.2.1 Cracking risk

A surface crack is hard to repair - if not irreparable -, especially when the slab has to follow a hot or warm charging procedure during limited time durations and is not allowed to cool down under critical temperatures which would result in slab scrapping. Apart from scrapping a semi-finished product, the risk of surface cracking is much higher than just losing a single cracked slab. Loss of a slab might be acceptable in any production lines compared to a possible schedule interruption of the production that might result in case of process breakdown, which is the real trouble. A slab with surface cracks or broken slabs might cost the CS or the HSM some production minutes/hours until the parts of the hot slab (mostly above 1000 °C) are removed and the production is ready to proceed again. Sometimes for safety reasons, getting rid of a broken slab cannot take place at high temperatures, which means it should be waited until the broken pieces cool down. Worst-case scenario is when a slab is broken in the reheating furnace in HSM and blocking the hot rolling process or preventing the continuity of the reheating furnace practice. An example of a broken slab in the HSM is shown in **Fig. 2.2**. Another example of a broken slab during storage in the stockyard is given in **Fig. 2.3**. According to the study done by Zappulla [1] in 2020, annual sales of steel products produced by CC represents approx. 1.04 trillion US dollars. If only 0.1% of the continuously cast steel products are related to defects, this will result in an affected revenue of more than 1 million US dollars per day in a worldwide scale. A huge care should be given to such a critical and expensive process.

2.2.2 Grades

In this industrial analysis by SZFG, the production history over four years of all cracked slabs and their melts/charges from CC, transportation and stockyard of the HSM shows surface cracking in 637 cases. Failure by cracking of the slabs concentrated on only 50 steel grades with – on average – less than 0.5% of their specific total production amount. However, as mentioned above, it is not only about the loss or scraping a slab, but it is about assuring a non-stop casting and rolling processes without process disturbance due to cracked or broken slabs. If the average slab failure of certain grades is 0.5% (resulted from this study) is close to a worldwide failure values, the economic impact would be very huge and needs to be studied and reduced.

The concerned cracked grades vary according to their chemical compositions. For simplicity, they are classified into two groups. Group one represents low carbon steels with a

carbon content between 0.05 - 0.3% - all chemical composition contents in this work are given in wt.% unless otherwise mentioned - and micro-alloying elements like Ti, Nb and V. While group two represents high carbon steels with carbon contents between 0.6 - 1% and alloying elements such as Cr, Mn, Si and Mo. The number of cracked slabs from each of the 50 concerned grades varies between 4 and 70 pieces depending on the grade and processing conditions. For slab history analysis, five grades with the highest repetition of occurrence were studied in detail in terms of casting and handling conditions.

Fig. 2.2: Broken slab in HSM reheating furnace (Furnace breakdown time: 5.5 h)

Fig. 2.3: Broken slab in the HSM stockyard

2.2.3 Slab history and potential cracking reasons

Around 22% of the cracked 637 slabs root from only five grades (representing 142 defected slabs), which are the scope for this statistical and processing history analysis. The main objective here is to find out by statistics what was different in processing and history of these slabs that might have led to cracking, while the other slabs out of the same melt/charge were not prone of cracking. This leaves us to studying the history not only of

the failed 142 slabs, but also of every slab within their melts. Studying the history of a slab in this manner means checking the casting procedure, in terms of solidification, casting temperatures, primary and secondary cooling, slab sequence in the melt, casting speed and deformation. Moreover, slab handling after casting, slab route to HSM, slab handling in the storage area, temperature profiles before charging in HSM are all critical parameters to study. Most importantly, checking the data from the process control system, if there were any parameters went out of the allowable set values. If yes, then how often does this deviation happen and finally, compare it with the situation of the slabs, which did not fail. This will be shown in detail later on in this chapter.

Before analyzing the history of the 142 melts, it is important to refer to the concept of ”correlation does not imply causation” which was applied to judge/rank the important factors. In statistics, this phrase refers to the inability to legitimately deduce a cause-and-effect relationship between two variables solely based on an observed association or correlation between them [2]. In other words, it is important to keep in mind that not all recorded deviations from set/ideal values of an ideal process are critical reasons for cracking or even relevant to it. A factor with deviation from set values should only be considered when it is related in a way to cracking mechanism. Avoiding false statistics will lead to more precise results and a better experimental plan. That was considered in this work.

After studying the 142 melts with more than 1100 slabs and their history, the cracking potential causes were listed as basis for the further experimental work. Before starting any experiments or simulations, the frequency of occurrence of those factors was checked within the total production over the same time range to avoid any misleading causes or statistical fallacies. For example, low casting speed and changing the tundish were recorded for many of the cracked slabs in the casting shop. Comparing the frequency of the appearance of these two factors for the same grades and the total production at the same time range shows clearly that changing the tundish is not – or much less - a crack related factor. That was clear after observing that many/most of slabs with the same “changing tundish” record didn’t show any cracking problems. While on the other side, many slabs with low casting speed record were always related to cracking during CC or later on during further processing steps. This could also be proven by experimental work and literature. It is important to filter the potential causes through comparison with sound slab records and literature work before planning a research program.

After analyzing and comparing the casting and handling history of the 142 melts (more than 30,000 tons) production of this five grades in a time frame of four years, the following factors are the potential causes of the surface cracking, that took place only in relation to defected slabs. The findings of the analysis of the 142 melts are the base of the experimental and research work. The cracking potential factors could be categorized in three groups, listed in **Table 2.1** below, according to how often they occurred (frequency arrangement).

Table 2.1: Potential cracking factors

Group-1	Deviation from ideal casting procedures	(70%)
Group-2	Failure in handling between CS and HSM	(55%)
Group-3	Delayed charging into HSM	(12%)

No especial effect of a certain time/season over the years could be stated after condensing the CC production and HSM charging dates and times. In this analysis, the cracking was related to the factors listed in **Table 2.1**, whenever it took place during the year. Factors from Group-1 appear in 70% of the cracked slabs, bearing in mind that many cracked slabs

had causes from more than one group at the same time. Failures in Group-1 include slab shell breakthrough (break-out) in the casting machine, low casting speed, and deviation from chemical composition with high nitrogen content. Those slabs were broken mostly in the area of the CS.

Group-2 represents 55% of the cracked slabs and includes slabs being first or last in the casting sequence of their melts and the slabs with length adjustment requirements (longer slab length than the width of the HSM furnace, which need further handling by cutting off some meters from the head). Those slabs failed mostly in the slab storage area.

Group-3 represents 12% of the cracked slabs and this took place when hot/warm charging of certain grades failed to be fulfilled for any logistics reason and cracks could not be observed before furnace charging. Those slabs had a cold charging procedure after abnormal/unexpected cooling conditions during storage in the stockyard. Cracking is mostly observed in the reheating furnace of the HSM or directly after furnace discharge before hot rolling or latest after few passes in the roughing mill. Examples of transverse surface cracks after slab discharge from the reheating furnace and during roughing are shown in **Figs 2.4** and **2.5**, respectively.

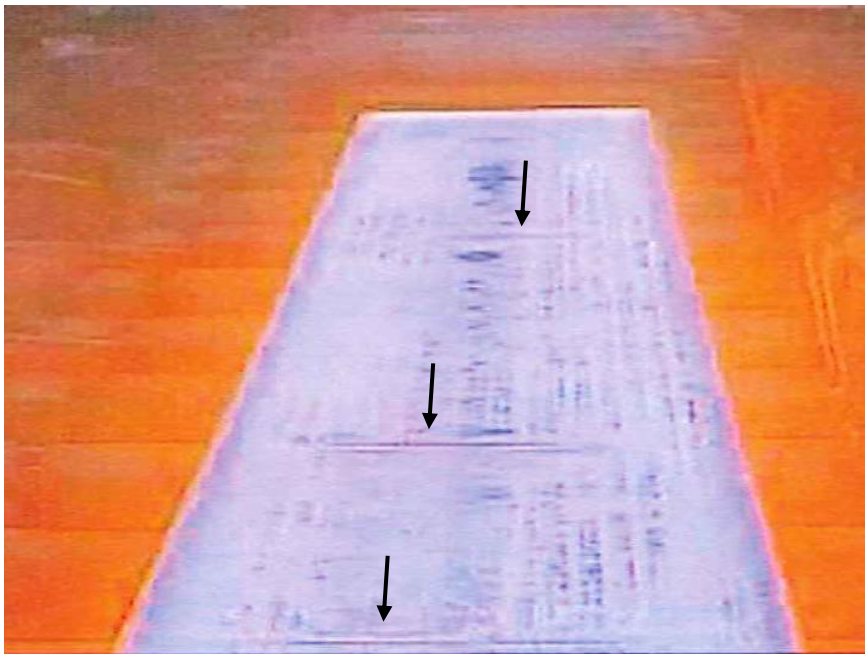

Fig. 2.4: Surface cracking after slab discharge from reheating furnace

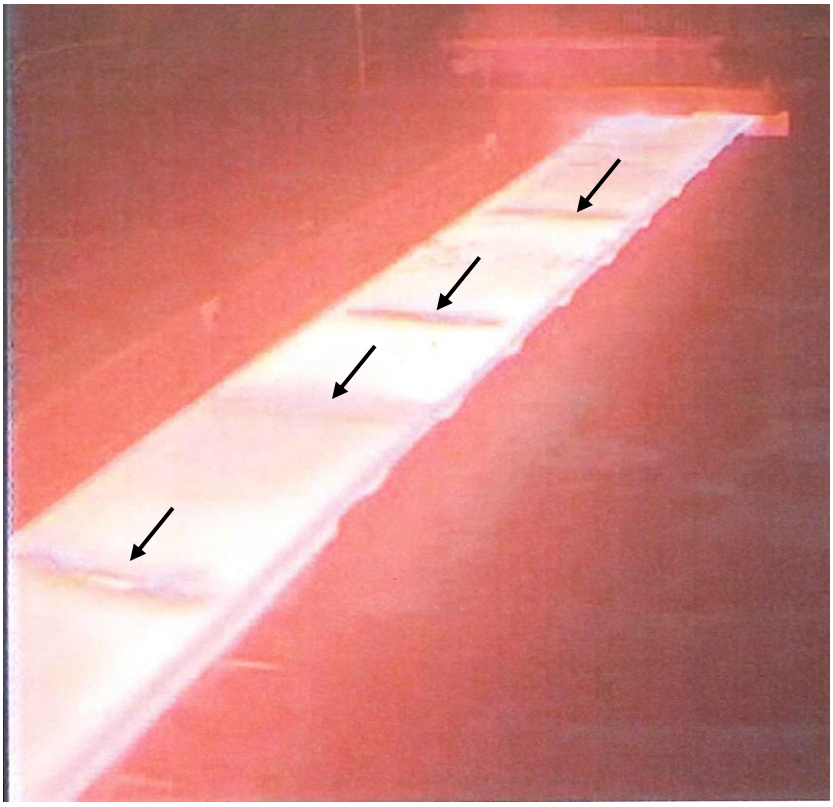

Fig. 2.5: Surface cracking during roughing rolling

2.3 Objectives

The previous analysis is proving that surface cracking is more a consequence of a critical situation composed of different factors taking place at the same time, than just being limited to be based on a critical chemical composition. CSG will not crack under set/ideal production conditions, which happens in 99.5% of the cases according to this study. Also grades which are not CSG might be prone to cracking under severe abnormal casting and handling conditions. The main objective here is to define the critical situations in the first place and to avoid their fulfillment in real production. In this context, CSG will be more relevant and risked than other grades.

A critical situation in the industrial context is composed of deviations in one or more factors like: chemical composition, casting speed, straightening temperature and deformation, and cooling and charging practices. In scientific research work, a deviation is defined critical by occurrence or reaching critical values of the following parameters; hot ductility, grain size, amount of micro-alloying elements, size and distribution of fine carbonitrides, deformation and cooling rates, ferrite formation, phase transformation, and precipitation kinetics.

In accordance with the findings of the previous analysis, the factors affecting crack sensitivity will be studied in two parts on laboratory experimental level using industrial values. Part one (**Chapter 5**) is related to the CC process and part two (**Chapter 6**) to slab transport and handling after casting until HSM. The plan of the experimental work packages is illustrated in **Fig. 2.6**.

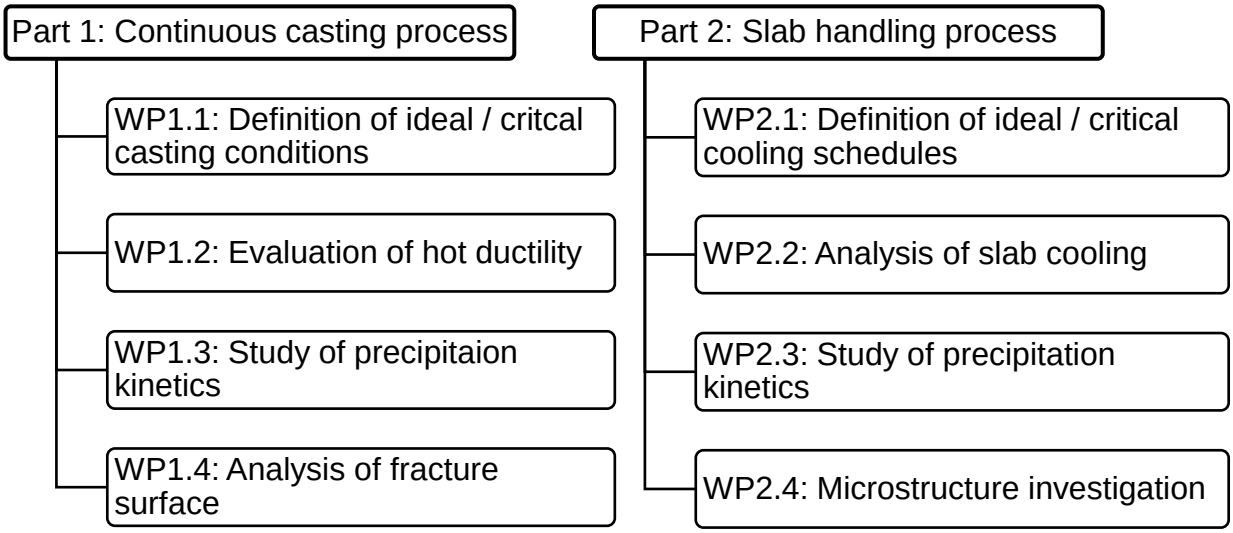

Fig. 2.6: Experimental work packages

The objectives of the experimental work in Part 1 are as following:

1. Evaluation of hot ductility and precipitates distributions (types and sizes) in the temperature range of ideal casting process
2. Evaluating the effect of deviation in casting speed and straightening temperature on hot ductility and precipitates sizes under abnormal casting conditions based on selected industrial cases
3. Studying the microstructure evolution and failure mechanism during CC under ideal and abnormal casting conditions
4. Defining critical situations for cracking

The objectives of the experimental work in Part 2 are:

1. Studying the transformation temperature, microstructure, phase distribution and precipitates (types, sizes and distribution) at the slab surfaces during storage cooling and by charging into HSM under ideal transportation and handling conditions
2. Evaluating the effect of different cooling conditions representing different handling routes and slab positions during storage on microstructure, phase transformation and precipitation kinetics of slab surface before charging into HSM
3. Studying the effect of charging temperature
4. Defining critical situations for cracking

Chapter 3: Literature survey

Many researchers [3-14] exerted decent efforts over many years of intensive research studying the process of continuous casting (CC), surface and inner defects of steel slabs, the phenomena of transverse cracking and the factors affecting it. Their work is nowadays the base for most of the published literature in this field.

3.1 Continuous casting process

3.1.1 Process

In CC process, illustrated in **Fig. 3.1**, the process starts with molten steel flowing from a ladle, through a tundish, then into the mold. A slag cover over each vessel and ceramic nozzles between the vessels ensure that the steel is protected from exposure to the air. Once in the mold, the molten steel - covered with a slag, working as protection against oxidation and as a lubricant - solidifies by cooling of the water-cooled copper mold walls to form the first solid shell, which is referred to as the primary cooling. The newly solidified shell is continuously withdrawn from the mold by the drive rolls at a rate or “casting speed” that control the flow of incoming metal, so the process ideally runs in steady state. Below mold exit, the solidifying steel shell acts as a container to support the remaining liquid. Rolls act as support to minimize or avoid any possible bulging that might arise because of the ferrostatic pressure. Between the rolls, strand surface cooling is fulfilled by water and air spraying at defined rates to control its surface temperature until the molten core is solid, which is referred to as secondary cooling [15].

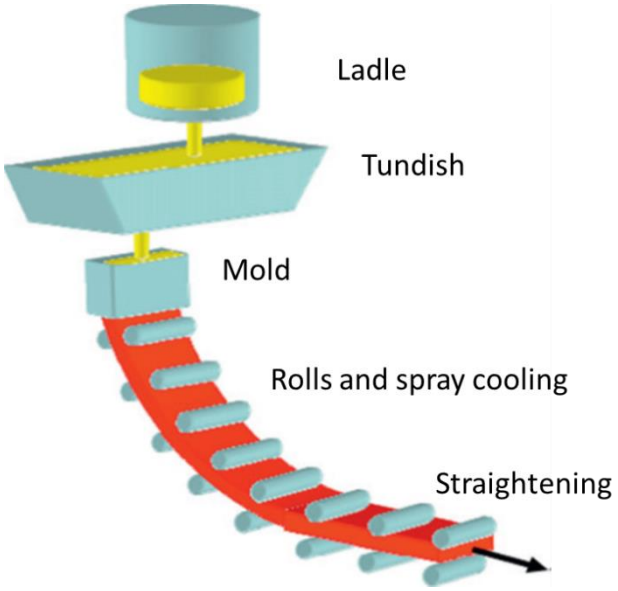

Fig. 3.1: Schematic of steel continuous casting process [16]

Finally, after the strand has solidified throughout its cross section, it is straightened by unbending rolls, if processed in a bow-type CC plant or vertical bending type continuous slab caster. This straightening or unbending operation causes tension stresses on the top surface of a slab. Depending on the steel quality, the temperature at unbending is in the range of (750 - 1000 °C) [17-19]. After the center is completely solid (at the “metallurgical length”), the strand can be torch cut into slabs [15] in defined dimensions. Finally, slabs are lifted by cranes and transported on wagons to the slab storage area or direct rolling.

Starting from the point where the skin begins to solidify in the mold until after the solidification is complete, the continuously cast section is subjected to a complex history of thermal and mechanical stresses [12]. Lankford [12] studied these stresses and strains in solidifying continuous cast sections including mold friction forces, thermal stresses, ferrostatic pressure in/and beneath the mold and the bending forces. He stated that under some conditions of temperature and thermal history, the ductility of certain zones of the solidified portion of the cast section is reduced. Therefore, for high internal quality, it is important that the design and operating parameters of a CC machine should be such that tensile stresses in the solidifying section can be kept to a minimum [12].

3.1.2 Solidification

Solidification of steel in CC is an important parameter, especially in terms of grain sizes and distribution of micro-alloying elements. Solidification is predominantly dendritic in the columnar zone due to the constitutional super-cooling and preferred crystallographic growth [20,21]. Depending on the C-content of the steel, different solidification modes control the evolution of the cast structure. The solidification diagrams are usually for equilibrium cooling conditions, however, in actual steel solidification, the kinetic effects can modify the phases and sequences expected [20,22].

In the process of thick slab casting (200 – 250 mm), the first element to solidify at the interface with the water-cooled mold will be Nb depleted δ-ferrite. These areas in the slab will be later on associated with the surface and subsurface regions of the rolled plate. Solidification at the subsurface region will generally be completed as δ-ferrite, due to increased cooling rate resulting in non-equilibrium solidification. This might consequently lead to micro-segregation of elements such as Nb in the interdendritic or cellular boundary areas to coincide within the δ-ferrite/δ-ferrite grain boundaries. The position and timing of the formation of Nb and/or Ti rich phases in this early stage of solidification, plays an important role of the properties of the slab in its final stages. If full transformation from δ-ferrite to austenite occurs prior to precipitation of Ti and Nb rich phases, then the center of the austenite grains will correspond to the solute enriched region whilst austenite/austenite grain boundaries will be solute depleted [20]. Otherwise, it would be expected that more solute content might be located on the austenite grain boundaries if microsegregation overtakes a complete δ-ferrite to austenite transformation.

In the case, where the transformation δ-ferrite to austenite occurs prior to the solute elements precipitation, the solute content in the austenite grain centers will be higher as cooling proceeds. This will result in a greater driving force for precipitation to take place and formation at higher temperatures. This gives more time for growth and a higher volume fraction to form due to the higher amount of solute. The number density of the particles will depend on the nucleation rate. Depending on the slab cooling practice, the austenite might transform to a matrix composed of ferrite (mostly on grain boundaries) and pearlite (mostly

in grain center). In this case, it can be expected that in low carbon steels there will be a greater Nb(C,N) precipitate size and number density in the pearlite and the ferrite grains close to the pearlite regions with limited pearlite content. Therefore, the separation between the high precipitate number density regions is expected to be similar to the separation between δ-ferrite grain boundaries. This means the secondary dendrite arm or cellular spacing as reported by Kundu in [20]. Nb rich carbo-nitrides (Nb(C,N) or (Nb,Ti)(C,N) or (Nb,Ti,V)(C,N)) can be found in polyhedral, globular and plate-shape (10 - 300 nm) and are expected to form at ~ 1000 °C in austenite [20,23-25].

At room temperature, traces of particle arrays following the grain boundaries of prior austenite (or even δ-ferrite) were recorded by many researches. Similar findings will be illustrated in the coming chapters. The particles of Nb, Ti and V carbo-nitrides appear to settle on particular locations, as well as taking a random distribution form [20,24]. With increasing the Ti content (0.03%) at the presence of sufficient N (0.012%), cuboidal TiN particles can form in the liquid steel at high temperatures (> 1350 ºC). those particles can grow to large sizes (up to 3 µm). Such precipitates – called primary precipitates in terms of Scheil solidification pattern - can even be visible under light optical microscope (LOM) [20,25] and are distributed randomly in the matrix. Finer precipitates in nano-size formed later after complete solidification are called secondary precipitates and can form on both grain boundaries and/or dislocations. Fine secondary precipitates are only visible under high magnifications as by scanning electron microscope (SEM).

With a drop in Ti (0.001 - 0.009%) and N (0.006 - 0.008%) content, cuboidal TiN particles become smaller in size (70 – 800 nm) [20,23]. Zhang studied the regions where those TiN are forming and according to [23], a higher number density of TiN particles was found at the interdendritic regions compared to dendritic regions. Moreover, a higher number density at the mid-thickness position due to the effect of particles sweeping into the slab center during solidification was reported [23].

3.1.3 Oscillation marks and hooks

Oscillation marks (OM) and sub-surface hook formation can strongly affect the surface quality of CC steel slabs [26-28], leading to cracks and/or slivers defects in the final rolled product. OM are defined according to Sengupta and Thomas [29] as transverse depressions (**Fig. 3.2 a**) running around the strand perimeter, formed during each vertical oscillation of the mold. Periodic oscillation of the mold aims preventing sticking of the solidifying shell to the mold walls. Providing a “negative strip time” period in each oscillation cycle, when the mold moves downward faster than the casting speed, also encourages infiltration of the mold slag into the gap between the mold wall and steel shell [29].

A “hook” is a distinct sub-surface microstructural feature [30-32], that often accompanies an oscillation mark, which varies according to the casting procedure and the chemical composition of the melt [33]. Danger of hooks will be more obvious with decreasing carbon content, slow oscillation, and low casting speed. Hooks tend to entrap mold slag, floating inclusions and gas bubbles, which often lead to surface defects such as slivers and blisters [34,35] during subsequent rolling processes. Examples of typical “curved hook” and “straight hook” shapes are shown (shaded in blue) in **Fig. 3.2 b** and **c**, respectively [30,31]. To eliminate the negative effects of OM and hooks, the slab surface must be machined depending on the defects thickness, which costs time, money and negatively influences the productivity [29,30].

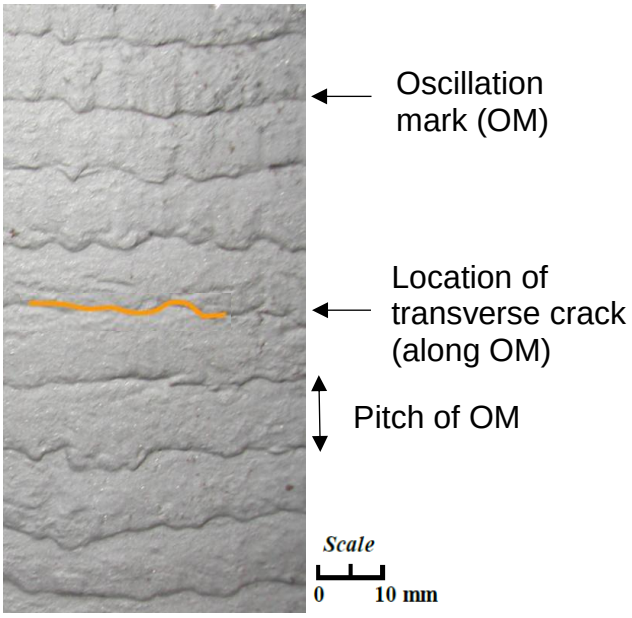

(a) Oscillation marks

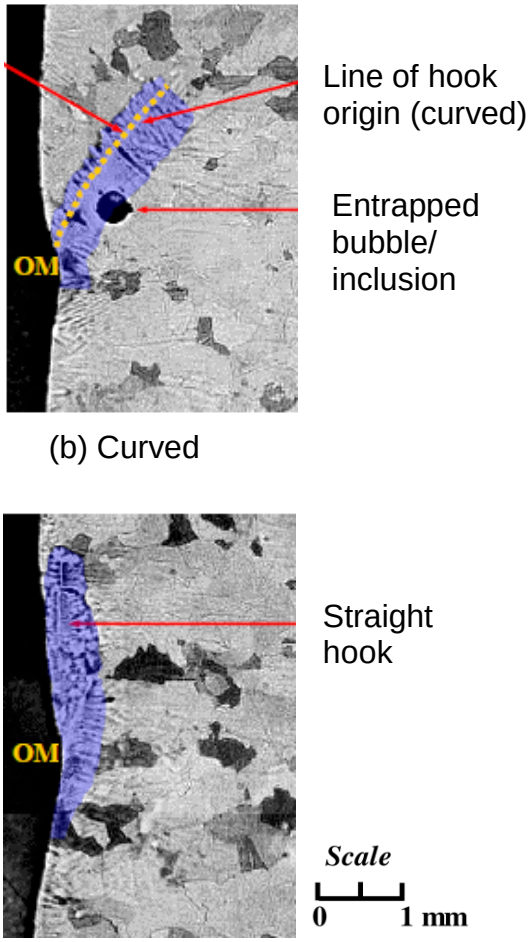

(b) Curved

(c) Straight hooks adjacent to OM

Fig. 3.2: (a) Photograph of oscillation marks (OM) on the surface of an ultra-low steel slab, and optical micrographs showing distinctly different features of (b) curved and (c) straight hooks adjacent to OMs [29,31,32]

Sengupta and Thomas [29] explained a mechanism for the formation of hooks and OM, which is related to the interaction of many complex time dependent physical phenomena near the meniscus where the molten steel surface meets the mold wall, as shown in **Fig. 3.3**.

The meniscus shape will be changed due to the pressure fluctuations in the liquid slag channel caused by mold oscillation. The turbulent flow patterns in the mold cavity bring liquid to the meniscus region with various amounts of transient momentum and superheat. Heat is conducted from the solidification front to the mold through the steel shell, liquid and re-solidified slag layers. The meniscus region might solidify, depending on the local superheat of the liquid, the availability of nuclei sites, the ease of nucleation and growth, and alloy properties such as freezing range. The mold or slag rim may interact with the meniscus and shell during the negative strip period, especially if it is large. Rapid changes in temperature gradient may cause thermal distortion of the shell tip, which depends on the steel mechanical properties and the extent of level fluctuations relative to the shell tip. These events together determine the shape and size of sub-surface hooks and their corresponding OM [29].

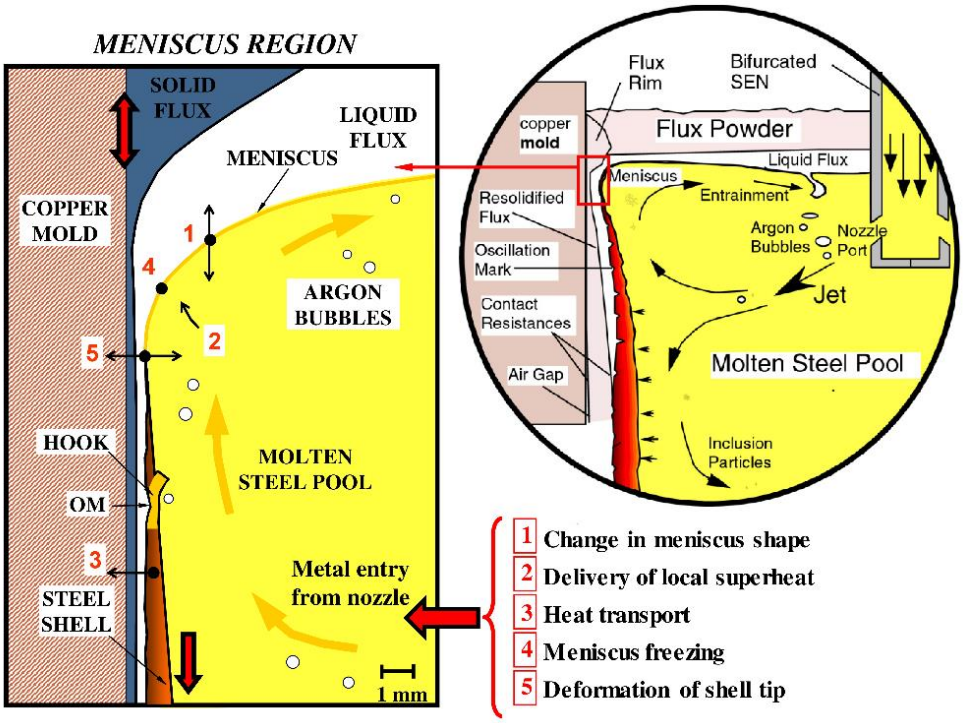

Fig. 3.3: Complex phenomena occurring inside a continuous caster mold (right), influence initial solidification in the meniscus region (left) [29]

Zhang et. al [36] studied the causes and formation of OM and hooks at the corner of CC steel slabs and was able to build a 3D mold model to investigate the shape of the steel-slag interface and measure the height difference between the OM at the corner of the slab compared to those which are further from the corner. According to his analysis, the concave OM and hooks at the corner were caused mainly by the interfacial tension between liquid steel and liquid slag.

3.1.4 Segregation

Segregation can simply be defined as any non-uniformity of chemical composition, which occurs during solidification/freezing of an alloy. Segregation takes place when the solid has a different (usually lower) solubility for alloying elements compared to the liquid causing the alloying elements to partition preferentially into the solid or liquid [20,37]. Micro-segregation forms in a relatively small scale in the range of (10 – 100 µm), while macro-segregation takes place in ranges > 1 mm. One more important difference - besides the size - is the location of segregation, where micro-segregation results from freezing of solute enriched liquid in the interdendritic spaces, while macro-segregation is non-uniformity of composition in the cast section on a larger scale. Centerline segregation can cause many quality problems due to high degree of positive segregation in the central parts of a continuously cast sections as in slabs for example [20,38]. The detrimental effect of segregation is significantly influencing the crack sensitivity of slabs.

3.1.5 Defects

During CC, different surface or internal defects can appear which could result in material scrapping or interruption of further transportation and rolling schedules. **Fig. 3.4** and **Fig. 3.5** show the classification of surface and internal defects, respectively [3,39].

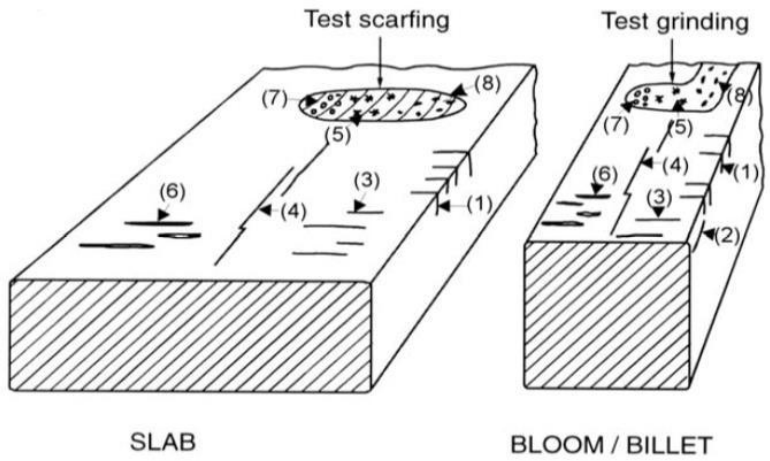

Fig. 3.4: Surface defects [3,39] 1. Transverse corner cracks; 2. Longitudinal corner cracks; 3. Transverse cracks; 4. Longitudinal cracks (broad face); 5. Star cracks; 6. Deep oscillation marks; 7. Pinholes; 8. Macro inclusions

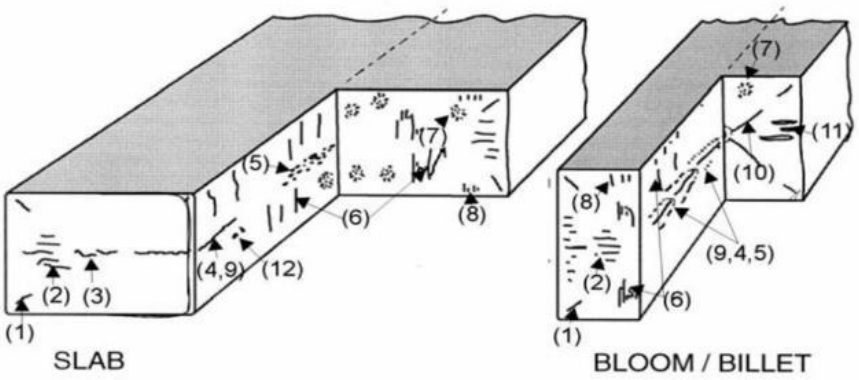

Fig. 3.5: Internal defects [3,39] 1. Internal corner cracks; 2. Side halfway cracks; 3. Centreline cracks; 4. Centreline segregation; 5. Porosity; 6. Halfway cracks; 7. Non-metallic inclusions, clusters; 8. Sub-surface ghost lines; 9. Shrinkage cavity; 10. Star cracks, diagonal cracks; 11. Pinholes; 12. Semi macrosegregation

Brain G. Thomas stated [40] that avoiding internal cracks was a critical challenge to early CC and is still very critical nowadays. Intuitively, internal crack formation depends on the thermal and mechanical stresses to which the shell is subjected. To help investigate the fundamentals of this problem, Brimacombe with Grill [41] and Sorimachi [42] applied the first FE thermal stress models of solidification to understand the internal stress distribution in the solidifying steel strand below the mold. Computational thermal-stress models, also pioneered by Brimacombe, have led to an improved understanding of mold distortion, crack formation, and other phenomena [40].

3.1.6 Transverse cracking

Crowther [3] stated that of the many types of defect in CC products, only transverse surface cracking is strongly influenced by the presence of micro-alloying elements. He stated that Nb has a very huge detrimental effect in promoting cracking even by small additions of as low as 0.01% [3].

Harada et al. [43] studied the formation mechanism of transverse cracking in Al-Si killed steel slabs and referred to local micro-segregation to be the origin of cracks. That was related to the spreading of positive segregation over OM, which showed high phosphorous content. This positive segregation penetrated deeply into austenite grain boundaries, through which transverse cracks propagated [43].

The location of transverse cracks varies between forming on the broad and narrow face or even the corner of CC slabs. They might be difficult to be recognized by visual inspection unless the slab surface is dressed. Transverse cracks are usually associated with the depression of OM explained earlier, and are mostly found on the top slab surface. The cracks lengths can be several tens of mm in extreme cases, and generally follow austenite grain boundaries. They are partially oxidized, but there is little decarburization, and marginal oxidation at the inner end of the crack [3,44]. Fracture surface analysis of transverse cracks has indicated intergranular fracture with ductile dimples initiating at a variety of particle types, but predominantly MnS and AlN [3,45].

Yang et. al. [46] illustrated the factors affecting cracks found on some micro-alloyed steel slabs by some vertical bending type continuous slab casters as illustrated in **Fig. 3.6**. The solidus temperature in the mold interdendritic regions as well as for the OM area decreases due to micro-segregation of residual elements, such as S and P, at the solidifying dendrite interfaces, which eases the fracture along the segregation [46]. The regions of OM have relatively low heat conduction to the mold. A thinner solidified shell in this part compared to the rest of the cast exhibit a higher cracking potential. Any tensile stresses and strains generated on the surface of this weakened part might lead to slab transverse cracking. With decreasing temperature, the surface of the slabs fractured in the temperature zone of reduced ductility exhibits precipitates of various types including (Mn,Fe) sulfides and oxides in austenite grain boundaries [10,46,47].

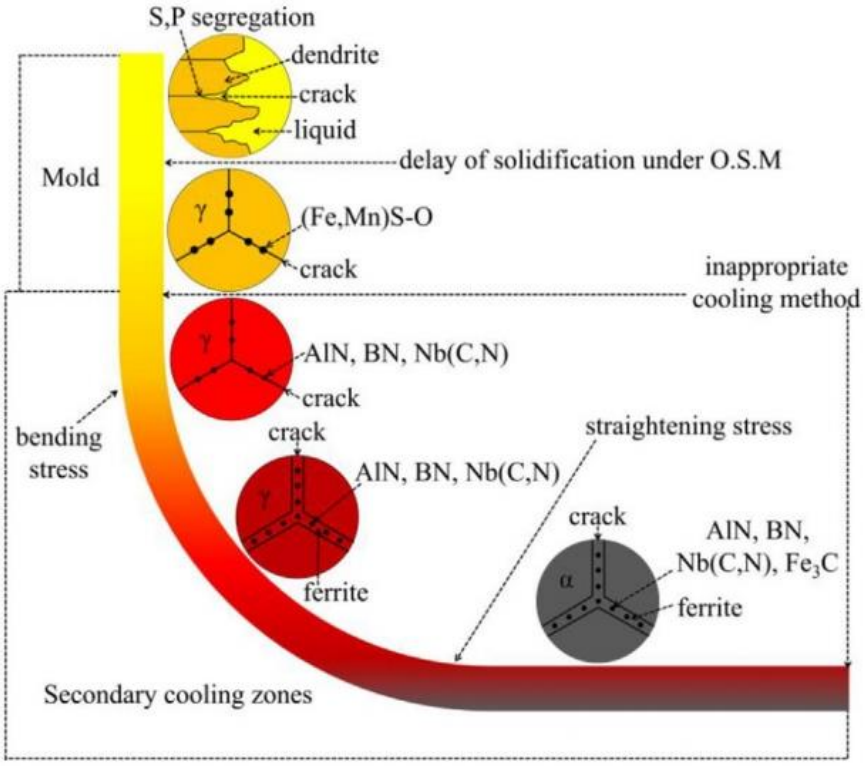

Fig. 3.6: Factors affecting cracks on continuous cast slabs [46]

According to Mintz et. al. [19] the grain boundaries precipitates will result in a strength difference between the grain boundaries and the grain interior. When the grain is subjected to an external force, the strength difference will lead to a stress concentration on grain boundaries, resulting in grain boundaries de-cohesion. Therewith, the hot ductility of the steel is reduced [46].

In CC process, and particularly during unbending, any possible transverse cracking is directly related to the loss of hot ductility. Stresses arising during bending, straightening and friction can lead to transverse cracking especially in regions of ductility troughs. Creep failure might take place in slab fracture due to the coalescence of cavities nucleating at the grain boundaries, including nitrides (AlN, Nb(C,N), BN, etc.), pro-eutectoid ferrite film, and cementite [4,17,46, 48-50].

3.2 Hot ductility of micro-alloyed steels

Many researchers [4,9,10,12,51,52] were investigating the problem of transverse cracking that occurs when the strand is straightened at some stage after exiting a curved mold during CC. The cracks are forming along the OM on the top surface and edges. Straightening takes place in a surface temperature range between 700 – 1000 °C, the same temperature range in which hot ductility - measured by reduction of area (R of A) in a simple hot tensile test - is often observed to give low values [4].

Brimacombe and Sorimachi [7] showed that the cracks observed can probably be linked to two zones of low ductility. Firstly, a high temperature zone, over 1340 °C, which seems to be the reason for most of the cracks, including all internal cracks, secondly, a low temperature zone in the region between 700 – 900 °C, which gives rise to transverse cracking problems at the surface. Combining the low ductility regions with the understanding of the stresses generated during CC makes it possible to propose mechanisms of crack formation and relate them to operating and metallurgical variables [7].

Hot tensile testing has been used to evaluate transverse cracking possibilities taking place during CC of micro-alloyed steels [8]. The original hot tensile test consisted of heating the sample up to (1250 - 1300 °C) to dissolve all existing carbo-nitrides and AlN precipitates and to produce a coarse grain size similar to that one of the as-cast microstructure, followed by cooling with 60 K/min (for a 220mm thick strand) until test temperature. Mintz suggests under these conditions that a reduction-in-area, RA, above 35 - 40% should be reached to prevent cracking [4,8,51].

Cracks are much more likely to occur in regions of low ductility. Several techniques are available to study hot ductility under the conditions relevant - as close as possible - to CC [3]. Calvo et al. [53] carried out tensile tests at temperatures range of (700 – 1100 °C) with an initial strain rate of 5×10^{-3} s^{-1}, to simulate the thermo-mechanical conditions of the straightening operation. After each test, the reduction in area of the samples tested to fracture was used as a measure of the hot ductility [53]. The observation of numerous, large transverse cracks in the final straightened slab, together with the fact that these are often most numerous on the top surface of the slab (i.e. the surface which is in tension during straightening) suggests that there is much crack propagation induced by the stresses endured during straightening [3].

3.2.1 Hot ductility curve

Mechanical properties of steel at high temperature are of major concern in this context as they have critical effects on the formation of cracks during CC, thermo-mechanical processing and heat treatment [17,52,54,55]. Three embrittlement regions at high temperature were reported in [3,56-59] for low carbon and micro-alloyed steel. A typical hot ductility curve as identified by Crowther done under test conditions relevant to CC is sketched in **Fig.3.7** [3].

The embrittlement/low ductility regions can be described as [3]:
Region I: embrittlement by incipient melting
Region II: a) embrittlement by second phase particles - (Mn, Fe)S
Region II: b) embrittlement by second phase particles - Nb(C, N), AlN, V(C, N)
Region III: embrittlement by transformation

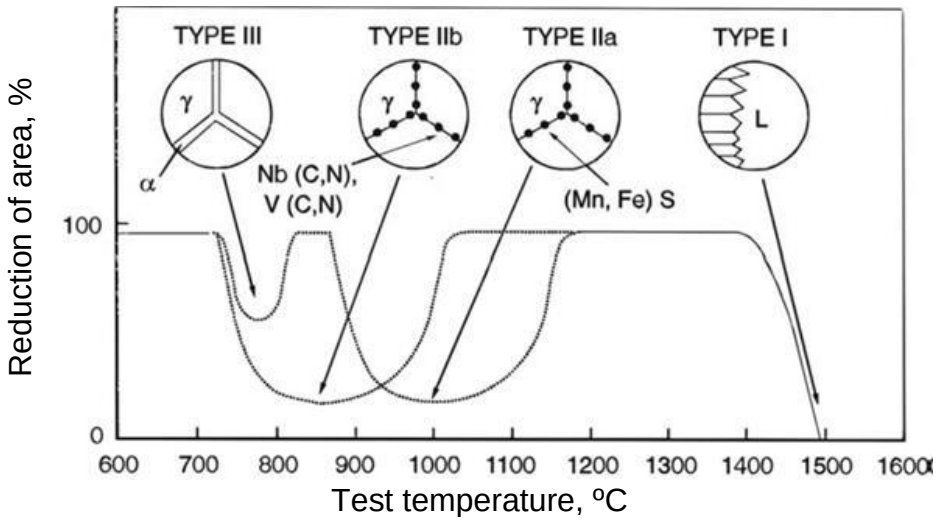

Fig. 3.7: Schematic illustration of types of ductility troughs [3]

The hot ductility curve is very useful for predicting the likelihood of transverse cracking occurring with new steel compositions. The curves can be produced using different testing techniques. Mostly, the hot tensile test is used, giving the R of A on the Y-axis corresponding to the temperature at failure on the X-axis [60]. The information, the curve is giving, can also be used to optimize the CC machine and avoid straightening at the regions of ductility troughs by modifying the secondary cooling and other casting parameters. After hot tensile testing under standardized conditions, a ductility of 40% is required to avoid the problem of transverse cracking [4].

Embrittlement Region-I:
Typically, it takes place at 20 - 50 K below the mean solidus temperature. Analysis of fracture surfaces showed an inter-dendritic failure and the presence of particles such as MnS. This embrittlement region is associated with incipient melting at inter-dendritics and grain boundaries. Low ductility is linked to segregation areas. The segregation of elements - such as S - to inter-dendritic regions during solidification is important for this type [3]. This low ductility region may be responsible for the initiation phase of transverse surface cracks, as small subsurface cracks have been observed associated with OM [61]. The OM are known to be regions of high degrees of segregation of elements, such as S, P and Mn [62]. Heat transfer to the mold decreases in the vicinity of the oscillation mark; this will probably keep temperatures high within the embrittlement region [3].

Steels undergoing a peritectic reaction and transformation make the CC process complicated. Hypo-peritectic steels (C < 0.16%) are particularly susceptible to crack formation [7,63]. Sensitivity to crack formation at the first solidified shell is escalated by additional stresses and strains resulting from the fact that the primary and secondary solid phases have different densities [64-68]. Peritectic transformation generates high tensile stresses and contraction, which can lead to crack formation in the initially solidified brittle material [69-72].

Saleem et al. [63] studied crack susceptibility and the surface cracks that can form during CC due to the volume changes during the peritectic transformation. It was confirmed that the strain caused by the peritectic transformation during CC of peritectic steel makes the cast susceptible to cracking. Segregated and non-segregated cracks were studied. The results show that, according to alloying content, some liquid will be left when all the δ-ferrite has transformed to austenite. The liquid film avoids the formation of inter-granular cracks but will however contribute - due to phase change strain - to a higher crack susceptibility on the grain boundaries between ferrite and austenite. Steel composition and cooling rate play an important role in defining the type of the crack. Based on the remaining volume fraction of the liquid after the peritectic reaction/transformation, inter or intra-granular cracks can be formed. [63].

The mechanical model by Saleem [63] takes into account the thermal, mechanical and phase change strains. The difference in densities between the austenite and the ferrite creates stresses and strains over the interface and results in the strain due to the phase change. Due to the larger molar volume of the δ-ferrite phase, it has been compressed at and close to the δ/γ-interface in order to match the lower molar volume of the γ-phase. It was also shown that the oxidation of the surface can promote the crack growth, cause the crack to thicken and enhance embrittlement of the surrounding material due to the precipitation of the oxides [63].

Hassani et. al. [73] studied hot ductility of micro-alloyed steels and showed a similar hot ductility curve with three low ductility zones [7,58]. In Zone I, which is from 1300 °C to the vicinity of the solidus temperature of steel, the presence of a liquid film - at the austenite grain boundaries during heating or at the interdendritic region during cooling from melting - causes embrittlement [74]. Ductility at the temperature at which this liquid film forms is independent of the strain rate [58,75]. It is mainly affected by the chemical composition and micro segregation of impurity elements such as C, P and S, which change the solidus temperature [58,74-78]. Low strength and ductility in this region is the cause of most of the cracks found in CC [7,73].

Embrittlement Region-II:
This region covers the temperature range of (1200 - 900 °C), depending on composition and test conditions. Fracture surfaces are typically along austenite grain boundaries, and sometimes show the presence of second phase particles, with ductile dimples around them. Sulfides, such as (Mn, Fe)S, and the ratio of Mn/S, in Region IIa, and carbo-nitrides such as Nb(C, N), V(C, N), Ti(C, N) and AlN, in Region IIb, are of big importance in this embrittlement region [3]. Which type of particles are stable at a given temperature, decides which region (IIa or IIb) is to be expected. Lankford [12] linked the ductility loss in IIa to the precipitation of liquid FeS particles and the reduction of grain boundaries de-cohesion due to S segregation. Type IIa of low ductility requires high strain rates, while type IIb ductility loss is becoming worse with decreasing strain rates [12,79,80]. The strain rates during the

processing of CC slabs are too slow for type IIa ductility loss, which means that Region IIa ductility loss is assumed not to be responsible for transverse crack formation, while type IIb will be more critical.

Failure mechanism in type IIb ductility loss starts by austenite grain boundary sliding (GBS), which encourages crack formation at grain boundaries [81] and the presence of carbo-nitrides and second phase particles such as Nb(C, N), V(C, N) or AlN, which was confirmed by the surface fracture analysis. These particles can delay the onset of recrystallization and reduce the strain required for fracture [3], which means that ductility improvement is delayed and fracture can take place at lower strains.

The onset of recrystallization can be linked to the high temperature end of this embrittlement region [82]. If recrystallization can take place prior to failure, any developing grain boundary cracks become isolated and further propagation is not possible. Micro-alloying elements, such as Nb, can retard the recrystallization in solution or as precipitates and can even extend the embrittlement region of IIb to higher temperatures [3].

Embrittlement Region-III:
At temperatures below Region II and depending on the chemical composition, Region III of embrittlement is to be located in the temperature range of (900 – 600 °C). Region II can even merge together with Region III and form a wide ductility drop. Fracture surfaces are characterized by intergranular failures, and the facets of the individual grains are often associated with void formation around second phase particles. Embrittlement in Region III is linked to the austenite to ferrite transformation, where ferrite film begins to form at austenite grain boundaries by cooling below the transformation temperature [3]. There is a directly proportional relationship between the temperature, in which ductility starts to fall at the high temperature end of Region-III and the Ar_3 temperature [83].

By any further deformation within or below the transformation temperatures, strain will be concentrated within the ferrite at grain boundaries, which is softer than austenite. Void nucleation at second phase particles and the growth of these voids continue within the ferrite film and cause ductile failure [57,81,84]. Thus, on a microscopic scale, fracture can be described as ductile, but overall the failure is brittle [3].

As the temperature decrease, ferrite volume fraction will raise, this will consequently result in a uniform strain distribution between austenite and ferrite and accordingly recovers the ductility. Moreover, the differential strength between austenite and ferrite becomes also less, which will again contribute to a more uniform distribution of strain between austenite and ferrite. Around 50% ferrite was suggested for a complete ductility recovery [83].

The improvement in ductility between Region-II and III is probably a result of the absence of this thin ferrite films. In this area, any possible failure takes place either by GBS or through strain concentration in the precipitate free zone (PFZ). In spite of that, at temperatures above Region-III, less precipitation is available in the matrix and at the grain boundaries, which will be detrimental if ferrite is present. Higher temperatures will generally cause lower flow stresses as well due to the increased dynamic recovery, which decreases stress concentrations at potential crack nucleation sites. One more possibility of ductility recovery at higher temperature, if Region-II and III are combined, is that higher grain boundary migration may occur. Cracks can grow inter-granularly during the early stages of deformation, and become isolated within the grains because of grain boundary migration [51,85].

3.2.2 Embrittlement mechanisms

The fracture analysis of the broken samples in the brittle temperature range always showed an intergranular fracture which can be caused by one or a combination of the following mechanisms [60,86]:

1. Formation of precipitate free zone (PFZ)

The presence of PFZ adjacent to austenite grain boundaries represents a region of less resistance to deformation than the rest of the matrix structure [60]. In certain temperature ranges, strain induced precipitants of Nb(C,N), AlN or V(C,N) can be formed at low strain rates [87]. Grain boundaries particles may act as crack initiation sites; or general matrix precipitations can result in strength increase, and hence an overall reduction in ductility [3,9,51,52].

In the regions of single austenite phases, precipitates form preferentially at the austenite grain boundaries as nucleation sites, resulting in soft PFZs adjacent to the grain boundaries. By any further strand deformation, strain will then concentrate in these regions. Micro-voids are formed by de-cohesion of the precipitate-matrix interface during deformation leading to void coalescence and crack propagation along the grain boundaries resulting in intergranular fracture. In **Fig. 3.8 a-c** [88], this mechanism is illustrated. This type of failure mechanism is mainly linked to fine precipitates on the grain boundaries [89].

2. Failure within the thin ferrite films

The thin ferrite films located at the austenite grain boundaries causes intergranular fracture at high temperatures [60]. Strain induced ferrite can start to form at temperatures above the expected Ar_3 temperature, or even as high as the Ae_3, during cooling [90]. Ferrite takes the shape of thin films along the austenite grain boundaries [58]. At any given temperature, ferrite has lower flow stresses compared to that of austenite because of its higher recovery rate. Higher strain concentration will be built up by ferrite, which will be softer than austenite. The failure mechanism caused by the de-cohesion [91] at precipitates on the prior austenite grain boundaries is illustrated in **Fig. 3.8 d-f**. Showing the same behavior, the ferrite film plays a similar role as PFZs [90]. Precipitates, such as MnS, are often found in the ferrite films, which enhance the failure. The strain concentration on grain boundaries will decrease, as the phase fraction of ferrite film increases, giving higher ductility values [86].

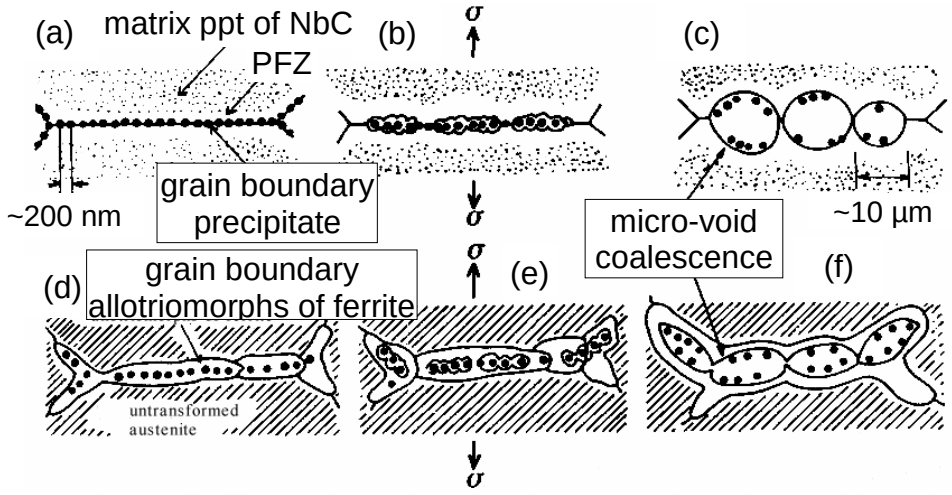

Fig. 3.8: Schematic illustrations showing intergranular micro-void coalescence by deformation in the low temperature austenite region (a-c) and in the two phase γ-α region (d-f) [88]

3. Grain boundary sliding (GBS)

GBS governed by the limited dynamic recovery of austenite and by the occurrence of work hardening build up at triple joints of grains [60]. Potential grain boundary fracture is seriously possible once the built up stresses at triple points of grain boundaries exceed the stress required for grain boundary failure. This leads to intergranular failure by nucleation of grain boundary cracks. Formation of wedge cracks by GBS is illustrated in **Fig. 3.9**. This is considered to be the main deformation and fracture mechanism under conditions of creep i.e. for strain rates at and below 10^{-4} s^{-1} [86,90]. These failure models are critical at high temperatures, when other embrittlement mechanisms, which are mostly linked to the formation of precipitates and the thin ferritic films, are not viable [85].

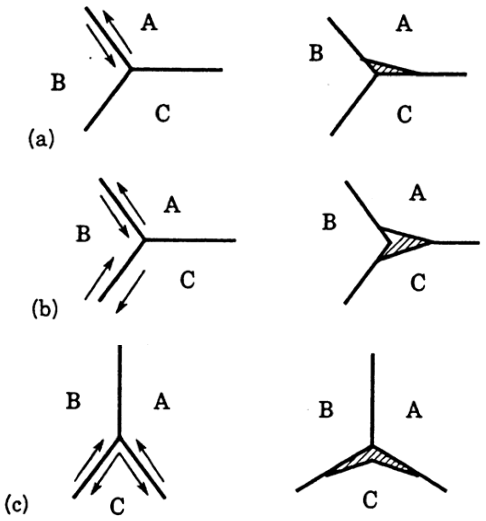

Fig. 3.9: Schematic models showing formation of wedge cracks by GBS. Arrows indicate sliding boundary and sense of translation [90]

4. Suppression of dynamic recrystallization

Dynamic recrystallization in austenite can be retarded by the precipitation of fine carbides or nitrides on grain boundaries during deformation [92]. The mobility of grain boundaries will decrease, which help the voids around the precipitates to grow, enhancing the propagation of intergranular cracks, even in a full austenitic matrix [89]. In [84], the effect of particle size on slab rejection was studied. It could be shown that, with coarse Nb(C,N) on grain boundaries, no plate rejection was recorded, while the rejected slabs had fine precipitates on the grain boundaries. The grain boundary mobility influences the hot ductility based on the size of existing precipitates. Coarser particles with a larger inter-particle spacing are less detrimental to grain boundary mobility and hot ductility than fine, densely-spaced particles [86,89].

Anelli et. al. [93] attempted to link the formation of cracks in Al-killed and Nb-Ti and V steels to the ductility troughs observed at high temperatures after hot tensile testing. Different steel grades were tested under hot tensile test conditions with four different thermal histories. Studying the fracture facets implies intergranular fracture, where the surface is either smooth or covered with fine dimples [51,93]. Anelli suggested two possible embrittlement mechanisms [93]: the segregation of P and S during solidification causing the incipient melting or the delayed solidification of interdendritic pockets [7,75,94], or the scraping of the mold walls and the preferential oxidation of iron, producing an accumulation of Cu at the surface of the strand. This enrichment can lead to the formation of a low-melting phase that can penetrate along the austenite grain boundaries [7,95].

The formation of cracks in Al-killed and Nb-bearing steels in the temperature range of (1100 - 700 °C) is associated to the ductility drop noticed in these steels by tensile testing at slow strain rates. The decrease in ductility was generally linked to a combination of the following factors [51,52,96]:

1. Formation of AlN/Nb(C,N) precipitates during deformation, which enhances the strength of the grain interior and hinders the dynamic recrystallization;
2. Presence of relatively coarser precipitates of AlN/Nb(C,N) on the grain boundaries of austenite, which under deformation conditions can act as potential sites for micro-void formation and linking. This increases the GBS;
3. Existence of a precipitate free zone (PFZ) or thin soft ferrite allotriomorphs on grain boundaries of a matrix of austenite, which results in strain concentration on the grain boundaries.

3.2.3 Relevance of hot tensile testing to crack sensitivity

Many researchers and steel plants use hot tensile testing to build the hot ductility curve over the temperature ranges including ductility drops. Hot ductility, calculated by the R of A of the sample after test to fracture, used to give an indication to cracking possibility at its corresponding test temperature. Steel plants use the hot ductility curves to optimize their casting process and avoid slab deformation at regions of low hot ductility. The regions of low hot ductility (ductility troughs) were recorded by many researchers as the regions where slabs have higher crack sensitivity.

In Dillinger Hüttenwerke AG in Germany, the use of hot tensile tests was first applied in 1973 as a first step towards the avoidance of cracking. According to Bannenberg [83] when the first Nb-alloyed heats were cast, they noticed very quickly that with the addition of Nb transverse cracks - which were not observable without the presence of Nb but with an otherwise identical steel composition - occurred on the strand surface. They established a relationship between the number of transverse cracks per slab and the R of A in hot tensile tests. Above a R of A value of 75%, no slabs failed by cracking [3,83]. Suzuki et. al. [97] suggested a value of 60% R of A to avoid slab cracking.

Another approach by Mintz [98] was carried out after studying the effect of strain rate, grain size and precipitation and suggested that a figure in the range of (30 - 40%) of hot ductility as a limit to avoid cracking is more in keeping with experimental and works data compared to [97]. Moreover, Mintz described some limitations of the hot ductility test in spite of the so much useful information being given from the test. Some thermal stresses were not taken into account in the hot tensile test, but those stresses are resulting from the thermal cycle arising by the temperature fluctuation on the slab surfaces as the strand moves below the mold between rolls. Mintz stated that precipitation is probably the most important variable controlling transverse cracking and the finer it is, the worse is the ductility [98].

Further comments regarding the grain structure after sample reheating in the test compared to columnar grains present at the slab surface were also mentioned. Moreover, the effect of precipitation and segregation patterns in laboratory compared to industrial practice was a matter of discussion. Other researchers worked on improving the simple hot tensile test itself or using other experiments like hot bending or torsion to reproduce the straightening process by CC, or even using other tools, like software simulation packages, to evaluate the missing parts in hot tensile tests, which nowadays is still widely used by steel plants as a measurement for crack sensitivity.

3.3 Factors affecting the hot ductility

3.3.1 Effect of the chemical composition

3.3.1.1 Carbon

The carbon content largely determines hot cracking susceptibility of low alloy steels during CC [85]. The peritectic composition region, (0.10 - 0.16%) C has the highest crack sensitivity [99]. Increasing the C content causes the ductility trough to shift to lower temperatures because of the corresponding decrease in the austenite to ferrite phase transformation [100].

Mintz and Banerjee studied the effect of C and Mn on the hot ductility behavior of plain C-Mn steels, with C amounts < 0.3% and its relationship to transverse cracking [101] in terms of ferrite formation. It could be stated that decreasing the C and/or Mn levels should generally be beneficial as increasing the Ar_3 temperature by narrowing the trough will always help in avoiding transverse cracking [101].

Steels with a C content > 0.28% exhibit a different fracture mode, where the trough position is shifted to approximately 100 K higher [100,102,103]. This shifting will now result in enabling the intergranular failure to take place in the austenite phase because of GBS rather than in thin films of ferrite at the prior austenite grain boundaries. The reason of this change in fracture mode was explained by the fact that the C content increase will be raising the activation energy for dynamic recrystallization and consequently, the critical strain for dynamic recrystallization. It was believed that this increase in the critical strain for dynamic recrystallization produced intergranular failure by enhancing the tendency for GBS in austenite [100,103].

3.3.1.2 Nitrogen

The presence of N has a detrimental effect to the hot ductility only with combination of Al or micro-alloying additions due to the formation of nitrides or carbo-nitrides, which can seriously affect hot ductility. The N as well as the Al levels, have to be kept as low as possible. Typical N levels are < 0.008% [3,9,104,105]. Electric arc furnace steels are more prone to hot cracking owing to the high nitrogen and residual elements content [93]. By Increasing N to 0.01%, a serious deterioration in ductility is possible [49]. Micro-alloyed steels with low N amounts, having C levels in the peritectic range (0.08 - 0.17%) do not show transversal cracking problems as long as the Al level is > 0.04% [104,105]. The nitride precipitates are formed before the carbides in Nb containing steels. High N content encourages the precipitation of Nb(C,N) in the austenite instead of that of NbC as the composition of the precipitate approaches to nitrides more than to carbides. Hot ductility is critical in the range (0.004 - 0.011%) N [9].

In Ti micro-alloyed steels, Ti will combine preferentially with N. The remaining N will combine with any available Al. The amount of N has to be low, to assure a high Ti/N ratio (4 - 5:1) which enhances precipitate coarsening and improves ductility. In these steels, low levels of N should decrease the precipitation temperature for TiN and result in a smaller volume fraction of finer precipitates [105,106].

3.3.1.3 Titanium

The effect of Ti addition is complex and depends on the T:N ratio [3]. Ti could be beneficial in reducing the transverse cracking but this is dependent on many factors. The presence and amount of N, other micro-alloying elements and the austenite grain size after the pinning effect of TiN play an important role. Other factors are the size of the formed Ti precipitates itself - especially when Ti is added to Nb steel - and the secondary cooling practice, which affects both the grain size and coarsening of the precipitates [3,9,107,108]. Banks et. al. [109] studied the influence of Ti on hot ductility of Nb containing steels and showed that the hot ductility depends strongly on the secondary cooling conditions. Increasing the secondary cooling will possibly decrease the ductility and may not lead to sufficient coarsening of the precipitates to give a chance for the Ti addition to improve ductility. He also concluded that after a closer simulation of the cooling conditions pertaining to the CC operation that Ti additions can enhance the hot ductility at typical off corner straightening temperatures (~ 900 °C). To reach the optimum R of A values, the Ti/N ratio and thermal cycles need to be well provided [109].

3.3.1.4 Niobium

Niobium is very harmful to the hot ductility. The Nb(C,N) precipitation has especially a huge influence on the width and depth of the ductility drops because of the following causes [9,19,51,100,110,111]:

1. In the matrix, very fine Nb(C,N) precipitates lead to matrix strengthening and raises the stress in the grain boundary regions,
2. In Nb containing steels, the strain is concentrated in the PFZ in grain boundary regions which are always relatively weaker,
3. Extensive grain boundary precipitation will enhance the voiding and the extension of the cracks formed by GBS. This means that Nb precipitates will enhance the GBS failure mechanism,
4. Nb can delay the ductility recovery to higher temperatures and delay the onset of dynamic recrystallization to higher temperatures.

Ma et al. [112] stated that slabs containing between 80 and 270 ppm Nb were likely to generate cracks [113].

3.3.1.5 Vanadium

Adding vanadium to steel helps in its strengthening due to precipitates formation. Fine precipitates of V(C,N) particles ranging from 5 to 100 µm in diameter are formed during cooling. The addition of V raises the yield strength by average of 5 - 15 MPa per 0.01% V, depending on C content and cooling rate [104,114]. On the other hand, the presence of V in the steel has a harmful effect on hot ductility. High amounts of V lead to less hot ductility [115]. Compared to Nb addition, the V addition has less detrimental effects to hot ductility, even for a steel with 0.1% of V [3,9,51,106,115,116]. This could be attributed to the higher solubility of V in austenite. As reported in [87], with N values less than 0.005%, the effect of V on transverse cracking is small, while in 0.15% V steels defects as transverse cracking at high N levels (0.02%) can take place [3,45,87].

3.3.1.6 Other elements

Many other elements could also play a role in the embrittlement mechanisms and influence the crack sensitivity. Al has a detrimental effect on the hot ductility in micro-alloyed steels due to the formation of AlN [104,117], which could influence GBS depending on the particle size. Copper residuals have also a detrimental effect as they remain in the steel as Cu cannot be preferentially oxidized during the steelmaking process. Cu can build up progressively in the subscale layer and result in hot shortness [9]. The lower the Mn:S ratio, the higher the tendency to the formation of iron-rich sulphides will be, which are harmful to the hot ductility. The segregation of sulphur to grain boundaries is higher than Mn because of the large misfit strain energy difference [12,86,118]. The presence of P improves the hot ductility, provided segregation is reduced [9]. P improves the oxidation rate of iron at 1000 °C as well, which could reduce the formation of FeS [119]. Moreover, P promotes the dispersion of Mn in the interdendritic region and refines the austenite grain structure, which can enhance the hot ductility. It was reported that addition of 0.20% P can reduce the grain size to the half [86,120].

3.3.2 Microstructural effects

3.3.2.1 Grain size

Generally, any decrease in the grain size should lead to a better hot ductility [51,100,121,122]. During an intergranular failure, the grain size refinement can hinder the crack propagation in many ways. A finer grain results in [85]:

- Reduction in the crack aspect ratio, which controls stress concentration at the crack tip [123].
- Increase in the triple points, which hinders the propagation of cracks occurring under sliding states [123].
- Reduction of the precipitates density in the grain boundary regions due to the raise in the specific grain boundary areas for a given volume fraction of precipitates [124,125].
- Increasing the nucleation sites at higher numbers of grain boundaries, which will result in decreasing the critical strain for dynamic recrystallization [126].

One should consider that grain refinement to be effective requires the grain size to be kept below 200 - 300 µm to be able to improve the ductility [51,100,122,127]. It is important to mention that refining the grain size might also not be sufficient to keep an acceptable hot ductility in micro-alloyed steels as, overall, the harmful effect of fine precipitates of Nb(C,N) or/and AlN can result in low ductility [51].

Steels with coarse austenite grains are prone to intergranular fracture through GBS, which leads to a very wide ductility trough. Grain size refinement and its effect on the hot ductility was reported by Moon [85] and showed an important effect especially in C-Mn steels, with 0.65% C. At higher C contents, the activation energy for dynamic recrystallization is increased. This results in expecting more GBS to be responsible for the deformation than grain boundary migration. Moon suggested that for those steels intergranular failure will probably take place below the Ar_3 temperature [85].

3.3.2.2 Precipitation

The huge effect of precipitation on the hot ductility behavior of an alloy [100] was studied by many researchers, especially the precipitation on grain boundaries which has the biggest effect, where the finer precipitates are linked to lower ductility values [51,88]. This

critical effect of precipitates on hot ductility depends mainly on their sizes, location and the spacing between the particles, which are controlled by the chemical composition of the alloy and the thermomechanical history during casting [51,85].

Carpenter [100] studied the influence of precipitates on the hot ductility of thin slabs of cast steel and reported the harmful effect of grain boundary precipitates. At higher temperatures, grain boundary precipitates will enhance voiding during GBS, while at low temperature, where ferrite films start to form on austenite grain boundaries, the grain boundary precipitates will enhance the void formation in these ferrite films as explained earlier in the embrittlement mechanisms. Higher phase fraction of precipitates will enhance micro-void coalescence. Fine precipitates are more detrimental, especially on their effect in pinning austenite boundaries during sliding, which enables failure by allowing time for cracks to link-up. In this manner, it can be said that fine precipitates, which can be produced during deformation (strain-induced precipitation), are more detrimental to ductility than precipitates being present before straining in the form of coarse primary precipitates [100].

The effect of fine precipitates was also reported by Mintz et al. [84], where excessive surface cracks were observed in slabs that contained fine precipitates less than 14 nm. Those fine precipitates pins the grain boundaries. When deformation occurs by GBS in the austenite, cracks were able to join up. Micro-void coalescence failures are also enhanced by an increase in the volume fraction of precipitates or inclusion density at the austenite grain boundaries, which act as preferential sites for void initiation. Therefore, at low interparticle spacing, typically less than 64 nm, excessive cracks might develop [84].

Zamberger et. al. [128] studied the evolution of primary and secondary precipitates of Nb(CN), Ti(CN) and AlN in micro-alloyed steels during CC. The presented investigation was carried out using MatCalc software, version 5.41.0021, for Scheil Gulliver and precipitation kinetics simulation. LOM and SEM were used for experimental verification. For the characterization of the fine secondary precipitates, transmission electron microscope (TEM) was used.

For the simulation of the CC process in [128], a temperature profile that matches the temperature profile at a distance of 10 mm from the bloom surface - featuring an industrial practice - was used. The microstructure analysis showed a typical ferritic – pearlitic microstructure with plenty of precipitates appearing as bright spots. Moreover, many relatively large precipitates/particles were observed in both the ferrite and the pearlite regions as shown in **Fig. 3.10**. The clear alignment of the precipitates in the figure's center could be linked to the nucleation of precipitates on some heterogeneous nucleation site such as a former austenite grain boundaries. In another TEM and HRTEM (high resolution TEM) performed analysis to characterize the fine secondary particles, linearly aligned Nb-rich precipitates were observed. Zamberger concluded that these particles have nucleated at heterogeneous nucleation sites, such as dislocations or former austenite grain boundaries, as suggested for the precipitates [37,128].

The radii of the Nb-rich precipitates arranged along lines were in the range of (10 - 15 nm), while for the ones found within the grain; their sizes were between 2 - 10 nm. The same pattern was reported for Ti-containing precipitates but with different sizes, where a radius of 10 to 15 nm was found for the linearly arranged precipitates, identified by their typical facetted morphology, while inside the grain, the Ti-containing particles were observed to be smaller with mean radii of about 5 nm [128].

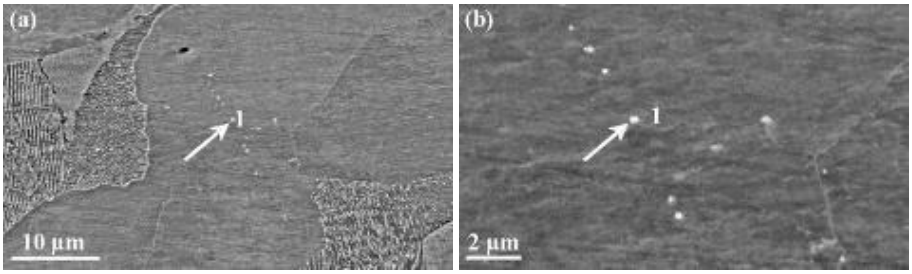

Fig. 3.10: Precipitates in SEM micrograph [128]

For NbC, the numerical simulation of the enriched interdendritic zone predicted similar results to the ones observed by TEM and micrograph analysis in terms of particle size in austenite (Simulation: 143 - 230 nm, micrograph analysis: 50 - 250 nm) and ferrite. The computation showed successfully good matching between the calculated particle sizes of TiN in the ferrite phase with the micrographs observations as well, while the predicted TiN in austenite could not be observed in the analyzed samples. In the depleted regions, particle size of precipitates of AlN (~ 15 nm), TiN (~ 5 nm) and NbC (~ 2 - 15 nm) by experimental sample analysis could be well predicted in the ferrite phase, while in austenite phase the predicted values could not be stated [128].

The limitation of numerical simulation should also be taken into consideration in spite of its good agreements with experimental validation in most of the cases. For example, the computations in the simulation are carried out under the ideal situation that the local microstructural environment is identical for each single precipitate, which does not happen in reality. However, the presented model still shows an interesting approach for application of software in precipitation kinetics calculation with high potential for more precise analysis of primary and secondary precipitation during CC from liquid to solid state [128].

Another approach in applying MatCalc for precipitation kinetics simulation was carried out by Lückl et. al. [129], where the effect of thermal history on the ductility behavior of a Ti micro-alloyed steel was investigated. It could be confirmed that remelting of the material (investigation of the primary solidification microstructure) compared to coarse-grain annealing at 1320 °C before the tensile tests showed no significant influence on hot ductility after the thermal history of surface structure control cooling under the mentioned experimental conditions reported in [129]. Another approach regarding the kinetics of AlN precipitation in micro-alloyed steel could be found in [130], where the thermodynamic parameters for AlN precipitation in Austenite compared to experimental precipitation kinetics was reviewed.

3.3.2.3 Parallel effects: Grain size vs precipitates

Yang et. al. studied the influence of Ti (C,N) precipitates on the austenite growth of micro-alloyed steel during CC at different cooling rates taking the pinning effect in consideration and the correspond effect on hot ductility and transverse cracking. It could be shown that, increasing the cooling rates from 1 to 3, 5, 7 and 10 K/s, decreased the austenite grain size from 2.16 to 0.69 mm (without pinning effect) and from 1.46 to 0.57 mm (with pinning effect). At the same time, increasing the cooling rate resulted in finer Ti(C,N) precipitates from 137 nm to 43 nm. After studying the diffusion and nucleation characteristics of Ti(C,N) precipitation, it could be shown that grain boundary nucleation is preferred for the nucleation location compared to homogeneous nucleation [131].

As the temperature decreases from 1430 °C to 1200 °C, the austenite grain size increased at all cooling rates; the less the cooling rate is, the stronger this effect is. Also by decreasing the temperature, the amount of Ti and N dissolved in austenite gradually decreases [131]. The study illustrated how increasing the cooling rate resulted in finer grain size, which can improve the hot ductility, but resulted at the same time in finer Ti(C,N) being detrimental to hot ductility. It could be stated that increasing the cooling rate at austenite transformation temperature should be adapted to produce small austenite grains. In terms of the casting machine, it was suggested to increase the water flow in the mold to strengthen the cooling intensity at 1400 °C to achieve a fine austenite structure, which enhances the hot ductility and helps in reducing transverse cracking during straightening [131].

3.3.2.4 Ferrite formation

The ferrite phase fraction, formation mechanism and starting temperature are important factors affecting the ductility trough and the possibilities of transverse cracking especially in Region III of low ductility in the hot ductility curve. During transformation of the austenitic grains, grain boundaries ferrite films start to develop. The thin films of ferrite surrounding the austenite grain boundaries result in transformation controlled intergranular failure [132]. Thin ferrite films at austenite grain boundaries are mostly forming during deformation (strain induced) and can form over a wide temperature range from the undeformed Ar_3 to Ae_3 [100,102,133], where the amount of strain, strain rate, and the austenite grain size are the critical affecting factors in the formation. Thin ferrite films can form in both fine grain and/or coarse grain steels even within very small strains [134]. The influence at low strain rates is important, where thin ferrite films are able to recover so they remain soft at the grain boundaries, where the strains remain concentrated. Therefore, low strain rates will lead to poor ductility [100,102,134,135].

3.3.3 Effect of the casting process

3.3.3.1 Mold heat transfer

The heat transfer in the mold strongly affects the thermal stresses and surface structure of the strand [3]. Non-uniform solidification in the mold causes a coarse-grained columnar layer near the surface of the strand, raising the cracking risk [86]. The control of mold heat transfer can be enhanced [136] by optimizing the casting powders with suitable viscosity characteristics, ensuring consistent powder feeding, maintaining stable mold level control, mold turbulence reduction and optimizing mold taper to secure a good contact between the slag layer and the mold [86].

3.3.3.2 Mold oscillation

The formation mechanism and effect of OM on hot ductility and crack sensitivity in steel slabs was explained earlier in this chapter. The harmful effect of the OM will increase the deeper they are. This depth can be reduced by decreasing the stroke to reduce the heal time and/or raising the frequency of the mold oscillation, which proved to reduce the incidence of transverse cracking [61]. Deep and irregular OM can also be a result of poor mold level control [3]. According to [87], the oscillation mark depth can also be reduced by a correct choice and application of the mold powder and avoiding the peritectic carbon range [86,99].

3.3.3.3 Casting temperature

The casting temperature strongly affects surface cracking. A low degree of superheat is beneficial to reduce cracking [137]. Degrees of superheat in liquid steel greater than 30 K will result in a higher cracking risk. So, the degree of superheat should be kept lower than 20 – 25 K, depending on the C content and the strain rate. On the other hand, very low superheat is critical. It is advised during CC to keep the minimal superheat temperature range of (± 2 to 4 K) in order to enhance both hot ductility and surface quality [104,138].

3.3.3.4 Casting speed

Optimizing the casting speed is a key factor for an optimum casting procedures. Casting speed directly influences the secondary cooling and the deformation rate of the strand surface at the straightening region. Increasing the casting speed could be beneficial to the surface quality, as the strand surface will reach the unbending zone at higher temperatures, which could help avoiding straightening within the temperature range of ductility troughs. Higher casting speed will increase the strain rate during deformation, which can avoid surface cracks as explained earlier in this chapter.

On the other hand, increasing the casting speed over a certain limit might have negative effects in the mold region. At high casting speeds, the flow of flux melt into the mold/shell boundary decreases, which leads to higher friction at the boundary locally with viscous flux melts. The resulting frictional force might cause transverse cracking at the bottom of the OM while still in the mold. Apart from the frictional forces, the crack formation might also be increased by the non-uniform formation of the initial shell produced by an uneven inflow of molten mold flux into the mold/shell gap during a turbulent sub-meniscus flow. Other critical parameters were stated as well, like the meniscus level fluctuation, low meniscus temperature and/or too high viscosity of the flux melt [132].

3.3.3.5 Cooling history

Soft and hard cooling are the most common types of cooling procedure for the strand after leaving the mold in CC. During soft cooling less water is sprayed, often in an air-water mist spray. Soft cooling leads to higher surface temperatures than the ductility trough during the unbending zone. On the other hand, by hard cooling the maximum performance of the water cooling nozzles is used to reduce the strand temperature below 700 °C at the unbending zone. Some process defects, such as blocked or worn nozzles, excess water, static spray control or poor cooling design, might result in problems with surface temperature control [86,87].

In hot tensile testing schedule, studying the influence of cooling rate on the hot ductility becomes particularly important with the advent of thin slab casting, where cooling rates are much higher than in conventional continuously cast steel. For conventional casting (220 to 250 mm thick slabs), the average cooling rates from the mold to the straightening temperature are 60 ~ 100 K/min, while values in the range of 200 ~ 300 K/min for thin slab casting (60 ~ 80 mm thick slab) was reported [132]. Abushosha [110] studied the influence of the cooling rate on MnS inclusions for hot ductility and mentioned the negative influence of increasing the cooling rate to the test temperature after solution treatment by deepening the ductility trough. Higher cooling rates resulted in finer sulphide re-precipitation at the austenite grain boundaries, that decreased the spacing between the particles making it easier for ductile cracks to link up and give failure [132].

The same effect was reported in [139-141] for steels containing Ti and Nb, where the ductility got worse by increasing the cooling rate. In other words, the ductility was improved using lower cooling rates, which at high temperatures allowed NbC to precipitate out on the coarse TiN precipitates. Coarser precipitation occurred and there was less Nb available to precipitate out dynamically on deformation [132]. Nb precipitates produced during deformation are generally finer and more detrimental to hot ductility.

Yang et. al [142] studied the effect of the thermal schedule of micro-alloyed steel during CC. Traditional thermal schedules and thermal schedules with temperature fluctuation were compared to thermal schedules for surface structure control (SSC), which showed improved values of ductility after hot tensile testing in the brittle zone III. Sample analysis on LOM, SEM and EDS (energy disperse spectroscopy) showed obviously the presence of pro-eutectoid ferrite films and aggregation of (Ti,Nb),(C,N) precipitates along the austenite grain boundaries for both traditional thermal and temperature fluctuation thermal schedules. On the other hand, ferrite films and aggregated particles formed around the grain boundaries could not be observed for the SSC schedule. This explains the much-improved values of the ductility knowing that the tensile testing was carried out at the same temperature for the three different schedules [142].

3.3.3.6 Strain rate

Tensile strains during unbending/straightening is a main cause for transverse cracking on the slab's upper surface [87]. The strain rate is a very important factor affecting the cracking during straightening and it is mainly dependent on the casting machine geometry and the casting speed. Negative effects of lower strain rates on hot ductility can be a result of its effect on promoting the GBS, the strain-induced precipitation and the formation of deformation induced ferrite on the austenite grain boundaries, which are all detrimental to hot ductility [88]. Multiple point unbending can decrease the average strain rate and result in harmful effects on hot ductility at lower temperatures, in spite of that it was reported to promote stress relaxation at higher temperatures at ~1300 °C [51,86]. In addition, it is reported [143] that at low strain rates, the amount of strain energy is not sufficient to reach the values needed for full recrystallization to take place in normal testing conditions [144].

Yamanaka et al. proposed an approach [145] for evaluating the critical strain for internal cracking in CC. It was mentioned that the critical strain for internal crack are between 0.5 - 3.8%, while the analyzed strains in any location of the strand are max. 0.3%. The cumulative effects of strain was tested, where the accumulated strain between ZST (zero strength temperature) and ZDT (zero ductility temperature) for every roll was considered. Tensile testing with liquid core was used resulting in a new evaluation of critical strain showing that internal cracking occurs when the total amount of strain applied between ZST and ZDT exceeds the critical strain, independent of the deformation mode, whether continuous or intermittent. The accumulated strain by every roll shall be accounted [145]. ZST is the temperature during cooling at which forces can first be transmitted perpendicular to the solidification direction. ZDT is the temperature at which the transition occurs from brittle to ductile behavior and mostly linked to solid fraction between 0.98 and 1 [176,177].

3.3.3.7 Thermal stresses

Cracking could be reduced if care is given to reduce thermal stresses [42]. Thermal cycling along the continuous caster could be caused due to roll contact or secondary cooling after exiting the mold and can result in cracking at any part during the process. Surface cracking

could be reduced by minimizing the mechanical loads on the strand surface, which is demonstrated by the lack of surface cracks in the corner regions, when strand soft cooling is applied [41,104].

In summary, the effects on hot ductility are complex and depend on many different factors that strongly influence each other. So we can't separate one factor on its own and study its effect solely because some other parameters will be accordingly changed and influence the result. It would be wiser to evaluate a situation/process case, which represents a set of different factors taking place on the same time. This approach will be explained in detail in **Chapter 5** and **6**.

3.4 Cracking by transportation and charging

After a successfully complete and defect-free casting process, the steel slabs are still susceptible to cracking downstream during transportation, storage, charging into the hot strip mill (HSM), inside reheating furnace or even during the first steps of hot rolling. Surface cracking after the casting shop related to transportation and storage handling in terms of slab solid state phase transformations and charging temperature, received much less attention in literature compared to the work published in topics related to CC and failure related to mold, unbending and secondary cooling.

3.4.1 Air cooling before charging

Li et. al. [146] studied the effect of slab air cooling after the caster and charging temperature into the HSM on solid phase transformation, precipitation formation and the fracture tendency of steel slabs of certain grades. They stated that brittle phases and internal stress, might cause cracking defects during/by cold charging, which could be eliminated by reasonable slow cooling using stacking practice for example. Feathery upper bainite forms after the casting process when the local cooling rates of slabs are higher than the critical cooling rate of bainite formation during phase transformation from austenite to ferrite, which might happen when a slab is exposed to air immediately after leaving the caster and cutting. Once bainite dominates in the structure, an increasing crack tendency for the slabs upon handling is given [146].

Increasing the contents of elements such as C, Mn, Ni, Mo, Si, Cu, and B, retards the transformation from austenite to eutectoid ferrite and pearlite because of the difficult nucleation of the pearlite phase and due to the lower transformation temperature [147-149]. The internal brittle bainite structure was observed in the slab after air-cooling for Mo containing steels; this could be seen due to the drop in the critical cooling rate and incubation time of bainite formation caused with higher contents of Mo elements. Li suggested that for grades like Q550D, furnace hot charging should be kept above the bainite transformation temperature (600 °C) [146,150,151].

3.4.2 Effect of volume change

Even by slower cooling in some conditions, where no bainite transformation takes place, care should be taken for grades with alloying elements. Schöbel [152] performed an experimental simulation of thermally induced stress during cooling of cast low carbon steel slabs with and without Ni. He showed that the austenite to ferrite phase transformation is accompanied by a volume increase of approx. 1% when changing from FCC austenite to BCC

ferrite, a cause for internal stresses within the thermal stress gradients by cooling from the surface. The localized induced stress phenomena due to transformation is caused by the volumetric expansion in a narrow temperature interval between Ac_3 and Ac_1, and is linked to the second minimum of ductility. The lower the transformation temperature, the higher the stress gradients will be, this is due to less relaxation/diffusion at low temperatures. It could be shown that the crack sensitivity of the Ni-containing slabs is linked to higher internal stresses within the austenite caused by the lower transition temperature compared to the Ni-free steel [152].

Another study focused on cooling of hypo-eutectoid steels, showing that grain boundary ferrite appears as the initial austenite transformation product, which will lead to large volume expansion and normal stress at the austenite grain boundaries. After charging into HSM, the grain boundary ferrite film will transform to austenite with volume shrinkage while the slab is reheated. This might lead to the effect that the surrounding austenite is not active enough to compensate the local phase transformation shrinkage, so the grain boundaries will be under large tensile stresses. Since the microscopic void or porosity defects are likely to form around the inclusions (such as (Fe,Mn)S and (Fe,Mn)O) at the grain boundaries, the material is prone to surface transverse cracking during the following rolling process [153].

3.4.3 Charging in reheating furnace and rolling

In some plants, slabs with different temperature histories experience mixed furnace charging operations during the production process, which results in an unsteady quality of the rolled products under the same reheating schedule. This could be critical for steel batches with different sensitivities to hot cracking. The study done by Li [146], showed that the formation of surface transverse cracks of slabs in CC and rolling processes is attributed to both the carbonitrides and stress concentration at the grain boundaries, but the effects of carbonitrides size on surface cracks are different. For micro-alloyed steels, surface transverse cracks of primary rolled slab are attributed to the spread of transverse cracks of slab during the casting process and the transverse crack formation during the rolling process [146]. Here, the precipitates types, sizes and distribution plays an important role. The finer the particles are, the higher the transverse cracking tendency will be. According to ductility measurements, the ductility of steel slabs starts to be reduced when the size of carbonitrides particles is less than 50 nm and turns to be very critical to transverse cracking when the size is around 10 nm [9].

During the reheating in the furnaces, the grain boundary carbonitrides - which precipitated earlier during CC, further cooling and charging process - would gradually enter dissolving and Ostwald ripening periods. In spite of the partial dissolving, since some large-scale carbonitrides at the austenite grain boundaries may not fully dissolve, surface transverse cracks may frequently occur under the high stresses during rolling with unreasonable hot charging temperature [146,154,155]. It could be stated that surface transverse cracks may occur during the rolling process in a certain hot charging temperature range, as the number and size of the formed carbonitrides depend on the temperature and cooling/heating rate [146].

In other words, it can be stated that the unresolved coarse carbonitrides remaining at the austenite grain boundaries after reheating and the hypo-eutectoid ferrite films surface, will lead to weaken thermal ductility and will result in cracking during rolling. According to the nucleation and growth theory, the precipitation size decreases with a higher nucleation rate

per unit volume. Coarse precipitates may occur at the austenite grain boundaries in the hot charge temperature range with low nucleation rate and high precipitation speed. The formed precipitates, their location and sizes should be taken in consideration when choosing the reheating temperature and rates to avoid/reduce surface cracking during rolling. Li studied this effect on J55 steel slabs and suggested that the sensitive hot charging temperature range of (625 - 775 °C) should be avoided. Steels with higher contents of carbonitrides forming elements have higher crack susceptibility in the improper hot condition. Avoiding the sensitive hot charging temperature range or even cold charging process was suggested for similar grades [146].

Slab cracking in the HSM is highly affected by the microstructure, which depends on the chemical composition and cooling rate during CC and storage. After the caster, the slabs - depending on their chemical compositions - are usually air cooled in stacks that can be either covered (box) or not. According to industrial observation, it could be shown that air-cooling rates are in the range of 9 K/min, while cooling of covered stacks are around 0.3 K/min. The major difference on cooling rate between air and box cooling is observed in the range between 800 - 600 °C [156].

For a specific chemical composition, the cooling rate from the austenite phase will define the final microstructure of steels, which can have various microstructure consisting of different forms and combinations of pearlite, bainite, martensite, cementite, and ferrite [157]. The volumetric changes during cooling or heating, caused by these microstructure types, can lead to quality problems in low ductility steels [158]. Phase distribution (shape, location and presence of precipitates) can also be related to surface quality problems [88,159-163]. Giacomin et. al. studied the 3rd generation of advanced high strength steel and the mechanism of cracking in their steel slab focusing on the effect of the cooling route (box or air) and the effect of Si, which plays an important role in its microstructure development [156,164].

Three alloy with C= 0.19%, Mn ≈ 3% and Si amounts varying between 0.5%, 1.5% and 3% were chosen. The results of the microstructure investigations showed that at lower Si content (0.5%) and slow cooling a matrix with predominantly granular bainite was built, while granular bainite and martensite was present for the same alloy at air-cooling. It was also indicated that increasing the Si content led to more ferrite after slow cooling and presented a notable change in microstructure from furnace (box or slow) cooling to air cooling. The alloy with 3% Si showed a matrix composed of large ferrite grains and pearlite in slow cooling, which explains the role of Si as a ferrite stabilizer, while by air cooling (faster than slow box cooling), smaller amounts of ferrite were present for 1.5% and 3% Si in their martensite matrix structures [156,164]. This illustrates the effect of defining the route for slab storage and handling on the resulted microstructure before charging, which in return affects its mechanical properties and crack sensitivity by the mechanisms mention above.

Chapter 4: Tools and materials characterization

This chapter gives information about the investigated materials in this thesis and the instrumentation/software used to carry out the experimental work. It includes also the first characterization of the investigated alloys in the as cast condition before their further process treatments and simulations which will be explained in detail in **Chapter 5** and **6**.

4.1 Materials

Analysis, experimental investigation and simulation of two chosen grades are to be illustrated in this part. Alloy-1, the alloy showed the highest number of cracking problems in the industrial analysis (discussed in **Chapter 2**) and Alloy-0 with similar chemical composition except for the micro-alloying elements as a reference alloy. The chemical compositions of Alloy-0 and Alloy-1 are shown in **Table 4.1**.

Table 4.1: Chemical composition of Alloy-0 and Alloy-1

Element, %	C	Mn	Ti	Nb	V	N
Alloy-0	0.08	0.5	0.001	-	0.01	0.004
Alloy-1	0.08	1.9	0.12	0.05	0.01	0.005

For this experimental work, samples (near surface) from the slab middle region (in width) were taken after continuous casting (CC). The dashed boxes in **Fig. 4.1** shows the position of the received material in the slab. All samples were taken from the upper third (Top) of the block far enough form center segregation. Material from the upper surface of Top region (0 - 30 mm) was avoided for sample preparation to be sure enough to avoid the surface problems. Samples were prepared in the casting direction.

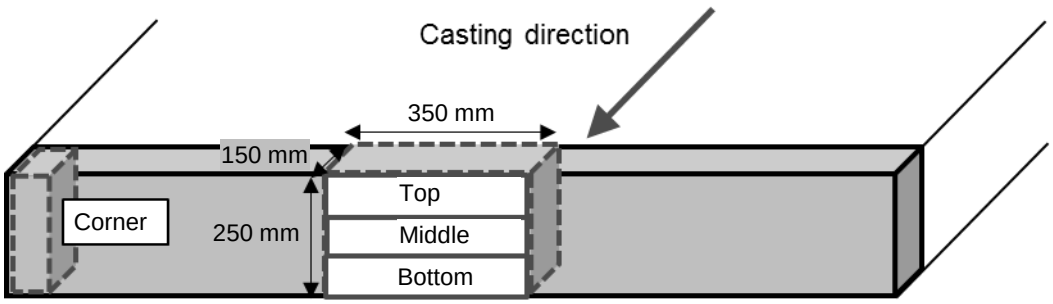

Fig. 4.1: Position of the received material in the slab

The upper part of the received block material was carefully machined into layers for sample preparation. Two types of samples were prepared for the current investigations. Firstly, cylindrical samples for heat treatments by Dil805A and secondly, flat tensile sample for hot tensile testing by Dil805T. Sketches of the cylindrical and flat tensile samples with their dimensions are shown in **Figs. 4.2** and **4.3**, respectively.

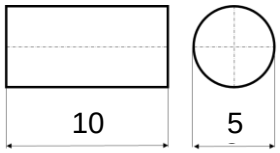

Fig. 4. 2: Dil805A cylindrical sample

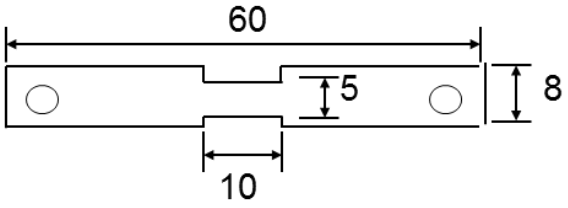

Fig. 4.3: Dil805T flat tensile sample (thickness 2 mm)

4.2 Instrumentation

4.2.1 Dilatometry thermomechanical simulator: Baehr Dil805A/D/T

Quenching dilatometers are used to study the heat treatment of steel and metal alloys, helping to identify the heating rate, quenching rate, and isothermal dwell times. This is necessary in metals manufacturing to yield the crystalline structure necessary to meet the required physical properties of the finished product. The related microstructural changes may be observed through process simulation with real-time monitoring of dimensional change. The DIL 805 series quenching dilatometers provide accurate measurements over the widest range of heating, cooling and deformation conditions, providing the most sophisticated characterization and optimization of metals processing conditions [165].

The DIL 805A is used to observe dimensional changes under controlled heating and cooling conditions. A solid or a hollow sample is inductively heated to a temperature plateau and is then continuously cooled with defined and controlled (linear or exponential) rates. The phase transformation occurring during cooling or in the isothermal plateau (which may also be a multi-step transition) is indicated by the (measured) change of length. The beginning and end of the transformation indicate the alloy phase boundaries, e.g. ferrite, carbide, graphite, pearlite, bainite, martensite or other eutectoid phase batches. [165].

The instrument Dil 805 was used in two different modes using an inductive coil for heating. The first is Dil805A: configuration of a quenching dilatometer and the second in Dil805T: tensile deformation with a maximum deformation force of 25kN. The device is designed for measuring length changes under heating, cooling and mechanical deformation in a temperature range between 20 – 1500 °C depending on the sample material. The maximum heating rate for Dil805A is 4000 K/s, while in tensile mode Dil805T is 100 K/s and the resolution of the sample length change is 0.05 µm/K. the complete device specifications are shown in **Table 4.2**.

Table 4.2: Device specification of quenching and deformation dilatometer

Technical specification	**Quenching dilatometer DIL 805A**	**Deformation dilatometer DIL 805T**
Sample geometry [mm]	Solid / hollow samples d=5-8; l=10	Solid samples d=5 mm, l=10 mm
Temperature range [°C]	20 - 1500 °C	
Max. deformation rate [mm/s]		125
Max. strain rate (ϕ°) [s^{-1}] (with 10 mm samples)		12.5
Max. true strain (ϕ)		1.2
Max. deformations force [kN]		25
Max. heating rate [K/s]	4000	100
Max. cooling rate [K/s]	2500	100
Heating principle	Inductive	
Cooling medium	N_2, Ar, He, H_2	
Vacuum [mbar]	10^5	
Atmosphere	Inert gas, vacuum, air	
Resolution Δl/K [µm]/[K]	0.05 / 0.05	
Thermocouples (resolution [K])	0.05	

To study the phase transformation and the formed microstructure constituents, cylindrical samples of 5 mm^{Ø} and 10 mm length, shown in **Fig. 4.2**, were used on Dil805A. Thermocouples type S “Pt/Pt-10% Rh” with 0.1 mm^{Ø} were welded on the sample surfaces center. The experiments were run under vacuum condition by inductive heating using a high frequency generator. He or N_2 gas were used for cooling and quenching. The dilatometric changes in length and temperatures were recorded as a function of time and consequently the relative change in the sample length could be represented as a function of temperature in which a phase change by heating or cooling could be clearly observed.

DIL 805A/D/T (shown in **Fig. 4.4**) further extends the capabilities to alternate tensile and compressive loading to emulate mill processing. Moreover, tensile loading to fracture gives additional information about material’s final performance and allows generating true-stress vs true-strain or stress/strain cycling plots [165]. Cylindrical and flat tensile samples are shown in **Fig. 4.5 and 4.6**, respectively.

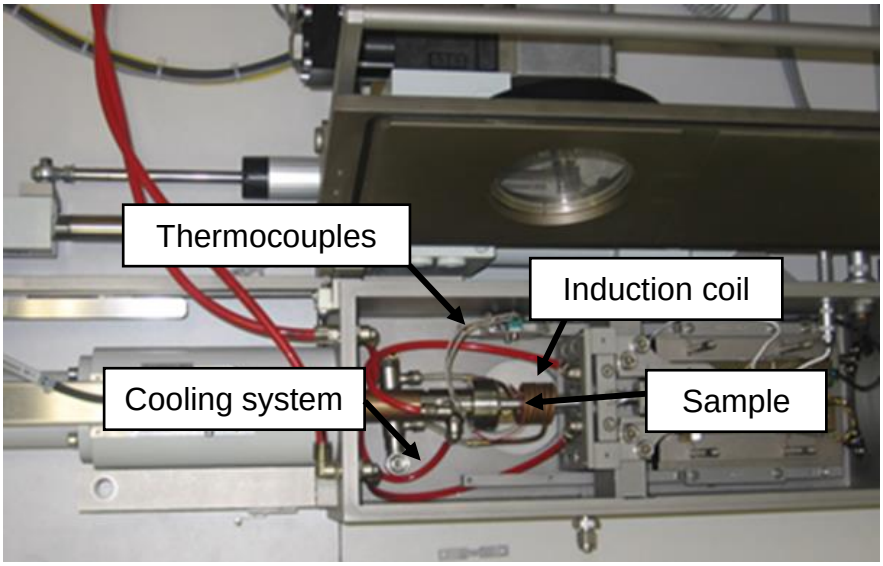

Fig. 4.4: Device Dil805A/D/T

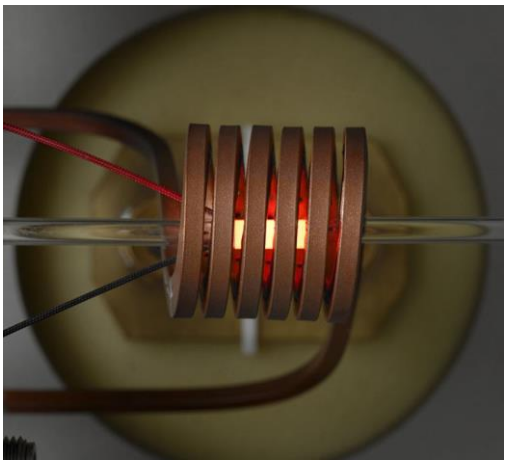

Fig. 4.5: Cylindrical sample in Dil805A [165]

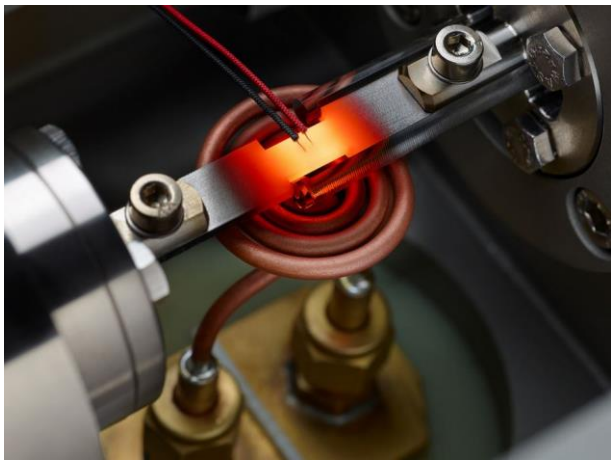

Fig. 4.6: Flat tensile sample in Dil805T [165]

Hot tensile testing at high temperature is the most common test used for hot ductility evaluation. There is no standardized test, and different procedures have been adopted by different researchers. The thermal cycle starts with heating up to a solution temperature in the range of (1200 - 1350 °C) and austenitization holding to produce a coarse austenite grain and dissolve any micro-alloying precipitates in the material. Afterwards, cooling to the test temperature with a rate that represents the secondary cooling experienced at the surface of a continually cast product (typically 60 K/min), then finally straining to failure at a strain rate of 10^{-3} to 10^{-4} s^{-1} to simulate the condition experienced during the straightening of a CC slab [3].

The hot ductility in this work was evaluated by the elongation to rapture (ER), measured in a hot tensile test. The deformation behavior of each alloy was investigated using DIL805T in deformation mode, which is capable of monitoring the strain, load, time and temperature during the course of hot tensile test. To assure a high starting temperature and reproducible test procedure, the steel samples were heated to a temperature close to melting - approx. 20 - 30 K below NST (Nil-strength temperature) - to generate an initial microstructure re-

sembling that one in the CC machine. Measurement of NST will be explained later in section 4.4.5. Kozeschnik in [129] found out that remelting of the material compared to holding at higher temperature shows no significant influence on hot ductility results for an alloy having close chemical composition to Alloy-1 used in this work.

In the experiments, heating up the samples to high temperature was followed by 10 min austenitization, then cooling to the test temperature - representing the straightening temperature range -, and finally followed by tensile deformation under defined load and deformation rates until failure before rapid cooling to room temperature to conserve the microstructures for further metallographic analysis. Cooling rates and slab surface reheating before deformation have also been considered in the thermo-mechanical cycle. Moreover, the fracture surfaces were examined using light optical microscope (LOM) and scanning electron microscope (SEM). The defined heat cycle and deformation conditions will be explained in **Chapter 5** in detail.

4.2.2 Metallographic preparation

To investigate microstructural constituents, the specimens were prepared for microscopic analysis, first by sample mounting using Demotec 35 (a two-component resin system), followed by mechanical grinding on a Buehler-Alpha machine. Polishing was performed on a Struers-Tegramin-30 machine using diamond suspension, then OP-S NonDry SiO_2 solution up to a 0.25 µm, and finally etching with Nital; 100ml ethanol and 3ml nitric acid (65%) [166]. Repeating light polishing and etching increased the contrast.

Etchant in [167] was used to etch steel samples for microstructure investigation as well. With this method, the parent/prior austenite grains could be clearly distinguished from ferrite. The microstructure constituents and the prior austenite grain size were analyzed and statistically evaluated.

4.2.3 Light optical microscope (LOM)

Microstructure analysis by LOM using Olympus BX60M was used to study the microstructure phases and the precipitates of carbides and nitrides after sample preparation explained in 4.2.2. LOM pictures were used afterwards as well for the evaluation of grain size and calculation of phase fractions percentages using PXF Workbench Point Count software.

4.2.4 Scanning electron microscope (SEM)

After the LOM analysis, the samples are ready for further investigation by SEM using Camscan 44 including an EDX analysis. After the preparation as explained in 4.2.2, the polishing and etching was repeated for a longer period (20 - 30 s extra etching) for getting a better contrast by the SEM. After drying, the samples were coated with a gold layer in the sputtering chamber of the device before Ar ions spraying on the coated surface for a homogenous distribution of gold particles. Afterwards, Cu strips were attached to the samples surface connecting it to the device holder. SEM was used to study the fine precipitates (in nano-size) that could not be observed using the LOM under the available LOM magnification. With the help of the adjusted EDX (energy dispersive X-ray spectroscopy) device, the composition of the fine (Ti,Nb),(C,N) precipitates could be analyzed.

4.2.5 Hardness testing: Wolpert Dia-Testor

Hardness tests using Vickers method were performed by applying the square shaped diamond indenter with a predefined load on the sample center at room temperature to measure the hardness of each sample after finishing the microstructure analysis. The hardness values give an indication of the mechanical properties of the material after certain treatments; this will be discussed in detail in **Chapter 6**. The depth of the indentation was automatically recorded on a dial gauge in terms of arbitrary hardness numbers based on the measured diagonal of the formed square/rhombus due to the indentation. The average of six to eight measurements with enough relative distance for each sample was calculated covering the middle area of the specimen to estimate hardness values, while the standard deviation was accordingly calculated as well. A load of 20 kg was applied on the specimen surface for 10-12 s.

4.3 Software

4.3.1 MatCalc simulation package

MatCalc is a computer simulation software package for calculating transformations in metallic systems using the CALPHAD method and a kinetic based on the classical nucleation theory. MatCalc uses a mean field approach and allows the description of precipitate sizes, number densities and chemical composition. The Scheil-Gulliver module of the thermokinetic software package MatCalc was used for a first information on the amount of elements becoming bound in the form of primary precipitation during solidification before and during the CC [129].

With the help of MatCalc modelling, multiple simulations were performed for every alloy at different conditions aiming on studying the precipitation kinetics during CC. The software is useful due to its ability to calculate amounts of carbide and nitride precipitates according to a defined heating/cooling cycle and its ability to take the nucleation sites into account, i.e. the nucleation site, either if it is on grain boundaries or by dislocation or both together. One more interesting feature of MatCalc is its ability to take into account deformation to the heating/cooling cycle and study its effect on the precipitation mechanism enabling simulating to a high extent the process during casting and especially straightening.

MatCalc was used for gaining three information for each alloy. Firstly, to define the transformation points of each alloy under equilibrium conditions. Melting point and phase transformation regions were calculated. Comparing the melting point with the temperature resulted from the NST test is important to define the starting temperature for the hot tensile testing. The austenite to ferrite transformation temperature from MatCalc had to be compared to the results from the Dil805A experiments. Secondly, it was used to perform a Scheil-Gulliver model to predict the primary precipitates during solidification. Before starting precipitation simulation for a given alloy for a certain thermo-mechanical treatment, first we need to know how much precipitates were already formed during solidification and the rest elements, which are still available in the matrix and able to precipitate during further cooling and deformation during casting. The third application of MatCalc was to run a precipitation calculation step for a thermo-mechanical treatment exactly as the one used for hot tensile testing.

Finally, we have the necessary information about the precipitates, amounts, sizes and distribution of a thermo-kinetic treatment, while hot tensile test will give us the hot ductility

values corresponding to that treatment. The values of the parameters used in the thermo-mechanical cycle such as the cooling/heating rate, strain rate during straightening and re-heating rate, are given data representing a typical commercial CC process.

The expected results from MatCalc simulations will give an overview of the kinetics of precipitates formation by calculating the evolution of phase fraction, mean radius and number of density. Comparing the types and amounts of precipitates to the ductility values helps in understanding which type of surface fracture is dominant in the sample and can be linked to the type of ductility loss and cracking. Based on these information one will be able to correlate the loss of ductility to the precipitation behavior and define a certain range of precipitates, particle size and composition being linked to the low ductility and consequently to the crack formation.

4.3.2 Abaqus CAE: Finite element modelling program

Abaqus is a suite of powerful engineering simulation programs, based on the finite element method that can solve problems ranging from relatively simple linear analyses to the most challenging nonlinear simulations. Abaqus contains an extensive library of elements that can model virtually any geometry. It has an equally extensive list of material models that can simulate the behavior of most typical engineering materials including metals, rubber, polymers, composites, reinforced concrete, crushable and resilient foams, and geotechnical materials such as soils and rock [168].

Designed as a general-purpose simulation tool, Abaqus can be used to study more than just structural (stress/displacement) problems. It can simulate problems in such diverse areas as heat transfer, mass diffusion, thermal management of electrical components (coupled thermal-electrical analyses), acoustics, soil mechanics (coupled pore fluid-stress analyses), piezoelectric analysis, electromagnetic analysis, and fluid dynamics [168].

The application of the program will be fully discussed in **Chapter 6** in the field of heat transfer modelling and cooling profiles simulation. Abaqus/CAE 2016 was used to build, analyze and evaluate the FEM (finite element method) model.

4.3.3 PXF Workbench Point Count software

The actual percentages of the different phase structures in the pictures resulted from the LOM investigation were manually calculated by using the “PXF Workbench Point Count software”. Grain sizes were evaluated by using grid and diagonal methods, while phase fractions were calculated by grid point counting. The average values of 20 pictures from different positions for every sample were calculated. The results of phase fraction analysis depend on the heat treatment performed on each sample. The results will be fully discussed in **Chapter 6**.

4.4 Alloy characterization

4.4.1 As-cast microstructure analysis

Samples from the as-received material were investigated under LOM and SEM after the preparation mentioned in section 4.3 to study the received conditions after CC and before starting the experimental program. **Fig. 4.7** shows a schematic illustration of the as received sample from the centre of slab width (cut form slab centre, **Fig. 4.1**), while in **Figs. 4.8** to **4.11** the as cast microstructures of the inner surface – section 90 degree to casting direction - for Alloy-1 for different locations of the received material are illustrated.

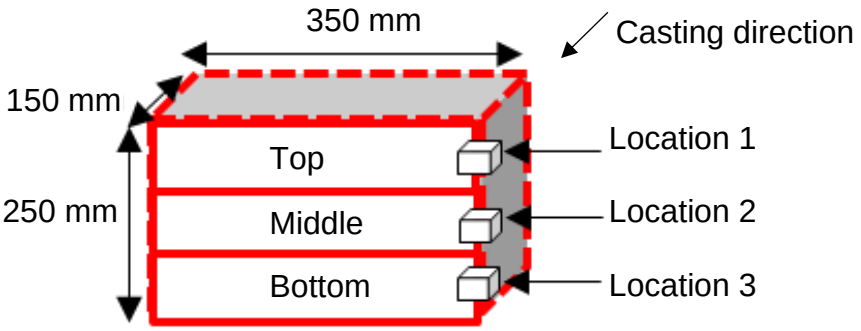

Fig. 4.7: Location of as-cast samples in the received material

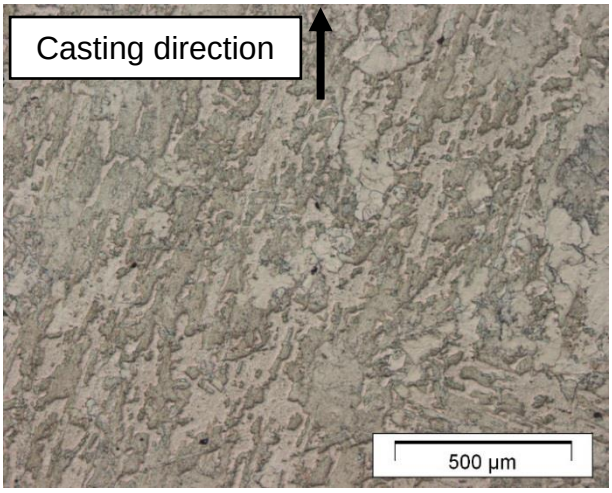

Fig. 4.8: As-cast microstructure (50X), Location-1, Alloy-1

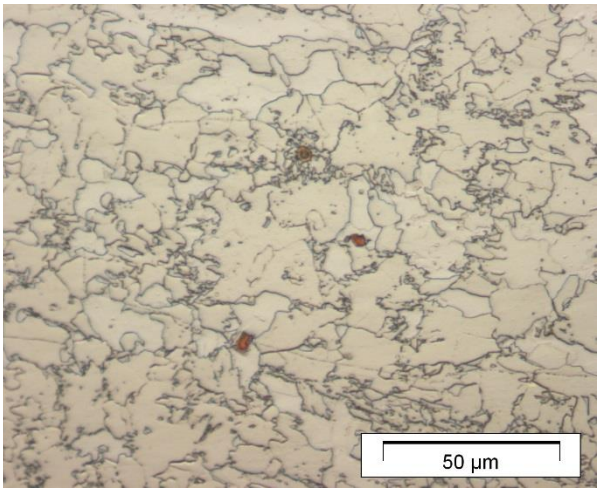

Fig. 4.9: As-cast microstructure (500X), Location-1, Alloy-1

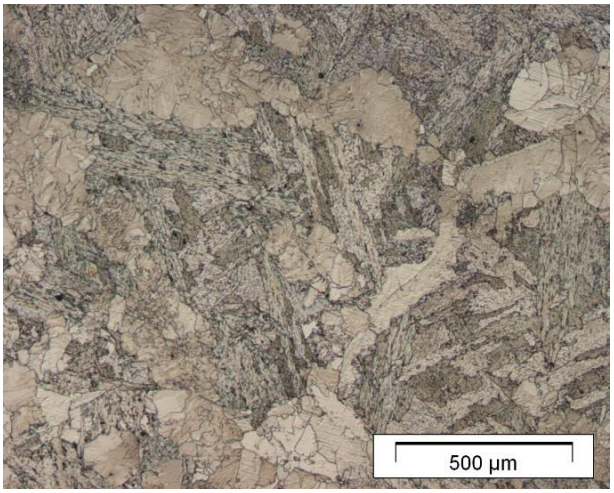

Fig. 4.10: As-cast microstructure (50X), Location-2, Alloy-1

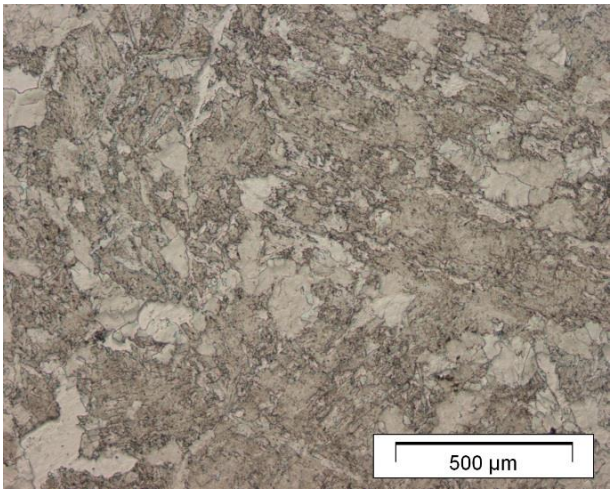

Fig. 4.11: As-cast microstructure (50X), Location-3, Alloy-1

The as cast samples for Alloy-1 show a mixture of ferrite, bainite and pearlite structures with different morphologies randomly distributed in the matrix. The grain size also differs from one area to another. Relatively high amounts of (Ti,Nb),(C,N) particles are spreading randomly in the matrix in different sizes, which could be observed by LOM (**Figs. 4.12** and **4.13**) and SEM (**Figs. 4.14** and **4.16**) and confirmed by EDX (**Figs. 4.15** and **4.17**) analysis.

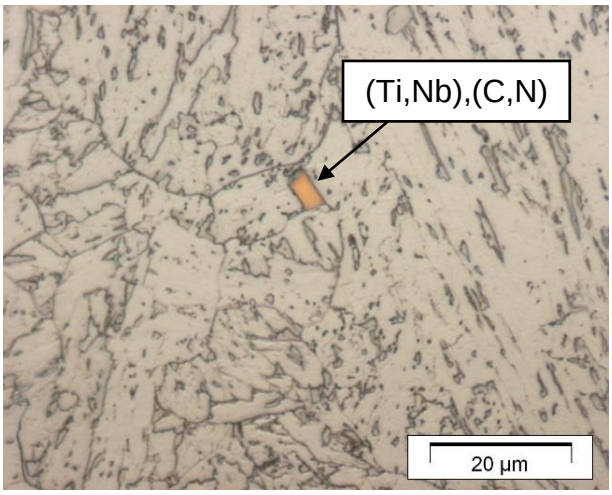

Fig. 4.12: As-cast microstructure 1 (1000X), Location-1, Alloy-1

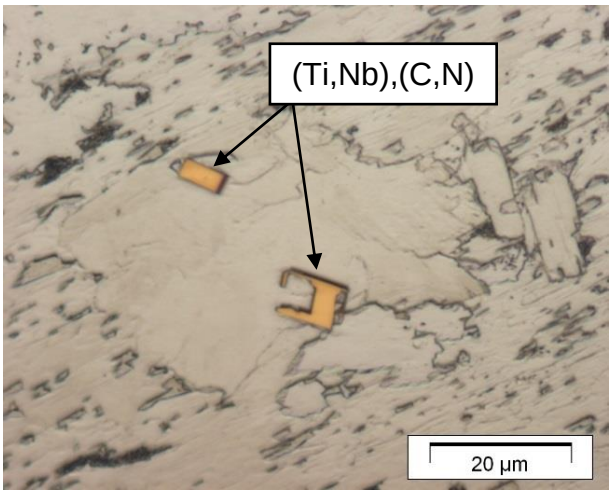

Fig. 4.13: As-cast microstructure 2 (1000X), Location-1, Alloy-1

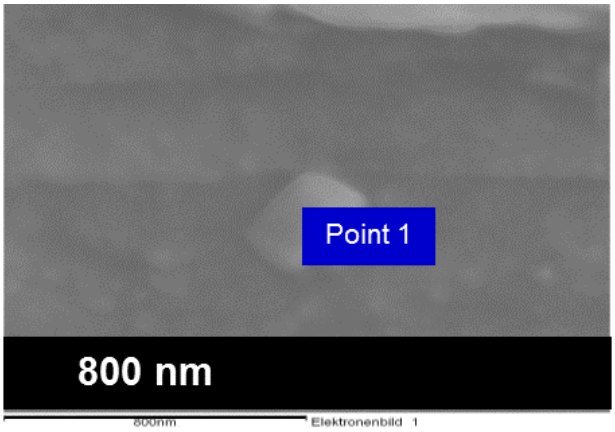

Fig. 4.14: As-cast microstructure, Alloy-1, Point-1

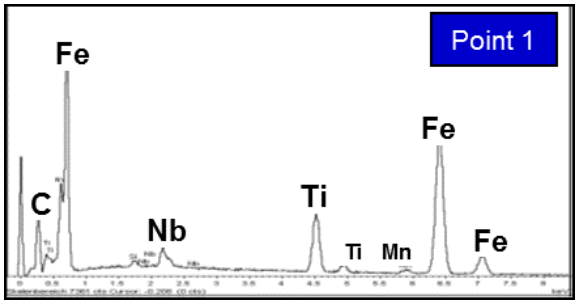

Fig. 4.15: EDX spectrum of Point-1

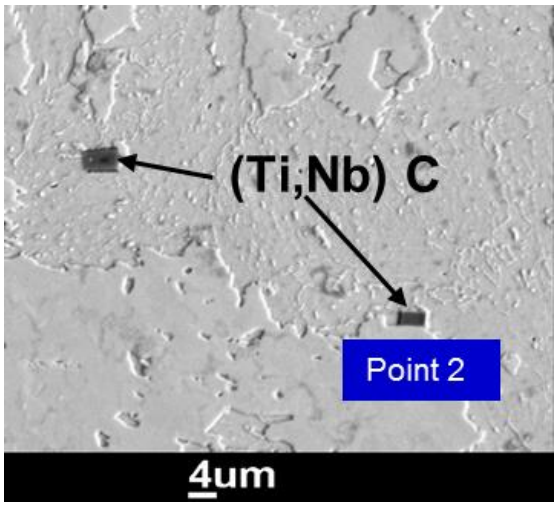

Fig. 4.16: As-cast microstructure, Alloy-1, Point-2

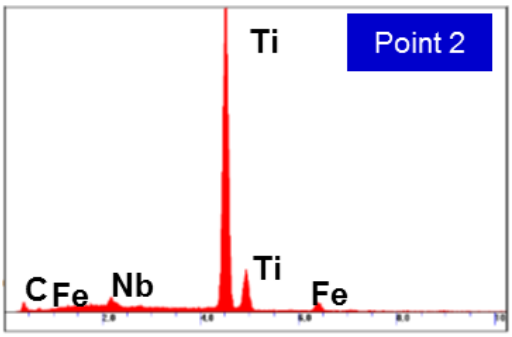

Fig. 4.17: EDX spectrum of Point-2

Samples from the slab corner, see **Fig. 4.1**, were also studied using LOM to compare the resulting microstructure between slab centre and corner under the effect of air/yard cooling. Many corner cracks could be observed in the fully bainitic structure at the slab corner regions. Examples are shown in **Fig. 4.18**.

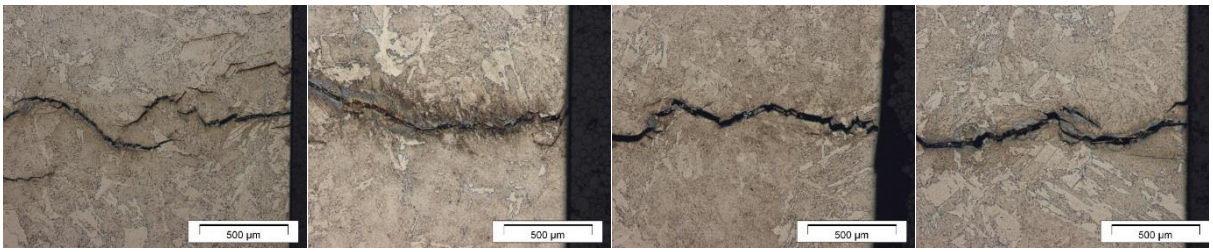

Fig. 4.18: Cracks in corner regions of the receive material, Alloy-1

On a bigger scale, LOM analysis was performed for relatively large samples to study the grain structure at the slab corner and centre on larger areas over the slab thickness in casting direction. **Figs. 4.19** and **4.20** show the as-cast microstructure of Alloy-1 in corner

regions at upper and middle/central areas, respectively. A bainitic matrix with some martensite formation could be seen on the big scale, which could be attributed to the higher cooling rates taking place at the corner areas compared to the rest of the slab. Cracks at the centre of the slab corner were also present. At higher magnification, relatively large particles of (Ti,Nb),(C,N) were recorded similar to the ones found in the slab width centre shown in the **Figs. 4.12** and **4.13**. The effect of the cooling practice on the microstructure of the slab surface at centre and edge compared to the corner regions (in slab transverse direction), will be discussed in **Chapter 6** in detail.

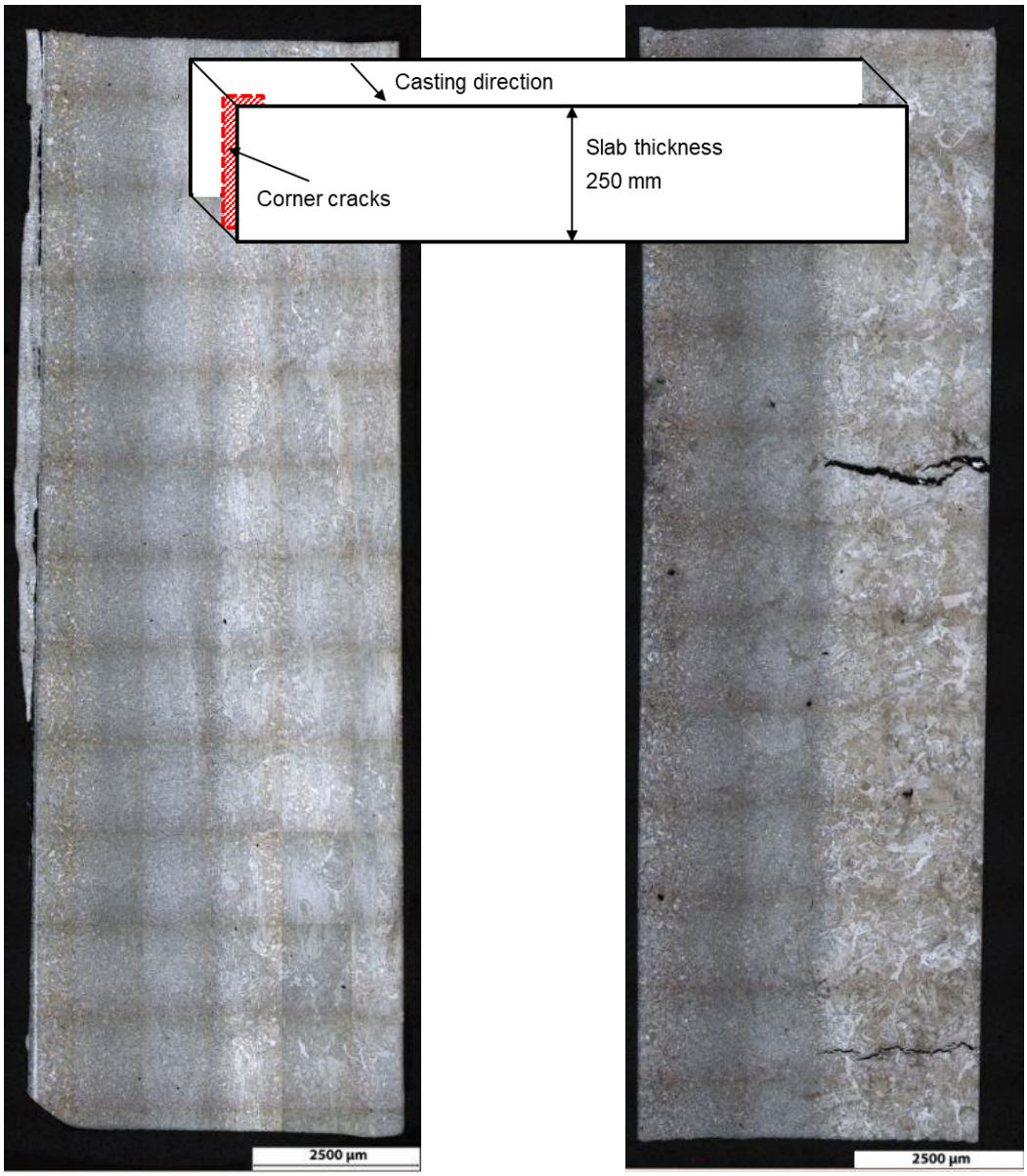

Fig. 4.19: Corner microstructure in slab corner upper area, inner surface parallel to slab thickness section, Alloy-1

Fig. 4.20: Corner microstructure in slab corner central area, inner surface parallel to slab thickness section, Alloy-1

LOM analysis for relatively large sample size was also performed for three regions in the centre width of the slab, defined as Location 1, 2, and 3 in **Fig. 4.7**. As can be seen in **Figs. 4.21 – 4.23**, the microstructure in the slab centre is different from that of the corner (**Figs.**

4.19 and **4.20**) in terms of grain size and formed phases, which can be related to the relatively slower cooling at the slab centre. **Fig. 4.21** represents the microstructure at Location-1, located near the slab surface, which is the area of interest in this work. The LOM analysis shows a matrix of bainite with ferrite (8%) formed on the austenite grain boundaries in Location-1. Another LOM analysis was performed to measure the grain size using another etching material (explained in 4.2.2) which was made to detect austenite grain boundaries clearly in the ferrite regions.

Fig. 4.22 shows the as cast microstructure exactly in the slab centre with the highest amount of ferrite (37%) in Location-2. Finally, in **Fig. 4.23**, the microstructure in Location-3 (slab bottom) is illustrated with (26%) ferrite phase fraction. The presence of the (Ti,Nb),(C,N) at higher magnifications could also be clearly observed. Finer precipitates in the range of a few micros or in nano-size for both centre and corner regions were observed at high SEM magnifications similar to the ones in **Figs. 4.14** and **4.16**.

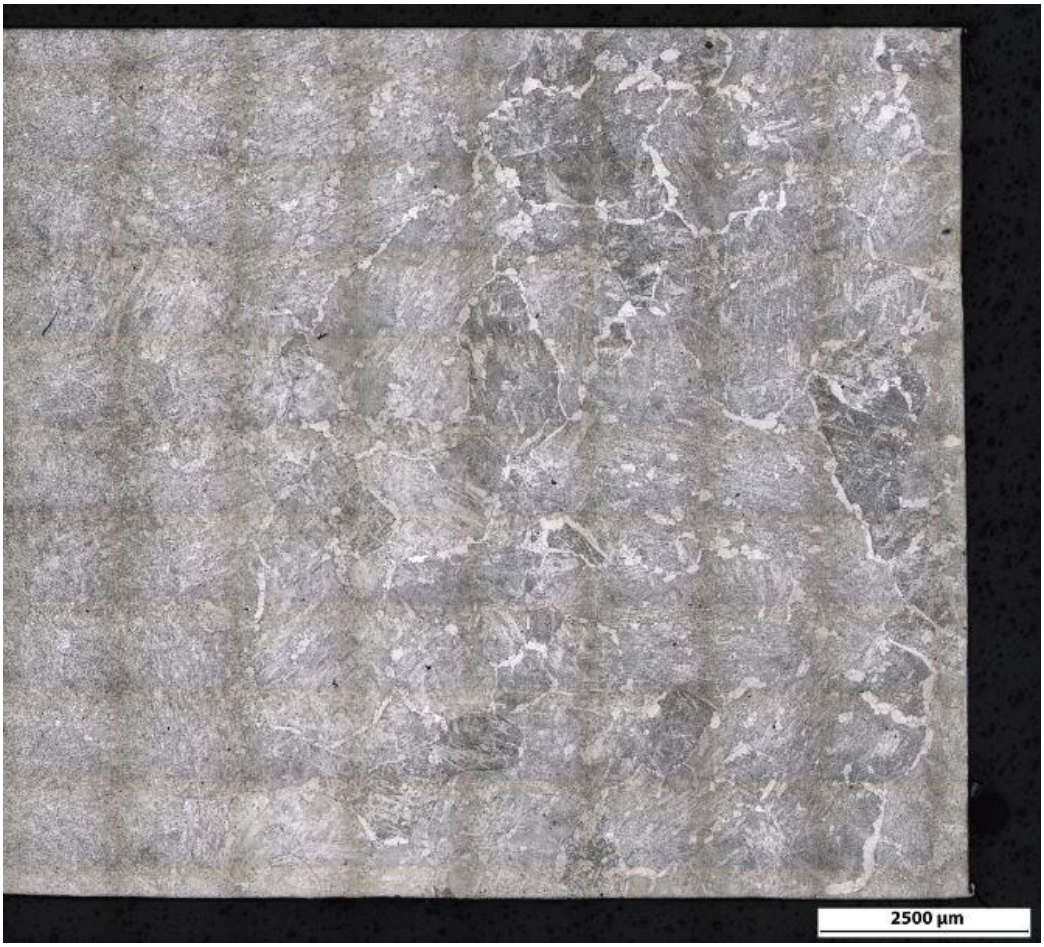

Fig. 4.21: As-cast microstructure, Location-1, inner surface parallel to slab thickness section, Alloy-1

Fig. 4.22: As-cast microstructure, Location-2, inner surface parallel to slab thickness section, Alloy-1

Fig. 4.23: As-cast microstructure, Location-3, inner surface parallel to slab thickness section, Alloy-1

For Alloy-0, the observation for the as cast structure was different. A more homogenous (compared to Alloy-1) structure of ferrite/perlite matrix could be observed in all parts of the received material at all locations. **Figs. 4.24 - 4.27** show examples of the microstructure.

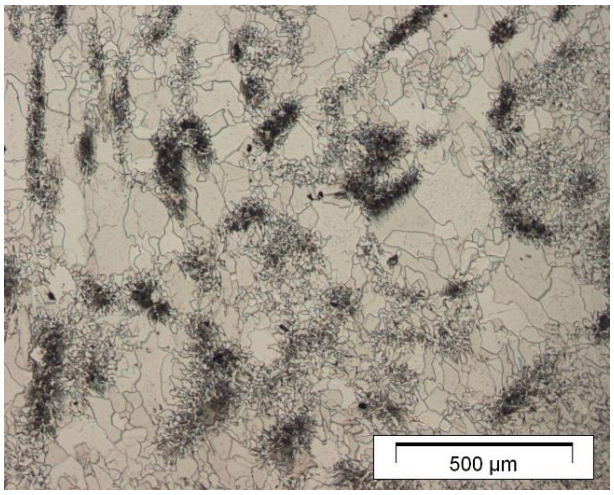

Fig. 4.24: As-cast microstructure (50X), Location-1, Alloy-0

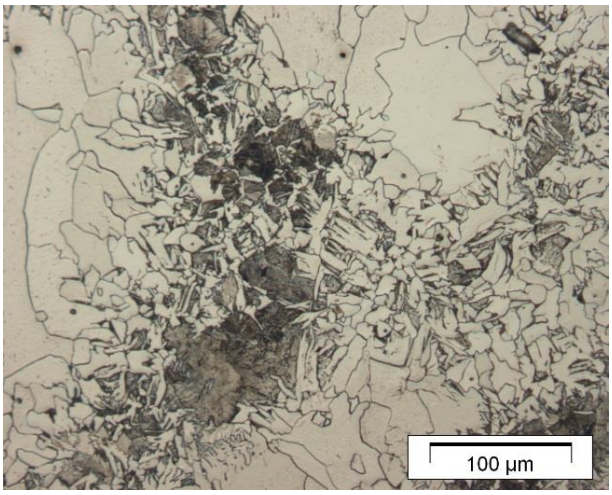

Fig. 4.25: As-cast microstructure (200X), Location-1, Alloy-0

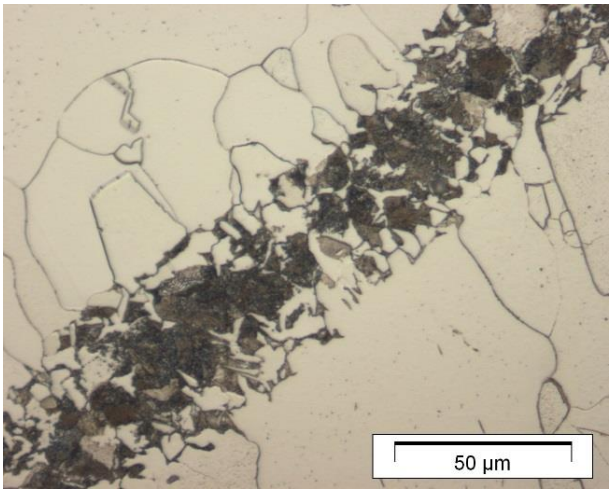

Fig. 4.26: As-cast microstructure (500X), Location-1, Alloy-0

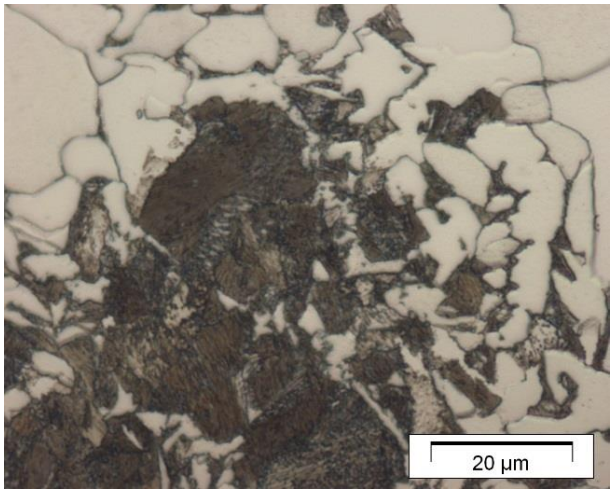

Fig. 4.27: As-cast microstructure (1000X), Location-1, Alloy-0

4.4.2 Grain size measurement/calculation

Based on the previous LOM analysis, grain size evaluation of the micrographs of the different samples from each alloy (after etching method explained in 4.2.2) was performed to measure the original austenite grain size using PXF Workbench Point Count software. The average grain size was measured by grid and diagonal method. Evaluation of the results gave an average grain size for Alloy-1 of 0.93 mm (± 0.3 mm) in Location-1, while the austenite grain size for Alloy-0 was 1.4 mm (± 0.3 mm) at the same location. These average austenite grain size values will be used for further precipitation simulation by MatCalc in order to build a simulation model with values as close as possible to reality.

4.4.3 Austenite to ferrite phase transformation – Dilatometer Dil805A

Ferrite formation is an important parameter in studying the low temperature ductility troughs, where it is important to define the limits of the third embrittlement region. Here, the austenite to ferrite transformation temperature is important due to its relation to stress concentration, grain boundary effects and enhancement of embrittlement mechanisms. With the beginning of the ferrite formation on grain boundaries, void nucleation at second phase particles and the growth of these voids continuing within the ferrite film are becoming more critical [81,84,169]. On a microscopic scale, it could lead to a ductile fracture, but overall the failure is brittle [3].

To observe the austenite to ferrite transformation, dilatometry tests with 10 mm x 5 mm$^{\varnothing}$ samples (**Fig. 4.2**) with slow cooling (0.015 K/s) after austenitization at 1000 °C for 5 min was carried out according to the schedule shown in **Fig. 4.28**. Every test was carried out three times for each alloy. An example of the dilatation curve for Alloy-1 is illustrated in **Fig. 4.29**. The aim of the experiment is to measure the $\gamma - \alpha$ transformation (Ar_3) by observing the sample's relative change in length over temperature indicating phase changes. In this test (**Fig. 4.29**), ferrite started to form at 775 °C (Ar_3) and transformation ends at 607 °C (Ar_1). The test average values of the transformation temperatures after three runs were calculated and summarized in **Table 4.3**. These values are also to be used for building the MatCalc simulation model to be based on measured transformation temperatures.

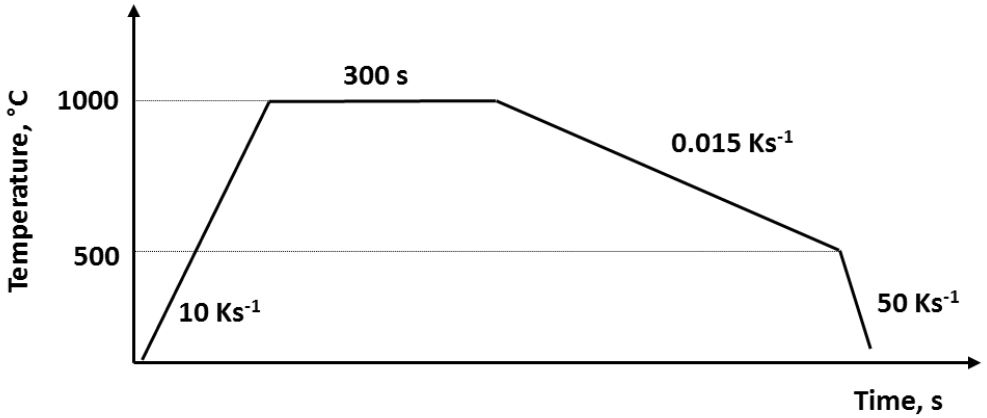

Fig. 4.28: Time - Temperature schedule to study austenite to ferrite transformation

Table 4.3: Ferrite start and end temperatures for Alloy-0 and Alloy-1

	Ferrite start	Ferrite end
Alloy-0	837 °C (±2)	677 °C (±6)
Alloy-1	757 °C (±7)	607 °C (±10)

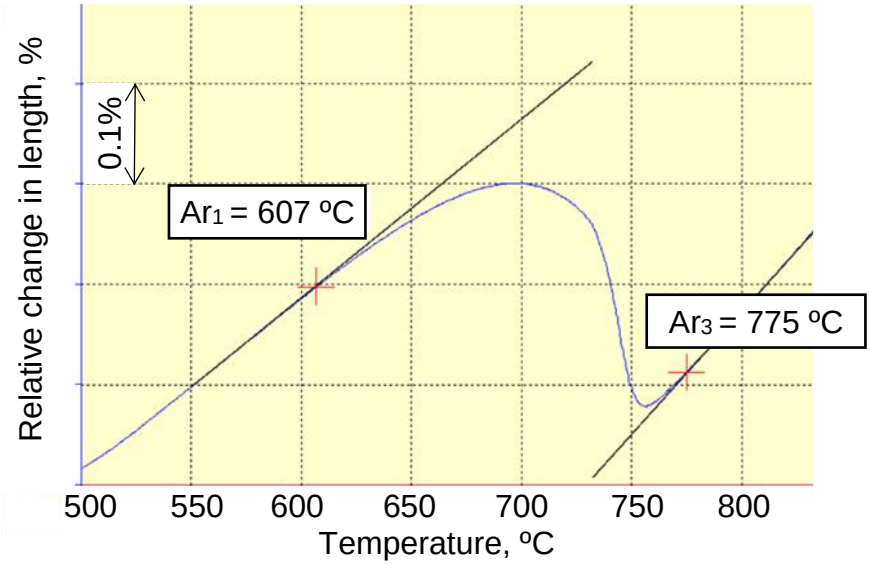

Fig. 4.29: Austenite to ferrite transformation curve, Alloy-1

4.4.4 MatCalc Scheil solidification model

The MatCalc program was used for different applications in this work. In this part, the solidification procedure of each alloy by performing a Scheil-Gulivar simulation will be introduced. Back diffusion of C and N was considered as well as the peritectic reaction. **Fig. 4.30** represents the Scheil model for Alloy-0. By cooling from 100% liquid to complete solid (assumption: 1% rest liquid), the constituents of each alloy are calculated in a phase fraction vs temperature diagram.

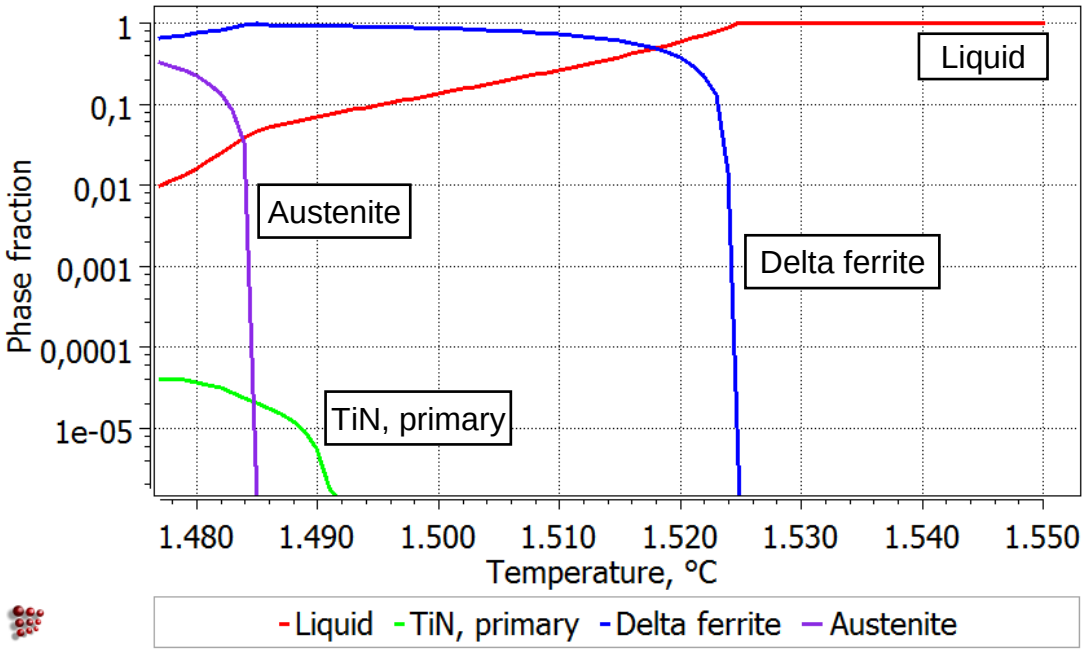

Fig. 4.30: Scheil solidification model, Alloy-0

The result of Scheil solidification model for Alloy-0 suggests a microstructure by the end of solidification (liquid=1%) composed of a mixture of delta ferrite (≈ 66%) and austenite (≈ 33%). The chemical composition by the simulation included 0.001% of Ti and 0.004% of N

according to the alloy composition (**Table 4.1**) which produced a very small amount of TiN of 0.004%. The sensitivity of hot ductility to the amount of formed precipitates will be discussed in **Chapter 5**.

Scheil solidification model of Alloy-1, see **Fig. 4.31**, illustrates that a peritectic reaction has started and finished. The model suggests an almost fully austenitic matrix structure by the end of solidification with 1% liquid. The presence of 0.12% Ti and 0.05% Nb beside 0.005% N in the chemical composition of Alloy-1 resulted in the presence of a high amount of Ti- and Nb-carbonitrides. The model calculated by the end of solidification the precipitation of 0.1% of primary TiN and 0.02% of primary NbC in the matrix. These precipitates could be clearly seen in the as cast microstructure in section 4.4.1. The precipitation of TiN starts very early at ~ 1510 °C, after the beginning of solidification, while NbC starts at ~ 1423 °C, shortly before the end of solidification.

According to the MatCalc Scheil models, the solidification for Alloy-1 ends at 1408 °C and for Alloy-0 at 1477 °C. These values will be used in the further MatCalc application in models regarding precipitation kinetics.

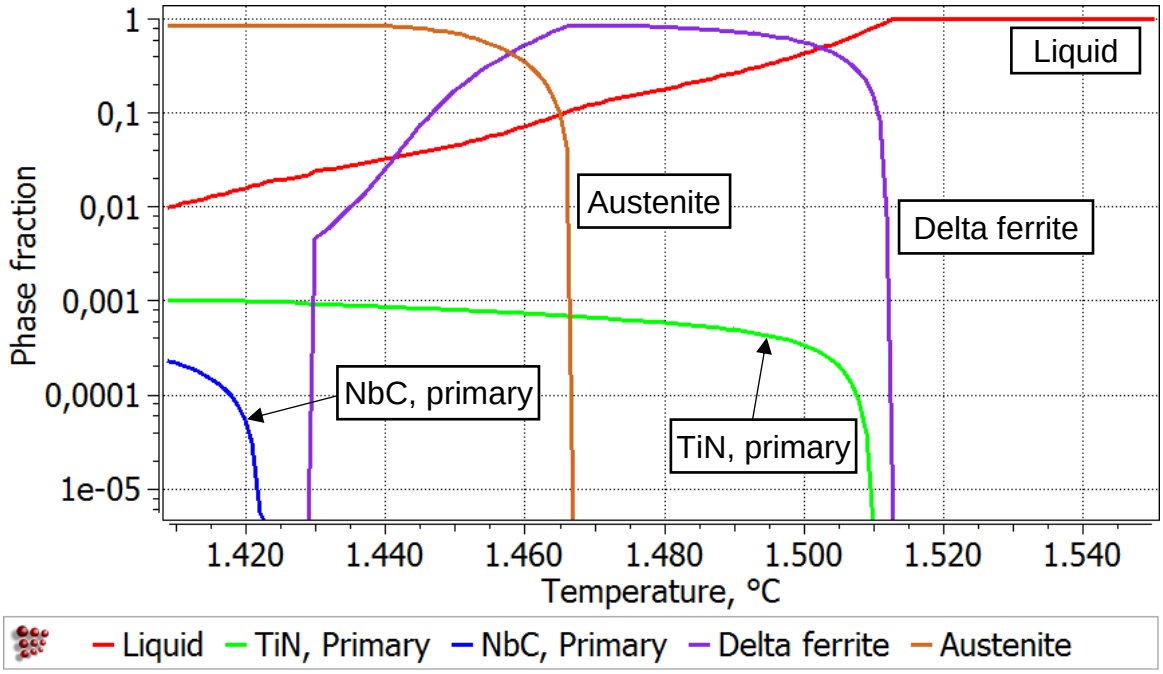

Fig. 4.31: Scheil solidification model, Alloy-1

4.4.5 Measurement of Nil-strength temperature (NST)

NST is very important for cracking susceptibly studies of metals and alloys, such as in welding and casting. At this temperature, as is defined, a material cannot stand any load. Therefore, any tensile stress applied at temperatures close to and above the NST would lead to a crack or failure. A 6 mm$^{\varnothing}$ x 90 mm sample was used for the NST measurement on a Gleeble device together with a pair of specially designed copper grips on the Nil-strength jaw system. When the specimens are loaded into the grips, the free span should be constant. This yields repeatable test results [170].

A small load of 8 kg is applied before heating by an air cylinder equipped with the Nil-strength jaw system. It is kept constant during the tensile test until the specimen is broken. The specimen is heated with a heating rate of 20 K/s to a temperature 100 K below the liquidus temperature of the material, before changing the heating rate to 1-2 K/s until the specimen is broken. The temperature at fracture is registered as the NST of the material. The test was run in inert gas environment and type S or R thermocouples are usually used when the NST value is higher than 1250 °C [170].

For the NST evaluation of Alloy-1, four experiments were performed. The Time-Temperature evaluation until sample fracture for the four samples are shown in **Fig. 4.32**, while the resulted NST values of the experiments and the calculated average of the NST measurements are shown in **Table 4.4**.

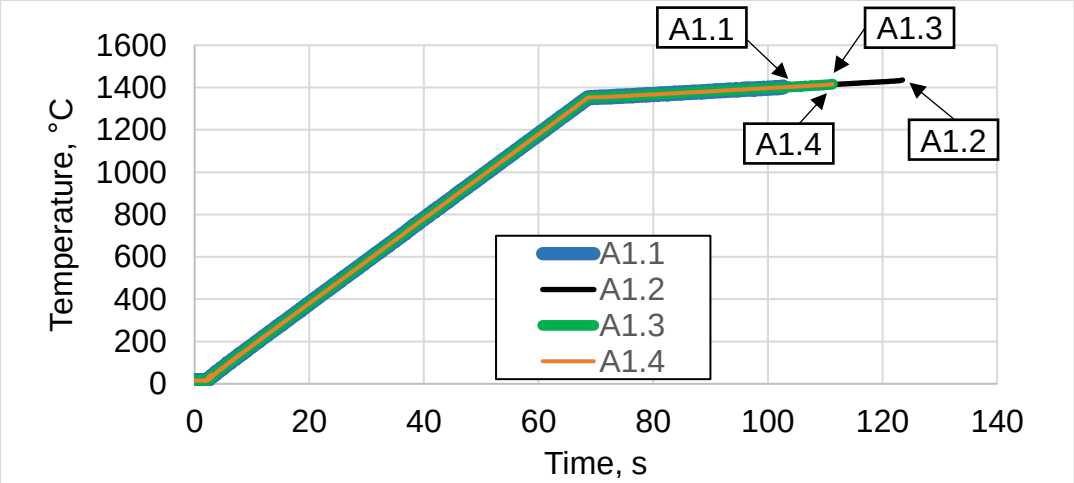

Fig. 4.32: Time - Temperature evaluation of the NST test, Alloy-1

Table 4.4: Results of the NST experiments, Alloy-1

Sample	NST, °C
A1.1	1402
A1.2	1436
A1.3	1417
A1.4	1416
Average:	1418 (±12)

The NST is an important value to define the austenitization temperature in the hot tensile testing. The cooling cycle and austenitization temperature will be illustrated in **Chapter 5**. To avoid sample melting and assure a reproducible hot tensile test procedure, the austenitization temperature must be taken 20-30 K below NST. An example of the sequence of important temperatures below the liquidus temperature are shown in **Fig. 4.33**.

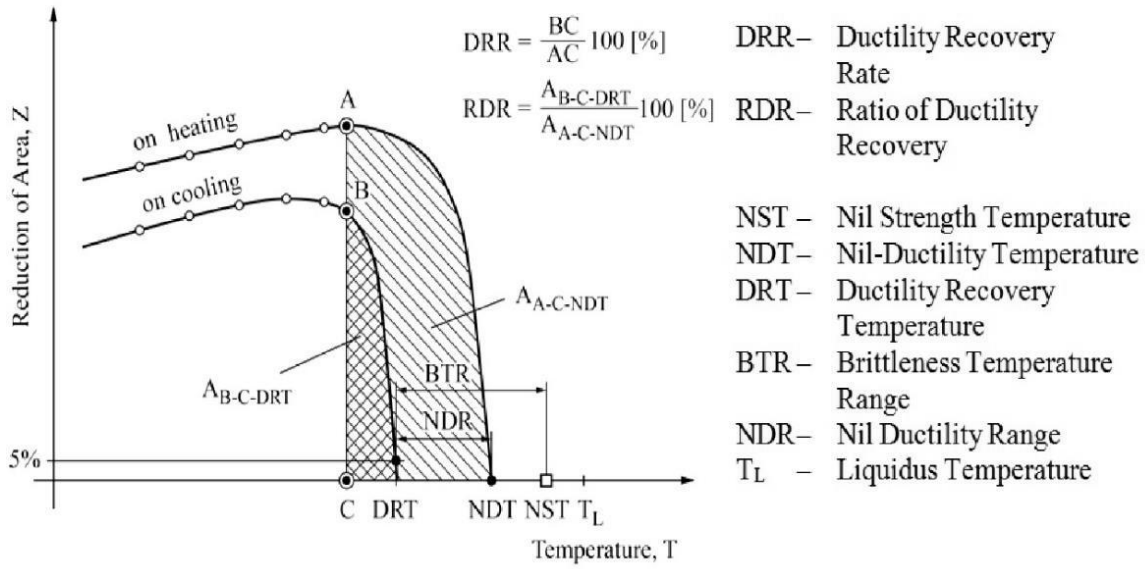

Fig. 4.33: Relation between NST, liquidus and hot tensile test temperatures [171-174]

4.5 Summary and Conclusions

This chapter gave an overview of the used devices and instrumentation as well as the investigated materials. The primary analysis of the as received material and the base experiments and simulations were discussed. The following points can be stated:

- For Alloy-0, the as cast microstructure of the received slab material is composed of ferrite/pearlite matrix at all areas of slab centre and corner. While for Alloy-1, the microstructure varied from bainite matrix (at corner regions) and ferrite/pearlite/bainite (in the centre of the slab width). More ferrite was observed in the centre of the slab width.
- Corner cracks in the slab samples could be observed for Alloy-1, but were missing in Alloy-0.
- Relatively large particles of primary (Ti,Nb),(C,N) precipitates were observed in random manner all-over the Alloy-1 regions, but could not been detected at any of the Alloy-0 samples.
- For further hot tensile testing and precipitation kinetics modelling (explained in **Chapter 5** and **6**), some experimental work was carried out with the aim of setting the further work on experimental measurements and industrial sample analysis rather than assumptions or literature values.
- The austenite grain size for Alloy-0 is 1.4 mm, while for Alloy-1 it is 0.93 mm in the slab Location-1, where the hot tensile samples are to be prepared. The austenite grain size plays an important role, as the precipitation simulation is strongly influenced by it, acting as nucleation sites for precipitation in the CC model.
- According to dilatation testing (Dil805A), the ferrite start temperatures (Ar_3) by cooling are 837 °C and 757 °C for Alloy-0 and Alloy-1, respectively.
- Equilibrium calculations using MatCalc resulted in Ae_3 values for Alloy-0 and Alloy-1 of 870 °C and 845 °C, respectively.
- Simulation for the solidification process was performed using MatCalc 6 and a Scheil modelling approach. A complete solidification was assumed reaching 1% rest liquid. Peritectic reaction and back diffusion of C and N were considered in the solidification calculation. Based on the model results for Alloy-1, the matrix after complete solidifica-

tion at 1408 °C should be composed of a fully austenite structure with primary precipitates of TiN (0.1%) and NbC (0.02%), which could be obviously detected in the microstructure analysis of the as received material. While for Alloy-0, after complete solidification at 1477 °C, a matrix of delta ferrite (66%) and austenite (33%) resulted. Very few TiN (0.004%) was produced. The effect of precipitates amounts on hot ductility will be evaluated in the coming chapters.

- The MatCalc precipitation model of the CC process will include the amounts of primary precipitation resulted from Scheil model as a part of the matrix before further secondary precipitation to start after leaving the mold.
- The precipitation of carbonitride particles in the matrix before a complete delta ferrite to austenite transformation, might increase the probability of precipitation to form on austenite grain boundaries, which is very detrimental to hot ductility and might cause transverse surface cracking, the finer the precipitates are. A remaining liquid film on the ferrite/austenite grain boundaries might increase cracking probability due to the strains resulting from the phase change. This effect is strongly affected by the primary cooling practice in the mold and the chemical composition of the alloy, which defines the phase transformation temperatures and amounts.
- The experiments for the evaluation of the NST temperature for Alloy-1 resulted in an average NST of 1418 °C. For a reproducible hot tensile testing, the austenitization temperature will start at 1380 °C.

Chapter 5: Continuous casting process

The process of continuous casting (CC) is analyzed in this chapter followed by presenting and discussing the results of experiments and simulations. This chapter will include illustration of ideal casting cycles according to industrial set values, deviation from this cycle in case of process interruptions and study of the effects of this interruption on crack sensitivity. The effects will be studied and quantified using hot tensile testing (DIL805T), MatCalc precipitation kinetics modelling and a microscopic approach by LOM, SEM and EDX.

5.1 Different casting conditions

This section gives the needed overview for the process before the results are introduced in the next section. Molten steel follows two successive cooling steps in the casting machine. First, rapid cooling in the mold, referred to as primary cooling, where primary solidification takes place and the first solid shell is built, followed by secondary cooling using side nozzles spraying water and gas under controlled amounts during further movement of the strand downwards between support rolls. The intensity of the secondary cooling controls the strand surface temperature and influences the solidification of the strand center. By the end of the casting machine and before the torch cut off line, where slabs cutting takes place after the metallurgical length, straightening rolls are responsible for bringing the curved strand into a straight/flat position to produce flat slabs. This straightening region brings tensile stresses on the upper surface of the strand and compression ones on the lower surface.

Two important parameters are mainly affecting an ideal process and their control can strongly influence the avoidance of surface cracks during the straightening process. Those two factors are the casting speed and the secondary cooling conditions. The combination of both factors defines the temperature profile of the strand, surface cooling rates and surface deformation during straightening. Their influence differs from one casting machine to another depending on machine's geometry and slab thickness.

Fig. 5.1 illustrates a schematic drawing starting from mold exit (without values of temperature and distance form meniscus) of the temperature profile under ideal/typical casting conditions to the set values. The casting speed is 1 m/min and the surface temperature during straightening is around 1000 °C on average (temperature fluctuation between maximum 1080 °C and minimum 950 °C due to roll contact). The ideal temperature profile before straightening is illustrated in the diagram by the dashed curve. It can be seen that the secondary cooling was deactivated/reduced at a certain point from the mold downstream, which allows surface reheating of the strand surface before straightening. In case of no change in the performance/intensity of the secondary cooling nozzles, the strand straightening would have happened in a much lower temperature range (below 1000 °C) which is not desired. Unbending during straightening produces around 1 - 2% of surface tensile

strain on the upper slab surface. The strain rate depends on the casting speed, slab thickness and machine geometry that is around 2 x 10^{-3} s^{-1} according to industrial data.

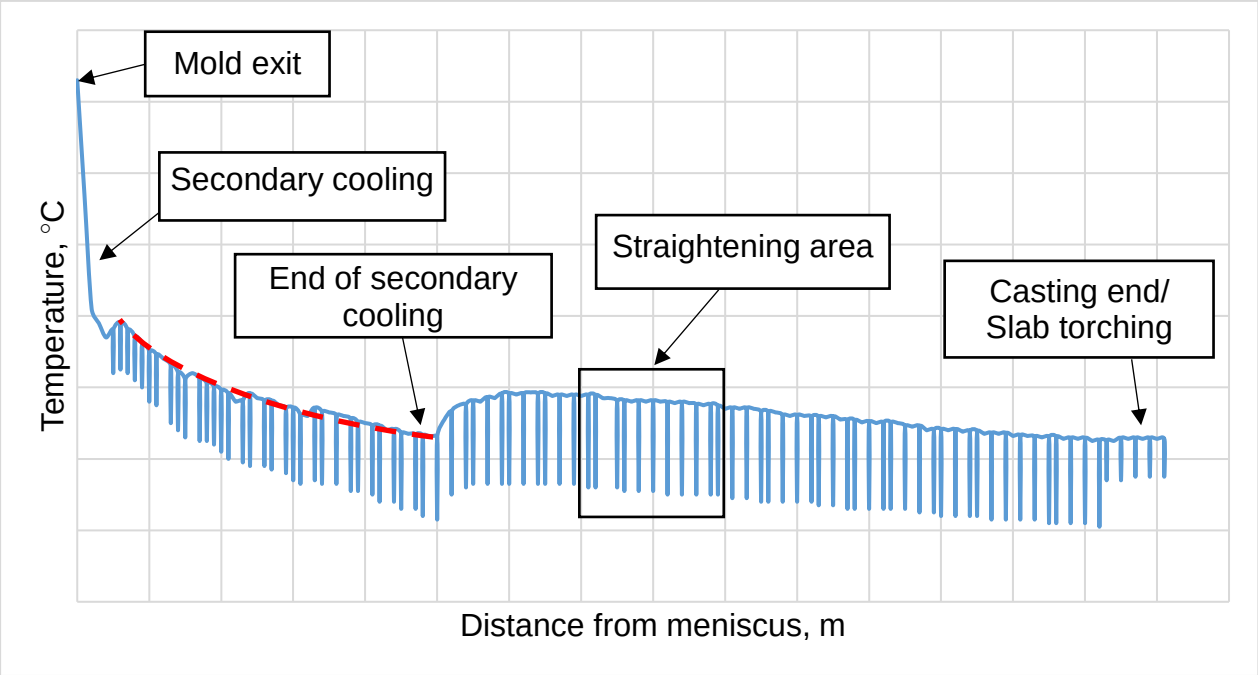

Fig. 5.1: Temperature profile under ideal/set CC conditions

Slab surface quality and crack free cast products are possibly improved by the optimization of casting speed and secondary cooling. Under irregular (undesired but unavoidable) casting conditions, a compromise should be met to avoid machine damage and getting as acceptable material quality as possible. Important example is the case of a break-out in the mold, where the casting speed is reduced to a minimum and cooling intensity (upper part of the machine) is increased to avoid molten steel to flow from the broken strand into the machine. By successfully saving the strand flow and reproducing a growing and thicker solid shell, the regular casting conditions are to be proceeded again.

What happens during this switching from normal casting speed (1 m/min) into the break-out situation (0.2 m/min) and then leveling back to the normal casting conditions is studied in this chapter within the scope of the effect of this speed switching on surface cracking of the strand.

The changes during casting once a break-out takes place until normal conditions are resumed, can be observed over four consecutive segments represented schematically in **Figs. 5.2** to **5.5**. First, once a break-out takes place, the casting speed will be reduced to 0.2 m/min and the surface temperature of the upper region of the strand will fall and reaches values less than 900 °C before it rises up again. An illustration of the beginning of the break-out is shown in **Fig. 5.2**. The deviation of the break-out temperature profile from the ideal temperature profile is clear by observing the deviation from the dashed curve representing the ideal temperature profile.

In the straightening area at the same moment, where the break-out begins, the average straightening temperature is still similar to ideal casting, while the casting speed is dropped to lower values, which reduces the deformation rate at the slab surface. The conditions in the straightening area in this case will be referred to as Break-out-1.

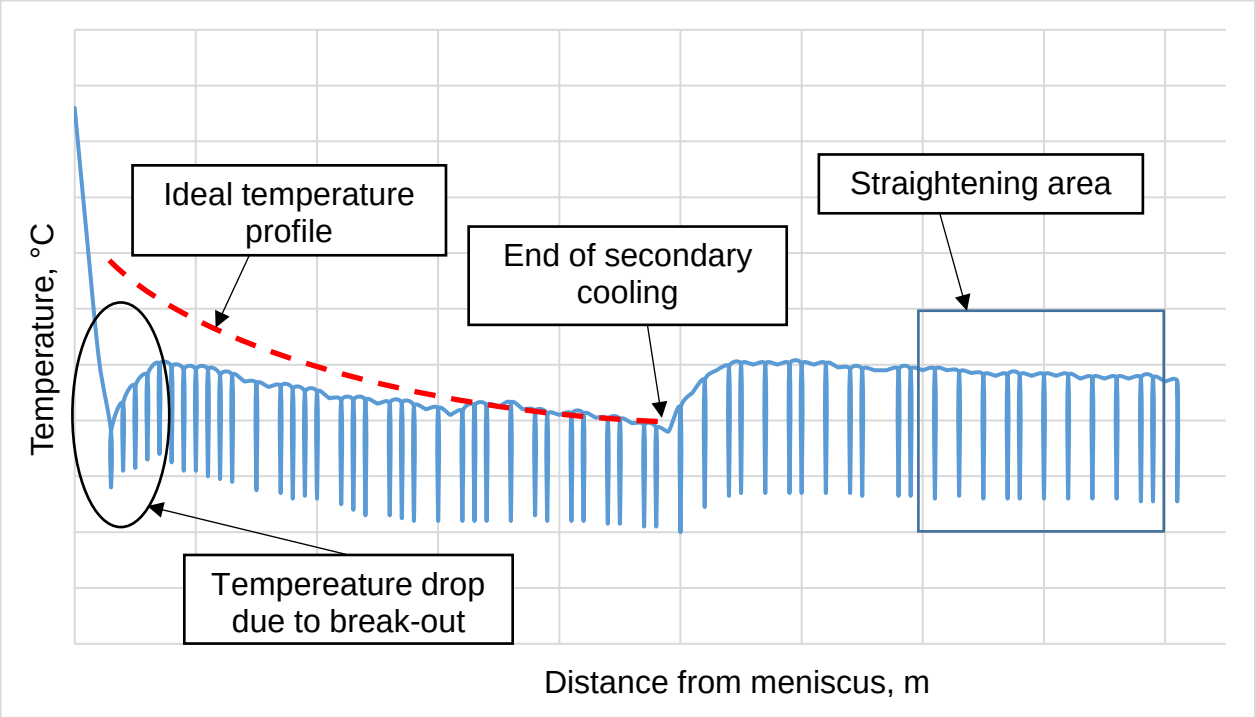

Fig. 5.2: Temperature profile during break-out (1/4)

Once the break-out is over and the casting speed is allowed to be gradually increased back to ideal conditions, the cooling nozzles set up should be used to improve/repair the part of the strand with the undesired temperature drop. The secondary cooling intensity will be set to its minimum in the relatively cold part of the strand resulted from the break-out to allow reheating of the strand surface from the molten/hotter slab center. This area will receive less secondary cooling by further strand movement downwards to slowly merge with the flow of the strand and gradually reach the set/ideal temperature profile values again. This recovery practice can be seen in **Fig. 5.3**.

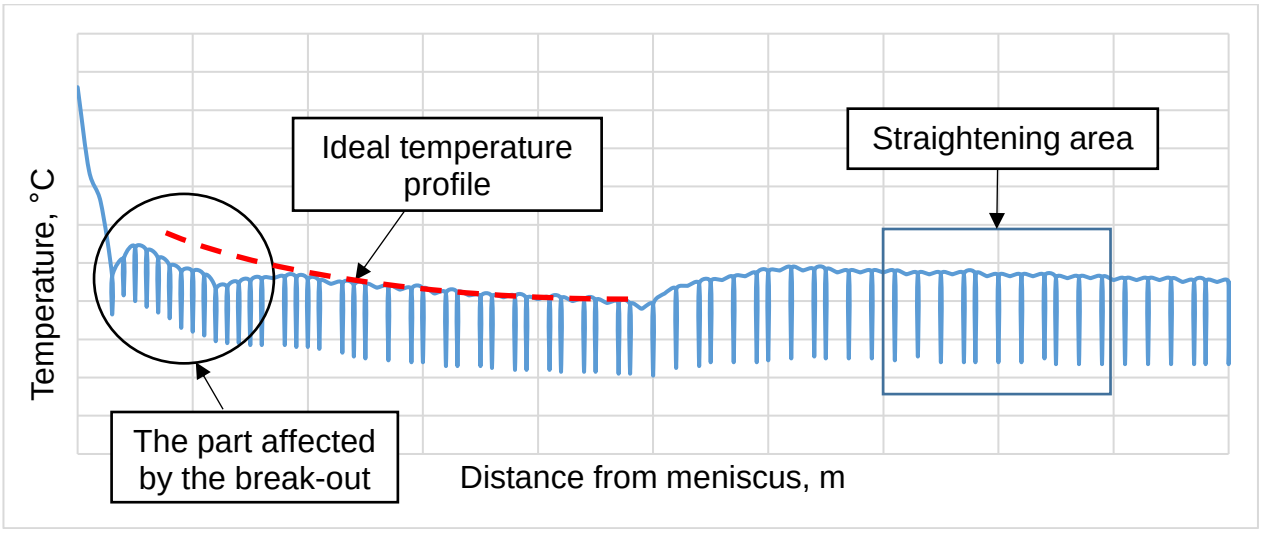

Fig. 5.3: Temperature profile during break-out (2/4)

Under the conditions presented in **Fig. 5.3**, the part of the strand in the straightening area will experience a low casting speed/deformation rate, while the straightening temperature is in the range of (1060 - 850 °C). This case will be referred to as Break-out-2.

Further increase in the casting speed from 0.45 m/min (**Fig.5.3**) to 0.65 m/min (**Fig.5.4**) moves the break-out affected region further as shown in **Fig. 5.4**. The upper part of the strand is fully recovered and fits back with the ideal temperature profile of the strand, while the lower part with the temperature drop earlier is still recovering by slab surface reheating and merging with the rest of the strand that didn't experience the rapid cooling of the break-out. The current straightening temperature range is (1050 – 830 °C) while the casting speed of 0.65 m/min which results in a lower deformation speed compared with the one in the ideal case resulting from 1 m/min. These conditions will be referred to as Break-out-3.

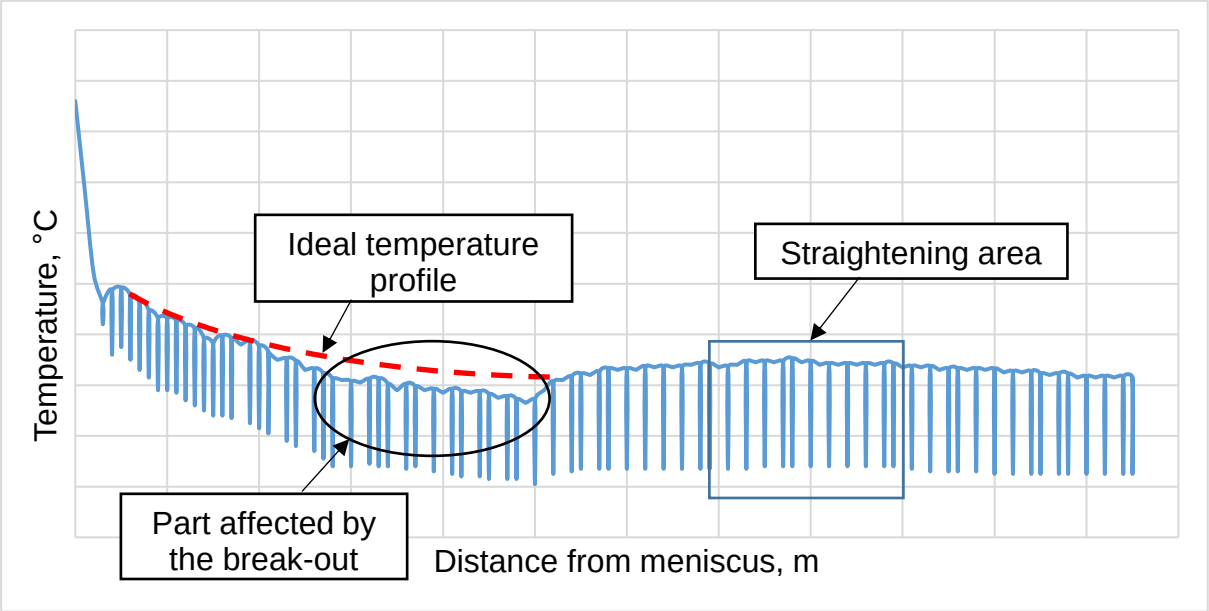

Fig. 5.4: Temperature profile during break-out (3/4)

After some minutes from the break-out start, the break-out affected region reaches now the straightening rolls in the machine and the casting speed is regulated to its original value of 1 m/min. This switching to regularity is illustrated in **Fig. 5.5**. In the straightening area, the surface temperature is fluctuating between 1000 °C at its maximum value and 800 °C at the lower one. Those values strongly depend on the secondary cooling practice, slab thickness and casting speeds. This condition, where the casting speed is back to 1 m/min and the straightening temperature is fluctuating between 1000 °C and 800 °C, will be called Break-out-4. The part of the strand coming afterwards (dashed box) has already higher temperature range as it was cast after the finishing of the break-out and it represents casting according to the ideal temperature profile and the set casting speeds. Starting from this point, a complete normal condition will proceed. When the 1 m/min is reached again, the casting conditions are back to normal, but it is important to note that starting from the break-out point until the point where the normal casting process proceeds again, all the material in between has a different casting history in terms of cooling and deformation. In other words, the steel strand related to the break-out (~length of 4 slabs), experienced different secondary cooling profiles and deformation rates in the straightening region. A comparison between the ideal casting conditions with the four different break-out cases is shown if **Table 5.1**.

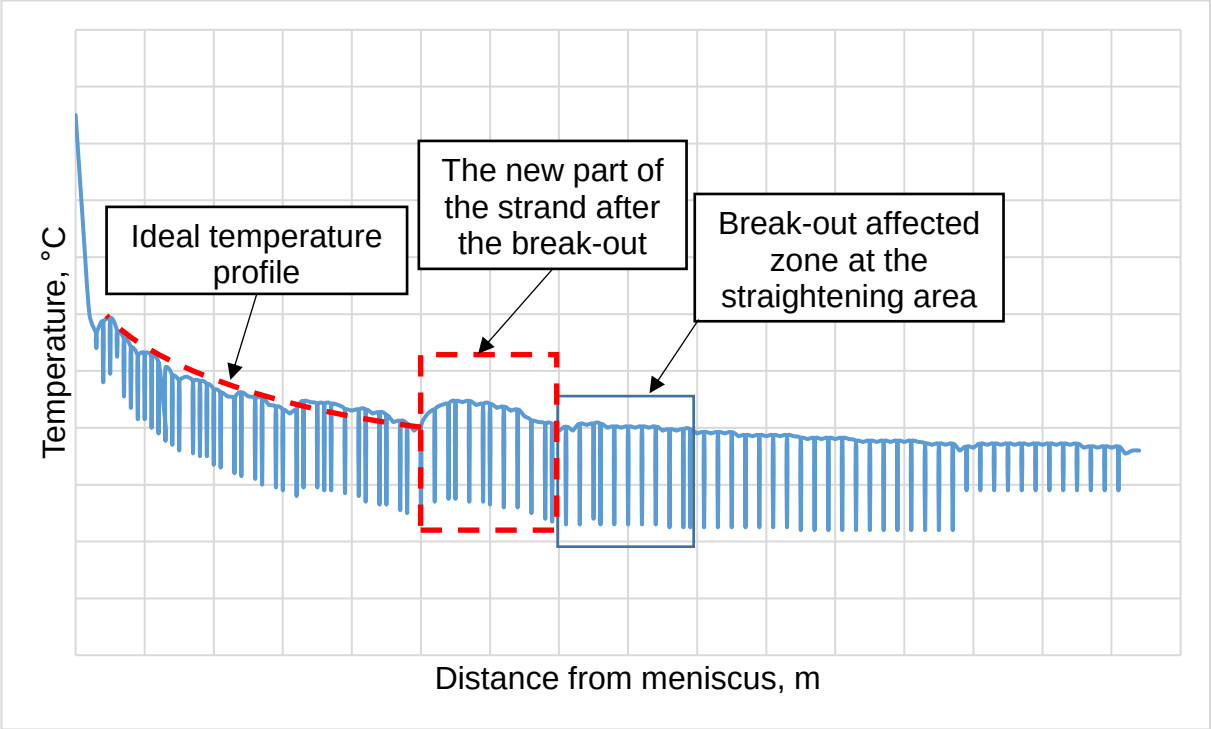

Fig. 5.5: Temperature profile during break-out (4/4)

Table 5.1: Comparison between ideal/set and break-out casting conditions

Case	Straightening temperature range, °C	Cooling rate, K/s	Casting speed at straightening, m/min
Break-out-1	1080-950	0.1	0.2
Break-out-2	1060-850	0.04	0.45
Break-out-3	1050-830	0.05	0.65
Break-out-4	1000-800	0.1	1
Ideal casting	1080-950	0.1-0.3	1

From the figures and the values, it could be observed that the Break-out-4 case is the one where the slab suffers the most abnormal casting conditions compared to the others. It is the slab that experiences the sudden cooling at the beginning of the break-out (which can lead to finer secondary precipitation), the slowest casting program (which can lead to relatively large austenite grain size) and the straightening takes place at the lowest temperature range (down to 800 °C).

However, in both of the ideal casting condition (**Fig. 5.1)** and the condition of Break-out-4 (as in **Fig.5.5**), the casting speed during the straightening is 1 m/min with a difference in the temperature range for unbending and cooling history. In spite of the same deformation speed taking place in the two cases, the effect of the cooling schedule (at a fixed strain rate in both cases) on the hot ductility is remarkable, which is studied in this chapter to evaluate the crack sensitivity of a slab with a Break-out-4 history compared to slab cast under the set/ideal values. Slabs that represent the Break-out-1, 2 and 3 cases are also believed to be critical in terms of cracking as lower casting speeds will result in lower strain rates which is detrimental to hot ductility despite that the straightening takes place at relatively high temperatures even closer to the ideal casting range. The effect of different strain rates was also studied. Finally, the results of this analysis will be compared with the findings of the industrial statistical analysis.

Based on the previous description, some cases for further experimental procedure were chosen to study the effect of different cooling cycles. Cycle-1 (**Fig. 5.6**) represents a slab with an ideal/set casting conditions where cooling rate before deformation varies between 0.1 - 0.35 K/s, while Cycle-2, shown in **Fig. 5.7**, represents a slab cast under the conditions of Break-out-4 case. Cycle-1 and 2 will be used in the further hot tensile testing for hot ductility evaluation and MatCalc precipitation simulation. In the hot tensile testing on Dil805T, the samples were austenized at (1350 – 1380 °C) for 10 minutes then cooled down to test temperature according to the defined cycle until the deformation step. After deformation to fracture, the samples are quenched with 100 K/s to room temperature for subsequent microstructural analysis.

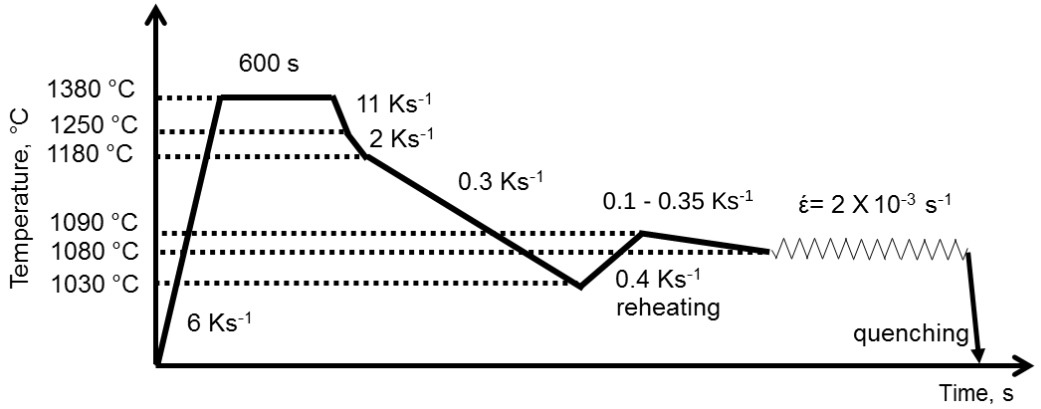

Fig. 5.6: Cycle-1 temperature profile during ideal/set casting conditions

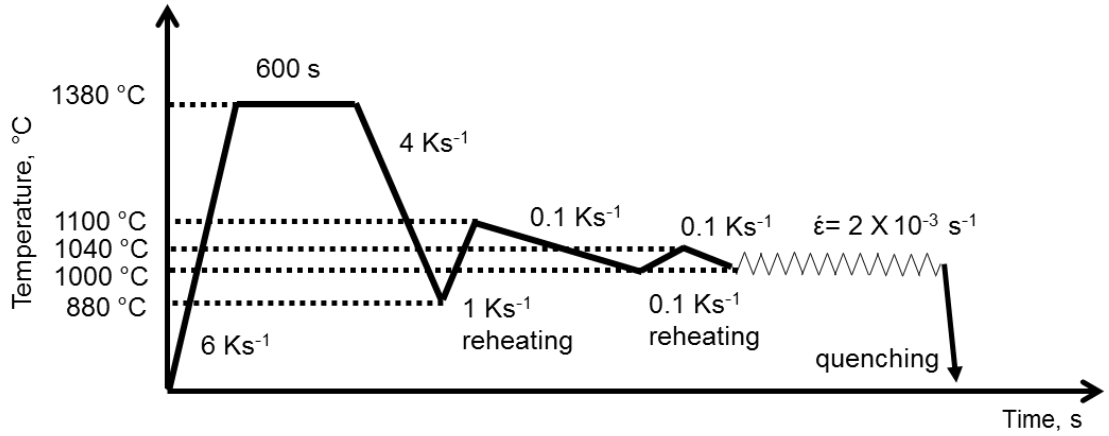

Fig. 5.7: Cycle-2 temperature profile for Break-out-4 case

5.2 Evaluation of hot ductility and precipitation kinetics

The hot ductility behaviour of samples from Alloy-0 and Alloy-1 was tested using Baehr quenching and deformation dilatometer 'DIL 805 T' under the condition selected in the previous section. DIL805T is capable of monitoring the strain, load, time and temperature during the course of hot tensile test. The elongation to rupture (ER) was taken as measure for hot ductility and was calculated according to **Equation 5.1**, where ΔL is the difference of the sample gauge length before and after the test. L_0 is the sample gauge length before

test. The average value of at least 2-3 hot ductility tests for every case was evaluated and presented in the results. A sketch of the sample geometry of a hot tensile test was shown in **Fig. 4.3**. Analysis of the fracture surface followed the test to study the fracture mechanism resulted at every selected condition and the accompanying effects at its corresponding temperature.

$$\mathrm{ER} = \frac{\Delta \mathrm{L}}{\mathrm{L}_0} * 100 \quad [\%] \tag{5.1}$$

A precipitation kinetics model for the secondary precipitation on grain boundaries and dislocations was built using MatCalc 6. The model is based on the Scheil and primary precipitation results from the simulation presented in **Chapter 4.** The objective of the model is to evaluate precipitates amounts, sizes, distribution and number density formed during each thermal cycle (**Fig. 5.6** & **Fig. 5.7**) applied in the hot tensile testing. This gave information to precipitation kinetics that could be correlated with the hot tensile testing results run under the same program/thermal cycle. The results presented in this chapter will answer the following questions in this sequence:

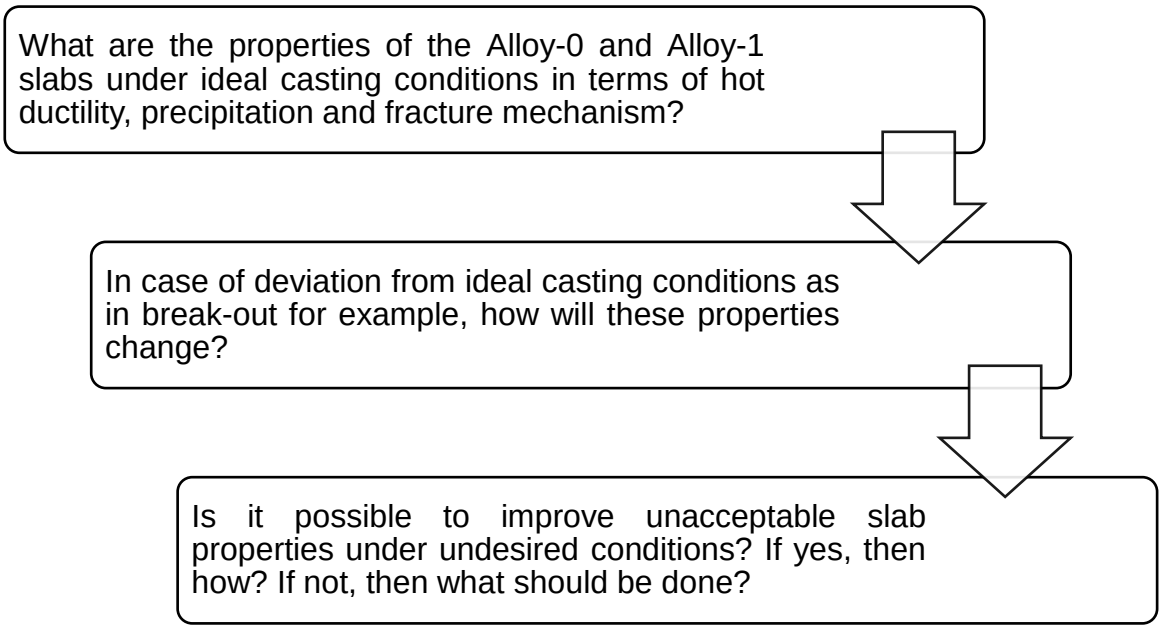

For the hot tensile testing, **Table 5.2** summarises the important studied effects and the different test conditions of each case. Effects of four different parameters/combination of parameters on hot ductility were evaluated. First, the effect of cooling cycle at a fixed strain rate to compare ideal casting conditions with break-out. Secondly, the effect of different strain rates for the same cooling cycle to study the effect of different casting speeds for the same cooling history. Third, is to combine the improvements resulted from the first and second effect by simultaneously optimizing the cooling and strain rates, and finally studying the effects at low temperatures on hot ductility after ferrite transformation.

Table 5.2: List of the studied effects and testing conditions

Effect	Case	Cooling rate [K/s] / cycle	Deformation	
			Temperature range [°C]	Strain rate [10^{-3} s^{-1}]
5.2.1 Cooling cycle	Case-1	0.1 / Cycle-1	1080 - 950	2
	Case-2	0.1 / Cycle-2	1000 - 800	2
5.2.2 Strain rate	Case-3	0.35 / Cycle-1	1080, 800	1
	Case-4	0.35 / Cycle-1	1080, 800	2
	Case-5	0.35 / Cycle-1	1080, 800	5
	Case-6	0.35 / Cycle-1	1080, 800	10
5.2.3 Simultaneous change in cooling and strain rates	Case-7	0.1 / Cycle-1, 0.35 / Cycle-1	1080 - 800	1 & 2
5.2.4 Lower temperature	Case-8	0.1 / Cycle-1	800, 700, 600, 50	1

In Case-1, the ideal cooling cycle during casting (Cycle-1 – **Fig. 5.6**) was tested at different temperatures (1080, 1030, 1000 and 950 °C) with the same cooling rate of 0.1 K/s and strain rate of 2 x 10^{-3} s^{-1}. Case-2 has the cooling cycle of a Break-out-4 slab (Cycle-2 – **Fig. 5.7**) and was tested at its related temperature values (1000, 900 and 800 °C). Both cases 1 and 2 were tested under the same strain rate as they have the same casting speed in reality but different thermal history and straightening temperature ranges. Further (lower) temperatures (at 800 °C and 700 °C) were tested in Case-1 and 2 for a better study and comparison, even if they are not valid in industrial practice under regular conditions. The effect of different strain rates for two chosen temperatures (1080 °C and 800 °C), representing the possible maximum and minimum straightening temperatures, was studied in Case 3, 4, 5 and 6 under a fixed thermal cycle of Cycle-1 with a secondary cooling rate of 0.35 K/s. The results of cases 1 - 6 lead to the idea of hot ductility improvement by simultaneous optimization of secondary cooling and deformation speed as will be presented for Case-7. For extreme cases, low temperature deformation was applied in Case-8 to evaluate the hot ductility after the appearance of the ferrite phase at 700 °C and 600 °C. Tensile testing at 50 °C was carried out to study the microstructure and fracture surface and investigate if further effects/mechanisms might take place at much lower temperatures.

5.2.1 Effect of cooling cycle

To start with, the hot ductility of both alloys was measured under the ideal casting conditions of Cycle-1. The aim is to evaluate a range of reference values of the hot ductility coming with set/ideal casting temperature and deformation profiles. This is important for further comparison purposes. Then tests under Cycle-2 were run to evaluate the effect of break-out. The results for each alloy will be separately presented in this section.

5.2.1.1 Hot ductility: Alloy-0 (no alloying elements)

For Alloy-0, **Table 5.3** shows the results of Case-1 (test conditions see **Table 5.2**), while in **Table 5.4**, the results of the break-out cycle (Case-2) are presented. Discussion of the results will follow the SEM results.

Table 5.3: Results of Case-1: Ideal casting, Alloy-0

	Ideal/set casting conditions – Cycle-1						
Temperature, °C	1080	1030	1000	950	900	800	700
Alloy-0 hot ductility, %	82	85	84	80	80	80	80
Standard deviation ±, %	0	4	5	9	1	0	4

Table 5.4: Results of Case-2: Break-out, Alloy-0

	Break-out – Cycle-2			
Temperature, °C	1000	950	900	800
Alloy-0 hot ductility, %	81	79	80	54
Standard deviation ±, %	0	0	10	8

Fig. 5.8 shows a comparison of the hot ductility under ideal casting conditions against the hot ductility after a break-out for Alloy-0. The arrow in the diagram points to the ferrite start temperature (Ar_3) at 837 °C.

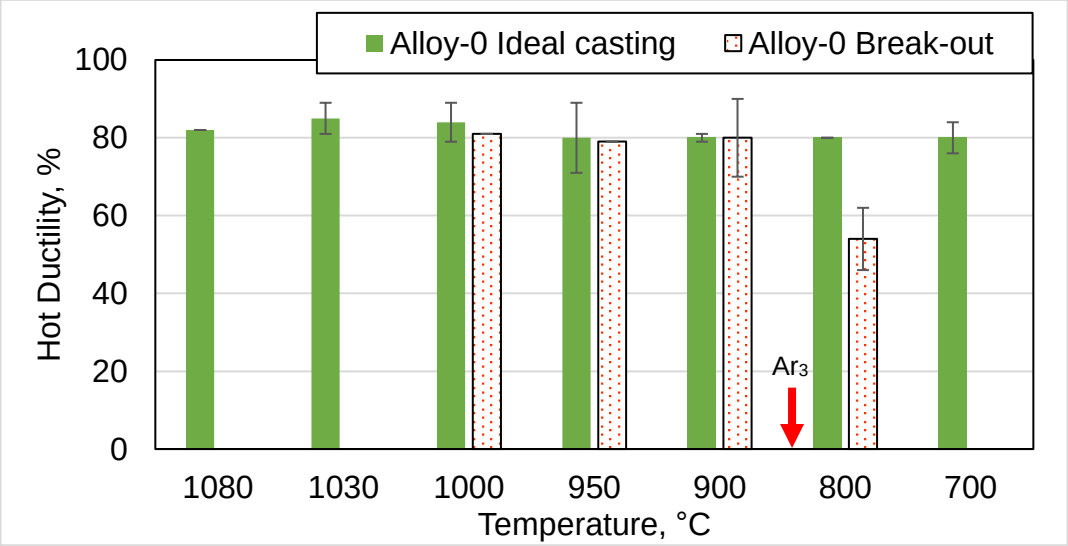

Fig. 5.8: Hot ductility of ideal casting vs break-out, Alloy-0

5.2.1.2 Fracture surface analysis: Alloy-0

The fracture surface of the broken samples were analyzed using SEM to study the fracture mechanisms and compare different cases of Alloy-0. **Fig. 5.9** shows the fracture surfaces for experiments run under ideal casting condition of Cycle-1 at its temperature range between 1080 °C and 950 °C, while **Fig. 5.10**, shows the fracture surfaces for experiments run under break-out conditions of Cycle-2 at 1000 °C and 800 °C.

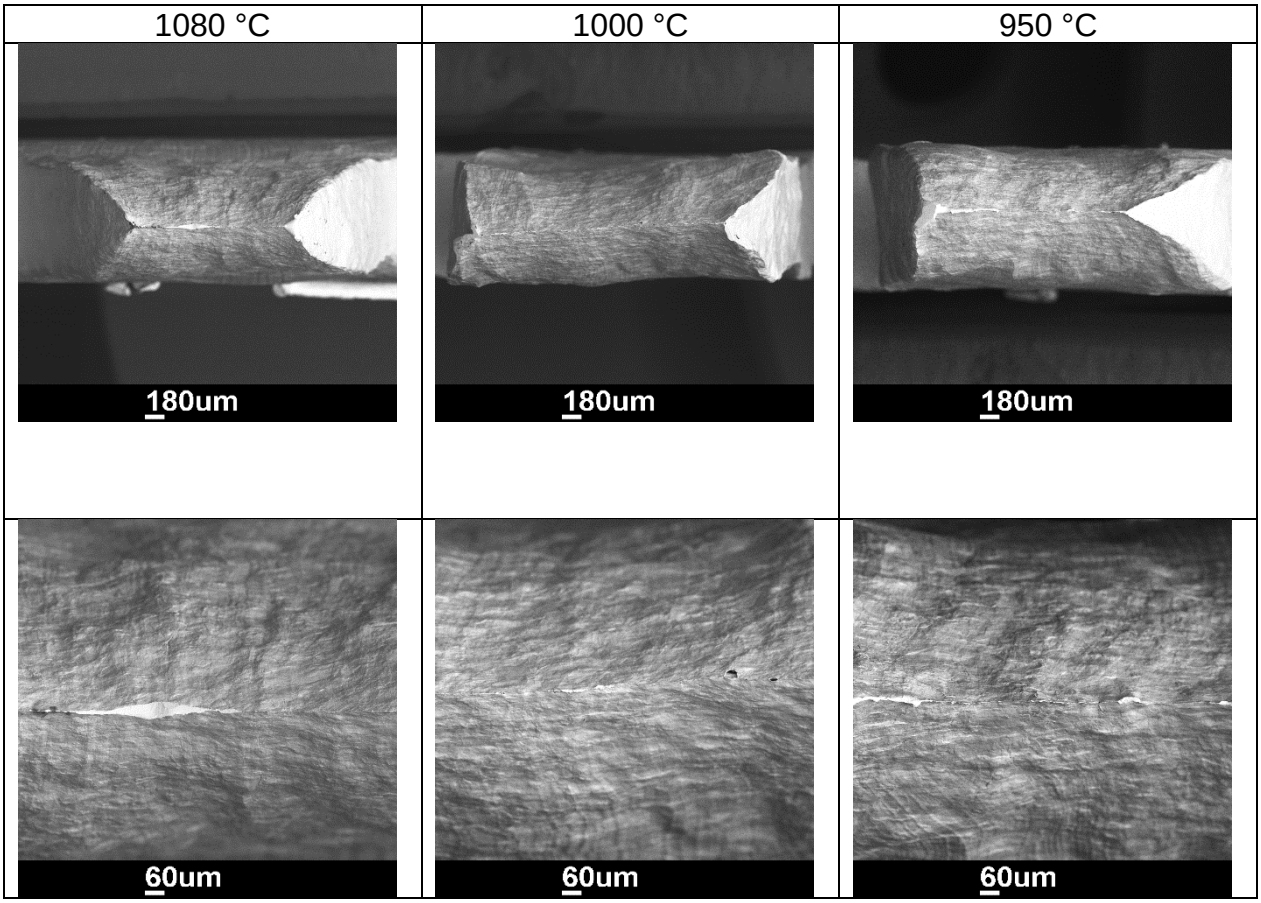

Fig. 5.9: Fracture surface after Cycle-1, Alloy-0

As it can be observed, Alloy-0 will always have high hot ductility values (≈ 83%) under ideal casting conditions of Cycle-1 between 1080 and 950 °C, moreover, a ductile fracture could be seen on the surface of the broken samples. Even at lower temperatures below the ferrite start (Ar_3= 837 °C), the hot ductility values did not drop at the temperature range (900 - 700) °C, which is considered to be the temperature range during transportation and storage after leaving the casting shop. On the other hand, a different fracture surface under the break-out program (Cycle-2) could be clearly seen at 800 °C (hot ductility 54%), while acceptable hot ductility values resulted for all other temperatures between 1000 - 900 °C during the break-out. The fracture surface at 800 °C, Cycle-2, shows a mixture of intergranular fracture and voids coalesced dimples accompanied with a relatively low hot ductility (54%), which did not take place at the same temperature of 800 °C under Cycle-1. Treatments on both cycles at 800 °C were further evaluated under another cooling/quenching treatment on Dil805A to study the microstructure, grain size and ferrite formation on both cases after sample quenching at 800 °C at the two different cycles. The results are summarized in **Table 5.5**.

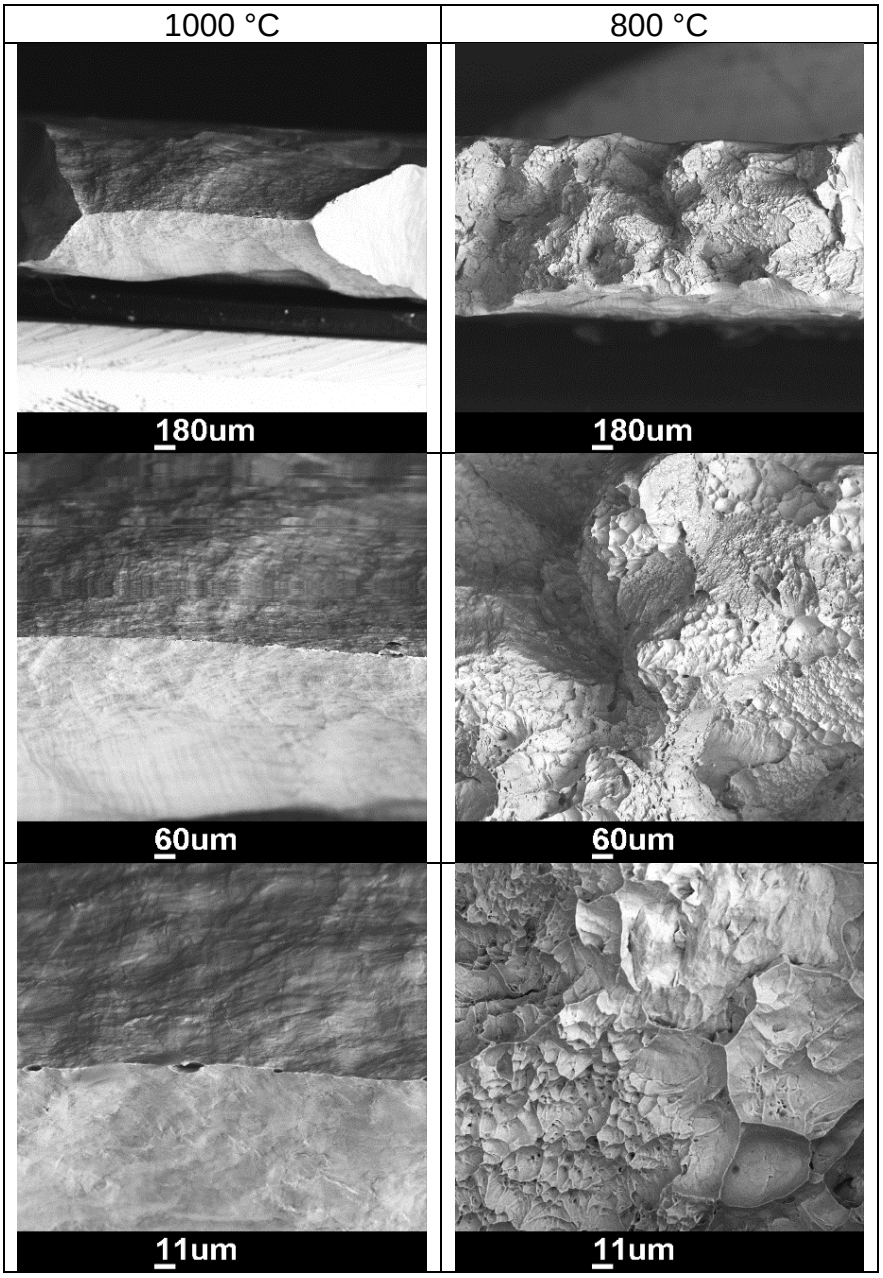

Fig. 5.10: Fracture surface after Cycle-2, Alloy-0

Table 5.5: Comparison between Cycle-1 & 2 at 800 °C, Alloy-0

Sample	Cycle-1, 800 °C (ideal casting)	Cycle-2, 800 °C (break-out)
Grain size, µm	103±7	203 ±23
Hot ductility, %	80 %	54%
Ferrite content, %	54%	22%

The metallographic analysis after quenching the samples at 800 °C for the two different cycles showed that the break-out resulted in a larger grain size and that the phase fraction of the ferrite films on the grain boundaries was much less compared to the case of 800 °C under Cycle-1 conditions without break-out. The results for Cycle-1 and Cycle-2 at 800 °C are shown in **Fig. 5.11** and **Fig. 5.12**, respectively.

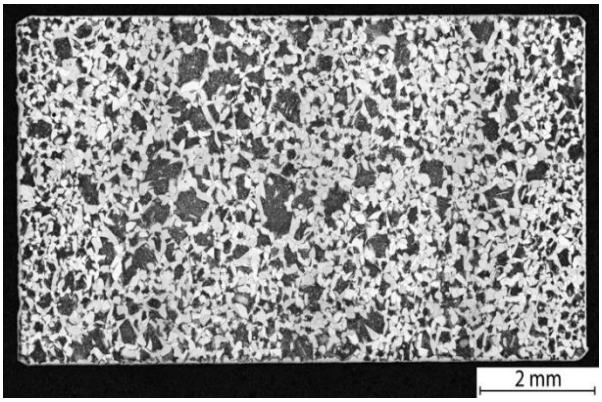

Fig. 5.11: Microstructure at 800 °C after Cycle-1, Alloy-0

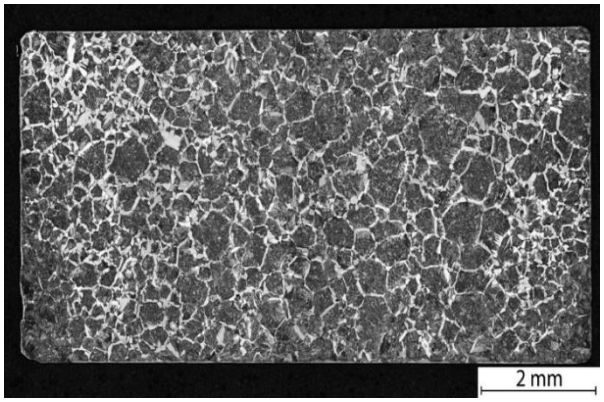

Fig. 5.12: Microstructure at 800 °C after Cycle-2, Alloy-0

Generally, the straightening process should take place at temperatures above Ar_3 for each alloy, which is the case for Alloy-0 between 1080 - 950 °C with hot ductility of ≈ 83% under Cycle-1. The break-out forced the strand surface to reach the unbending zone relatively late where the surface temperature could partially fall down to 800 °C, which is below the ferrite start temperature (Ar_3). The formation of thin ferrite films (22%) encouraged the failure at the grain boundaries and resulted in dimples. The critical effect of the overall break-out cooling cycle is that it resulted in a relatively higher grain size (203 µm) with less ferrite content, giving less resistance to fracture. On the contrary, reaching 800 °C within the normal Cycle-1 (which is anyway not much likely to happen under normal casting condition) results in a finer austenite grain size (103 µm) with a higher ferrite content (54%) on the grain boundaries as well as a higher grain boundary density and triple points. These effects result in a longer resistance to failure and higher overall ductility due to higher ferrite content and finer grain size.

For alloys of type Alloy-0, unbending at temperatures above Ar_3 (for both cooling Cycle-1 and 2) will not result in higher cracking risks as long as there are no precipitation. Below Ar_3 with small ferrite content, the strain during deformation will mostly be concentrated on the small ferrite contents built in the austenite grain boundaries and cause failure within the thin ferrite film as it is softer. With a higher ferrite content (>50%), the overall matrix ductility is increasing and the strain distribution between austenite and ferrite will be more uniform. This effect was reported by [3,57,81,83,84] as well, as explained in **Chapter 3**.

5.2.1.3 Hot ductility: Alloy-1 (micro-alloyed)

By the analysis of Alloy-1, the influence of precipitation should be considered as it strongly contributes to the resulting hot ductility values, which did not happen to be the case in studying Alloy-0 (no precipitation). **Table 5.6** shows a summary of the results of Case-1 (test conditions in **Table 5.2**) for Alloy-1 under ideal casting conditions, while in **Table 5.7**, the results of the break-out cycle (Case-2) were presented. **Fig. 5.13** shows a comparison of the hot ductility under ideal casting condition vs after a break-out cycle for Alloy-1. The arrow in the figure points to the ferrite start temperature (Ar_3) at 757 °C. Discussion of the results will follow the SEM results.

Table 5.6: Results of Case-1: Ideal casting, Alloy-1

	Ideal/set casting conditions – Cycle-1						
Temperature, °C	1080	1030	1000	950	900	800	700
Alloy-1 hot ductility, %	83	89	82	80	73	55	31
Standard deviation ±, %	2	1	8	5	6	5	3

Table 5.7: Results of Case-2: Break-out, Alloy-1

	Break-out – Cycle-2			
Temperature, °C	1000	950	900	800
Alloy-1 hot ductility, %	82	64	61	55
Standard deviation ±, %	7	0	8	1

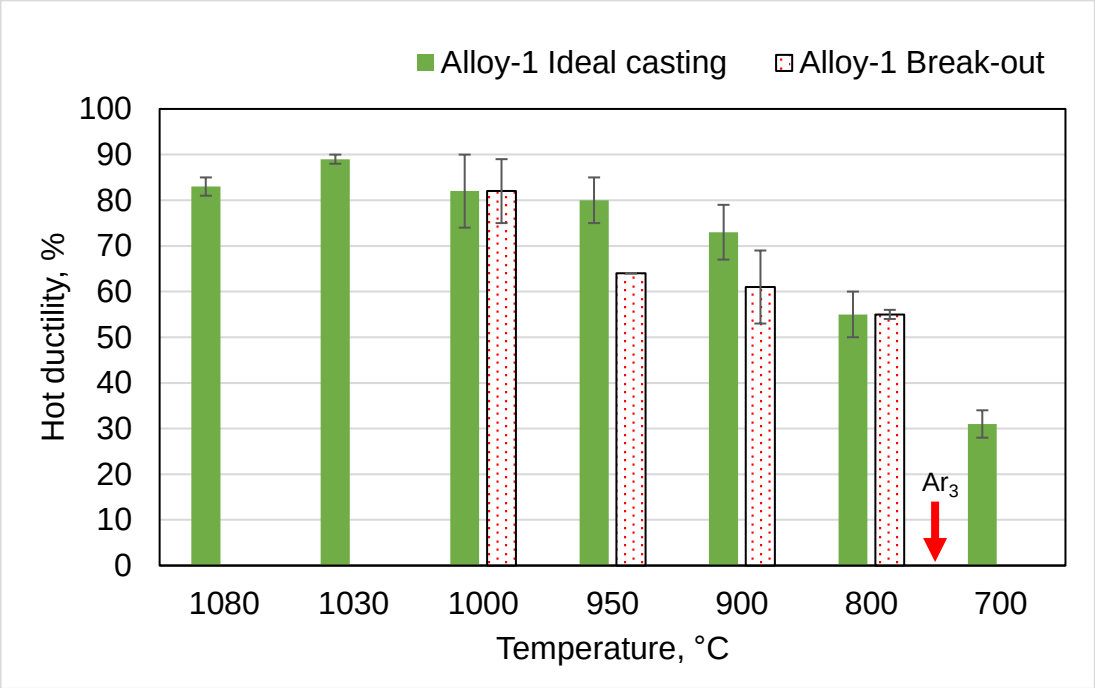

Fig. 5.13: Hot ductility of ideal casting vs break-out, Alloy-1

5.2.1.4 Fracture surface analysis: Alloy-1

Analysis of the broken samples surfaces using SEM was applied here as well for studying the fracture surfaces and failure mechanisms. **Fig. 5.14** shows the fracture surface of samples run at the ideal casting conditions of Cycle-1 between 1080 °C and 950 °C, where ductile failure on sample surfaces could be observed. On the other hand, **Fig. 5.15** shows the fracture surface in the case of break-out Cycle-2 in the temperature range of (1000 - 800 °C). Below 1000 °C, the fracture surfaces show more dimples density at the fracture interface by lowering the test temperature down to 900 °C and more dimples at 800 °C mixed with a partial intergranular failure.

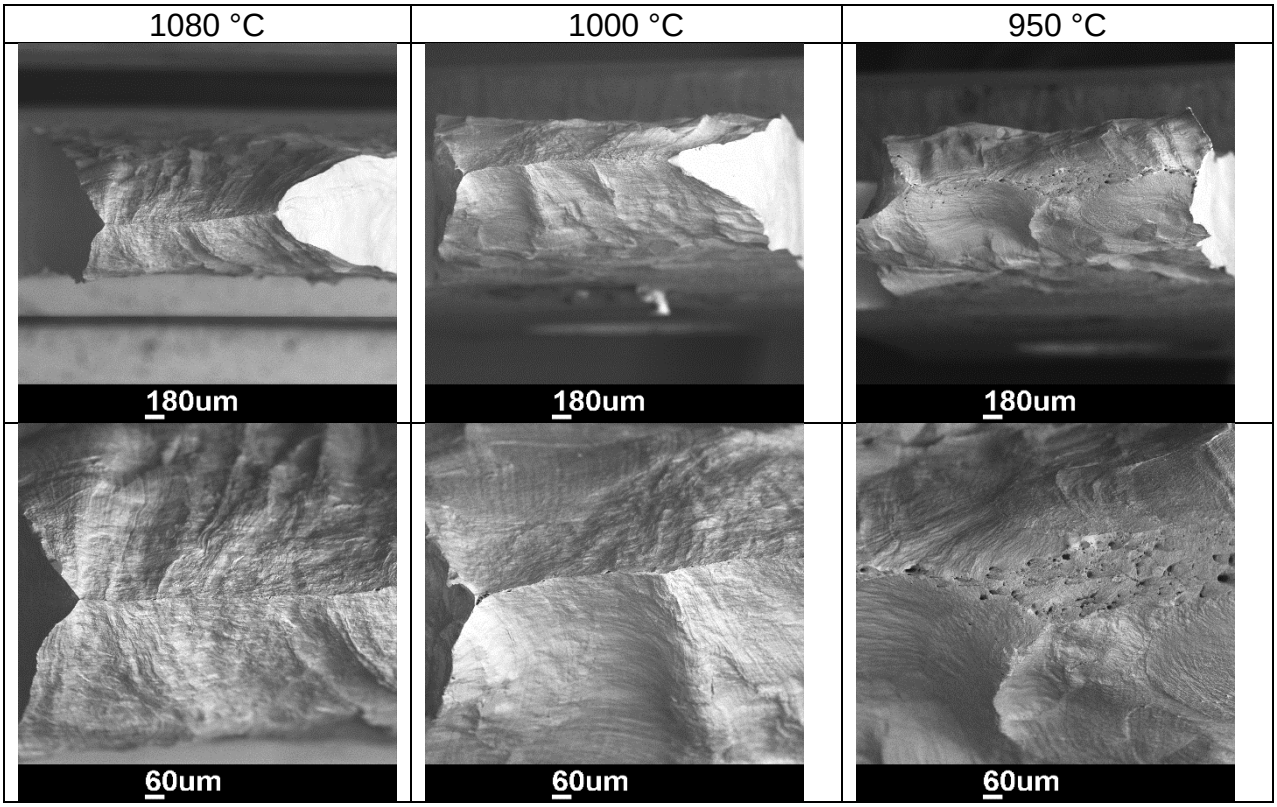

Fig. 5.14: Fracture surface after Cycle-1, Alloy-1

From the results of Alloy-1, it could be observed that under ideal casting conditions of Cycle-1, high average hot ductility values (> 80%) are present accompanied by ductile fracture surface in the temperature range of (1080 - 950 °C). On the other hand, during break-out (Cycle-2), the fracture surfaces show higher density of dimples regions especially at 800 °C. Below 1000 °C, the hot ductility values start to drop in the break-out temperature to 61% at 900 °C until it reaches 55% at 800 °C illustrating the higher risk of cracking during break-out compared to normal/ideal casting conditions.

At further lowered temperatures (below 950 °C) during ideal casting of Cycle-1, the hot ductility is dropping as well to values of 73% at 900 °C, 55% at 800 °C and even to 31% at 700 °C (below Ar_3). This fact indicates high cracking risk especially after the beginning of ferrite film formation at 757 °C, which will strongly contribute to lower hot ductility, but those temperatures values between 900 – 700 °C are usually not reached during ideal casting. While critical hot ductility values (less than 70%) will possibly be reached at the lower temperature part in case of break-out between 1000 °C and 800 °C. This is most probably the reason why a break-out is possibly leading to surface cracking more than any process defect. Generally, lower surface temperatures (below 900 °C) during straightening will have a negative influence on hot ductility in both cycles, but the effect will be more severe at temperatures values below the Ar_3 or under the break-out cycle.

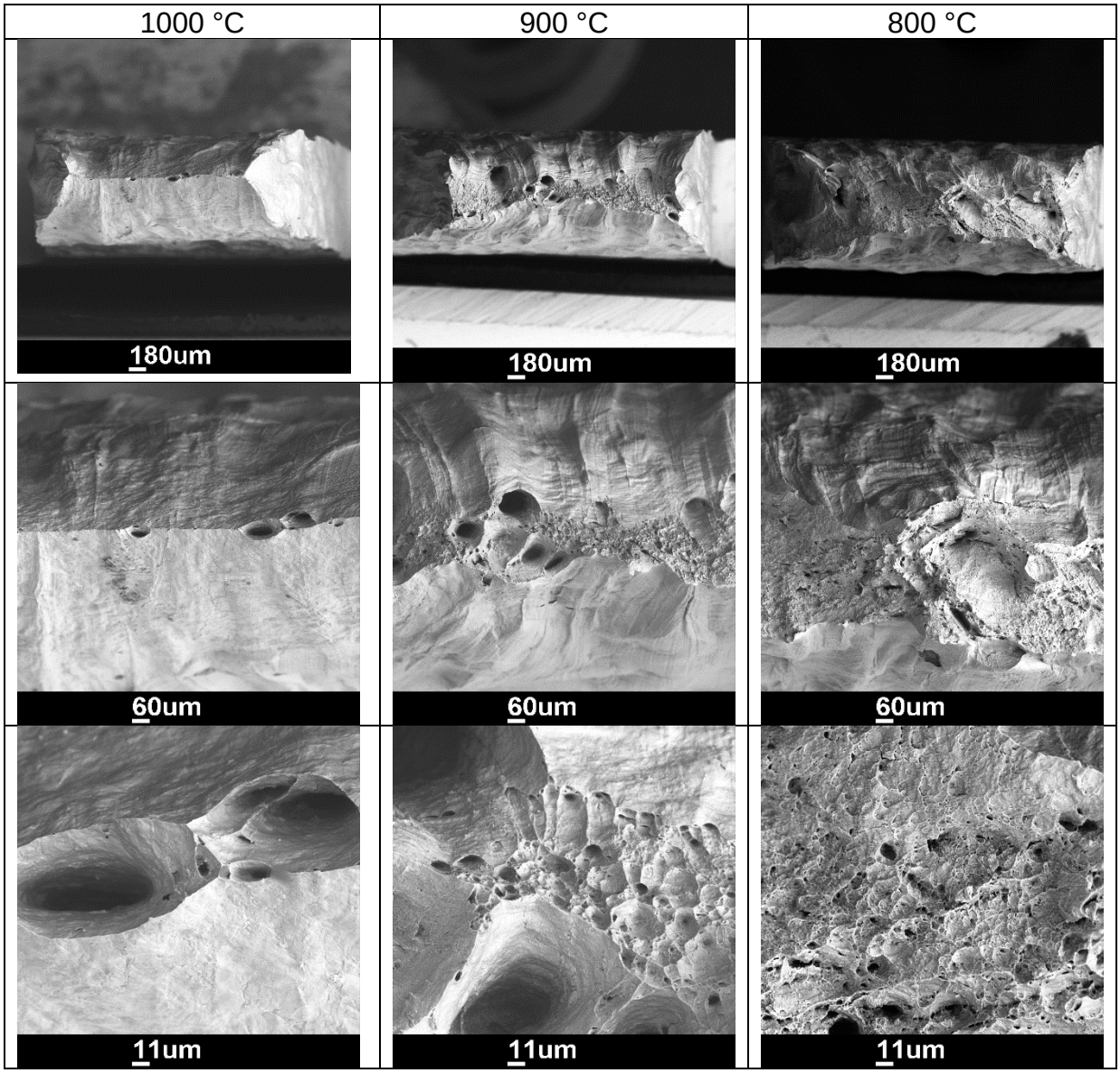

Fig. 5.15: Fracture surface after Cycle-2, Alloy-1

The low ductility during break-out of Alloy-0 could be explained by failure at the ferrite film formed before/during the unbending, which is not the case for Alloy-1. Low hot ductility values (55%) during unbending at 800 °C of Alloy-1 resulted due to the precipitation formation before ferrite was formed. The ductility values got even worse (31%) after the appearance of ferrite (Ar_3= 757 °C) in tensile testing at 700 °C due to the combined influence of the presence of fine precipitates and ferrite phase, which didn't take place in Alloy-0. The precipitation kinetics of Alloy-1 will be studied in detail in the following section.

5.2.1.5 MatCalc precipitation simulation: Alloy-1

Two precipitation models were built using MatCalc 6 to study the kinetics of secondary precipitates during Cycle-1 and Cycle-2 at different temperatures and its effect on the resulting precipitates sizes and phase fractions. Both models start from the final temperature where the Scheil model (see **Chapter 4**) ended at 1408 °C after a complete solidification was reached. The coarse primary precipitates of TiN and NbC formed during solidification will stay at fixed sizes and phase fractions in the matrix during the secondary precipitation

is taking place in the solid state as will be shown in the figures. Each model was set up to enable the secondary precipitates to form on both grain boundaries (gb) and dislocations (dln). The first model (Model-1) represent the ideal casting conditions in the temperature range of (1080 - 950 °C) as in Cycle-1, while the second one (Model 2) represents the break-out case in the range of (1000 - 800 °C) as in Cycle-2.

The complete results and values of particle size and phase fraction of both models after running at the different temperature ranges are summarized in **Table 5.8** and illustrated in **Fig. 5.16**. As could be observed, the primary precipitates of TiN and NbC have an average mean radius of 2 µm with relatively high phase fraction (TiN: 0.001, NbC: 0.0002). Break-out (Cylce-2) resulted in much finer secondary precipitates and higher precipitates phase fractions compared to ideal casting (Cycle-1). The results of the MatCalc models will be explained in respect to the results of the hot tensile testing later on in this section.

Table 5.8: Results of MatCalc simulation for Model-1 & 2, Alloy-1

Model	Model-1			Model-2
Cycle	Cycle-1			Cycle-2
Temperature, °C	1080 - 950	800	700	1000 - 800
TiN (secondary) mean radius, nm	50-72	67	67	7-10
TiN (secondary) phase fraction	1-5 x 10^{-10}	3 x 10^{-10}	3 x 10^{-10}	2-80 x 10^{-5}
TiN (primary) mean radius, µm	2			
TiN (primary) phase fraction	0.001			
NbC (secondary) mean radius, nm	10-49	1	3	18
NbC (secondary) phase fraction	2-40 x 10^{-6}	0.0002	0.0021	0.002
NbC (primary) mean radius, µm	2			
NbC (primary) phase fraction	0.0002			

For Alloy-1, the first model is a simulation of ideal casting conditions of Cycle-1 in the temperature range of (1080 - 950 °C). Further lowered temperatures were evaluated by the model for a better comparison. Some selected cases from both models will be fully presented in this section to illustrate the critical influences on particle size. Straightening after Cycle-1 at 1080 °C (ideal casting temperature), 800 °C (before Ar_3) and 700 °C (after ferrite start) are illustrated in **Figs. 5.17 - 5.19**. The results are showing the phase fraction, number density and mean particle radius for each case. An example of the results of Model-2 is illustrated in **Fig. 5.20** representing the break-out situation at 800 °C. Changes in the cooling rates during a cycle, reheating and/or formation of new nucleation sites due to deformation or ferrite formation, affects the resulting average mean radius and consequently the number density and phase fraction.

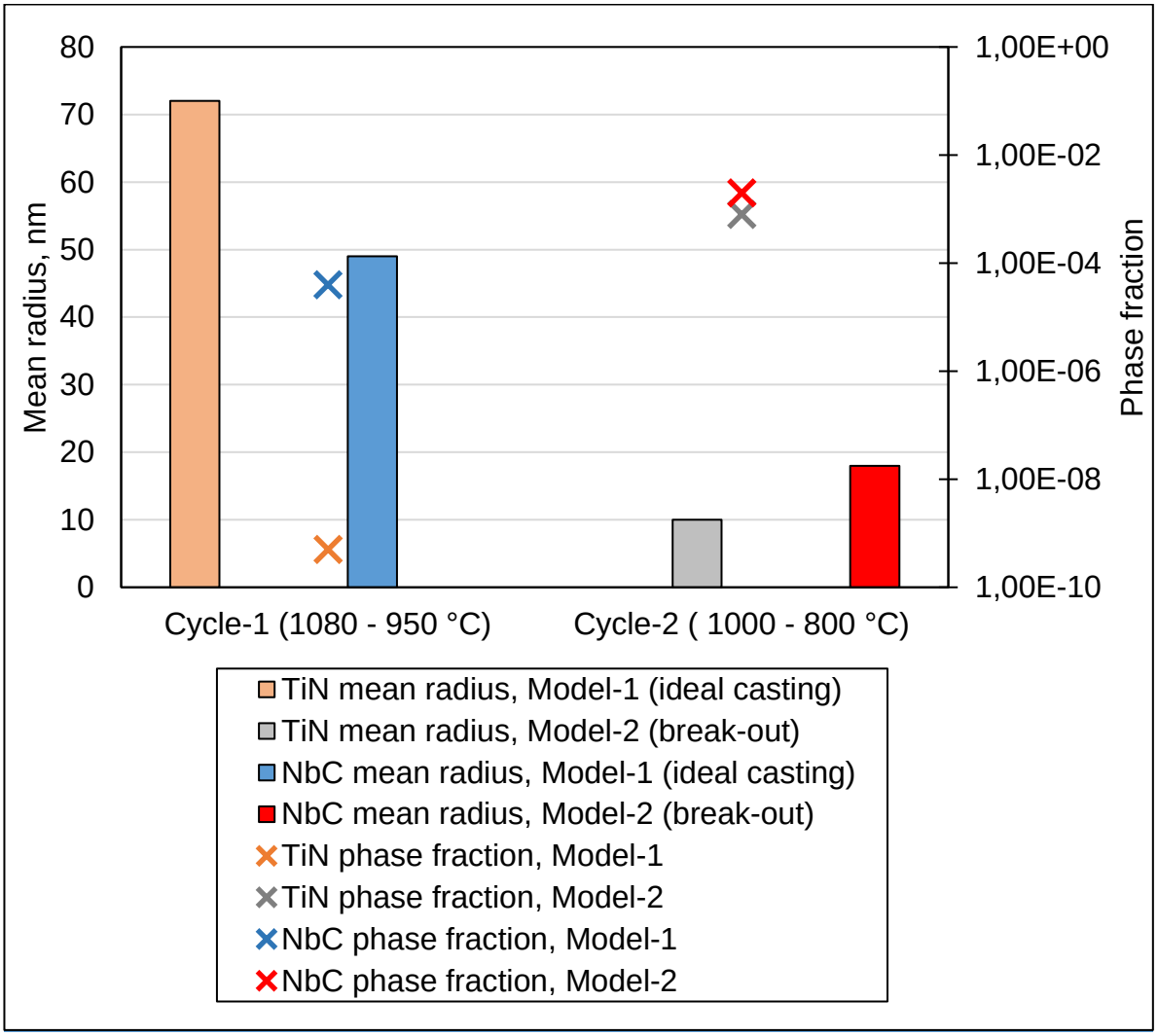

Fig. 5.16: Comparison of particle size and phase fraction between Model-1 and 2

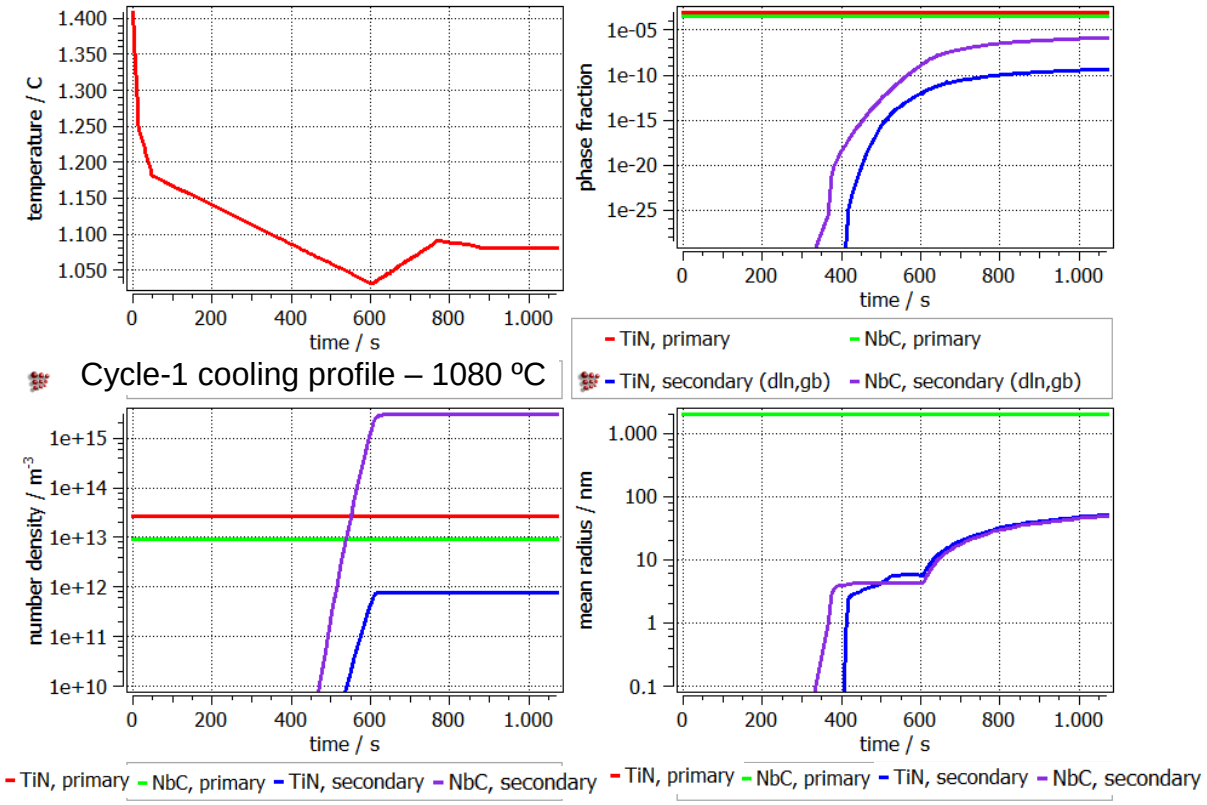

Fig. 5.17: MatCalc Model-1 at 1080 °C, ideal casting, effect on particle size, Alloy-1

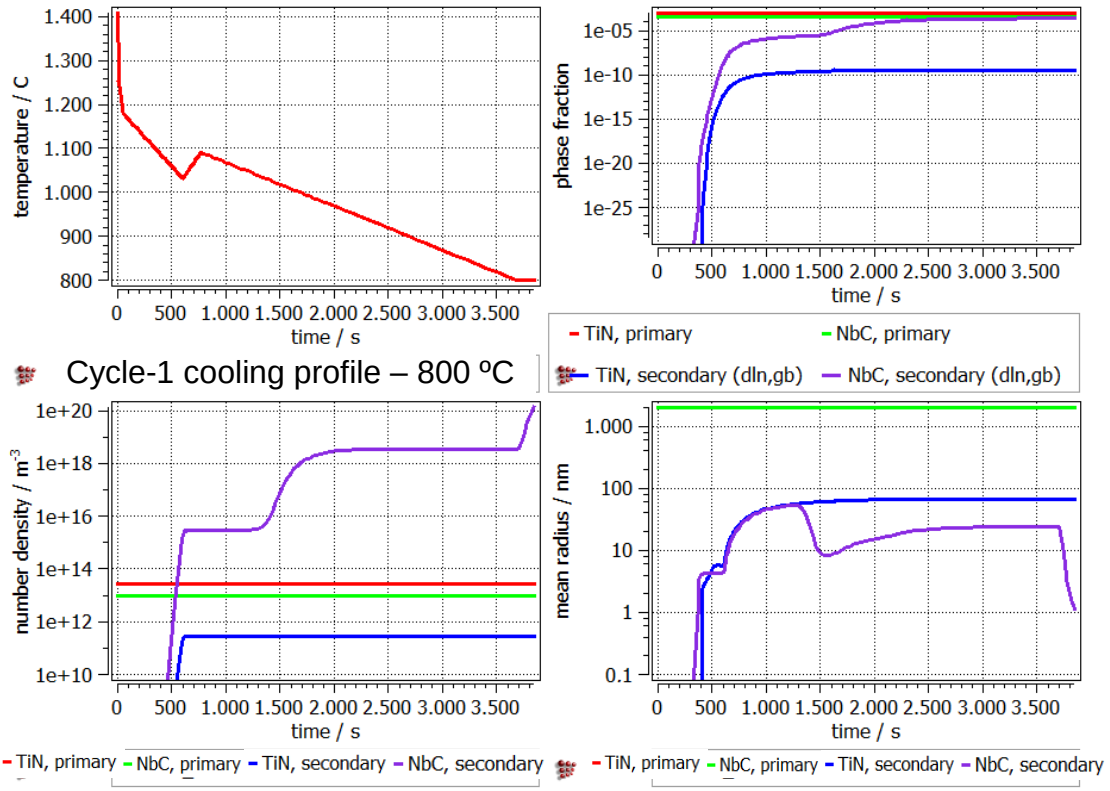

Fig. 5.18: MatCalc Model-1 at 800 °C, effect on particle size, Alloy-1

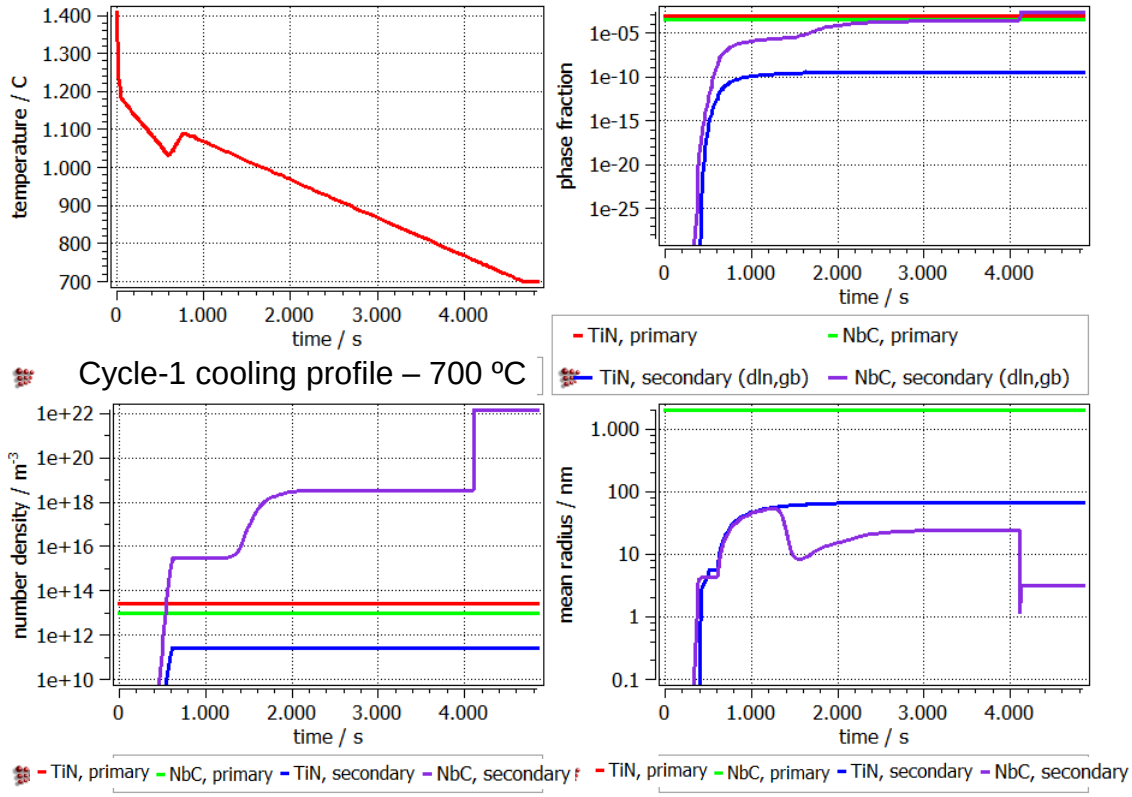

Fig. 5.19: MatCalc Model-1 at 700 °C (below Ar_3), effect on particle size, Alloy-1

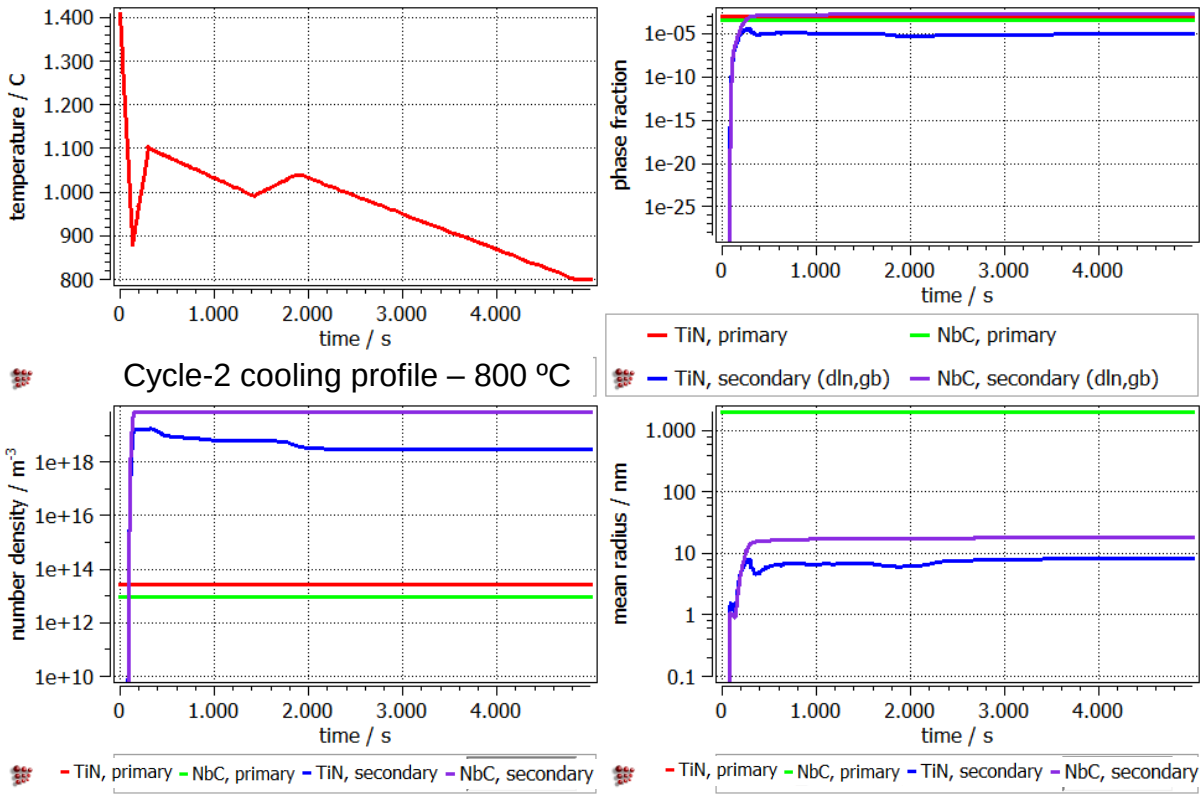

Fig. 5.20: MatCalc Model-2 at 800 °C, effect on particle size, Alloy-1

From the results, it could be observed that during the break-out temperature profile (Cycle-2) a higher phase fraction of TiN and NbC with much finer sizes (TiN:7-10 nm, NbC:18 nm) resulted compared to Cycle-1 (TiN: 72 nm, NbC: 49 nm), which explains the low hot ductility values for Cycle-2. At 700 °C, NbC will precipitate with a high phase fraction (0.0021) - even higher than the primary precipitates phase fraction (0.0002) formed during solidification - with very fine average mean radius of 3 nm showing the strong influence of deformation below ferrite start temperatures (Ar_3= 757 °C). This corresponds to the lowest recorded hot ductility of 31% resulted at 700 °C as well.

Finer precipitates - especially with higher phase fraction on grain boundaries - are more detrimental to hot ductility and will lead to a higher cracking risk as they will enhance decohesion on the prior austenite grain boundaries and promote failure by void nucleation at second phase particles. Growth of these voids will continue within the austenite grain boundaries especially if thin ferrite film is available. The influence of precipitates sizes on failure mechanism was explained in 3.2.2 and 3.3.2.2.

Fine precipitates below critical sizes can form in case of casting outside the temperature range of (1080 - 950 °C) of ideal casting with Cycle-1, as for example at 800 °C (even worse at 700 °C, below Ar_3) or at any temperature at the break-out Cycle-2, where precipitation started earlier (in time) with finer particles. This could happen in case of break-out for different reasons. Firstly, high cooling rate occurring at the beginning of the break-out results in finer particles. Secondly, break-out is accompanied by much slower casting speed, which allows longer time periods for strain induced precipitates to form. Finally, the intense secondary cooling might result in straightening temperature range below the Ar_3. The detrimental influence of fine precipitates for both cases could be confirmed with / correlated to the low hot ductility results. At break-out condition, TiN particles have sizes of 7-10 nm in the temperature range of (1000 - 800 °C). Mintz [4] mentioned that slabs with precipitates < 15 nm recorded high slab rejections.

As mentioned in 5.1, the Break-out-4 was expected to give the highest cracking probability (lowest hot ductility) compared to the other break-out conditions (1, 2 and 3). Model-2 of MatCalc was tested under the temperature profile history of the four break-out situations with applying straightening deformation at the corresponding unbending temperatures for each case. The model considers that each break-out situation has its corresponding casting and deformation speeds and therefore, the particle size of the precipitates were calculated accordingly. A summary of the results in shown in **Table 5.9**. The results confirm that the case of Break-out-4 had the smallest particle size of both TiN (7nm) and NbC (18 nm) which proves that slab 4 is the most critical one of the strand in case of break-out. The ability of avoiding its cracking by optimizing/improving the casting conditions of this slab means the ability to avoid cracking for the other less sensitive slabs. Improving hot ductility by optimizing casting conditions will be introduced in the next sections.

Table 5.9: Particle size calculation of break-out slabs

Mean radius, nm	Break-out-1 (1050 °C)	Break-out-2 (1050 °C)	Break-out-3 (1030 °C)	Break-out-4 (1000 °C)
TiN	55	55	59	7
NbC	62	62	55	18

As a short summary of this section, all the important factors influencing crack sensitivity and hot ductility are summarized in **Fig. 5.21** according to the previously discussed results. All casting conditions leading to acceptable hot ductility values (> 80%) are considered safe

to surface quality, where slabs did not record surface cracking according to the statistical analysis (**Chapter 2**). Other conditions leading to critical (50-75%) or unaccepted (< 40%) hot ductility should be treated with care. The following section will show how optimization of casting conditions through casting speed and secondary cooling adjustments could be beneficial, in order to shift the unaccepted and critical values into less critical and more accepted ones.

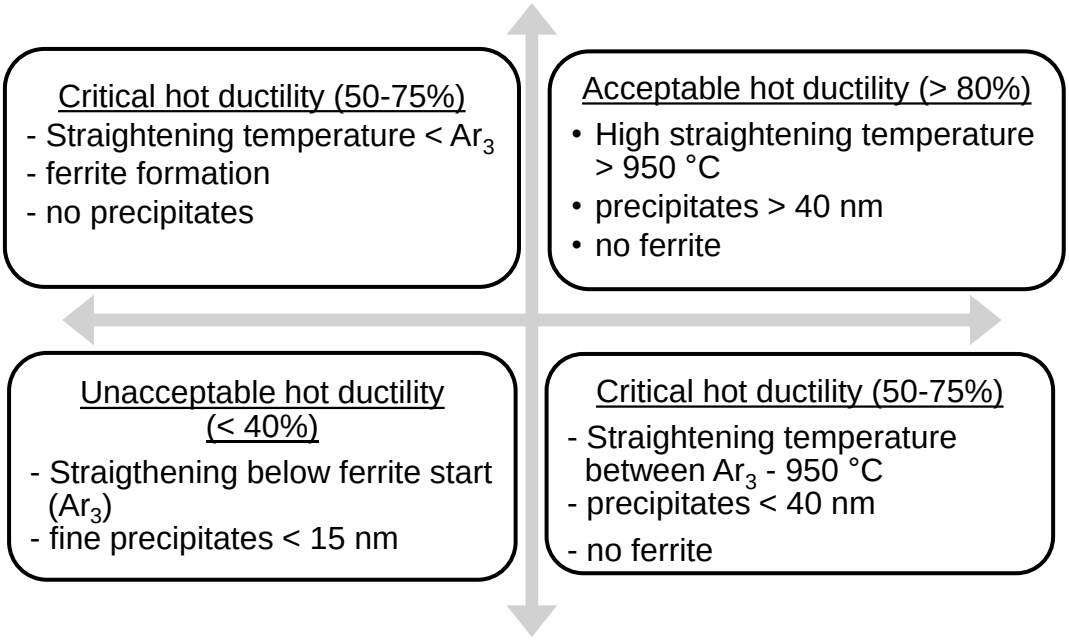

Fig. 5.21: Summary of factors affecting hot ductility

5.2.2 Effect of strain rate in Alloy-1

5.2.2.1 Hot ductility

In the previous part, the conditions leading to low hot ductility and high crack sensitivity were illustrated in terms of the effect of a break-out. It could also be shown that certain temperature ranges and deformation speeds should be avoided during slab straightening. In cases where some parameters are out of control due to unexpected failure during the casting process, adjusting some other casting parameters is still possible to save the slab's quality.

Two temperatures were chosen for this analysis. Firstly, 1080 °C, representing a safe temperature for ideal casting, and secondly, 800 °C, which was always related to lower ductility values with or even without break-out. For a fixed secondary cooling practice in both cases (cooling with 0.35 K/s), four different deformation speeds were tested to study the effect of strain rate on the resulting hot ductility. In reality, deformation speed is controlled by the casting speed, casting machine geometry and slab thickness. The hot tensile testing results of cases 3, 4 and 5 for Alloy-1 are summarized in **Table 5.10** and **Fig. 5.22**.

Table 5.10: Hot tensile testing results of Cases 3, 4, 5 & 6, Alloy-1

Temperature, °C	1080 °C (cooling 0.35 K/s)			
Strain rate, 10^{-3} s^{-1}	1	2	5	10
Alloy-1 hot ductility, %	79	80	80	79
Standard deviation ±, %	0	2	1	0
Deformation time, s	615	215	105	52
Temperature, °C	800 (cooling 0.35 K/s)			
Strain rate, 10^{-3} s^{-1}	1	2	5	10
Alloy-1 hot ductility, %	27	31	37	47
Standard deviation ±, %	2	3	0	2
Deformation time, s	279	120	61	36

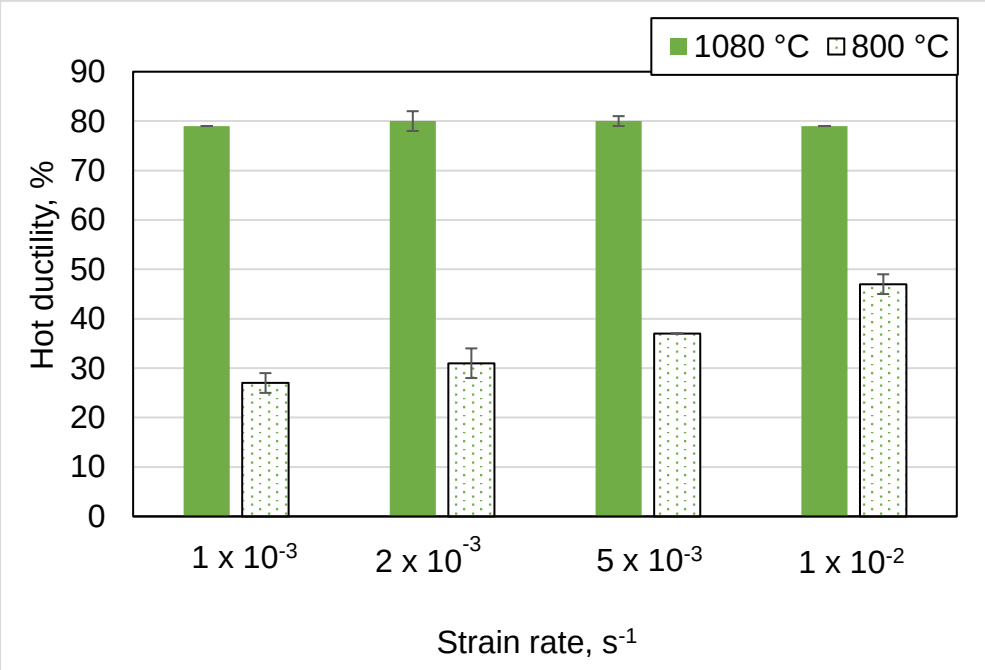

Fig. 5.22: Effect of strain rate on hot ductility at 1080 °C and 800 °C, Alloy-1

5.2.2.2 Fracture analysis

The broken samples after the hot tensile testing at 1080 °C and 800 °C at different deformation speeds were analyzed using SEM. **Figs. 5.23** and **5.24** illustrates the results for 800 °C and 1080 °C, respectively.

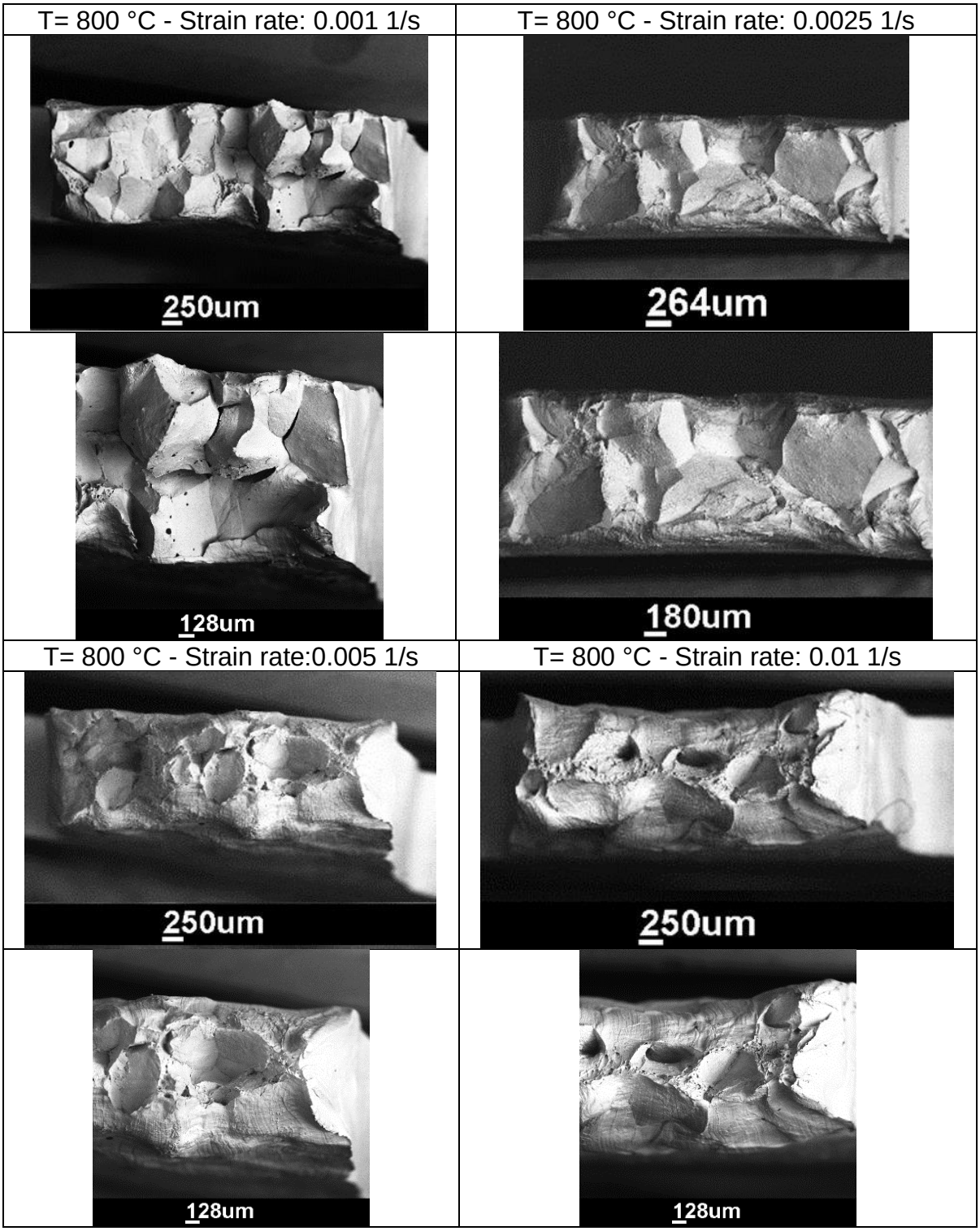

Fig. 5. 23: Fracture surface at 800 °C, different strain rates, Alloy-1

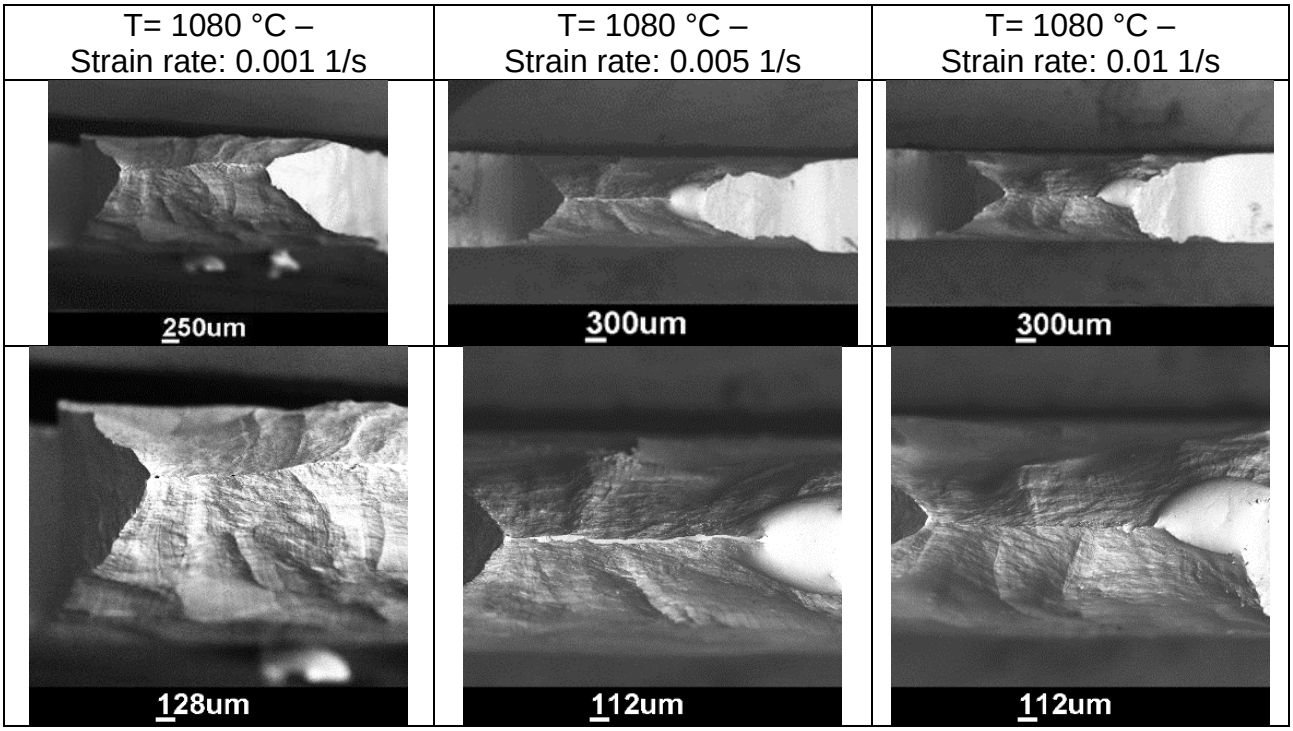

Fig. 5.24: Fracture surface at 1080 °C, different strain rates, Alloy-1

As shown in the **Fig. 5.22**, at a high straightening temperature of 1080 °C the hot ductility was always high (≈ 80%) showing no influence on changing the strain rate. On the other hand, the effect of increasing the strain rate was obvious at 800 °C, where increasing the strain rate improved the hot ductility from 27% (at 0.001 1/s) to 47% (at 0.01 1/s) with the same cooling rates. The mechanism leading to an improvement of the hot ductility at higher deformation rates was studied further by investigation of the fracture surfaces.

As in **Figs. 5.23** and **5.24**, the fracture at 1080 °C was always ductile for all deformation speeds, while at 800 °C intergranular fracture on austenite grain boundaries occurred suggesting grain boundary sliding (GBS) to be taking place. The intergranular failure at 0.001 1/s gave the lowest hot ductility values (27%) and showed the sharpest intergranular fracture surface of all the studied cases. The intensity of the intergranular failure was getting less severe through a transition to less sharp intergranular fracture edges at the austenite grain corners by increasing the casting speed, which gave higher hot ductility values up to 47%. At the low straightening temperature, the occurrence of lower ductility values was accompanied by GBS and intergranular failure. This is enhanced by lower deformation speed allowing more time for GBS to proceed and more time for strain induced precipitates to form. This could be seen in the fracture surface analysis and was confirmed by the evaluation of the deformation time until complete failure, which was recorded by Dil805T as illustrated for 1080 °C and 800 °C in **Figs. 5.25** and **5.26**, respectively (time duration values see **Table 5.10**).

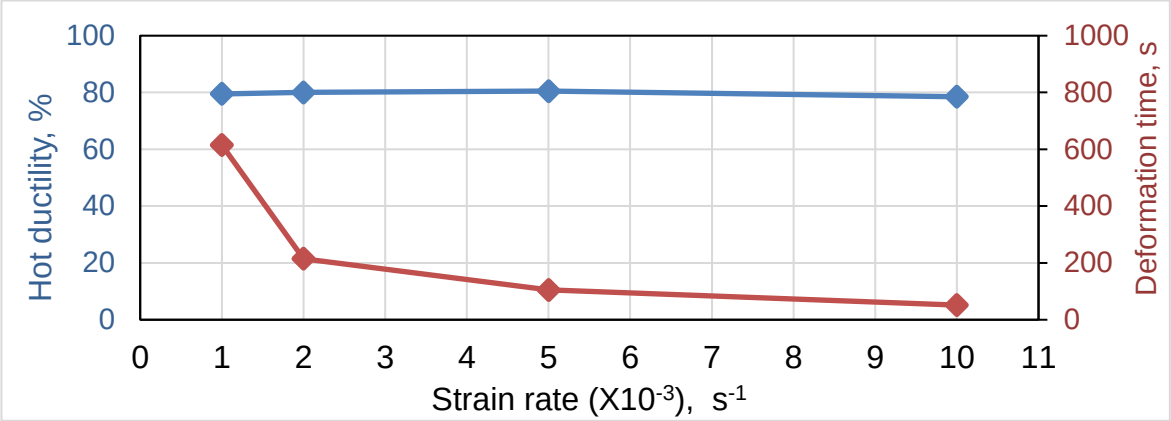

Fig. 5.25: Effect of deformation time at 1080 °C on hot ductility at different strain rates, Alloy-1

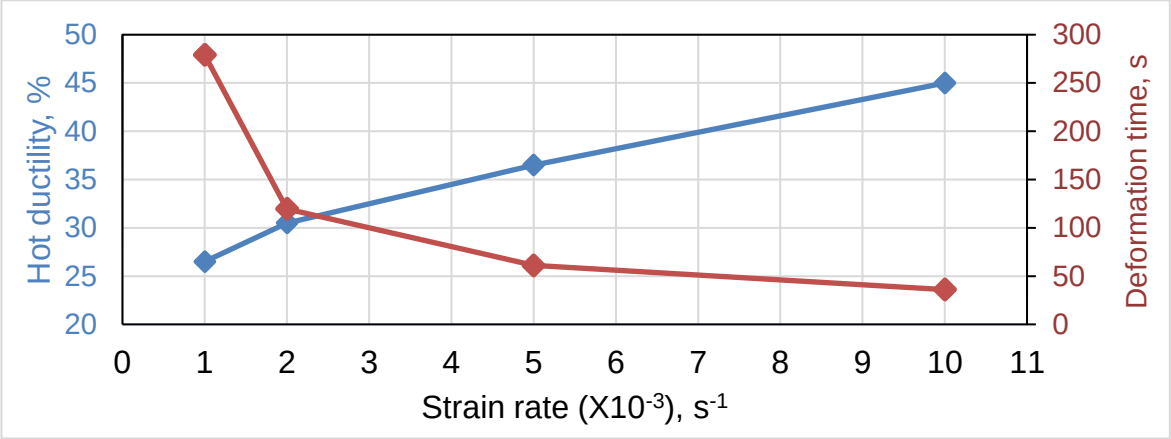

Fig. 5.26: Effect of deformation time at 800 °C on hot ductility at different strain rates, Alloy-1

The analysis of deformation durations shows that by increasing the deformation rate - at high temperatures (as 1080 °C) - the deformation duration will decrease as could be expected. In this case, no change took place in ductility values. This is because (at 1080 °C) the phase fraction of precipitates is much less, compared to the 800 °C condition, and the mean particle size is not fine enough to decrease the hot ductility. On the other hand, at 800 °C, increasing the deformation rate resulted, as expected, in less deformation time before failure, but also resulted in ductility improvement. Long deformation time as in low casting speed or due to break-out is considered detrimental to hot ductility as it permits more time for GBS to happen as was confirmed by the fracture surface analysis. This behavior illustrates the effect of casting speed in controlling/limiting time dependent deformation mechanisms. Similar effects of low strain rates on promoting GBS, formation of strain-induced precipitation and formation of deformation-induced ferrite were mentioned and confirmed in [51,86-88,144].

This fracture mechanism will continue to exist at lower temperatures especially at temperatures below Ar_3, where ferrite started to develop on the austenite grain boundaries enhancing GBS at low amounts of ferrite (at 750 °C and 700 °C) before ductility starts to recover as the ferrite content increases in the matrix (at 650 °C). The results of this effect is summarized in **Table 5.11** and the related LOM, SEM and EDX for samples tested at 750 °C and 700 °C are shown in **Figs. 5.27** and **5.28**, showing the fracture surface from top and side view of the broken samples (Strain rate 0.001 1/s, cooling rate= 0.35 K/s).

Table 5.11: Hot ductility values between 1080 °C and 650 °C, Alloy-1

Temperature, °C	Hot ductility, %	Standard deviation ±, %
1080	79	0
950	55	0
800	27	2
750	23	1
700	26	1
650	38	2

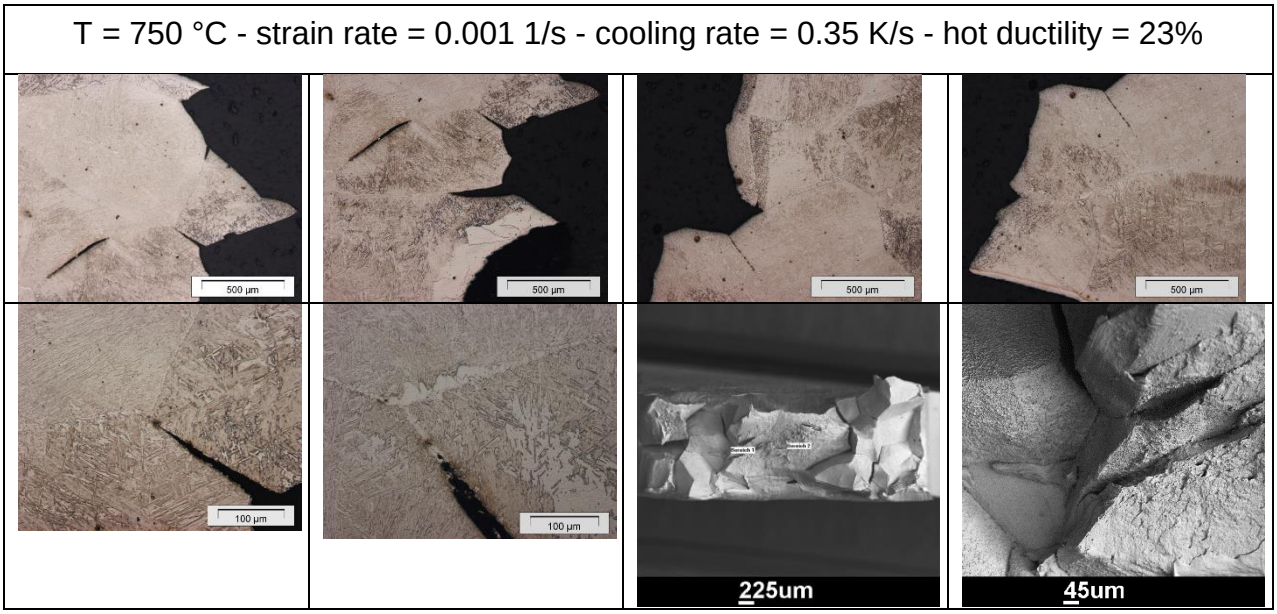

Fig. 5.27: Fracture surface at 750 °C, Alloy-1

In both cases in **Fig. 5.27** and **Fig. 5.28**, intergranular failure within the thin film of ferrite located at austenite grain boundaries could be observed on the top view of the samples (LOM) and the fracture surface side (SEM). The presence of ferrite enhanced the GBS. The relative recovery of the hot ductility at 650 °C (38%) is believed to be caused by the increase of the ferrite content of the matrix after reaching a level of a more homogeneous strain distribution between ferrite and austenite during deformation instead of strain concentration on the relatively weaker boundary ferrite film. This recovery depends on different factors related to the induced ferrite formation, chemical composition of the alloy and cooling rate.

In summary of this section, the influence of increasing the strain rate to improve the hot ductility at low unbending temperatures at a fixed cooling rate was studied as an approach to improve critical casting conditions leading to surface cracking. Increasing the strain rate could improve the hot ductility and reduce cracking risks. This could be achieved by increasing the casting speed while the critical strand part is passing through the unbending zone. Optimization of the intensity of secondary cooling could also play an important role in simultaneous improving of the hot ductility if it is combined with an increased strain rate. This will be explained in the following section.

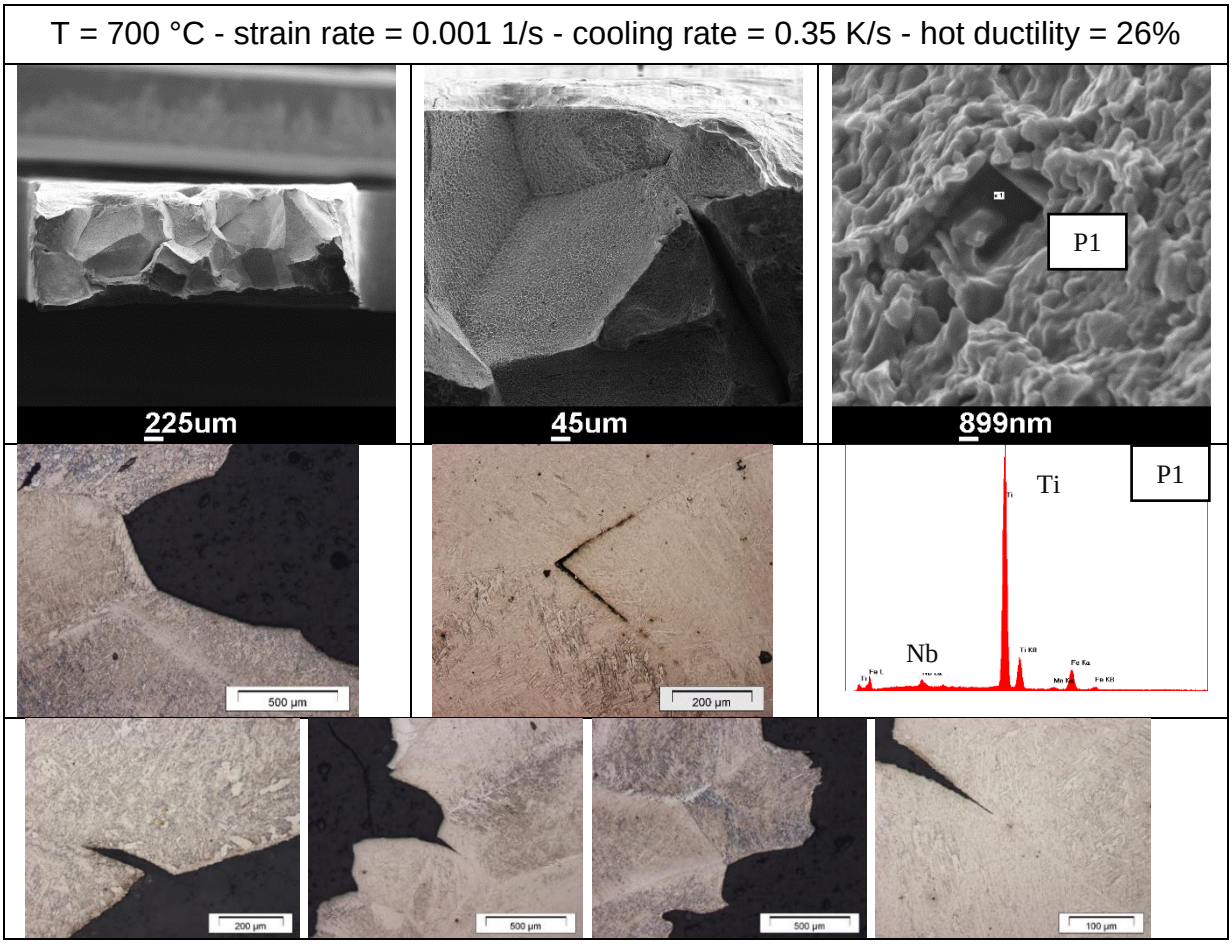

Fig. 5.28: Fracture surfaces at 700 °C, Alloy-1

5.2.3 Simultaneous optimization of cooling rate and strain rate in Alloy-1

In this part (Case-7 - **Table 5.2**), the influence of applying lower cooling rate until the un-bending zone and a higher strain rate at different straightening temperatures between 1080 °C and 800 °C will be presented. **Table 5.12** shows the hot ductility values at 5 different temperature values at a strain rate of 0.001 1/s after cooling with 0.35 K/s, while **Table 5.13** shows how the hot ductility values were improved after increasing the strain rate to 0.002 1/s and decreasing the cooling rate to 0.1 K/s. A comparison is shown in **Fig. 5.29**.

Table 5.12: Hot ductility results at low strain rate and high cooling rate, Alloy-1

0.001 1/s	Cycle-1 cooling with 0.35 K/s				
Temperature, °C	800	900	950	1000	1080
Hot ductility, %	27	52	55	68	79
Standard deviation ±, %	2	2	0	0	1

Table 5. 13: Hot ductility results at high strain rate and low cooling rate, Alloy-1

2 x 0.001 1/s	Cycle-1 cooling with 0.1 K/s				
Temperature, °C	800	900	950	1000	1080
Hot ductility, %	55	73	80	82	83
Standard deviation ±, %	5	6	5	8	2

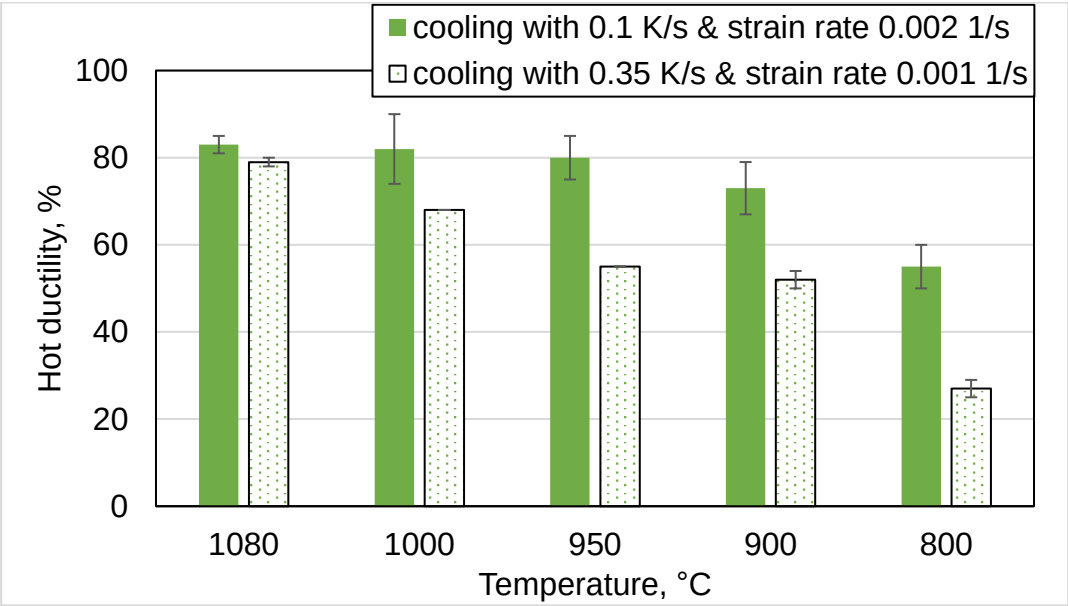

Fig. 5.29: The effect of deformation and cooling rates between 1080 °C and 800 °C, Alloy-1

The noticeable improvement caused by the lower cooling rate could be attributed to the coarser precipitates formed, which are less harmful to hot ductility. Higher cooling rates will produce finer precipitates, proved to be detrimental to hot ductility as presented earlier in this chapter. The higher strain rate limits the available time for the fine secondary precipitates to form and result in better hot ductility. Applying both, lower cooling rate and higher strain rate at the same time, is the optimum solution to improve the hot ductility conditions in critical regions and possibly avoid surface cracking.

An example of the effect of the two different cooling rates on particle size and phase fraction at 800 °C was studied using MatCalc. **Table 5.14** and **Fig. 5.30** give the summarized results of the MatCalc modelling. It can be stated that the higher cooling rate at lower strain rate results in much finer TiN (5 nm) precipitates with even a higher volume fraction by cooling with 0.35 K/s. These results fit very well with the ones by hot tensile testing and confirm the effect of finer precipitates size on hot ductility.

Table 5.14: Effect of cooling/strain rates on precipitation at 800 °C, Alloy-1

T= 800 °C	Cooling with 0.1 K/s	Cooling with 0.35 K/s
TiN, particle size, nm	67	5
NbC, particle size, nm	4	4
TiN, phase fraction	4×10^{-10}	2×10^{-6}
NbC, phase fraction	0.0014	0.0018
Hot ductility, %	55	27

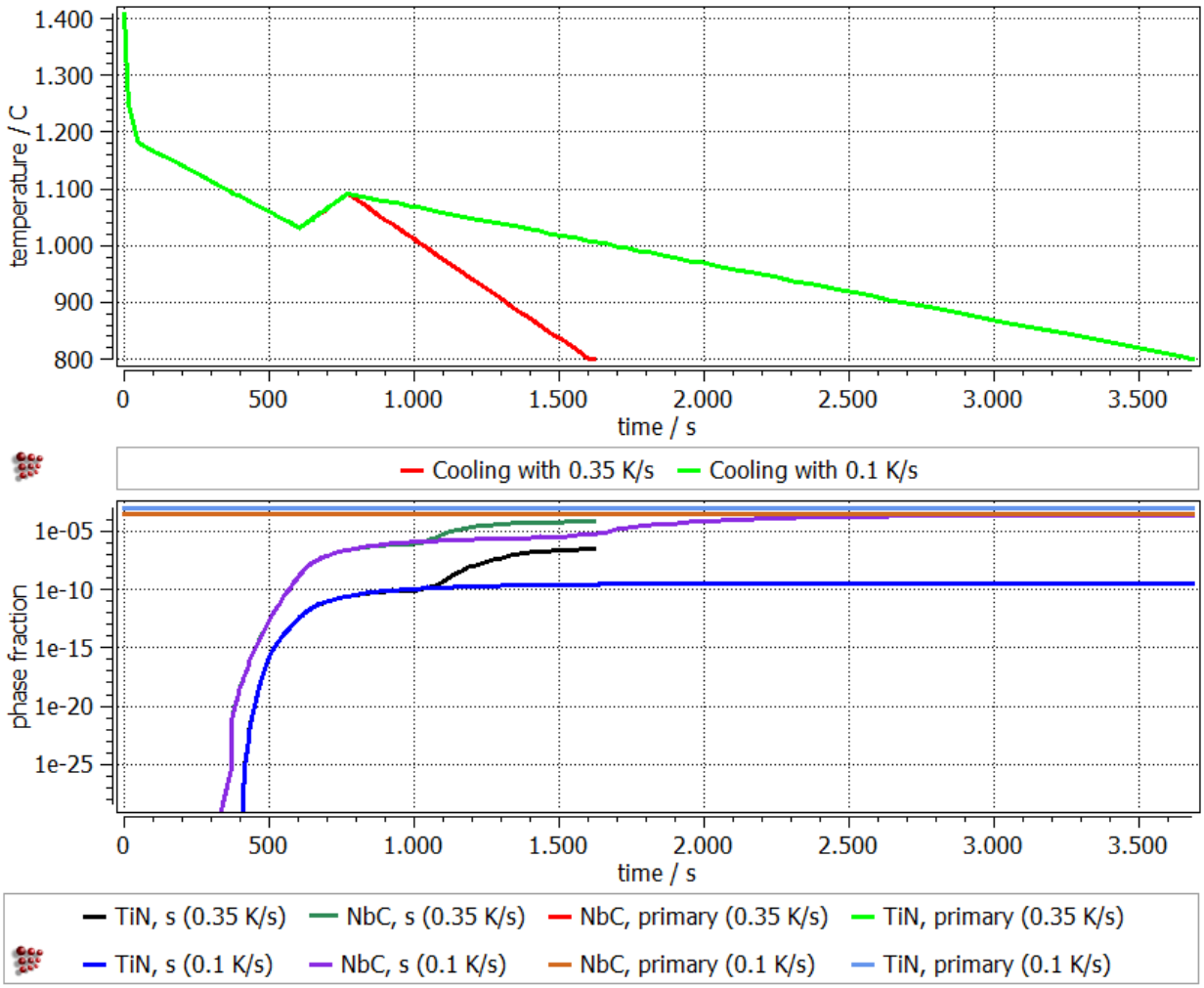

Fig. 5. 30: Effect of cooling rate on phase fraction of TiN and NbC at 800 °C, Alloy-1

5.2.4 Comparison between Alloy-0 and Alloy-1 at lower temperatures

5.2.4.1 Hot ductility

The hot ductility values at lower testing temperatures (< 800 °C) according to the test conditions of ideal casting (Cycle-1) as in Case-8 (**Table 5.1**) for Alloy-0 and Alloy-1 are shown in **Table 5.15** and illustrated in **Fig. 5.31**.

Table 5.15: Results of Case-8: Low temperature deformation (Alloy-0 & Alloy-1)

	Hot ductility, %			
Temperature, °C	Alloy-1	Standard deviation ±, %	Alloy-0	Standard deviation±, %
800	55	5	80	0
700	31	3	80	4
600	22	4	45	3
50	16	0	43	0

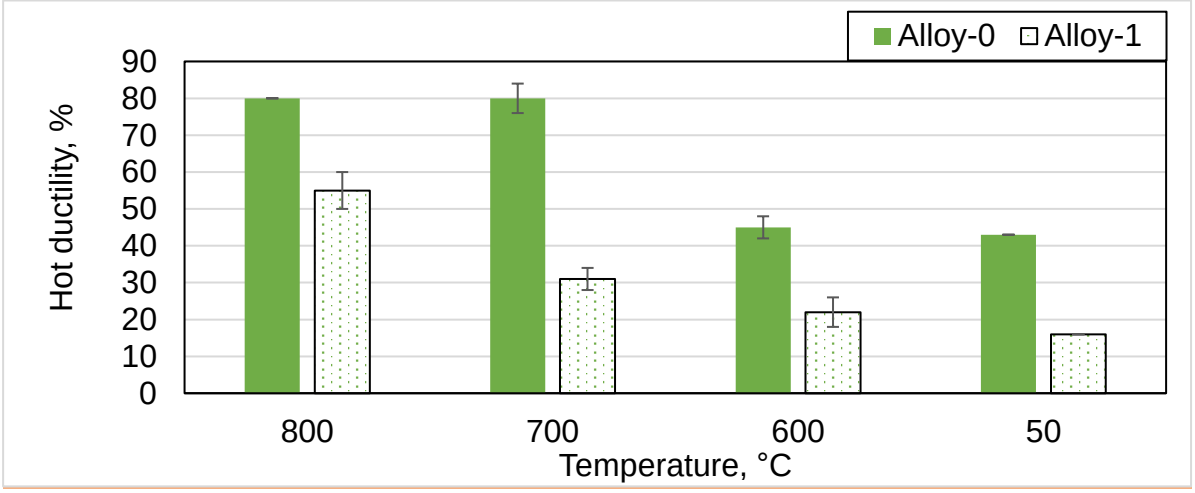

Fig. 5.31: Comparing the hot ductility of Alloy-0 to Alloy-1 at 800, 700, 600 and 50 °C

Alloy-0 shows high hot ductility values (80%) at 800 °C and 700 °C, then starts to drop to 45% at 600 °C, where the austenite to ferrite transformation was already finished and lower ductility values are to be expected with lowering the test temperature. The lowest value for Alloy-0 was 43% resulted by low temperature testing at 50 °C representing a cold charging temperature. No lower hot ductility values for Alloy-0 below 43% are expected at any temperature > 50 °C. No well-known effects or further phase transformation for Alloy-0 are expected to take place between 600 and 50 °C under the standard slab handling conditions and cooling rates. For Alloy-1, the hot ductility values were falling from 55% to 31%, 22% and 16% at 800 °C, 700 °C, 600 °C and 50 °C, respectively. The aim here is to study the fracture surface, microstructure, and relevant fracture mechanisms at lower temperatures at its worst case to compare it with higher temperature embrittlement cases. Studying the fracture mechanisms at low temperature will help to understand and possibly avoid embrittlement at higher temperatures.

After the end of CC and before charging, many other parameters will influence the crack sensitivity of the slabs, which could not all be studied by the hot tensile testing. The important factors of high influence on slab cracking after the casting shop should be studied to understand the properties of the materials before furnace charging. Those parameters are related to the phase transformation and their amount during slab transportation, handling, storage and charging and the effect of precipitation kinetics and particle size on the mechanical properties. Effects related to handling and storage procedures will be discussed separately in **Chapter 6**.

5.2.4.2 Fracture surface analysis

The fracture surfaces of the broken samples of Alloy-0 at 700 °C, 600 °C and 50 °C are presented in **Fig. 5.32**. As it can be seen, the area of the dimples is increasing with decreasing temperature, reaching its maximum at 50 °C. No intergranular fracture occurred.

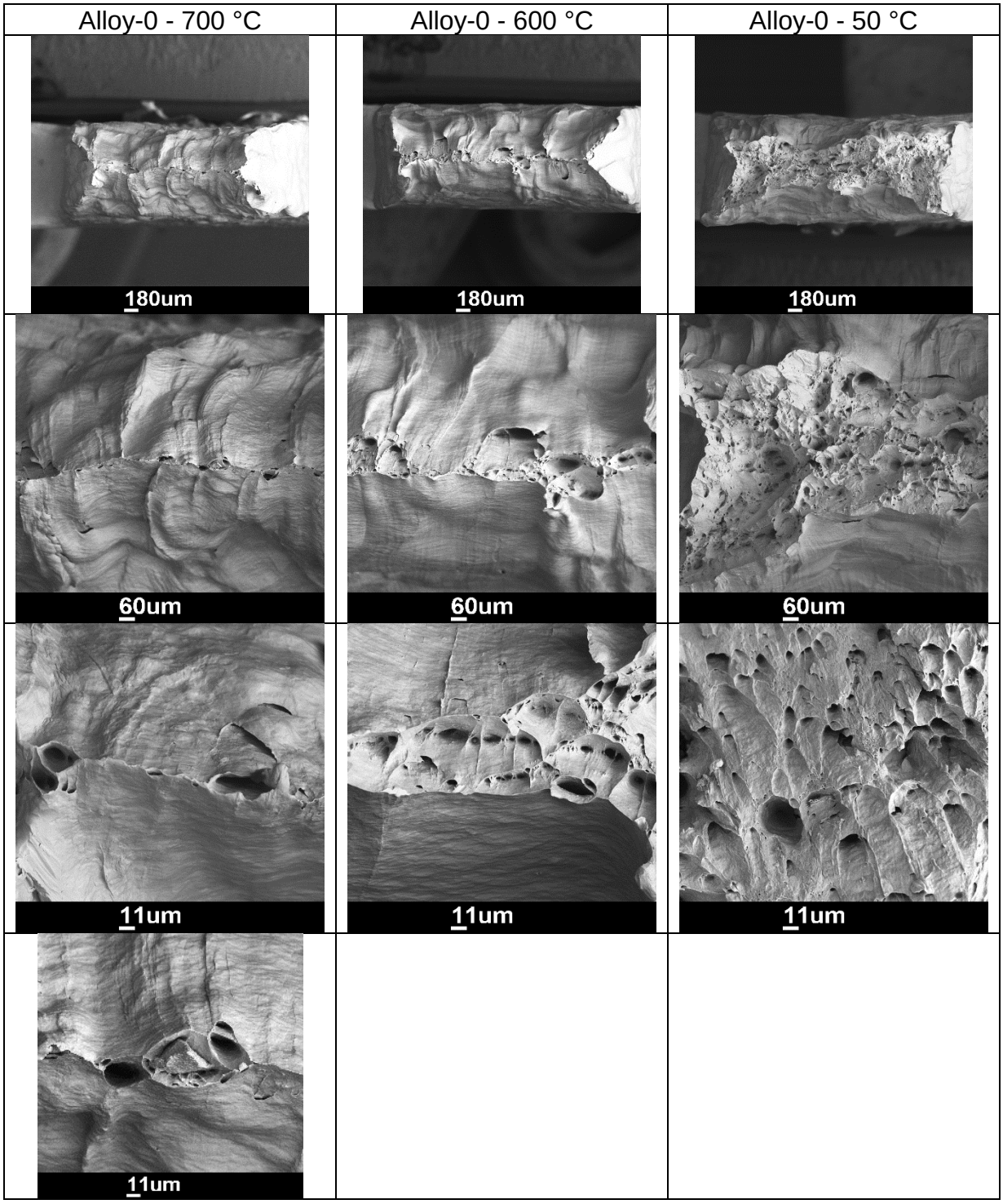

Fig. 5.32: Fracture surface at 700, 600 and 50 °C, Alloy-0

Similar analysis was done for Alloy-1, shown in **Fig. 5.33**, where a mixture of intergranular failure and dimples could be observed at 700 °C and 600 °C, while a complete and sharp intergranular failure is taking place at 50 °C representing the worst case. A similar observation was stated by Li [175] by studying the hot embrittlement of martensitic heat resistant steels. According to his results, the lowest hot ductility was accompanied by a mixture of dimples and intergranular fracture surface. Numerous micro-voids and micro-cracks were observed inside prior austenite grains, which could be related to the dimples. Multiple large intergranular cracks were observed along the austenite grain boundaries, which is assumed the cause for the intergranular fracture attributed to austenite GBS.

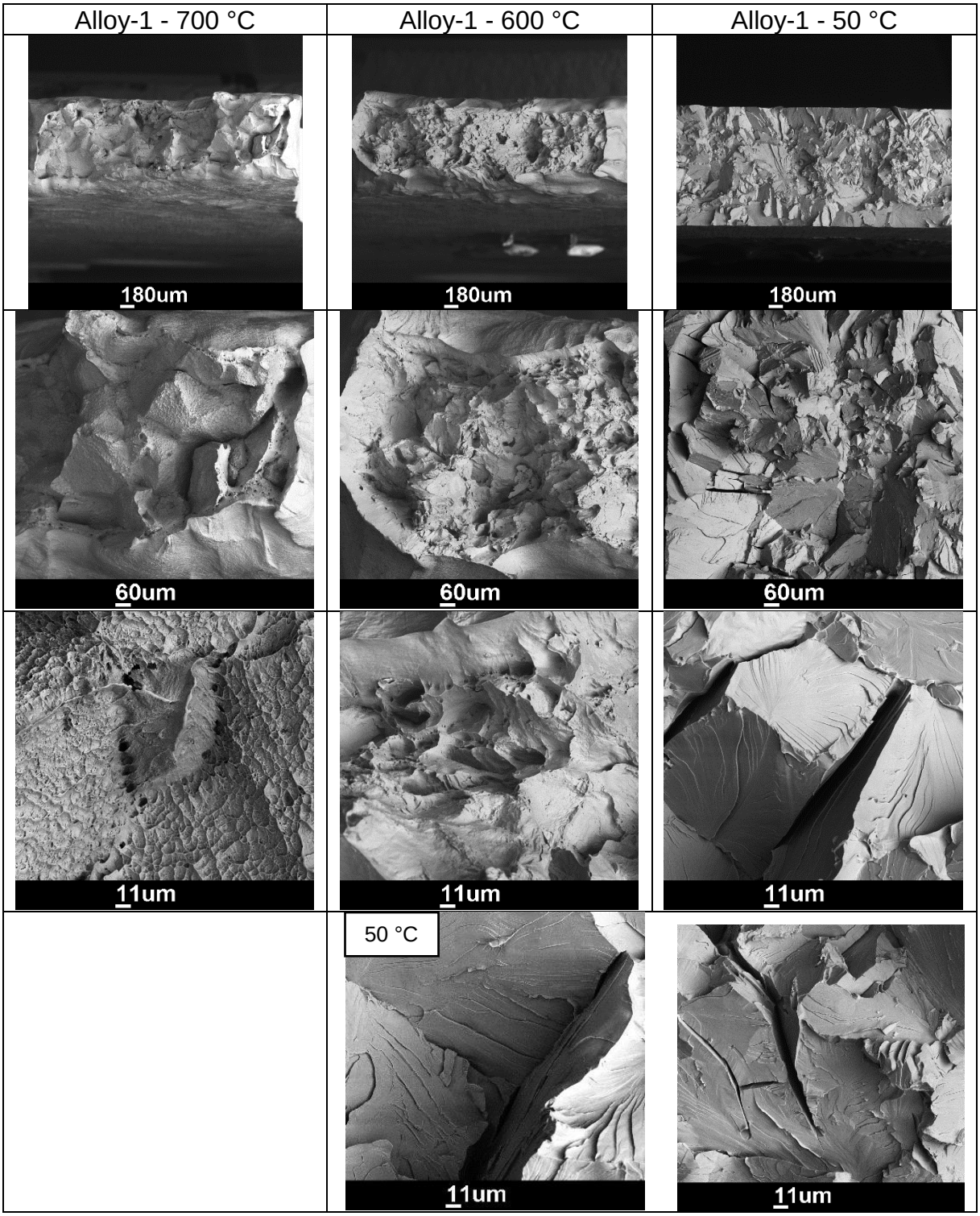

Fig. 5.33: Fracture surface at 700, 600 and 50 °C, Alloy-1

5.3 Discussion

The results presented in this chapter show the effects of different metallurgical parameters (representing industrial conditions) on hot ductility and crack sensitivity. First, the hot ductility, microstructure analysis and precipitation kinetics were evaluated/studied in terms of ideal casting conditions for both Alloy-0 and Alloy-1. Afterwards, the effect of different cast-

ing parameters representing process deviations for set/ideal values and improvement potentials were investigated through eight different cases.

In literature, the hot tensile testing in the temperature range of (700 - 1200 °C) was used to analyze crack sensitivity of steel slabs. The results presented in the form of hot ductility curves were of great importance for many casting shops worldwide in spite of the different opinions related to the testing conditions (explained in **Chapter 3**). This work represents a different approach of applying the hot tensile testing in crack sensitivity evaluation. In conventional hot tensile testing, cooling after high temperature austenitization (or even after melting) with a fixed cooling rate to test temperature (representing straightening temperature) and tensile deformation until failure, did not really copy the temperature profile taking place in reality. This gave misleading values in low temperature testing (700 – 900 °C) and resulted sometimes in inaccurate hot ductility curves.

An example to illustrate this problem is a hot tensile test at temperature of 700 °C. This temperature will not be reached in reality under the set values of ideal casting conditions and constant cooling rates. Even by reaching 700 °C due to abnormal failure conditions (as in beak-out), the temperature profile (and cooling/deformation rates) cannot be the same as the one used for 1000 °C under the normal conditions. This temperature profile before testing at low temperature ranges (700 - 800 °C) in most of the literature work didn't usually include the sudden surface cooling taking place immediately after mold exit and low secondary cooling (deactivation or minimum spray cooling values) and differences in deformation speeds. Those are all critical parameters influencing the grain size and precipitation evolution especially in micro-alloyed steels with high Ti and Nb amounts and will consequently influence the credibility of the measured hot ductility values. This work is an approach to use the hot tensile testing (together with other significant tools) to simulate the CC according to conditions as close as possible to industrial practice based on real industrial case studies and finally offering applicable solutions.

The results in this chapter illustrate the approach of using the hot tensile testing to calculate the hot ductility values for each defined case using its corresponding cooling history. Measurements were carried out in certain temperature range representing temperature fluctuation during casting and not at every possible temperature between 700 °C and 1200 °C using the same temperature schedule. Comparing the values of each case (inspired by industrial real problems) with the values of the ideal casting conditions indicated how far or close the case to a crack free condition under ideal casting was, which could be translated from lab testing and simulation values into industrial values. After analysis using different microscopy tools, the information needed in terms of grain size and phase constituents were collected. Parallel to this tensile testing/analysis, the same temperature casting profiles were used to run MatCalc simulation modelling to evaluate the part related to precipitation types/sizes and distribution. Correlation of all the information resulting from the three used tools gave a sharper image to understanding of the critical factors and their causes, investigating the cracking behavior and mechanisms and generated a better overview that could not be seen after hot tensile testing alone.

The austenite grain size showed to have an important influence on hot ductility, where a higher grain size resulted in lower hot ductility as it will be easier for a crack to propagate with less resistance through grain boundaries and triple points compared to finer grain structures. The influence of grain size is critical even in the absence of precipitates as in Alloy-0, illustrated in 5.2.1.2.This could be attributed to the failure within the thin ferrite film on the austenite grain boundaries, which is subjected to a higher stress concentration at

the early stage of ferrite formation. The hot ductility results could be better explained after metallographic investigation. A smooth ductile fracture surface resulted after deformation above Ar_3, while low ductility was always linked to ferrite formation, where a mixture of intergranular fractures and dimples coalesce could be observed. Higher ferrite phase fraction will help the recovery of ductility, which is easier to take place at higher grain boundary density in the case of finer grains, where ferrite nucleation sites are more available. The effect of grain size is less harmful to hot ductility at temperatures above the ferrite start (Ar_3) and more harmful by the presence of fine precipitates, especially below the Ar_3.

The effect of precipitation was studied in Alloy-1, where the influence of the cooling cycle showed a great effect on the precipitates sizes and phase fractions. The results of the MatCalc modelling is matching very well to the hot ductility measurements under the same temperature cycle, where the effect of break-out was explained in detail. The particle size resulting from MatCalc analyses was always fine in cases where low hot ductility resulted under break-out cooling cycle. The main problem of a break-out case is that it shifts the straightening temperature range to lower ranges of values, where the hot ductility is getting worse due to the increase of finer precipitates phase fractions. The break-out cycle resulted in much finer TiN (7 - 10 nm) and NbC (18 nm) precipitates with a higher phase fraction (NbC: 0.002, TiN: 2 - 80 $x10^{-5}$) compared to phase fractions after the ideal casting. Hot tensile testing of the break-out resulted in an average hot ductility of 66% compared to an average hot ductility of 84% for the ideal casting conditions. The fast cooling of the slab surface by the beginning of the break-out is believed to be the cause of the fine precipitates. The effect of fine precipitates are more detrimental to hot ductility at straightening taking place at temperatures below Ar_3. Straightening at 700 °C after a normal casting procedure (without break-out) resulted in a very fine particle size of NbC (3 nm) with a relatively high phase fraction of 0.0021. This enhanced the failure over the ferrite film and/or caused suppression of dynamic recrystallization and finally resulted in the lowest hot ductility value of 31%. The worst, critical and ideal cases regarding the hot ductility results are illustrated in **Fig. 5.21**.

Studying the effect of break-out showed that approx. four slabs should be affected by the abnormal casting conditions in terms of temperature profile (secondary cooling) and deformation rate (casting speeds) before the cast returns to regular flow under normal/ideal conditions again. Slab no. 4 was studied in this chapter as the MatCalc modelling showed that this slab will exhibit the finest particle size (at 1000 °C, TiN: 7 nm, NbC: 18 nm) compared to the other break-out slabs, see details in **Table 5.1** and **Table 5.9**. The successful approach to improve the properties of slabs similar to Break-out-4 will work as well for the other three break-out slabs, produced under less severe casting conditions, i.e. less sudden cooling at the beginning of the casting and coarser particle size.

The effect of different strain rates was studied in 5.2.2. As a result, higher strain rates result in better hot ductility values. Low strain rates (i.e. lower casting speeds, in case of break-out can't be avoided) will allow more time for strain induced fine precipitates to develop on austenite grain boundaries during deformation and will finally result in enhanced intergranular failure by GBS even before the presence of the thin ferrite film. This effect could be stated in Alloy-1 at 800 °C, where increasing the strain rate from 0.001 1/s to 0.01 1/s resulted in hot ductility improvement from 27% to 47%, respectively. The deformation time was recorded during the different hot tensile experiments at 800 °C. It is confirmed that longer deformation time (lower strain rate) will result in lower ductility values result. The microstructure investigation using different microscopy tools was illustrated in detail in 5.2.2.2. It showed clearly the intergranular fracture at the austenite grain boundaries for

different deformation speeds at 800 °C, where the sharpest intergranular failure occurred at the lowest both strain rate and hot ductility.

The influence of cooling rate was tested for Alloy-1, where it could be confirmed that low cooling rate (less intense secondary cooling) could strongly improve the hot ductility even in the critical temperature range especially when the strain rate is simultaneously increased. This improvement approach (testing condition 5.2.3) resulted in increasing the average hot ductility in the critical range of (800 - 950 °C) from 45% to 69%, which will result in a reduced cracking risk. Cooling at 0.1 K/s (strain rate: 0.002 1/s) instead of 0.35 K/s (strain rate: 0.001 1/s) resulted in less precipitates phase fraction and larger mean radius over the critical size. For example, at 800 °C, the mean radius of TiN= 67 nm (hot ductility= 55%) instead of mean radius of 5 nm (hot ductility= 27%) was calculated by the MatCalc precipitation model.

For a better comparison, further hot tensile testing was carried out at lower temperatures to study the extend of hot ductility loss even at low temperature as of 50 °C, representing the furnace charging temperature in one of the cases. Alloy-0 showed dimples fracture surfaces at temperatures below Ar_3. The higher dimples densities was always connected to the lower temperature. The lowest hot ductility was 45% at 600 °C and 43% at 50 °C. No intergranular failure in Alloy-0 could be observed. On the other hand, Alloy-1 showed sharper intergranular fracture, the lower the testing temperature was. At 50 °C, a clear sharp intergranular fracture was observed with a hot ductility of only 16%. Conditions leading to voids coalesce and intergranular brittle fracture should be avoided.

5.4 Summary and conclusions

In this chapter, the process of CC of steel slabs was studied in detail in terms of ideal casting conditions of temperature profile and straightening deformation with a detailed overview of the changes that take place by deviation from the ideal condition in the case of break-out and its influence on surface cracking sensitivity. The main objective was to study the cracking behavior, evaluate the related parameters and define critical situation that will most probably lead to cracking/breaking justified by case studies from the industry. The statistical analysis explained in **Chapter 2** illustrated that 70% of the broken slabs in this study were related to abnormal/undesired casting conditions connected to break-out and deviation in the set values in casting speed, temperature profile or the chemical composition. After the experimental procedures, microscopic investigation and precipitation simulation carried out in this work and illustrated in this chapter, the cracking causes could be explained and critical values leading to higher cracking risk were defined. Moreover, improvements procedures with defined values could be suggested.

The changes in the slab temperature and deformation history due to break-out were studied and were used to define four slab histories related to the break-out. The worst break-out slab was found to be Slab-4, in which its temperature profile (**Fig. 5.7**) was used to evaluate the effect of break-out on hot ductility and precipitation. Eight different cases were defined (**Table 5.2**) to study (using the three different tools mentioned earlier) the effect of different casting conditions/scenarios and investigate possible hot ductility improvements inspired by the industrial analysis. The studied cases included effects of cooling schedule/rate, straightening temperature, strain rate/casting speed and low temperature deformation. After analyzing the results presented in this chapter, the following recommendations/notes were made:

- Decreasing the intensity of secondary cooling after break-out, increasing the casting speed during straightening the defected part of the strand and avoiding low straightening temperatures in the unbending zone proved to be beneficial strategies in avoiding/reducing cracking. Applying those strategies will produce coarser precipitates, higher deformation rates and avoid ferrite formation, which are all considered as improvement potentials. This helps avoiding the embrittlement mechanisms leading to the undesired fracture surfaces and increasing the hot ductility values as explained earlier. Considering those improvement techniques could have been very beneficial to reduce cracking risks of 70% of the broken slabs included in this study. The summary of all the potential improvement strategies during casting and slab transportation/handling will be illustrated in **Chapter 6.**
- For Alloy-0 (and similar alloys), it is important to avoid cooling profiles (as in break-out) resulting in austenite grain size as large as 200 µm. Grain size of 100 µm resulted in high and acceptable hot ductility values and ductile surface fracture. Ferrite film formation before/during the unbending zone should be avoided.
- For Alloy-1 (and similar micro-alloyed steels):
  - Precipitates at/below the critical particle size of 15 - 20 nm will result in a very high possibility of cracking especially when straightening is taking place at temperature below Ar_3.
  - Coarse primary precipitates (size ~ 2 µm) and secondary precipitates (size > 40 nm) showed accepted hot ductility values (> 80%) and ductile fracture surfaces.
  - Casting temperature profiles and deformation rates leading to precipitates of sizes below 40 nm or/and unbending below Ar_3 are considered to be in critical status.
  - Increasing the casting speed, decreasing the intensity of spray cooling and casting/straightening at temperature above Ar_3 could possibly shift the slabs from a critical status into an acceptable conditions/quality area.
- Slabs cast under acceptable casting conditions corresponding to hot ductility values (> 80%), will proceed by further transportation and handling into the hot strip mill. Further cracking risks for those slabs are introduced in **Chapter 6**.
- Slabs with high cracking risk or with critical status after the previously mentioned critical CC conditions, should go through an extra visual surface control after CC. This should be applied in cases of unavoidable critical casting/processing conditions, where improvement strategies cannot be applied. In case of any observed transverse cracks or any related unaccepted surface quality by this inspection, the slab should be eliminated from the rolling schedule, if crack elimination by flame scarfing of the slab is not possible within the set transportation and charging regulations. Further transport and rolling of those slabs will possibly lead to break-downs in the rolling mill.
- Hot ductility analysis (combined with the results of other tools) appeared to be successful in estimating the cracking behavior during CC. However, it is not sufficient to fully describe / represent the crack sensitivity immediately before furnace charging, as many other parameters will play a role in enhancing embrittlement mechanisms after the end of the CC, which cannot be evaluated by hot tensile testing. The cooling routes, phase transformation during storage and material properties between casting and charging will be discussed in **Chapter 6**, where the complete critical situations for cracking will be introduced featuring all the potential cracking possibilities and combinations covered in this work.

Chapter 6: Slab handling process

6.1 Handling procedures and routes

After the torch cut-off point at the end of the continuous casting (CC), the slabs are lifted by cranes, stacked on wagons and transported to the storage area before transported and charged into the reheating furnaces of the hot strip mill (HSM). In some cases, slab length adjustment should take place by cutting 1 - 2 m of the slab head - slab is still warm (600 - 300 °C) - before storage and charging.

Slab handling includes three different routes as introduced in **Fig. 2.1**. Each steel grade should follow its optimum handling route and avoid any undesired fast cooling downstream. Planning the handling routes by customizing which grades should follow which route, has an important impact in reducing energy costs and optimizing the rolling schedule. The influence of the three cooling routes (Route-1: hot charging, Route-2: warm charging and Route-3: pile / cold charging) on microstructure and material properties before charging will be studied in this chapter. The key factor in this effect is the cooling rate of slabs between the casting shop and reheating furnace charging. For this purpose, a FEM cooling model was built using Abaqus CAE to calculate the temperature gradients and cooling profiles during handling and storage. Temperature measurements from stockyard on real slabs were used for model validation.

6.2 FEM temperature model

The aim of the model is to calculate the cooling rate of the slab surface for different conditions. The calculated cooling rates were used in further dilatometry experiments on Dil805A to study the phase transformation and final microstructure using a realistic and verified cooling schedule. Once the cooling rates from the FEM model were validated by temperature measurements at real slabs of Route-1, simulation for slab stack/pile (Route-3) was run and evaluated. Model features and case studies are discussed in this section.

6.2.1 FEM model: features / data

The slab dimensions and material properties used in the model are shown in **Table 6.1**.

Table 6.1: FEM temperature model data

Slab dimensions, m	L= 10, W= 2-2.5 ,T= 0.25
Slab surface temperature, °C	≈ 1000
Slab center temperature, °C	≈ 1350
Air temperature, °C	20
Slab surface emissivity	0.3 - 0.8
Convection heat transfer coefficient, W/(m^2 * K)	10 - 100

The results of the model are presented in the following diagrams showing 3/4 of the slab to express the temperature variation over the slab thickness.

6.2.2 Single slab model (Route-1)

Figs. 6.1 - 6.3 show the temperature distribution of a single slab from time= 0 (directly after casting: surface temperature ≈ 1000 °C, center temperature ≈ 1350 °C) until time= 30 h, where the slab temperature decreases to (50 - 100 °C). Single slab analysis/cooling profile in addition to the four-slab model (will be presented later in this chapter) will be used in studying and evaluating the hot charging procedure by Route-1.

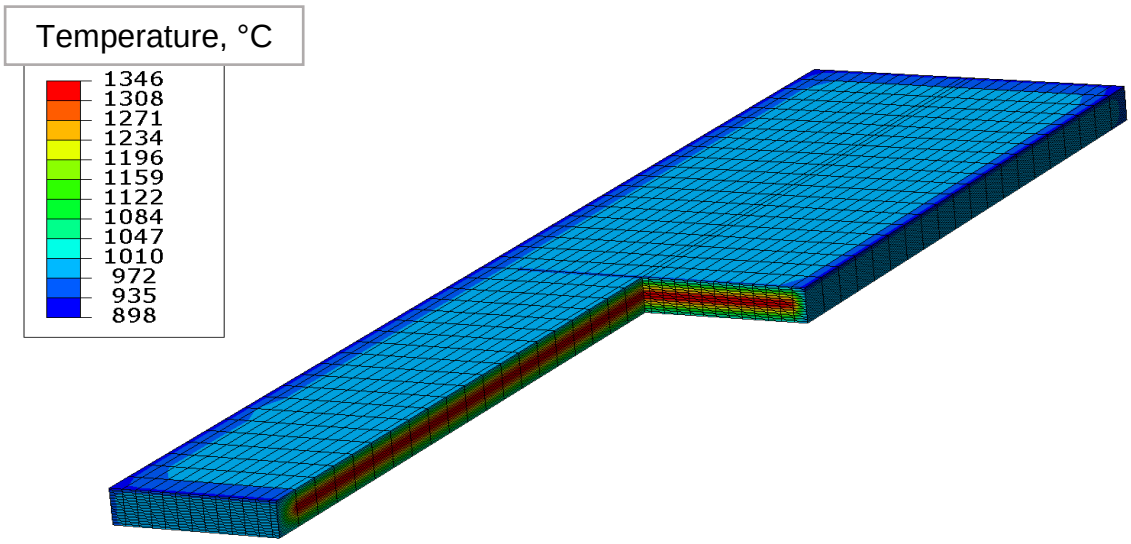

Fig. 6.1: Temperature distribution in a single slab at time 0, Abaqus FEM model

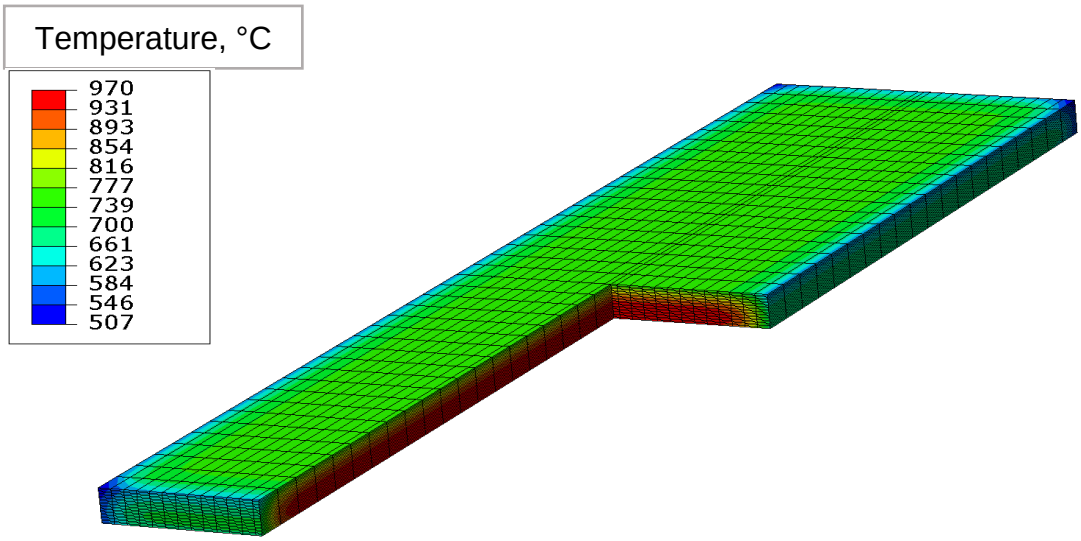

Fig. 6.2: Temperature distribution in a single slab after 1 h, Abaqus FEM model

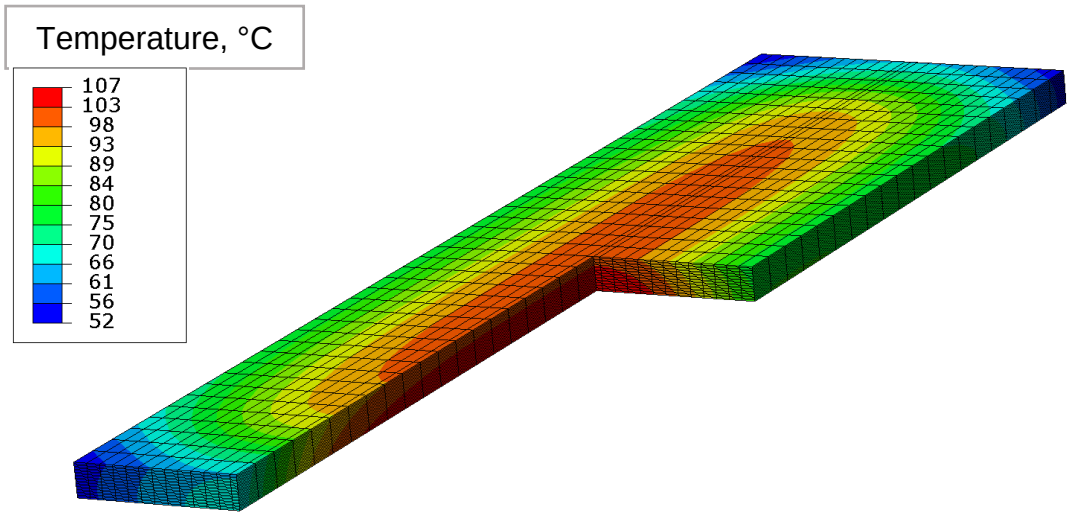

Fig. 6.3: Temperature distribution in a single slab after 30 h, Abaqus FEM model

6.2.3 Stack/pile 15 slabs model (Route-3)

The stack/pile cooling model was built to study Route-3 (pile/cold charging). The first step (piling) of the model starts at time= 0 by piling up 15 slabs after casting shop one after another within 10 min difference until a 15 slabs pile is done after 140 minutes. The second step (cooling) of the pile model starts by cooling of the 15 slabs pile for 200 h. For simplification in the piling step, starting temperature distribution/conditions of all slabs were assumed identical as in single slab case with the same slab dimensions, i.e. the average start temperature of each slab is; center= 1350 °C and surface= 1000 °C. Every slab was cooling down during the piling step according to the material properties, surrounding air temperature and piling conditions (time difference between slab additions and number of existing slabs at each time point). The complete cooling profile and total duration to reach a certain temperature are expected to be different from one slab to another depending mainly on its position in the pile and total number of slabs. The start of the piling-up process is shown in **Figs. 6.4** - **6.6**, the end of step 1 (piling) and the beginning of step 2 (cooling) is presented in **Fig. 6.7**. The temperature distribution after 50 h is given in **Fig. 6.8**.

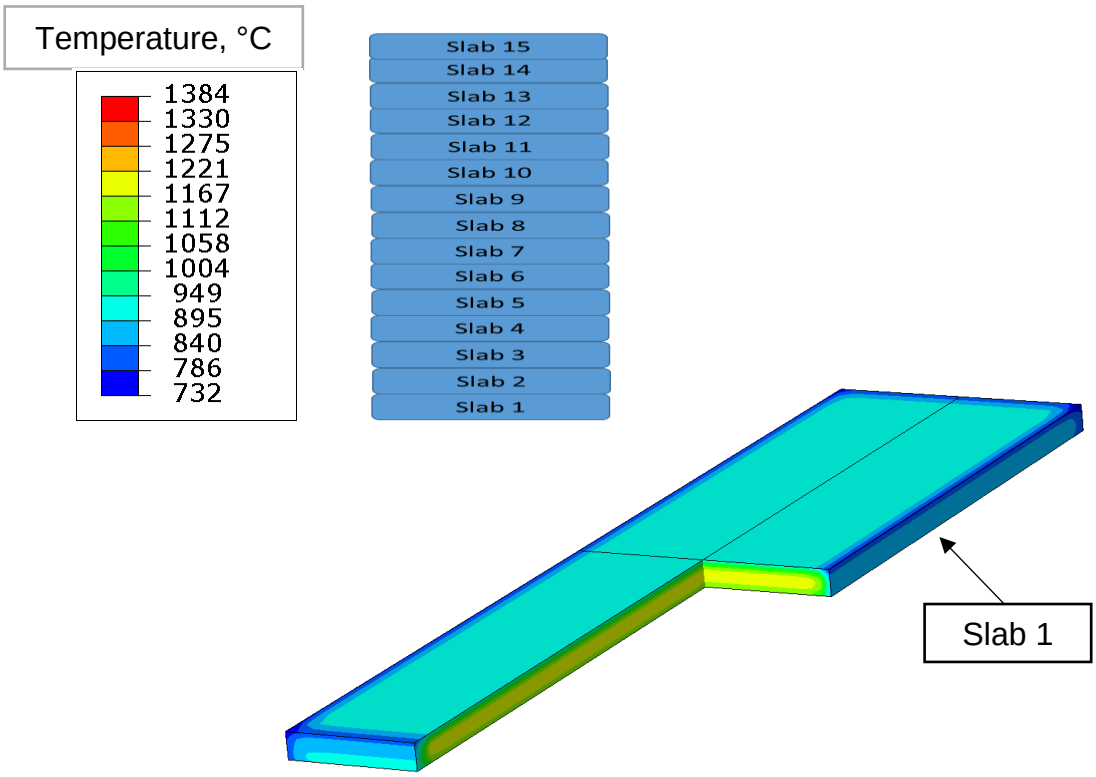

Fig. 6.4: Temperature distribution of pile slab 1 after 10 min, Abaqus FEM model

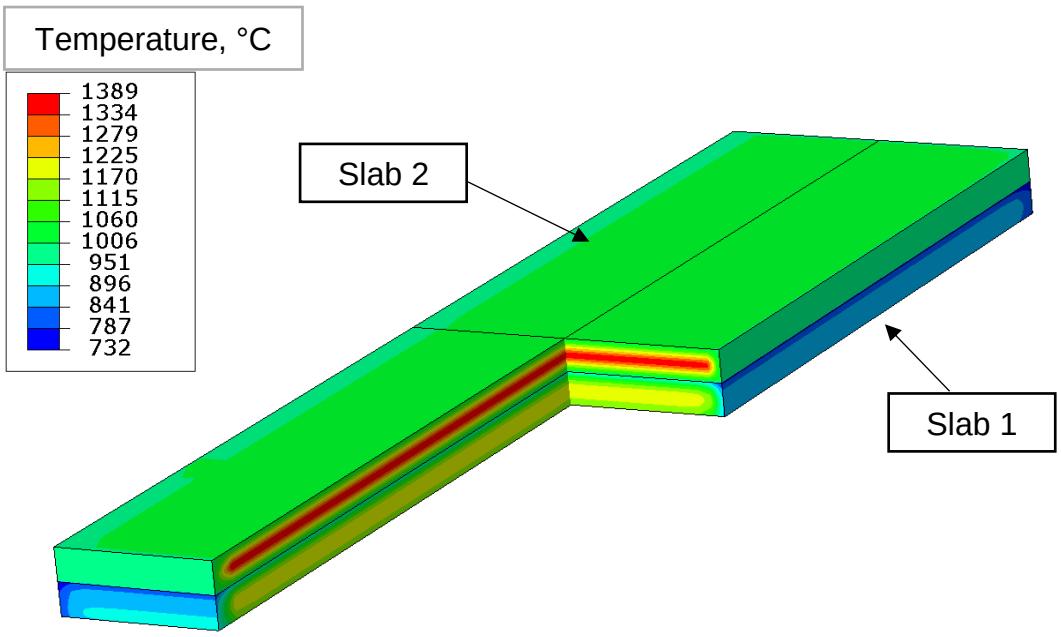

Fig. 6.5: Temperature distribution immediately after adding slab 2 to slab 1 after 10 min, Abaqus FEM model

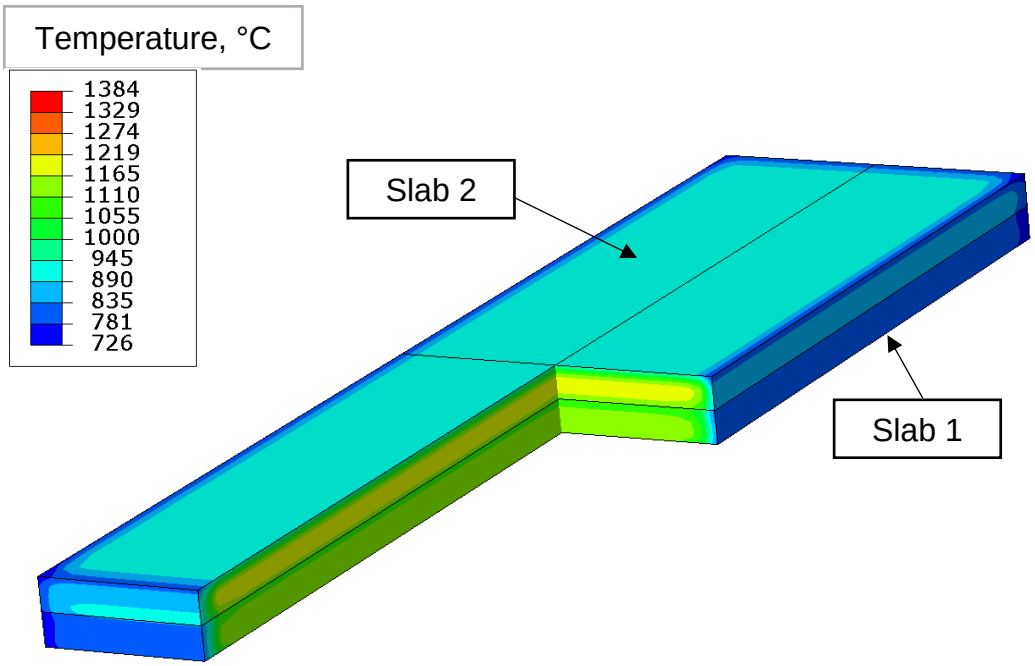

Fig. 6.6: Temperature distribution of pile slabs 1 and 2 after 20 min, Abaqus FEM model

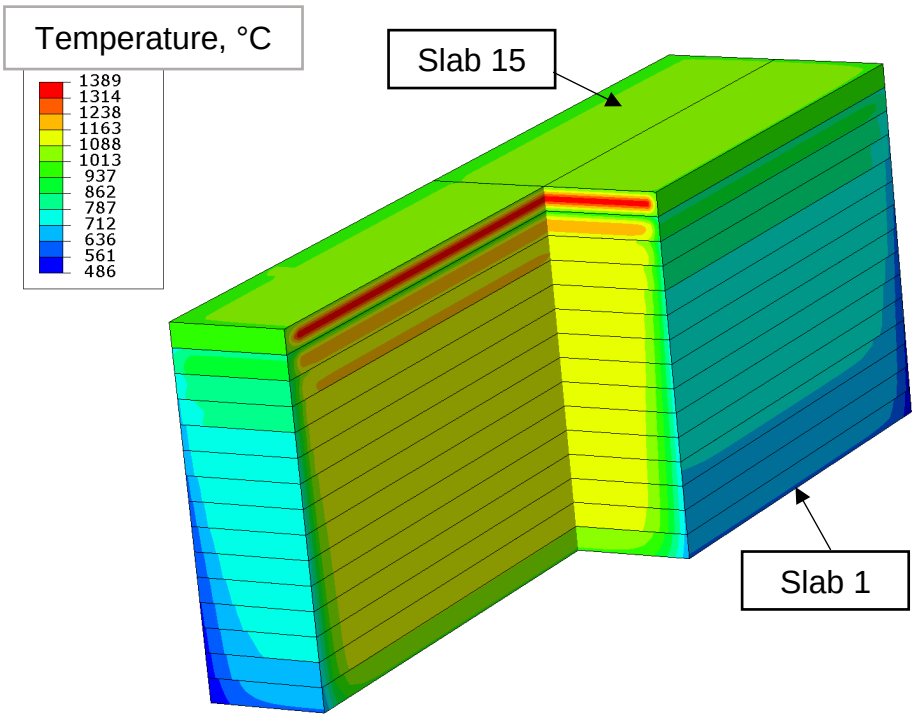

Fig. 6.7: Temperature distribution of pile slabs 1-15, end of piling / start of cooling after 140 min, Abaqus FEM model

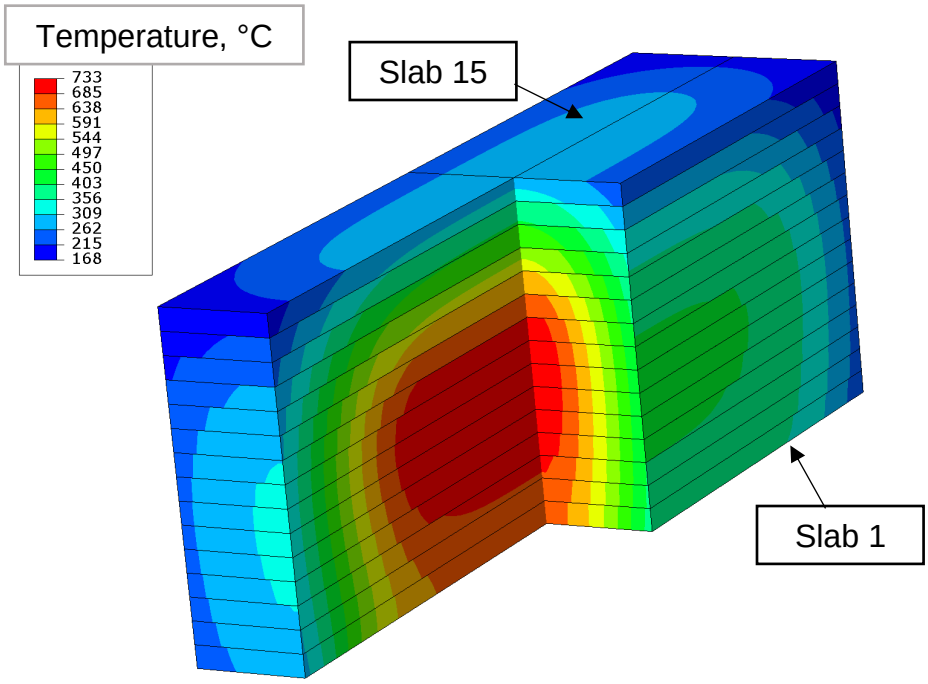

Fig. 6.8: Temperature distribution of pile slabs 1-15 after 50 h, Abaqus FEM model

6.2.4 Four slabs model (Route-1)

Handling of four slabs from casting shop to hot/direct charging (Route-1) is studied by the four slab model. The results of the four slab simulation after 30 h cooling is shown in **Fig. 6.9**. The model will be used to evaluate cooling profiles for Route-1. Cooling history of slabs planned for Route-1 (direct hot charging) should mostly follow the cooling rates from the four slabs model and in the worst case might be a mixture of both the four slab and single slab cooling models in case of length reduction before hot charging.

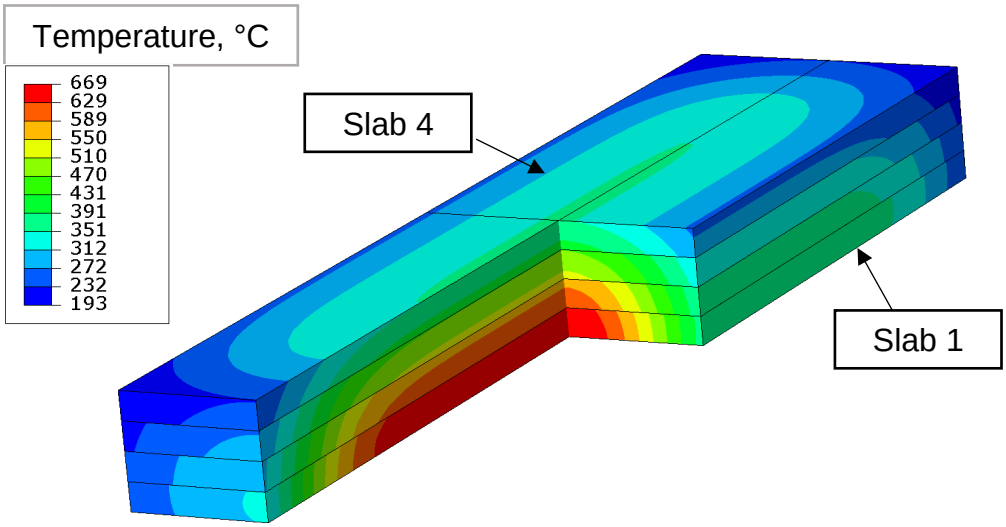

Fig. 6.9: Temperature distribution of the four slabs pile after 30 h, Abaqus FEM model

6.2.5 FEM model validation

Temperature measurements - on slab surface central region - in the stockyard for four slabs planned for hot charging were recorded. Measurements were taken directly after casting (in single cooling conditions), during storage and just before reheating furnace charging (after four slab pile conditions). Such a pile is shown in **Fig. 6.10**. The first measurements for single slabs - recorded after leaving the casting shop - were compared to the FEM single slab model as illustrated in **Fig. 6.11**. The rest temperature measurements of the four slabs after pile cooling, recorded just before furnace charging, were compared to the results of the FEM four slab model, see **Table 6.2**. The calculated temperature values were very close to the measured ones with minimum to maximum deviation of (3 - 20 °C).

The temperature prediction by the FEM model shows a good agreement with the stockyard measurements in single and pile case representing Route-1 of slab handling. The FEM model was extended to evaluate the cooling profiles of different slabs in a 15 slabs pile, representing Route-3. Analysis of Route-2 will be discussed later on this chapter.

Fig. 6.10: Four slabs pile for model validation

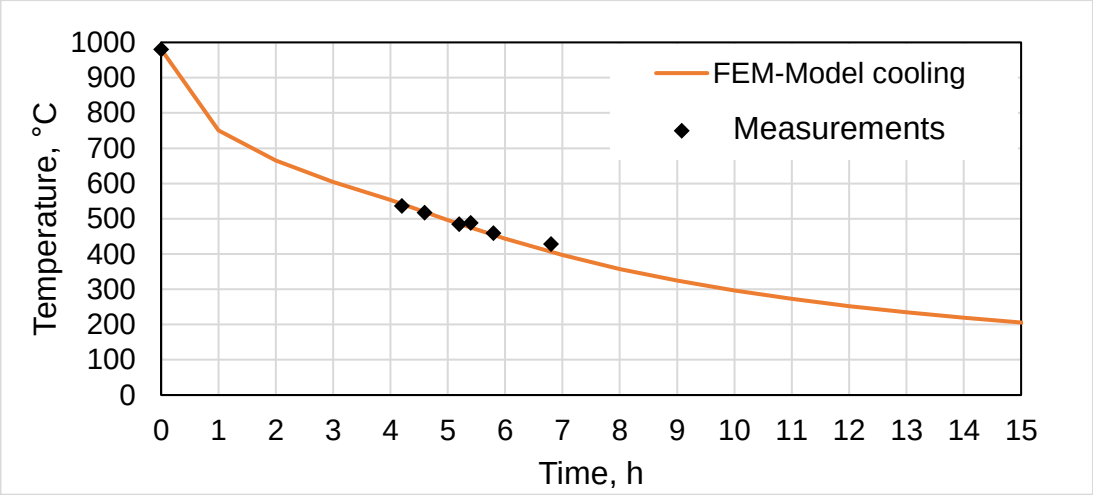

Fig. 6.11: Comparision between the stockyard temperature measurements and the calculated Abaqus FEM cooling profile for single slab cooling

Table 6.2: Comparision between slab temperature measurements and FEM results at the end of four slab model cooling

Four slab pile	Time duration: casting end- charging, h	Charging temperature FEM Model, °C	Charging temperature measurements, °C
Slab 4	21.5	327	307
Slab 3	22	319	316
Slab 2	22.3	354	360
Slab 1	22.5	365	361

6.2.6 Evaluation of slab surface cooling rates

After temperature model validation by the four slab model, the main objective of the FEM model is now the calculation of the slab cooling rates at different conditions and even at different areas in the slab to be used in the further analysis. A strong difference between the cooling rates at two different parts of the same slab - center and corner, for example - might result in different matrix microstructure constituents and precipitation distribution leading to locally different mechanical properties. This could result in local low temperature embrittlement during transportation and charging or further cracking risk at the phase boundaries during slab reheating. In the HSM reheating furnace, the transformation stresses of the formed phases as ferrite, pearlite or bainite (before charging) into austenite (after reheating) and its corresponding effect on any possible crack formation/propagation will be strongly dependent on the phase constituents, particle types, sizes and distribution before charging, charging temperature and reheating rate in the furnace.

To study the material properties in terms of microstructure, precipitation distribution and mechanical properties, calculation of the cooling rates in the stockyard using the FEM mentioned in the previous part was necessary. The rates were used in the MatCalc precipitation modelling to study the effect of cooling rate on particle size and phase fraction and furthermore for running dilatometry experiments for further metallographic investigations. Finally, hardness testing was performed to estimate the influence of the formed phases and precipitates sizes on the mechanical properties of the material.

The evaluation of the cooling profiles of four chosen slabs from all the carried out simulations are presented in this section to study and evaluate the dependency of the slab pile order/position on material properties and cracking risk before furnace charging. The four slabs are 1. the single slab, 2. pile slab no. 15 (stack top slab), 3. slab 14 in the pile and finally 4. slab 7 in the pile center. For each of those slabs, three temperature/cooling profiles were analyzed: at the slab corner, slab center and slab edge. The locations of the profiles are sketched in **Fig. 6.12**.

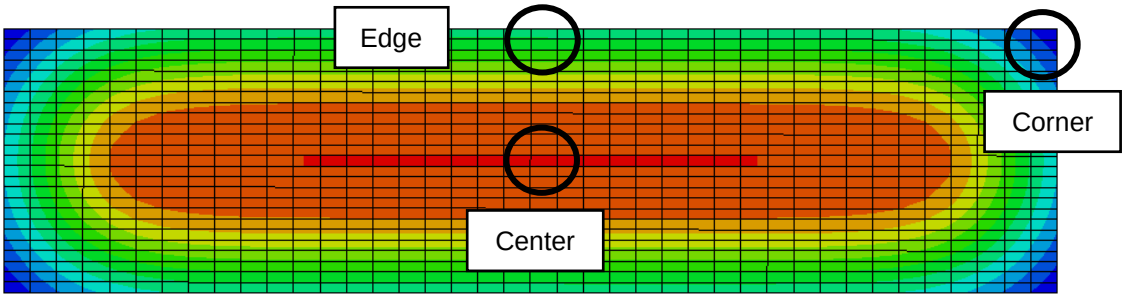

Fig. 6.12: Location of temperature profile evaluation - upper slab surface

The results of the evaluation for the single slab are shown in **Fig. 6.13**. For simpler representation and better comparison of the cooling pile slabs (15, 14 and 7) at the three different locations, comparison of cooling profiles will be illustrated in a separate diagram for the three different slabs at the same location. Cooling profiles of the pile slabs (15, 14 and 7) at the upper surface center, edge and corner are presented in **Figs. 6.14 - 6.16**, respectively. As expected, slabs in the middle of a pile (slab 7), especially in center slab regions, will show slower cooling rates due to slab reheating coming from the slab center or/and by the contact to other slabs that will slow down the cooling process. This effect will be less in slab 15 (top slab of the pile). The highest cooling rate is expected to be in slab corners of single slab and slab 15, while the relatively slower cooling due to slab to slab contact and less available surface for convection radiation heat loss, will be observed in more central regions of the pile as illustrated by slab 7, especially in slab center.

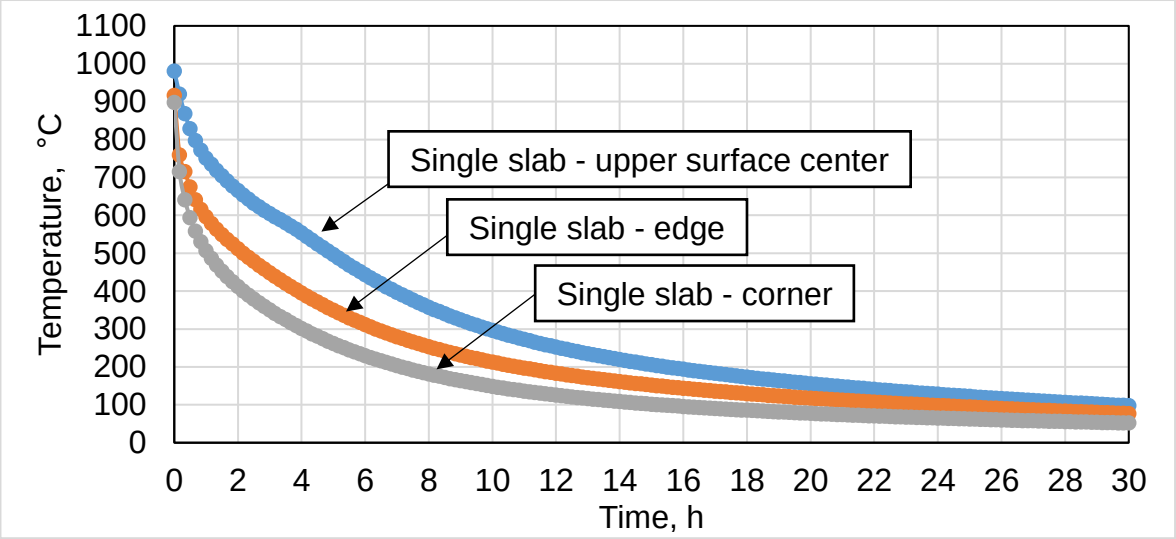

Fig. 6.13: Cooling profiles of single slab at corner, edge and upper surface center

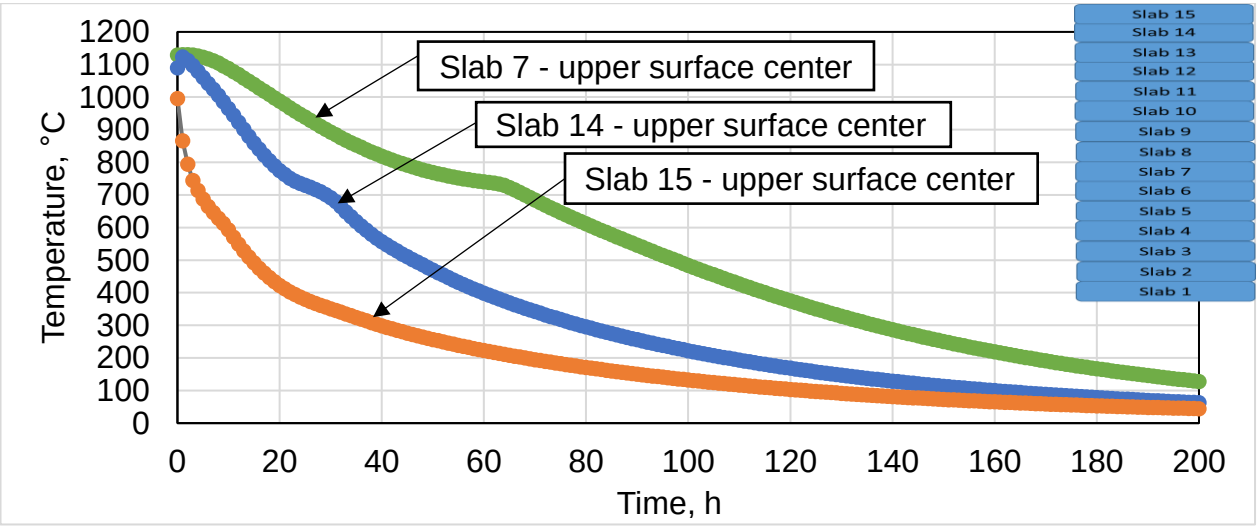

Fig. 6.14: Cooling profiles at the upper surface center of pile slabs 7, 14 and 15

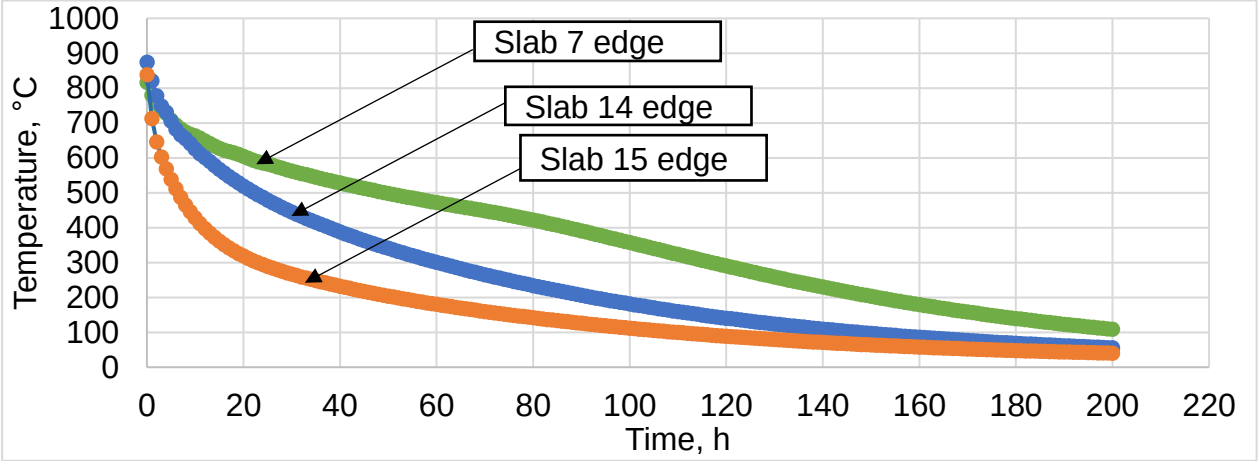

Fig. 6.15: Cooling profiles at the edge of pile slabs 7, 14 and 15

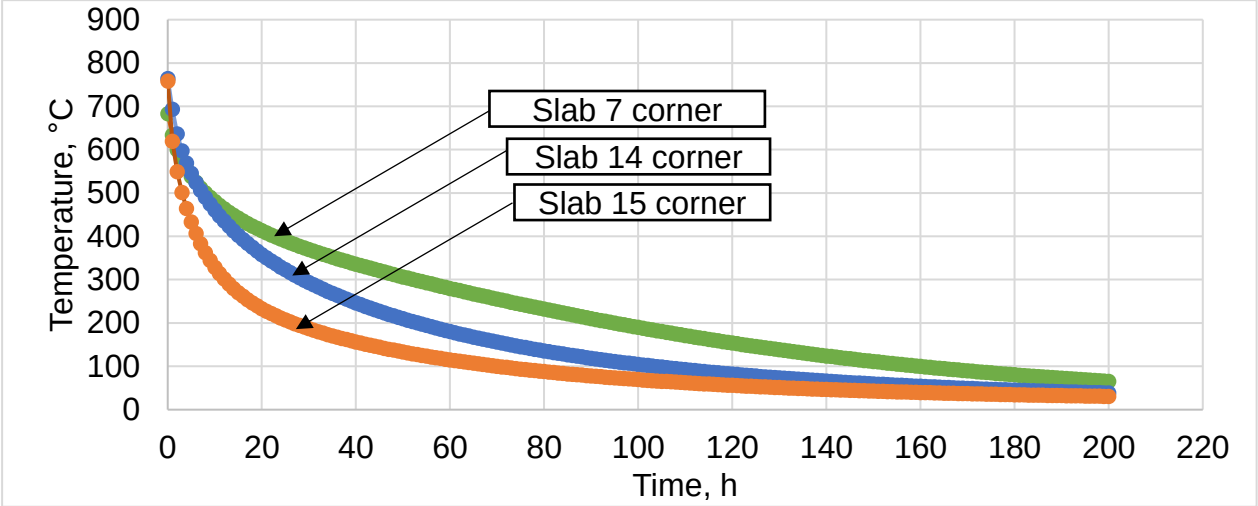

Fig. 6.16: Cooling profiles at the corner of pile slabs 7, 14 and 15

6.3 Evaluation of slab properties before charging

Using the ideal CC time-temperature profile (see **Fig. 5.6**: Ideal casting cooling cycle) followed by the three cooling rates of corner, edge and center of single slab cooling after casting (**Fig. 6.13**), dilatometry measurements were run to study the transformation behavior and formed phases at different slab regions. After cooling to room temperature, microstructure analysis was carried out to evaluate the amounts of phase constituents. Finally, hardness tests HV 20 were carried out. Transformation temperature results are evaluated after running 2 - 3 experiments for each cooling schedule.

6.3.1 Alloy-1 (micro-alloyed): single slab

For single slab cooling of Alloy-1 (C= 0.08%, Ti= 0.12%, Nb= 0.05%), a summary of the evaluation of the transformation temperatures, phase fraction calculation and hardness values (8-10 measurements/sample) is given in **Table 6.3**, while the transformation curves and the microstructure analysis are shown in **Figs. 6.17** and **6.18**, respectively.

Table 6.3: Phase transformation results of single slab, Alloy-1

Location in slab	Surface center	Edge	Corner
Transformation temperature, °C	Ferrite start 670	Bainite start 581	Bainite start 590
Phases fraction, %	49 ± 8 Ferrite 51 ± 8 Bainite	100 Bainite	100 Bainite
Hardness, HV 20	281 ± 7	284 ± 9	284 ± 6

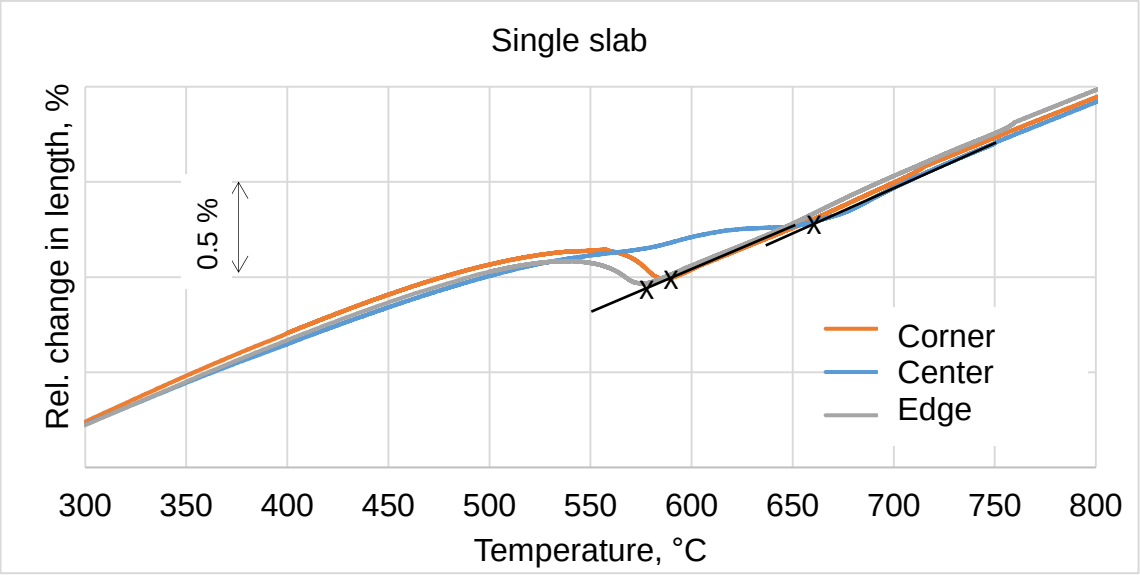

Fig. 6.17: Phase transformation curves of single slab at corner, edge and upper surface center, Alloy-1

Alloy-1: single slab upper surface center	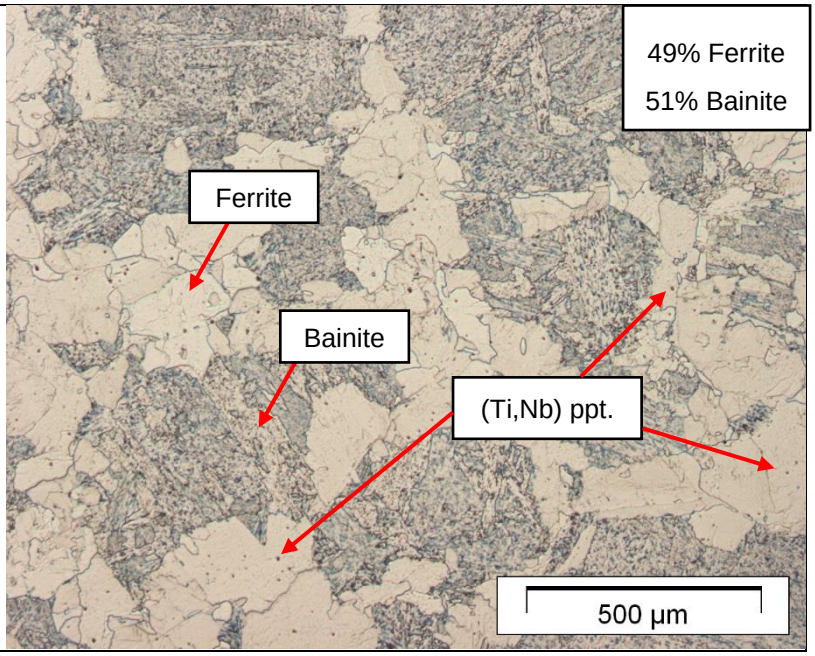

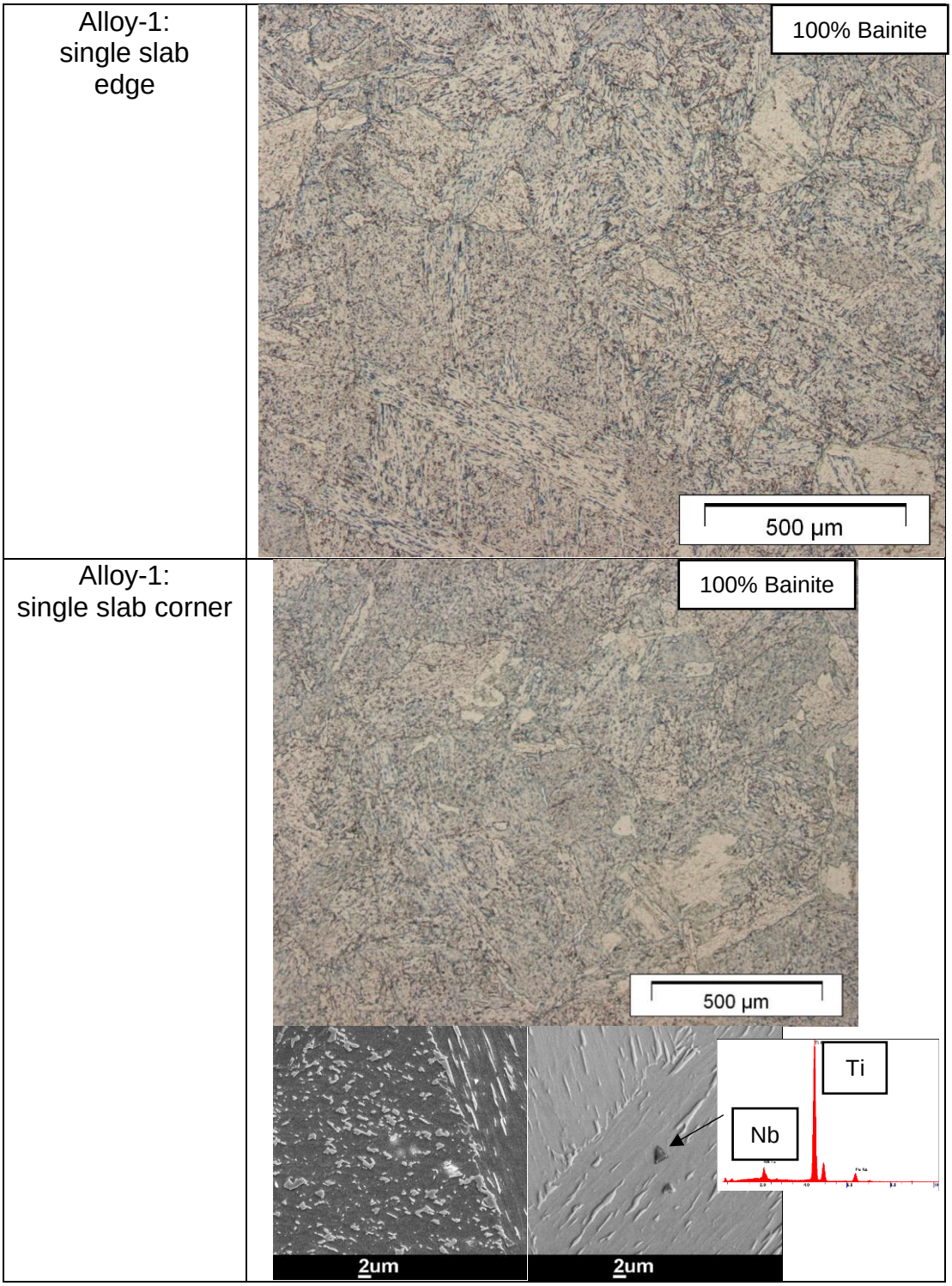

Fig. 6.18: Microstructure of single slab at upper surface center, edge and corner, Alloy-1

6.3.2 Alloy-1: pile slabs

The transformations at the three locations (corner, edge and center) of the slabs 14 and 15 in a 15 slab pile were evaluated. Summary of the results of the transformation analysis, phase fraction calculation and hardness testing (average of 8-10 measurements/sample) is shown **Table 6.4**. Transformation curves of slab 15, slab 14 and LOM microstructure analysis are shown in **Fig. 6.19, 6.20 and 6.21,** respectively.

Table 6.4: Phase transformation results of pile slabs 14 and 15, Alloy-1

Location in slab	Surface center slab 15	Edge slab 15	Corner slab 15
Transformation temperature, °C	Ferrite start 714	Ferrite start 687	Bainite start 592
Ferrite phase fraction, %	93 ± 3	79 ± 13	0
Hardness, HV 20	213 ± 8	270 ± 11	270 ± 8
Location in slab	Surface center slab 14	Edge slab 14	Corner slab 14
Transformation temperature, °C	Ferrite start 721	Ferrite start 725	Ferrite start 695
Ferrite phase fraction, %	90 ± 5	90 ± 3	87 ± 10
Hardness, HV 20	156 ± 6	201 ± 15	256 ± 9

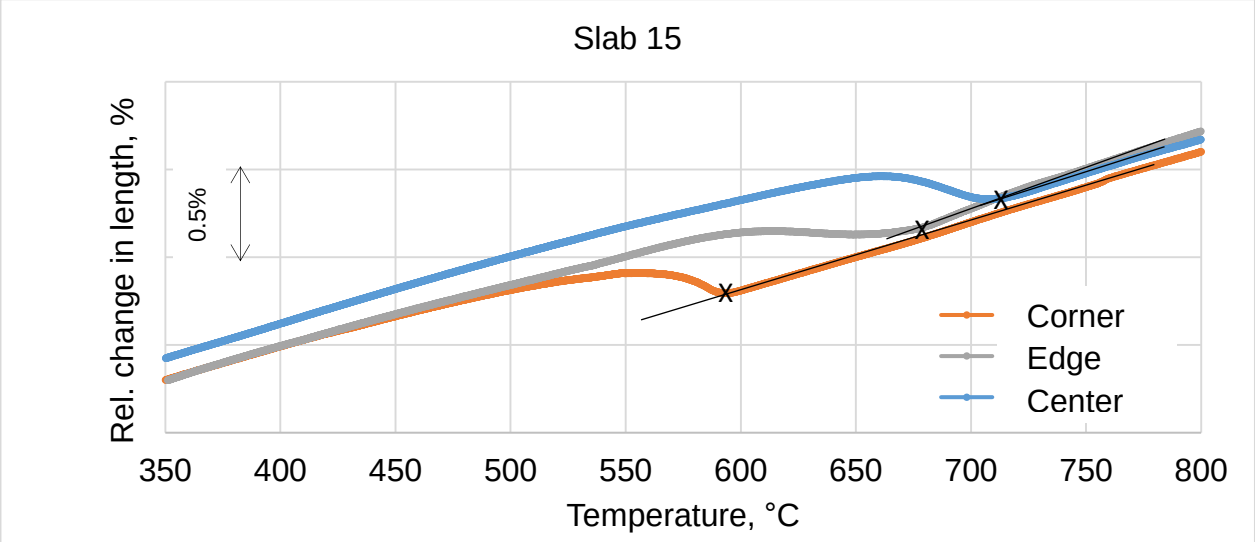

Fig. 6.19: Phase transformation curves of slab 15 at corner, edge and upper surface center, Alloy-1

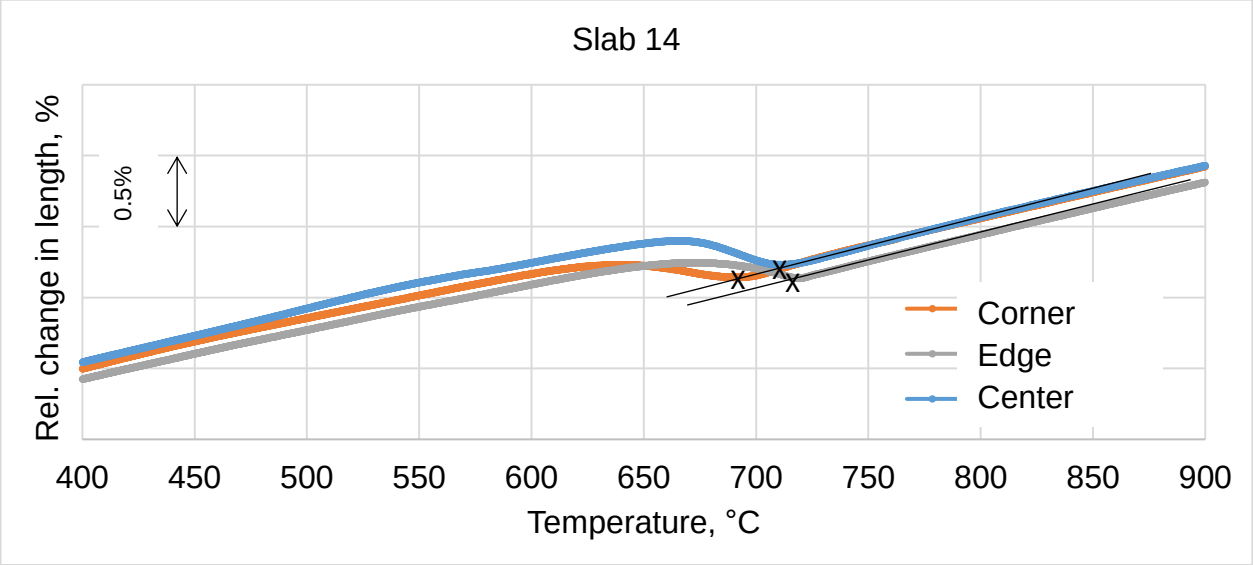

Fig. 6.20: Phase transformation curves of slab 14 at corner, edge and upper surface center, Alloy-1

The results of the three slabs (single slab, slab 14 and 15) in Route-3 pile were analyzed. It could be seen that the slow cooling for slab 14 results in a more homogenous ferrite/pearlite matrix - even in corner regions - with high ferrite content in all regions between 87 - 90% and lower hardness values (center: 156 HV 20, edge: 201 HV 20). This microstructure is expected for all slabs, placed below slab 14 in the stack/pile, as well as for slabs cooled following Route-2 (warm charging) in the box. This is based on the fact that the cooling rates of the slabs 1 to 13 (FEM 15 slabs model) as well as the box slabs (cooling in closed warm atmosphere) will always be slower than that of slab 14 under the same casting and delivery conditions.

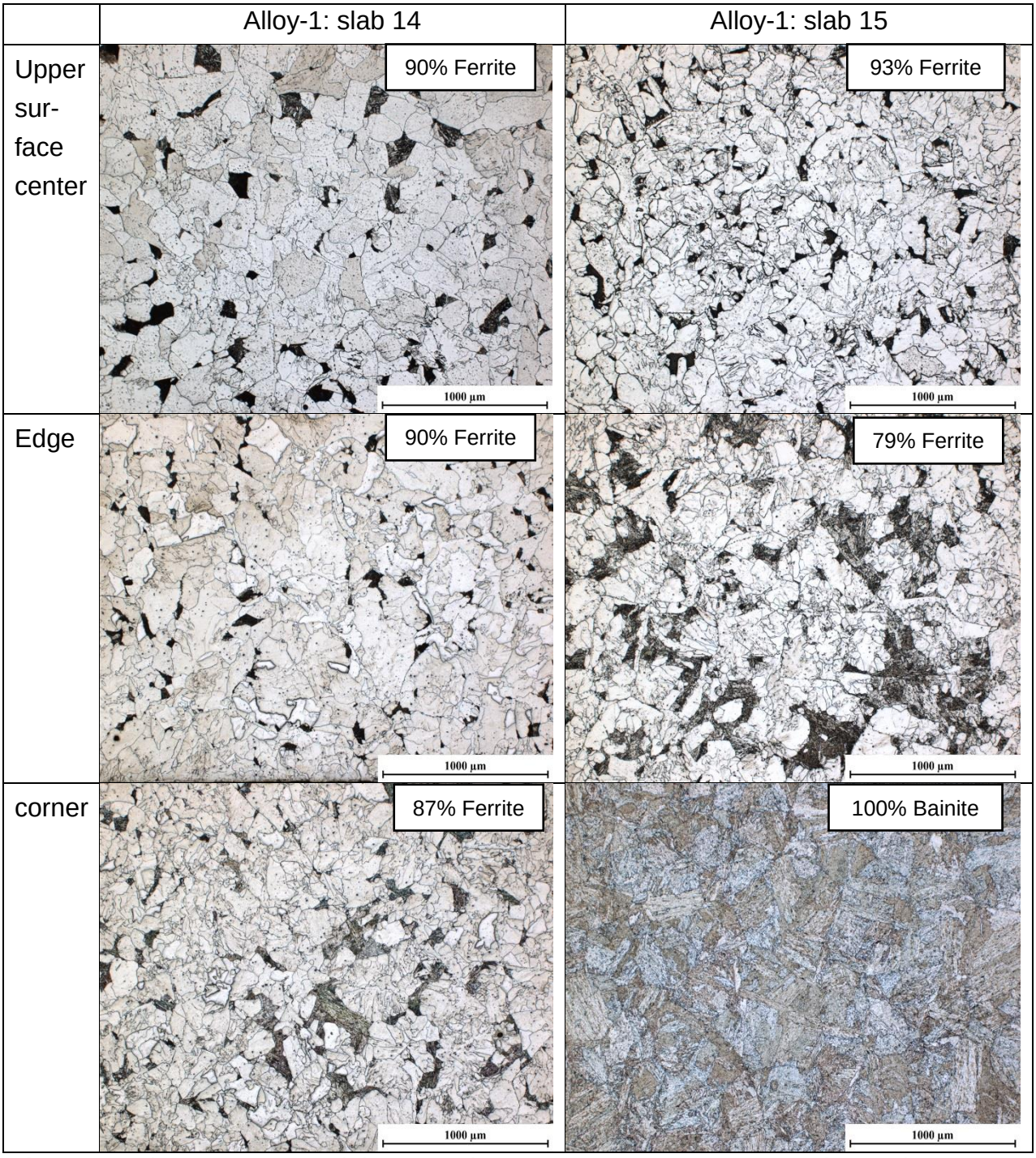

Fig. 6.21: Microstructure of slabs 14 and 15 at upper surface center, edge and corner, Alloy-1

On the other hand, slab 15 showed to have less (at center/edge) or no (at corner) ferrite content on the slab surface due to a higher cooling rate - in comparison to slab 14 - and lower transformation temperature, which resulted in higher hardness values (213 - 270 HV 20). As expected, the single slab (relatively faster cooling) gave the lowest ferrite content in the slab center (49%) compared to slab 14 (90%) and slab 15 (93%). Bainite was formed all over the corners and edges of the single slab and in 51% of the central region resulting in higher hardness values (281 - 284 HV 20). The fine precipitates did not allow the relatively small ferrite content to reduce the average hardness as the precipitates increase the matrix hardness.

The slab cooling rate strongly affects the precipitation distribution in the matrix and defines the phase constitutes to be formed, which consequently influences the mechanical properties of the slab before charging. This could be clearly observed in the hardness results. The boundary regions between a hard and soft phase will possibly be regions of low embrittlement where cracking can start. Generally, a relatively harder slab surface (high content of bainite or/and fine precipitates) means less overall ductility and higher cracking risks. To generate a significant value that represents the sum up of the properties of the slab before charging, more precise values regarding the whole surface hardness is needed which carries both the influence of phase structure and effect of precipitations. To calculate the overall average hardness of the slab surface before charging, Abaqus was used to calculate the average hardness values between the measured points (corner, edge and surface center) in a slab quarter before applying slab symmetry to screen the hardness over the complete slab surface. A linear relation between the measured points was assumed and an average hardness value was calculated from 1232 nodes/points on the slab surface.

Figs. 6.22 - **6.24** illustrate the hardness distribution on the slab's full upper surface area for the single slab, slab 15 and 14, respectively. The calculated average hardness of the whole slab upper surface is shown in each diagram.

Fig. 6.22: Hardness distribution of single slab upper surface, Alloy-1

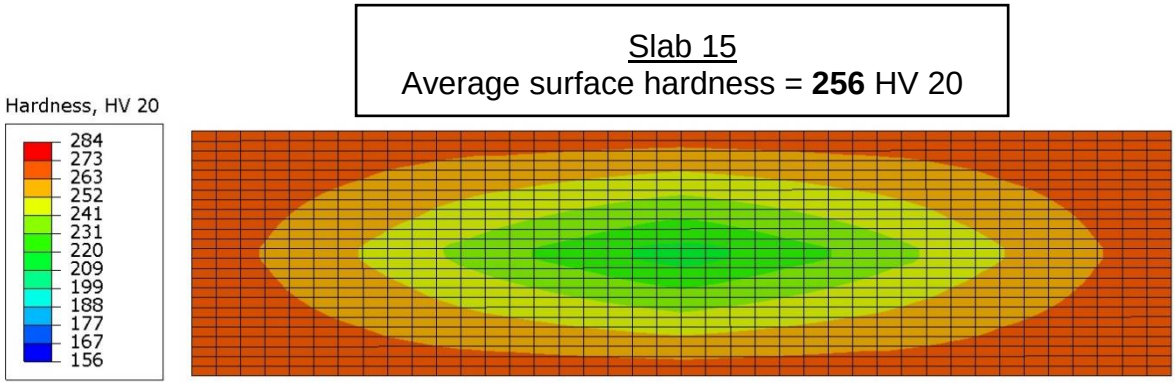

Fig. 6.23: Hardness distribution of slab 15 upper surface, Alloy-1

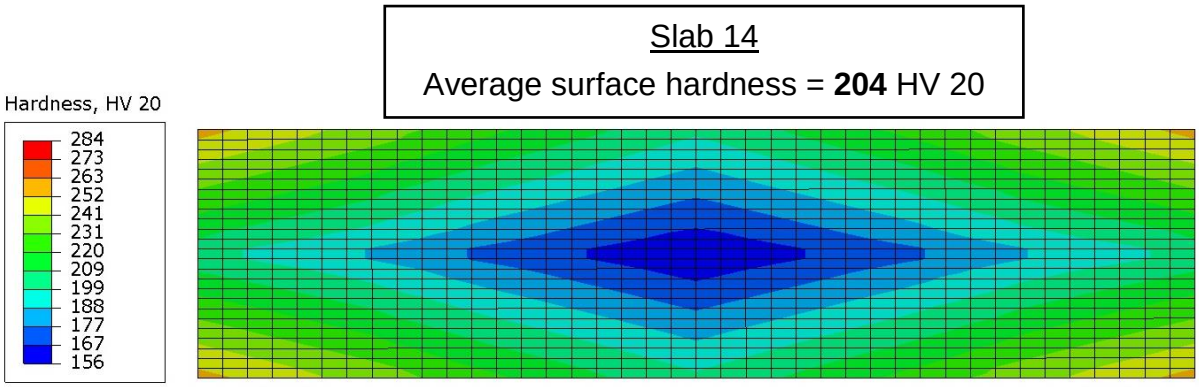

Fig. 6.24: Hardness distribution of slab 14 upper surface, Alloy-1

It could be seen from the top view of the slabs surfaces that for Alloy-1 the average hardness before charging differs clearly based on the slab route and position in the pile. This could explain many cases of slab cracking in the reheating furnace after slab history analysis carried out in **Chapter 2**. Now it is obviously important to study the conditions leading to higher surface hardness.

The average hardness values for the single slab, slab 15 and slab 14 were 283, 256 and 204 HV 20, respectively. The higher hardness could result from martensite or bainite formation, which means that slab charging should take place before the temperature of hard phase transformation is reached. This requires the knowledge of the chemical composition of each steel grade and if it will result in bainite or martensite transformation under the cooling procedure of the handling routes or not. Another reason for the higher hardness even in a ferrite/pearlite matrix is the precipitation of fine carbonitrides, which increases the matrix hardness and ceases grain growth and dynamic recovery. Slabs with homogenous ferrite/perlite matrix with relatively coarse precipitates are less likely to have cracking problems.

The bainite transformation was studied earlier in this section for the different handling routes. Furthermore, the effect of the same cooling practices/rates should be studied in terms of precipitation formation in the ferrite/pearlite matrix. The objective is to find out which ranges of particle size and matrix phases are formed under each condition and to compare/link it to the hardness values. Finally, comparing these results to the statistical

analysis will enable better understanding to the cracking cases and defining safe processing conditions. To study these effects, MatCalc precipitation modelling was used to study the influence of cooling rates on particle sizes in slab 14 and slab 15. Further investigations were carried out by SEM.

6.3.3 Alloy-1: MatCalc precipitation modelling

The effect of three different cooling rates (corner, edge, and center) on precipitates sizes was modelled using MatCalc 6. **Table 6.5** shows a summary of the TiN mean radius, hardness values for slab 14 and 15 at corner, edge and center regions. **Fig. 6.25** shows the three cooling profiles of slab 15 and the corresponding particle size of primary and secondary TiN. It could be observed that for slab center, relatively high particle size (average mean radius= 109 nm) was formed which corresponds to the hardness value of 213 HV 20, while at slab corner and edge, an average particle size of 18 nm resulted from the precipitation model, which corresponds to the hardness value of 270 HV 20 at both locations.

Table 6.5: TiN mean radius and hardness results of pile slabs 14 and 15, Alloy-1

	Corner		Edge		Surface center	
	TiN mean radius, nm	Hardness, HV 20	TiN mean radius, nm	Hardness, HV 20	TiN mean radius, nm	Hardness, HV 20
Slab 14	31	256	80	201	257	156
Slab 15	18	270	18	270	109	213

The corner will have the highest hardness anyway, either due to the formation of harder phases such as bainite/martensite, low ferrite content, or due to the fine particle size precipitates because of the relatively higher cooling rate. The fine precipitates of 18 nm in slab 15 edge and corner are considered to be below the critical size and therefore at risk for susceptibility to cracking. Small precipitates and hard phases such as bainite/martensite will result in hardness values above the critical limit, which means that such areas of the slab are particularly more prone to cracking. For comparison, the same simulation was run for slab 14 and the results were compared in **Table 6.5**.

The cooling profile and the corresponding primary and secondary mean radius of TiN in slab 14 are shown in **Fig. 6.26**. Slab 14 exhibits relatively high particle sizes of TiN (edge: 80 nm, center: 257 nm) which gave relatively low hardness values (edge: 201 HV 20 center: 156 HV 20) compared to slab 15. The particle size at the corner of slab 14 was relatively small (31 nm), this explains the high hardness (256 HV 20) in spite of the ferrite/pearlite matrix. The overall average hardness values of slab 15 and 14 were shown in **Fig. 6.23** and **6.24**, respectively. The results confirm that higher hardness values resulted whenever the precipitates are finer (smaller in mean radius), where the values of the hardness results are in an inversely proportional relationship with the precipitates particle size calculated by MatCalc simulation model.

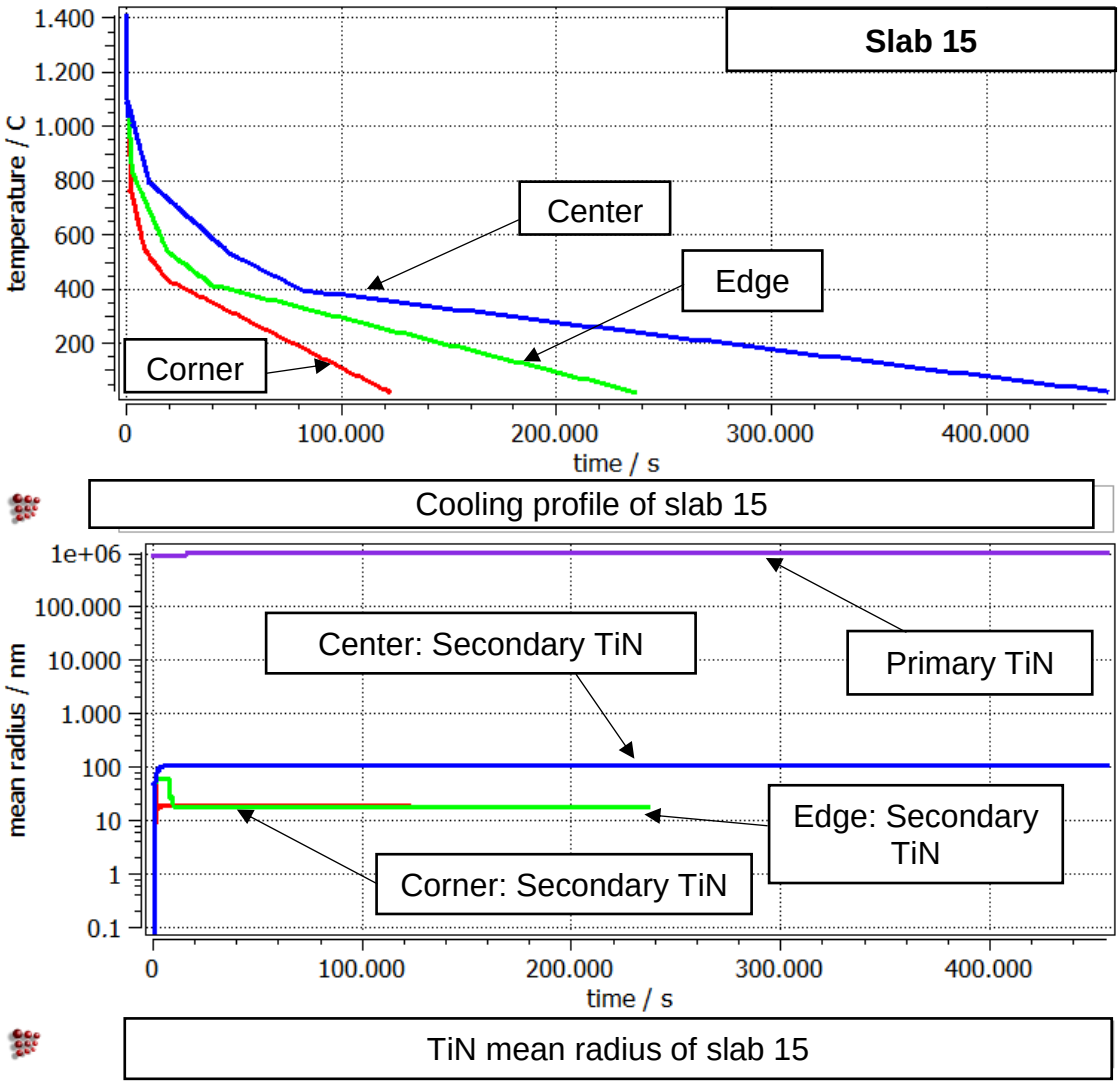

Fig. 6.25: Cooling profiles of slab 15 surface (upper surface center, edge and corner) and the corresponding mean radius of TiN by MatCalc, Alloy-1

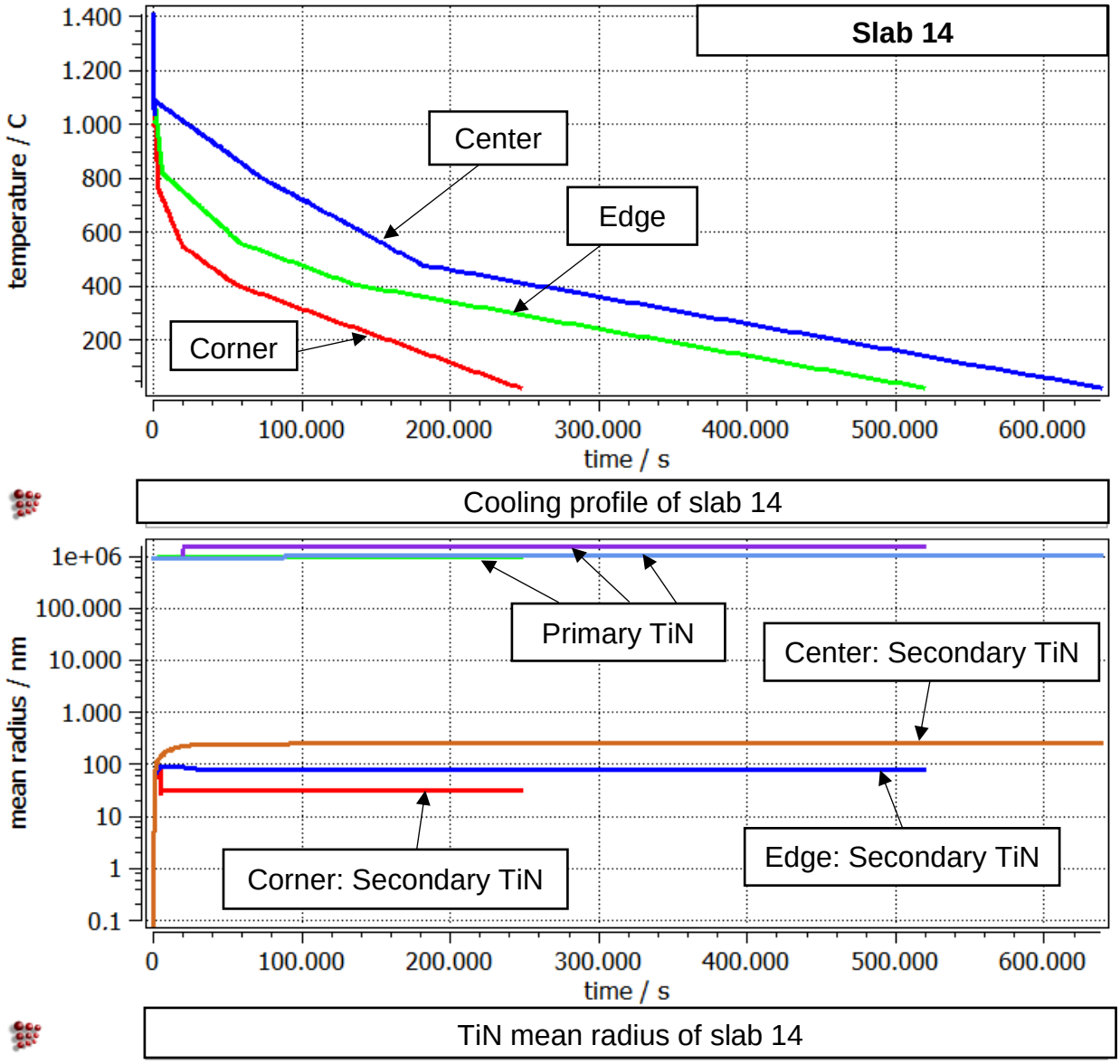

Fig. 6.26: Cooling profiles of slab 14 surface (upper surface center, edge and corner) and the corresponding mean radius of TiN by MatCalc, Alloy-1

The edge regions contributes strongly to the average surface hardness and play an important role in slab cracking during reheating or rolling. A comparison between edge particle sizes for slab 14 and 15 is shown in **Fig. 6.27**. The mean radius of secondary TiN at the edge regions of slab 15 is 18 nm, while it is 80 nm for the edge of slab 14.

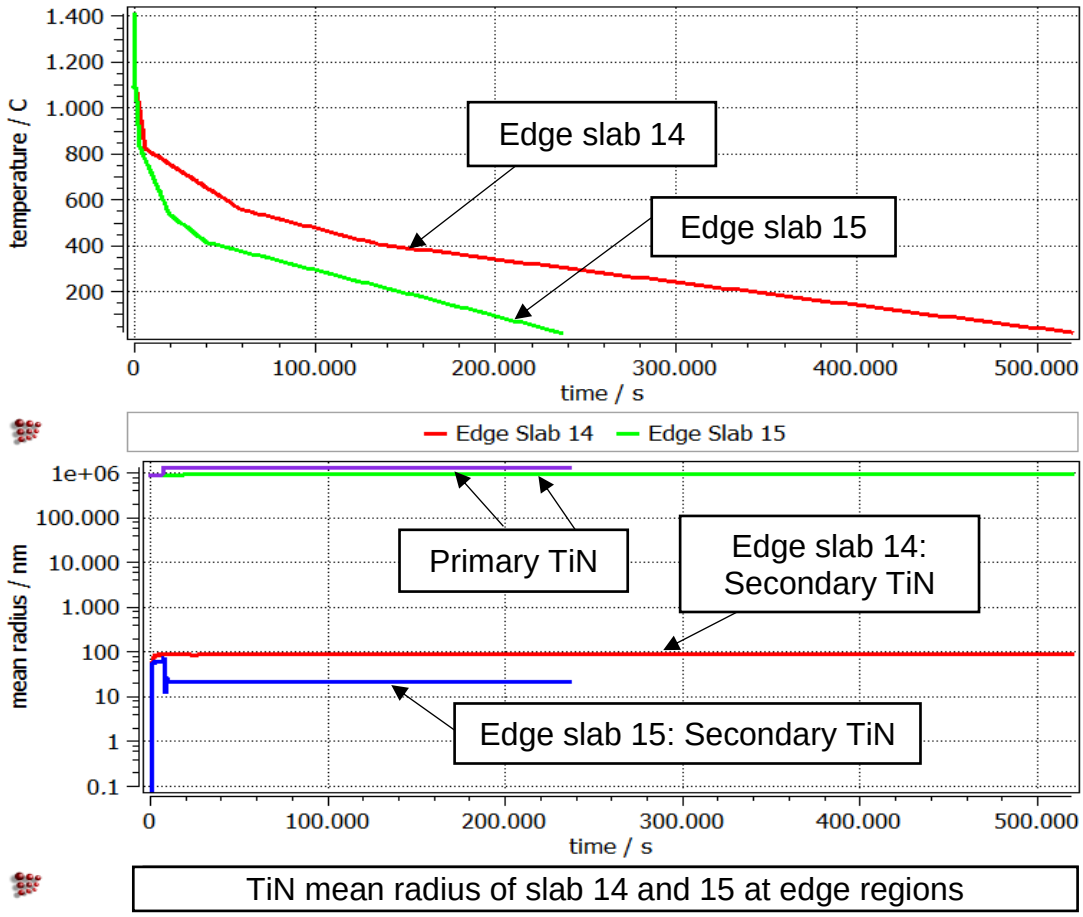

Fig. 6.27: Comparison between the cooling profiles and the corresponding TiN mean radius in the edge regions of slab 14 and 15 surfaces by MatCalc, Alloy-1

6.3.4 Alloy-1: SEM evaluation

The sample of slab 15 center was further investigated by SEM to measure the particle size and compare it with the results of the MatCalc model. As shown in **Fig. 6.25**, the average mean radius of primary TiN precipitates was 1 µm, while for the secondary TiN grew up to 109 nm. The sizes of approx. 1000 particles in the ferrite/perlite matrix of the sample were analyzed in different parts of the sample using SEM. An example is shown in **Fig. 6.28.** Traces of particle arrays could be observed following a certain order, which is believed to have nucleated on the austenite or prior austenite grain boundaries. The evaluation of 1000 particles of primary and secondary TiN precipitates resulted in an average mean radius of 276 nm, where the size range was observed to vary between min. 30 nm and max. 3 µm showing good agreement with the average primary and secondary mean radius values resulting from the MatCalc simulation model. For other regions (corner/edge) in slab15, the observation of finer particles below 20 nm was limited by the available SEM device.

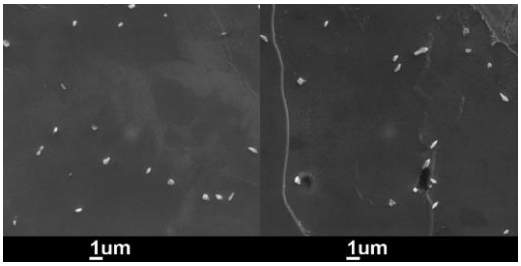

Fig. 6.28: Particle size analysis, pile slab 15 upper surface center, Alloy-1

Studying and comparing the microstructure of Alloy-1 samples in Route-1 after cooling once to 250 °C and once to RT showed that the microstructure at furnace charging will not differ in case of warm (250 °C) and cold charging (at RT) under the same cooling route. That was confirmed after comparing the microstructure constituents, grain size and the resulting hardness values in both cases on two different samples. On the other hand, the charging temperature might influence the transformation procedures during reheating inside the furnace and the corresponding stresses formation during reheating and phase transformation especially in the presences of TiN. The furnace reheating analysis needs further investigations.

6.3.5 Alloy-0 (no micro-alloying elements): single and pile slabs

For Alloy-0 (C= 0.08%), the single slab and pile slabs 14 and 15 all showed similar results for the different conditions. A comparison of the corner regions for the three slabs is introduced in this section. The summary of the evaluation of the transformation temperatures, phase fraction calculation and hardness testing is shown in **Table 6.6**. The transformation curves and the microstructure analysis are shown in **Figs. 6.29** and **6.30**, respectively.

Table 6.6: Phase transformation results at corner regions of single slab, pile slabs 14 and 15, Alloy-0

Alloy-0	Single slab corner	Slab 15 corner	Slab 14 corner
Ferrite start, °C	808	808	805
Ferrite phases fraction, %	92 ± 2	91 ± 2	92 ± 3
Hardness, HV 20	102 ± 4	92 ± 1	88 ± 2

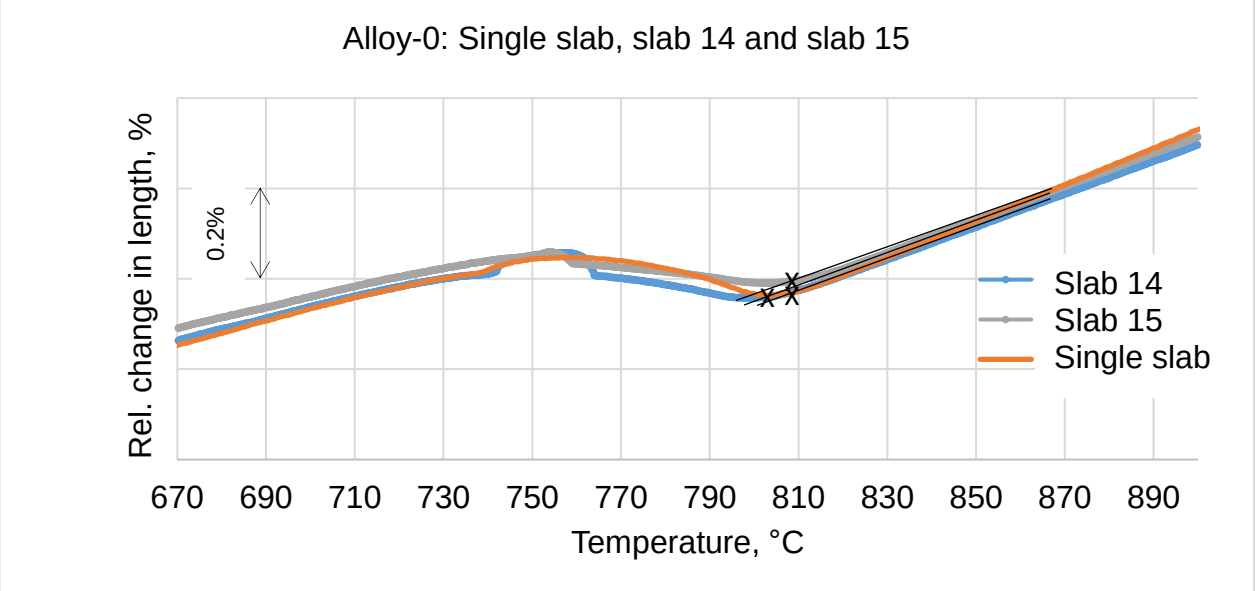

Fig. 6.29: Transformation curves at the corner of the single slab, pile slabs 14 and 15, Alloy-0

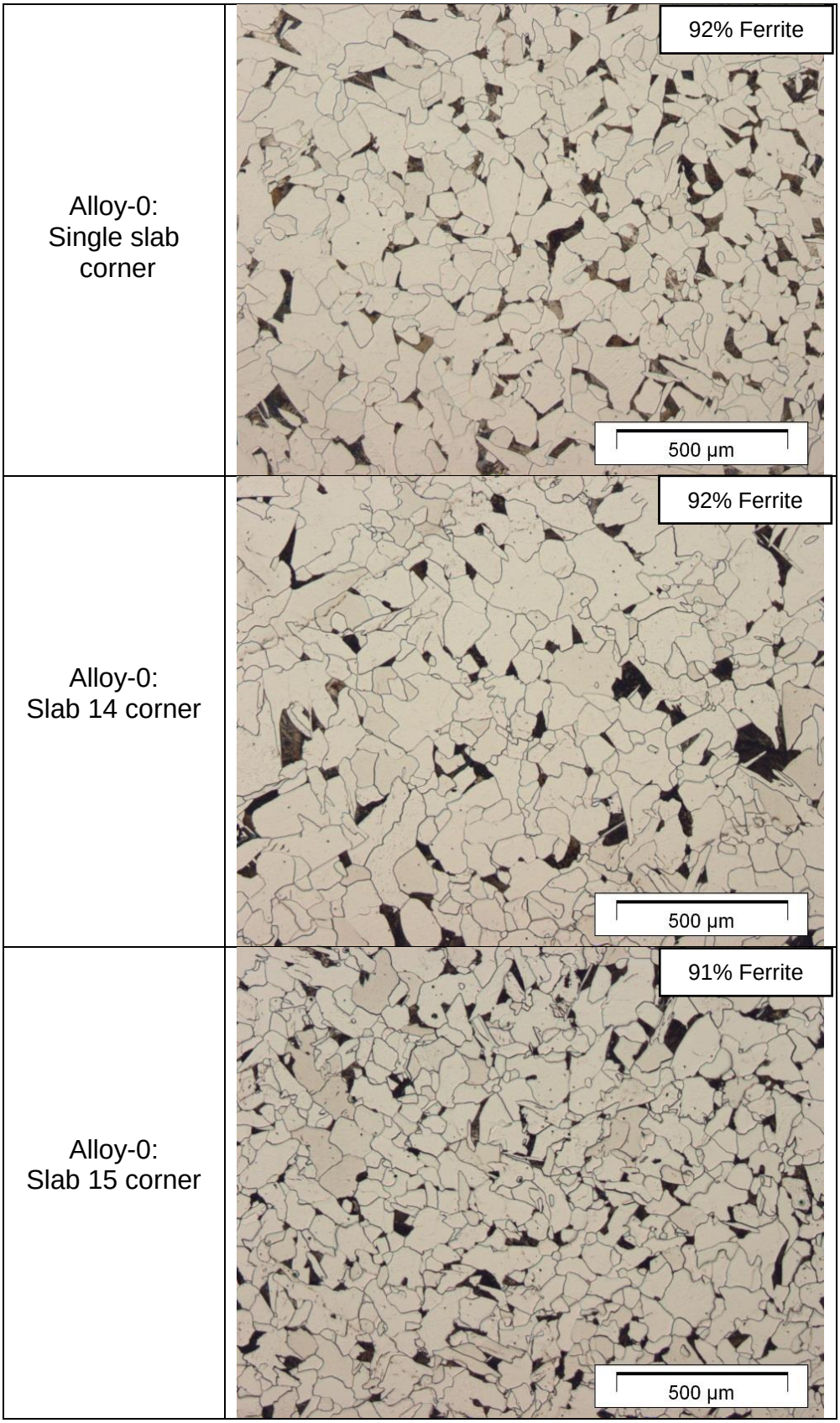

Fig. 6.30: Microstructure at the corner of the single slab, pile slabs 14 and 15, Alloy-0

This analysis for Alloy-0 shows that the measured ferrite start temperature of ≈ 807 °C, could be considered as the ferrite start temperature of the whole slab apart from its location or order in a pile. The results of Alloy-0 showed that the cooling rate and slab position during transportation and storage did not (locally) influence the microstructure or overall hardness. This is not the case for Alloy-1, where ferrite start is dependent locally on the slab region (corner, edge or center) and its order in the pile; in some cases, no ferrite will be formed. It can be concluded that if slabs of Alloy-0 leave the casting shop with no defects, most probably no further defects - due to fast slab cooling - will show up during handling and storage even by slab length adjustments and/or cold charging. While slabs of Alloy-1 should follow a especial treatment during handling and charging as a defect free CC process doesn't guarantee no further cracking by cooling in the slab stockyard or reheating in HSM. Recommendations for a safe slab handling process are mentioned in the next section.

6.4 Summary and conclusions

The analysis illustrated in this chapter represented a study on the phase transformation in steel slabs of two alloys (of same carbon content) by cooling after the casting shop, during transportation and storage procedure before charging into the HSM with focus on the stack/pile practice. The transformation temperatures and material properties before furnace charging were evaluated for Alloy-0 (no micro-alloying elements) and Alloy-1 (micro-alloyed). The routes of single slab, short pile slabs (Route-1) and 15 slabs stack/pile (Route-3) were studied. This gave a reasonable appraisal of the cooling and transformation trends for Route-2 (box slow cooling). The analysis included FEM modeling for cooling profiles evaluation - which was validated by measurements from stockyard -, dilatation testing on Dil805A, microscopic analysis by LOM, SEM and EDX, MatCalc simulation, and hardness testing. Parameters that strongly influence the crack sensitivity during storage until charging were studied in terms of phase distribution, precipitates sizes, hardness and charging temperature.

The microstructure and phase constituents before charging is strongly dependent on the cooling rates after casting which can locally differ inside the slab or from one slab to another based on its order in a pile and downstream condition. A higher cooling rate in case of single slab or the top slab in a pile can lead to bainite/martensite formation, less ferrite in a ferrite/perlite matrix and/or finer precipitates (<20 nm) in edge and corner regions, which are all reasons contributing to a higher cracking probability, defined by higher slab hardness (>250 HV 20). Alloy-1 slabs below slab 15 in a pile (slab 1 - 14) or slabs planned for storage in the box handling - Route-2 (very slow cooling) - will have a more homogenous ferrite/perlite distribution and coarser precipitates (>100 nm) and consequently less average surface hardness. Slabs with higher hardness values are believed to have higher embrittlement and higher risk of cracking.

Long slabs that should follow length adjustments procedures by cutting 1 - 2 m from the slab head - before further storage or charging - are exposed to higher cracking risk. Those slabs will cool for longer periods as single slabs and will join the planned pile relatively late, i.e. they had higher cooling rates. Once the undesired phase (as bainite) or precipitation particle sizes (below 20 nm) are reached, the slab will have a higher cracking probability even if warm charging above 250 °C was kept. According to the statistical analysis of the cracked slabs (**Chapter 2**), slabs with handling failure in the planned/designed route before charging represented 55% of the whole broken slabs, mostly had to go through a length

adjustments step, where faster cooling is expected to occur. Correlating the analysis of cracked slabs with the results of this chapter give the chance to explain failure causes of 55% of the cracked slabs. The detrimental effect of slab fast cooling of micro-alloyed steels similar to Alloy-1 could be confirmed by this work.

No difference could be detected in the materials properties or phase constituents before charging between the warm charging at 250 °C and cold charging at RT. However, it is believed that the charging temperature will play an important role in terms of reheating energy costs and the influence of heating rate on phase transformation procedures and precipitation kinetics during slab reheating in the HSM furnaces. The reheating practice inside the furnace strongly affects the reaustenitization process and the melting of certain precipitates. The statistical analysis confirmed that slabs of certain grades were broken (12% of all broken slabs) when cold charging was followed instead of the planned warm charging temperature over 250 °C. The situation/effects during furnace reheating and its influence on cracking is not presented in this document. Otherwise, this study confirms that slabs that followed the casting and handling rules including the set route and charging temperature were not recorded to produce cracks during hot rolling, which means that avoiding cracking/breakage in the reheating furnace or during hot rolling could be secured if certain guide/rules for casting and handling are set and followed.

The transportation and handling routes between the CS and HSM and their effect on phase constituents and slab properties before charging were studied/simulated in this chapter. The critical conditions that are believed to be the causes of the undesired phase as bainite/martensite, fine precipitates and high slab hardness before charging were discussed and evaluated, the following recommendations/notes can be made:

Alloy-1:

- For Route-1, hot charging into the HSM should take place above the bainite transformation temperature of ~ 600 °C. Cooling rate higher than 65 K/h is considered to be critical.
- Slabs planned for direct hot charging should be cooled as slow as possible to avoid fine precipitation formation. Particle size < 20 - 30 nm is considered to be critical.
- If length adjustments cannot be avoided, cutting should take place with the lowest possible slab temperature loss and as fast as possible (without slab damage), to avoid harder phases formation. Similar failure cases were recorded in the 55% of the broken slabs.
- If warm charging after a stack/pile cooling (Route-3) is planned, care should be given to the top slab in the pile, as it will have relatively low temperature.
- If warm charging after Box cooling (Route-2) is planned, care should be given to the charging temperature into the box. A delay in the box charging due to transportation delay or length adjustments, could already lead to hard phase formation before box charging. In this case, - even after slow cooling inside the box - the slab is still in cracking risk even by warm charging as long as the undesired phases and critical precipitates sizes were reached.
- Visual inspection for cracks before charging is recommended. In some cases, some transverse surface cracks could be detected by naked eye.
- Slabs with high cracking risk - according to the previous analysis - should be eliminated from the rolling schedule to avoid process break-down in case a “critical” slab is broken in the reheating furnace.

Alloy-0:

- Slabs of Alloy-0 (and similar alloys) are less likely to crack after a defect-free casting process, as the possible handling procedures will not result in critical phases or precipitation formation.
- It is advised that slabs of Alloy-0 (or similar) would be placed on the top of stacks/piles of Alloy-1 (or similar) in Route-1 and Route-3 procedures to ensure slow cooling of Alloy-1 slabs and avoid cracking risk of the top slab of the pile.

6.5 Slab ranking system, Alloy-1

After the previous analyses in **Chapter 5** and **6**, the slab properties of Alloy-1 during CC, handling and charging were evaluated and discussed. The results of the experimental work and simulations are showing four possible situations during casting and processing that would strongly influence the crack sensitivity of a slab during casting, transportation, storage and charging into the HSM. The classification of the four situations is based on two values. First, the hot ductility, representing the influence of casting conditions and straightening deformation on crack sensitivity. The lower the hot ductility value, the higher is the cracking risk. Secondly, the average/overall slab hardness after cooling, showing the influence of the cooling procedures during transportation and handling up to furnace charging on the material properties. The higher the average hardness value, the higher is the cracking risk. The classification of the four situations are summarized in **Fig. 6.31** and are explained as follows:

1. Best-case scenario

This is the case for most of the slabs, where casting conditions and handling procedures are kept according to the set values. Keeping the set values for both casting speed (~ 1 m/min) and secondary cooling will result in an acceptable deformation speed during the unbending in the desired temperature range between 950 – 1080 °C. This will result in high hot ductility values. After casting, slabs having low cooling rates during transportation and storage air cooling < 60 K/h will have a homogenous ferrite/pearlite structure before HSM furnace charging. Slabs produced under those best-case scenario conditions did not record any cracking problems according to the industrial study presented earlier.

2. Critical situation 1

Some slabs will follow the set casting conditions, having acceptable values of hot ductility, will suffer later from undesired cooling conditions in the storage area. Those slabs mostly have to go through slab length adjustment. Those slabs will go through higher cooling rates (> 65 K/h) in the stockyard, due to undesired slab position in a pile or delay in transportation and/or processing. This will result in higher hardness values of a slab by formation of hard phases and/or fine precipitates (size < 20 nm). Those slabs were recorded to have cracking problems in the HSM even when the casting process did not show any deviation from set conditions.

3. Critical situation 2

The other possible critical situation happens when a trouble takes place during CC that leads to deviations in crack-related parameters from the set values, while the handling and storage guidelines were kept according to the desired/planned procedure. The important parameters related to the cracking behavior are the casting speed, straightening temperature and cooling schedule. As a result of the deviation in the values of these parameters,

lower hot ductility values are reached. This will take place in this situation either by formation of fine precipitates < 40 nm, or by low temperature straightening < Ar_3 resulting in ferrite formation before or during the unbending zone deformation. Such slabs are mostly cracked/broken in the CC area and their casting should be followed by a slab surface inspection to check the presence of any unacceptable defects before further processing.

4. Worst-case scenario

Slabs with low hot ductility values < 40% (during CC) and high average hardness > 250 HV 20 (during slab cooling) are the most risky slabs to the HSM. Those slabs went through critical casting conditions where - in some cases - the formed cracks could not be visually detected. Afterwards, those slabs had another problem during handling and charging either due to slab length adjustments, fast cooling or cold charging. All these factors together lead to fine (Ti,Nb),(C,N) precipitates < 15 nm and formation of hard phases (bainite or martensite) before furnace charging. These results in the highest cracking possibility compared to all other situations representing the highest risk to the HSM. Those slabs should be removed from the rolling schedule. The properties of such slabs could be worse – in terms of crack sensitivity – in case of alloys with carbon content between ~ 0.08 - 0.17 % (peritectic range), high content of micro-alloying elements (Ti > 0.04% and Nb > 0.01%) and high N content > 0.004%.

Finally, each slab should have a value representing its crack sensitivity - proposed from the ranking system - according to its specific processing conditions and current material properties based on the previously explained experimental work, simulations and statistical analysis. The results of the slab ranking system are able to explain the findings of the industrial study and analyses of the slab histories of defected material. After applying the proposed slab-ranking model, based on the results discussed in this thesis, to the cracked/broken slabs and their melts covered in the industrial study, it could be shown that most of the defected slabs had high/critical crack sensitivity values. This is a strong indication that many of the cracked slabs could have been detected using the proposed approach with a very good chance to avoid process interruptions in many situations, if some further guidelines and instructions are to be kept/followed. Further validation for different steel grades is in progress.

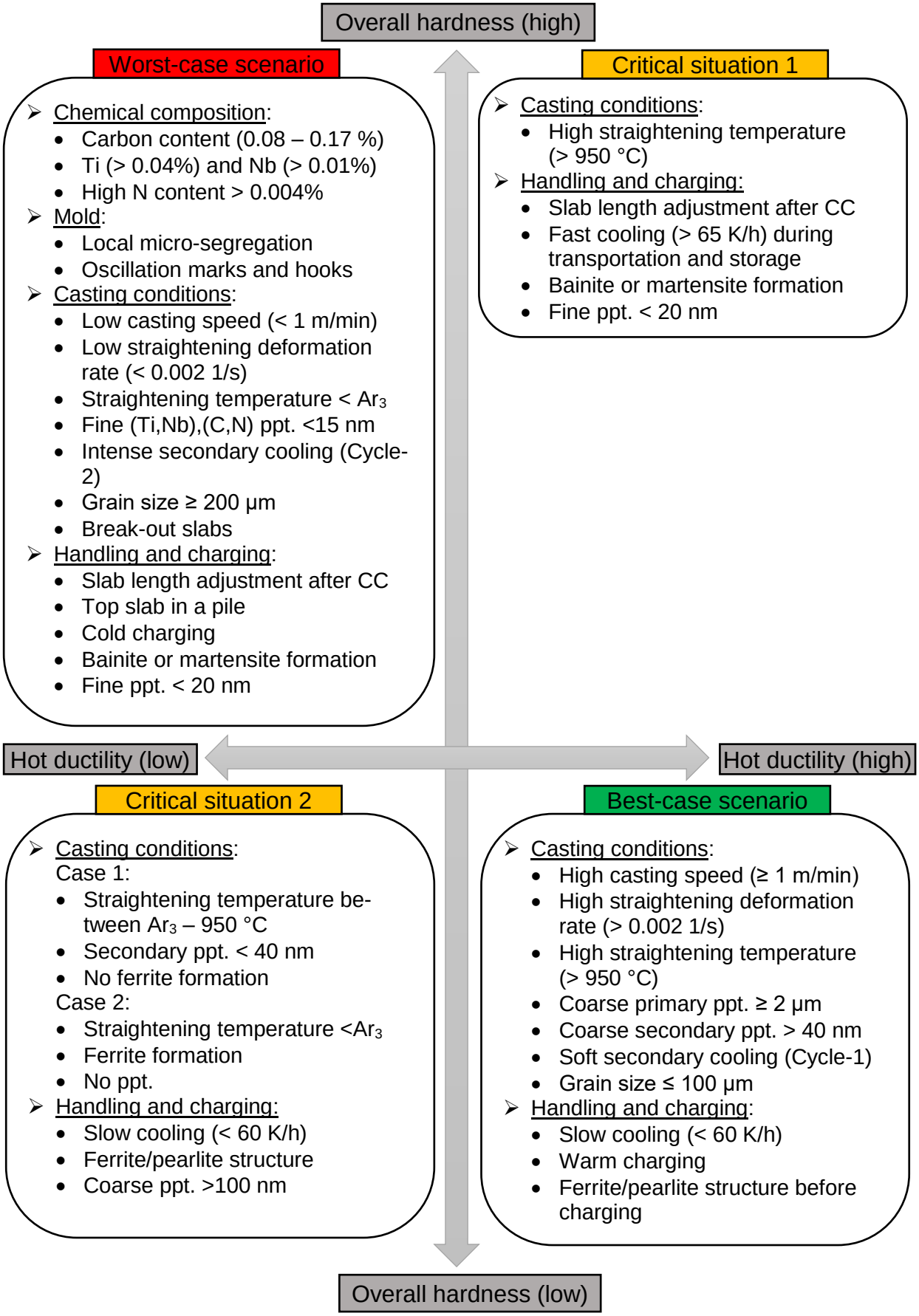

Fig. 6.31: Classification of processing situations influencing crack sensitivity, Alloy-1

Chapter 7: Summary and outlook

The problem of slab transverse cracking is still a serious defect during steel processing, which costs the industry hundreds of millions of euros every year in a global scale beside the environmental and logistical issues. The main objective of this work was to study the reasons and mechanisms of the cracking behavior through an industrial and laboratorial approach and offer the steel producers a practical solution to predict material damage and process disturbance.

The statistical analysis of the melts of the cracked/broken slabs in the industrial study showed that the potential cracking factors could be classified in three groups (see **Table 2.1**, p. 16). The factors are representing deviations from set/ideal processing values during CC and/or slab handling between CS and HSM. Selected critical parameters of these three groups were the base of the experimental work and simulations done in this thesis.

Following the literature and the findings of the industrial study, oscillation marks, hooks and local micro-segregation of residual elements formed in the mold area are mostly the initial origin of cracks. When the strand surface is subjected to further stress after the mold exit – due to bulging, friction, phase transformation or unbending forces –, a crack might appear/propagate if the material is in an embrittlement state (low hot ductility regions) and unable to support the applied stresses. Deviation in casting speed and/or secondary cooling practices can result in a critical temperature range in the unbending zone and extending the embrittlement regions. This could be enhanced by different mechanisms, especially in the presence of micro-alloying elements. Ferrite formation before/during straightening, low straightening deformation rates, fine precipitates within the austenite grain boundaries, coarse austenite grain size and retardation of dynamic recrystallization are further causes for crack propagation and failure. Intergranular fracture, especially below the Ar_3 temperature, and/or the presence of fine (Ti,Nb),(C,N) are common in many failure cases.

The slab microstructure constituents and precipitation distribution are important aspects to consider before slab charging into the HSM reheating furnace. Hard/brittle phases - such as bainite - and internal stresses will result in high cracking tendency during handling and by cold charging. Volume shrinkage during reheating by ferrite transformation into austenite will result in large tensile stresses at the grain boundaries. Moreover, by insufficient slab reheating, undissolved coarse carbonitrides - still located on the austenite grain boundaries - might result in surface cracking during hot rolling due to the reduced thermal ductility. Generally, failure within the thin ferrite film and by grain boundary sliding (GBS) are the most common embrittlement mechanisms. Retardation of dynamic recrystallization and formation of precipitate free zone (PFZ) were also recorded in many cases.

The thesis presents characterization of the investigated alloys in the as cast condition using LOM, SEM and EDX, before their further process treatments. Afterwards, the effect of process deviations during CC on crack sensitivity after hot tensile testing and precipitation

simulation at different conditions was studied. Finally, the influence of the slab handling process is evaluated in terms of the effect of slab position during storage on slab microstructure and mechanical properties before charging.

According to the results of this work, a set of critical values for certain process parameters were defined as potential cracking causes leading to cracking situations, as was confirmed by the industrial study. The appearance of several simultaneous critical values is an indication of a higher cracking sensitivity. **Fig. 6.31** (p. 127) shows a list of critical parameters and values for Alloy-1 (micro-alloyed steel) classified according to their crack sensitivity. The best-case scenario represents the ideal case, where no cracks were recorded and includes potential improvement strategies to be applied in case of a critical situation during casting or slab transportation/handling appear. The lower the hot ductility of a slab during casting and/or the higher the average/overall hardness before HSM furnace charging are - due to bainite/martensite or fine precipitates formation -, the higher is the cracking risk. Reducing material loss, enhancing a smooth/uninterrupted production process and improving production efficiency are achieved by defining the critical situations leading to a high cracking risk and overcoming the occurrence of these critical situations in real production.

Slabs undergoing critical processing conditions during CC, transportation and storage should be removed from the rolling schedule to avoid slab breakage in the reheating furnace or cracking during the early rolling steps. In some cases, optimizing the charging/rolling schedule could be a solution for some slabs. Slab charging before reaching the critical transformation temperature of bainite (or martensite) under certain processing routes will avoid the formation of brittle phase structures and fine precipitates during handling. Slabs undergone critical casting condition, as break-out, should go through further quality check / visual surface inspection before charging.

The study of the cracking behaviour of both investigated steel grades (Alloy-0 & Alloy-1) is considered being the base for the extension to further critical grades. The presented approach was more focused on the casting and handling processes, but the developed models have to be tested on different chemical compositions. The effect of deviation in chemical composition of slabs (which might take place under undesired secondary metallurgy practice) is one of the important factors, not been covered in this thesis. The tolerance of chemical composition of an alloy resulting in acceptable results under certain conditions should get more focus in a further work by defining critical/uncritical tolerance ranges.

Chapter 8: Zusammenfassung und Ausblick

Das Problem der Querrissbildung in Brammen ist immer noch ein kritisches Moment bei der Stahlerzeugung und -verarbeitung, das die Industrie neben Umwelt- und Logistikproblemen weltweit jährlich Hunderte Millionen Euro kostet. Hauptziel dieser Arbeit war es daher, die Gründe und Mechanismen der Rissbildung und des Rissverhaltens durch einen industriellen und experimentellen Ansatz zu untersuchen und dem Stahlhersteller eine praktische Lösung zur Vermeidung von Materialschäden und Prozessstörungen anzubieten.

Die statistische Analyse der Industriestudie von Schmelzen, die durch gerissene / gebrochene Brammen auffällig wurden, zeigte, dass die potenziellen Einflussgrößen in drei Gruppen eingeteilt werden konnten (siehe **Tabelle 2.1**, S. 16). Die Größen repräsentieren Abweichungen von Soll- bzw. idealen Verarbeitungswerten während des Stranggießens und / oder vom Brammenhandling zwischen Strangguss und Warmwalzwerk. Ausgewählte kritische Parameter dieser drei Gruppen bildeten die Grundlage für die in dieser Arbeit durchgeführten experimentellen Untersuchungen und Simulationen.

Laut der Literaturrecherche und den Ergebnissen der Industriestudie sind Oszillationsmarken, Haken und lokale Mikroseigerungen von im Kokillenbereich gebildeten Restelementen meist der initiale Ursprung von Rissen. Wenn die Strangoberfläche nach dem Austritt der Gießkokille einer weiteren Belastung durch Ausbeulung, Reibung, Phasenumwandlung oder Biegekräften ausgesetzt wird, kann ein Riss auftreten oder sich ausbreiten, sofern sich das Material in einem Zustand reduzierter Duktilität befindet und nicht in der Lage ist, die vorhandenen Spannungen zu ertragen. Abweichungen in der Gießgeschwindigkeit und / oder in der Sekundärabkühlung können zu einem unerwünschten, kritischen Temperaturbereich in der Richtzone führen, sowie zu einer Verbreitung der Versprödungsbereiche. Dieser Zustand kann durch verschiedene Mechanismen, insbesondere bei Gegenwart von Mikrolegierungselementen, verstärkt werden. Ferritbildung vor / während des Richtens, niedrige Umformgeschwindigkeiten beim Richten, feine Ausscheidungen an den Austenitkorngrenzen, grobe Austenitkorngröße und eine Verzögerung der dynamischen Rekristallisation sind Ursachen für die Bildung und Ausbreitung von Rissen und das Versagen durch diese. Ein intergranularer Bruch, insbesondere unterhalb der Ar_3-Temperatur und / oder bei Vorhandensein feiner (Ti,Nb),(C,N)-Ausscheidungen, ist Ursache vieler Versagensfällen.

Die Bestandteile der Mikrostruktur und die Ausscheidungsverteilung sind wichtige Aspekte, die vor dem Einsatz der Bramme im Wiedererwärmungsofen des Warmwalzwerks zu berücksichtigen sind. Harte bzw. spröde Phasen - wie Bainit - und innere Spannungen führen zu einer hohen Rissneigung während der Handhabung und beim Kalteinsatz. Eine Volumenschrumpfung während der Wiedererwärmung bei Umwandlung des Ferrits in Austenit

führt zu großen Zugspannungen an den Korngrenzen. Zudem können die ungelösten groben Karbonitride, die sich noch an den Austenitkorngrenzen befinden, bei unzureichendem Wiedererwärmen der Bramme während des Warmwalzens aufgrund der verringerten thermischen Duktilität zu Oberflächenrissen führen. Im Allgemeinen sind das Versagen innerhalb des dünnen Ferritfilms und das Gleiten der Korngrenzen die häufigsten Versprödungsmechanismen. In vielen Fällen wurde auch eine Verzögerung der dynamischen Rekristallisation und die Bildung von ausscheidungsfreien Zonen beobachtet.

Die Arbeit enthält die Charakterisierung der untersuchten Legierungen mit LOM, SEM und EDX im Gusszustand vor ihrer weiteren Prozessbehandlung. Anschließend wird die Auswirkung von Prozessabweichungen während des Stranggießens auf die Rissempfindlichkeit nach den Warmzugversuchen und der Ausscheidungssimulation unter verschiedenen Bedingungen analysiert. Schließlich wird der Einfluss des Brammenhandhabungsprozesses im Hinblick auf die Auswirkung der Brammenposition während der Lagerung und des Transports auf die Mikrostruktur und die mechanischen Eigenschaften der Bramme vor dem Ofeneinsatz untersucht und diskutiert.

Es konnten eine Reihe kritischer Werte für bestimmte Parameter als potenzielle Rissursachen definiert werden, die mit großer Wahrscheinlichkeit zu Rissbildungen führen, wie auch durch die Industriestudie bestätigt wurde. Das Auftreten kritischerer Werte ist ein Hinweis auf eine höhere Risswahrscheinlichkeit. **Abb. 6.31** (S. 127) zeigt eine Liste kritischer Parameter und Werte für Alloy-1 (mikrolegierter Stahl), klassifiziert nach ihrer Risssensibilität. Das Best-Case-Szenario stellt den Idealfall dar, in dem keine kritischen Risse auftreten, und enthält potenzielle Verbesserungsstrategien, die im Falle einer kritischen Situation während des Gießens oder des Transports beziehungsweise der Handhabung der Brammen anzuwenden sind. Je geringer die Warmdehnbarkeit (hot ductility) einer Bramme während des Gießens ist und / oder je höher die durchschnittliche Härte der abgekühlten Bramme - aufgrund der Bildung von Bainit / Martensit oder feinen Ausscheidungen - ist, desto höher ist das Rissrisiko. Ein reduzierter Materialausfall und damit ein reibungsloserer / nicht unterbrochener Produktionsprozess führt zu einer gesteigerten Produktionseffizienz und ist zu erreichen, indem die kritischen Situationen, die zu einem hohen Rissrisiko führen, definiert und deren Auftreten in der realen Produktion vermieden werden.

Brammen, die während des Stranggießens, des Transports und der Lagerung überkritischen Verarbeitungsbedingungen ausgesetzt waren, sollten aus dem Walzprogramm entfernt werden, um Brammenbruch im Wiedererwärmungsofen oder Risse während der ersten Walzstiche zu vermeiden. In einigen Fällen kann auch die Optimierung / Anpassung des Einsatzplans / Walzprogramms eine Lösung darstellen. Der Einsatz der Bramme vor Erreichen der kritischen Umwandlungstemperatur von Bainit (oder Martensit) unter bestimmten Verarbeitungsrouten vermeidet die Bildung einer spröden Phasenstruktur und feiner Ausscheidungen während der Handhabung. Brammen, die unter kritischen bzw. fehlerhaften Gießbedingungen gegossen wurden, wie Durchbruchereignisse beim Gießen, sollten vor dem Ofeneinsatz einer weiteren visuellen Oberflächeninspektion unterzogen werden.

Die Untersuchung des Rissverhaltens der gewählten beiden Stahlsorten (Alloy-0 und Alloy-1) wird als Grundlage für eine Ausweitung auf weitere kritische Sorten angesehen. Der vorgestellte Ansatz konzentrierte sich mehr auf die Gieß- und Handhabungsprozesse, jedoch sollten die entwickelten Modelle an verschiedenen chemischen Zusammensetzungen getestet und validiert werden. Der Effekt der Abweichung der chemischen Zusammensetzung von Brammen (z.B. bei unerwünschten Ereignissen in der Sekundär-Metallurgie) ist

einer der wichtigen Faktoren, die in dieser Arbeit nicht behandelt wurden. Die Toleranz der chemischen Zusammensetzung einer Legierung, die unter bestimmten Bedingungen zu akzeptablen Ergebnissen führt, sollte bei weiteren Arbeiten berücksichtigt werden, indem kritische und unkritische Toleranzbereiche definiert werden.

Bibliography

[1] M. L. Zappulla, “Mechanisms of longitudinal depression formation in steel continuous casting”, PhD Thesis, Colorado School of Mines, 2020.

[2] Tufte, “Correlations Genuine and Spurious in Pearson and Yule”, Statistical Science, vol. 10, no. 4, pp. 364-376, 2006.

[3] D. Crowther, “The effects of microalloying elements on cracking during continuous casting” , The Use of Vanadium in Steel - Proceedings of the Vanitec Symposium, Beijing, China, pp. 99-131, October 2001.

[4] B. Mintz and D. Crowther, “Hot ductility of steels and its relationship to the problem of transverse cracking in continuous casting”, International Materials Reviews, vol. 55, no. 3, pp. 168-196, 2013.

[5] K. Schwerdtfeger, “Metallurgie des Stranggießens : Gießen und Erstarren von Stahl”, 1992.

[6] K. Schwerdtfeger, “Rißanfälligkeit von Stählen beim Stranggießen und Warmumformen”, 1994.

[7] J. BRIMACOMBE and K. SORIMACHI, “Crack formation in continuous casting of steel”, Metallurgical Transactions B, pp. 489-505, September 1977.

[8] K. M. Banks, A. S. Tuling and B. Mintz, “Improved Simulation of Continuous Casting to Predict Transverse Corner Cracking in Microalloyed Steels”, International Journal of Metallurgical Engineering, vol. 2, no. 2, pp. 188-197, 2013.

[9] B. Mintz, “The Influence of composition on the hot ductility of steels and to the problem of transverse cracking”, ISIJ International, vol. 39, no. 9, pp. 833-855, 1999.

[10] B. G. Thomas, J. K. Brimacombe and I. V. Samarasekera, “The formation of panel cracks in steel ingots: a state of the art review”, ISS Transactions, vol. 7, pp. 7-20, 1986.

[11] B. Mintz and R. Abushosha, “Influence of vanadium on hot ductility of steel”, Ironmaking and steelmaking, vol. 20, no. 6, pp. 445-452, 1993.

[12] W. Lankford, “Some considerations of strength and ductility in the continuous casting process”, Metallurgical Transactions, vol. 3, pp. 1331-1357, June 1972.

[13] K. Schwerdtfeger and K.H. Spitzer, “Application of Reduction of Area–Temperature Diagrams to the Prediction of Surface Crack Formation in Continuous Casting of Steel”, ISIJ International, Vol. 49, No. 4, pp. 512-520, 2009.

[14] K. Xu and Brain G. Thomas, “Prediction of Grain Size, Precipitation and Crack Susceptibility in Continuous Casting”, Assoc. Iron Steel Tech., Warrendale, PA, Vol. 1, 2009.

[15] B. Thomas, “Continuous casting of steel”, Chapter 15 in Modeling for casting and solidification processing, pp. 499-540, 2001.

[16] S. Louhenkilpi, “Treatise on Process Metallurgy, Chapter 1.8: Continuous Casting of Steel”, Department of Materials Science and Engineering, Aalto University School of Chemical Technology, Espoo, Finland, 2014.

[17] E. HURTADO-DELGADO and R. D. MORALES, “Hot ductility and fracture mechanisms of a C-Mn-Nb-Al steel”, Metallurgical and materials transactions B, vol. 32B, pp. 919-927, October 2001.

[18] C. M. Chimani and K. Morwald, “Iron Steel Inst.”, Jpn. Int., vol. 39, pp. 1194-97, 1999.

[19] B. Mintz, J. R. Wilcox and D. N. Crowther, “Mater. Sci. Technol.”, vol. 2, pp. 589-94, 1986.

[20] A. Kundu, “Dissartation: Grain structure development during casting, reheating and deformation of Nb-microalloyed steel”, The University of Birmingham (UK), School of Metallurgy and Materials - College of Engineering and Physical Sciences, March 2011.

[21] M. C. Flemings and G. E. Nereo, “Macrosegregation-1”, Transactions AIME, vol. 239, no. 9, pp. 1449-1461, 1967.

[22] N. S. Pottore, C. I. Garcia and A. J. DeArdo, “Interrupted and isothermal solidification studies of low and medium carbon steels”, Metallurgical and Materials Transactions A, vol. 22, no. 8, pp. 1971-1980, 1991.

[23] L. P. Zhang, C. L. Davis and M. Stangwood, “Assessment of microstructural development during continuous casting of microalloyed bars”, Proc. Conf. on 'Thermomechanical processing of steels', pp. 764-775, 2000.

[24] A. J. Couch, “Grain growth and dissolution kinetics in high strength low alloy (HSLA) steels”, Ph.D Thesis, The University of Leeds, 2001.

[25] A. C. Kneissi, C. I. Garcia and A. J. DeArdo, “Characterisation of precipitates in HSLA steels”, Proc. 2nd Int. Conf. On ‘HSLA steels: processing, properties and applications’, (ed. G. Tither et al.), Baijing, China, TMS, Warrendale, pp. 99-105, 1992.

[26] E. Takeuchi and J. Brimacombe, “The formation of oscillation marks in the continuous casting of steel slabs”, Metallurgical Transactions B, vol. 15B, pp. 493-509, 1984.

[27] E. Takeuchi and J. Brimacombe, “Effect of oscillation-mark formation on the surface quality of continuously cast steel slabs”, Metallurgical Transactions B, vol. 16B, pp. 605-625, 1985.

[28] T. Emi, H. Nakato, Y. Iida, K. Emoto, R. Tachibana, T. Imai and H. Bada, “Influence of physical and chemical properties of mold powders on the solidification and occurrence of surface defects of strand cast slabs”, Proceedings of National Open Hearth and Basic Oxygen Steel Conference, vol. 61, pp. 350-361, 1978.

[29] J. Sengupta and B. G. Thomas, “Visualization of Hook and Oscillation Mark Formation Mechanism in Ultra-Low Carbon Steel Slabs During Continuous Casting”, JOMe (Journal of Metals – electronic edition), 2006.

[30] H.-J. Shin, B. Thomas, G. Lee, J. Park, C. Lee and S. Kim, “Analysis of Hook Formation Mechanism in Ultra Low Carbon Steel using CON1D Heat Flow - Solidification Model”, Materials Science & Technology, (New Orleans, LA, Sept. 26-29, 2004), TMS, Warrendale, PA, vol. II, pp. 11-26, 2004.

[31] J. Sengupta, B. Thomas, H. Shin, G. Lee and S. Kim, “Mechanism of Hook Formation during Continuous Casting of Ultra-low Carbon Steel Slabs”, Metallurgical and Materials Transactions A, vol. 37A, no. 5, pp. 1597-1611, 2006.

[32] J. Sengupta, H.-J. Shin, B. Thomas and S.-H. Kim, “Micrograph Evidence of Meniscus Solidification and Sub-Surface Microstructure Evolution in Continuous-Cast Ultra-Low Carbon Steels”, Acta Materialia, vol. 54, no. 4, pp. 1165-1173, 2006.

[33] K. Bo, G. Cheng, J. Wu, P. Zhao and J. Wang, “Mechanism of oscillation mark formation in continuous casting of steel”, Journal of University of Science and Technology Beijing, vol. 7, no. 3, pp. 189-92, 2000.

[34] K. Schmidt, F. Friedel, K. Imlau, W. Jager and K. Muller, “Consequent improvement of surface quality by systematic analysis of slabs”, Steel Research International, vol. 74, no. 11-12, pp. 659-666, 2003.

[35] J.-P. Birat, M. Larrecq, J.-Y. Lamant and J. Petegnief, “The continuous casting mold: A basic tool for surface quality and strand productivity”, Steelmaking Conference Proceedings, vol. 74, pp. 39-40, 1991.

[36] X. Zhang, W. Chen, W. Yang and L. Zhang, “Study on oscillation marks and hooks at the corner of continuous casting steel slabs”, The 7th International Congress on Science and Technology of Steelmaking, 2018.

[37] D. A. Porter and K. E. Easterling, “Phase transformations in metals and alloys”, 2nd edition, Chapman and Hall, London, 1992.

[38] M. C. Flemings, “Solidification Processing”, McGraw-Hill, New York, 1974.

[39] “Continuous casting of steel 1985 - A second study”, International Iron and Steel Institute, 1986.

[40] B. G. Thomas, “Modeling of the continuous casting of steel - past, present and future”, Electric furnace conf. Proc., vol. 59, pp. 3-30, 2001.

[41] A. Grill, J. K. Brimacombe and F. Weinberg, “Mathematical analysis of stresses in continuous casting of steel”, Ironmaking and steelmaking, vol. 3, no. 1, pp. 38-47, 1976.

[42] K. Sorimachi and J. K. Brimacombe, “Improvements in mathematical modelling of stresses in continuous casting of steel”, Ironmaking and steelmaking, vol. 4, pp. 240-245, 1977.

[43] S. Harada, S. Tanaka, H. Misumi, S. Mizoguchi and H. Horiguchi, “A formation mechanism of transverse crakcs on CC slab surface”, ISIJ International, vol. 30, no. 4, pp. 310-316, 1990.

[44] M. Hater et. al., “Results from a curved mould continuous casting machine making pipe and plate steel”, Open Hearth Proceedings, AIME, pp. 202-217, 1973.

[45] T. H. Coleman and J. R. Wilcox, “Transverse cracking in continuously cast HSLA slabs-influence and composition”, Mat. Sci. and Technol., vol. 1, pp. 80-83, 1985.

[46] X. Yang, L. Zhang, C. Lai, S. Li, M. Li and Z. Deng, “A Method to Control the Transverse Corner Cracks on a Continuous Casting Slab by Combining Microstructure Analysis with Numerical Simulation of the Slab Temperature Field”, Steel research, vol. 89, no. 5, 2018.

[47] T. Brune, D. Senk, R. Walpot and B. Steenken, Metall. Mater. Trans. B, vol. 46B, pp. 1400-08, 2015.

[48] X. G. Yang, L. F. Zhang, Y. Ren, S. S. Li and M. Li, Chin. J. Eng., vol. 38, p. 805, 2016.

[49] K. M. Banks, A. Tuling and B. Mintz, Mater. Sci. Technol., vol. 27, p. 1309, 2011.

[50] B. Steenken, J. L. L. Rezende and D. Senk, Mater. Sci. Technol., vol. 32, p. 567, 2016.

[51] B. Mintz, S. Yue and J. J. Jonas, “Hot ductility of steels and its relationship to the problem of transverse cracking during continuous casting”, Int. Mater. Rev., vol. 36, pp. 187-217, 1991.

[52] Y. Maehara, K. Yasumoto, H. Tomono, N. Tagamachi and Y. Ohmari, “Surface cracking mechanism of continuously cast low carbon low alloy steel slabs”, Mater. Sci. Technol., vol. 6, pp. 793-806, 1990.

[53] J. Calvo, A. Rezaeian, J. M. Cabrera and S. Yue, “Effect of the thermal cycle on the hot ductility and fracture mechanisms of a C–Mn steel”, Engineering failure analysis, vol. 14, pp. 374-383, 2007.

[54] M. Kvicala, A. Hendrych and K. Frydrysek, Acta Metallurgica Slovaca, vol. 20, no. 1, pp. 5-10, 2014.

[55] R. Misicko, M. Longauerova, M. Vojkto, J. Konradyova and S. A. Fedakova, “Effect of strain rate on hot ductility of low carbon steel”, Acta Metall. Slovaca, vol. 21, no. 2, 2015.

[56] A. Suzuki, Transaction of the iron and steel institute of Japan, vol. 25, no. 7, pp. 648-652, 1985.

[57] K. C. Ouchi, Transactions of the iron and steel institute of Japan, vol. 22, no. 3, pp. 181-189, 1982.

[58] H. Suzuki, S. Nishimura and S. Yamaguchi, Transaction of the iron and steel institute of Japan, vol. 22, no. 1, pp. 48-52, 1982.

[59] M. M. Wolf , Transaction of the iron and steel institute of Japan, vol. 24, no. 5, pp. 351-358, 1984.

[60] M. Vedani, D. Ripamonti, A. Mannucci and D. Dellasega, “Hot ductility of microalloyed steels”, 2008.

[61] N. A. McPherson and R. E. Mercer, “Continuous casting of slabs at BSC Ravenscraig Works”, Ironmaking and Steelmaking, pp. 167-179, 1980.

[62] S. Tanaka et. al., “Formation mechanism of surface cracks along the oscillation mark”, Trans. ISIJ, Vols. B-350, 1981.

[63] S. Saleem, M. Vynnycky and H. Fredriksson, “The influence of peritectic reaction/transformation on crack susceptibility in the continuous casting of steels”, Metallurgical and materials transactions B, no. 48B, pp. 1625-1635, June 2017.

[64] J. Miettinen, Metall. Trans. B, vol. 28B, pp. 281-97, 1997.

[65] J. Kristiansson, “J. Thermal Stresses”, vol. 5, pp. 315-30, 1982.

[66] M. El-Bealy and H. Fredriksson, Metall. Trans. B, vol. 27B, p. 999–1014, 1996.

[67] A. Jablonka, K. Harste and K. Schwerdtfeger, Steel Res., vol. 62, pp. 24-33, 1991.

[68] J. Konishi, M. Militzer, I. Samarasekera and J. Brimacombe, Metall. Trans. B, vol. 33B, p. 413–23, 2002.

[69] J. Brimacombe, F. Weinberg and E. Hawbolt, Metall. Trans. B, vol. 10B, pp. 279-92, 1979.

[70] J. Zou and A. Tseng, Metall. Trans. A, pp. 457-67, 1992.

[71] J. Miettinen, Scand. J. Metall., vol. 22, pp. 317-24, 1993.

[72] K. Hansson, PhD Dissertation, Royal Institute of Technology (KTH), Stockholm, Sweden, 2001.

[73] F. Hassani and S. Yue, “Detection of low hot ductility temperature zones in steels”, 34th MWSP conference proceeding, ISS-AIME, pp. 409-418, 1993.

[74] C. Adams, “Hot ductility and strength of strand cast steels up to their melting points”, Proceedings of Open Hearth Conference, vol. 54, pp. 290-302, 1971.

[75] F. Weinberg, “The ductility of continuously cast steel near the melting point - Hot tearing”, Metallurgical transactions B, vol. 10B, pp. 219-227, 1979.

[76] H. Suzuki, S. Nishimura and Y. Nakamura, “Improvment of hot ductility of continuously cast carbon steels”, Trans. ISIJ, vol. 24, pp. 54-59, 1984.

[77] J. Bailon and F. Weinberg, “Segregation at melted grain boundaries in steel”, Canadian Metallurgical Quarterly, vol. 19, pp. 251-257, 1980.

[78] A. Guillet, “Hot ductility and strength of five microallyoed steels in temperature range 800°C-Solidus”, Ph.D. Thesis, McGill University, 1989.

[79] G. A. Wilber et. al., “The effects of thermal history and composition on the hot ductility of low carbon steels”, Trans., vol. 6A, pp. 1727-1735, 1975.

[80] Y. Yasumoto et. al., “Effects of sulphur on the hot ductility of low carbon steel austenite”, Mat. Sci. and Technology, pp. 111-116, 1985.

[81] H. G. Suzuki et. al., “Embrittlement of steels occurring in the temperature range from 1000 to 600 °C”, Trans. ISIJ, pp. 169-177, 1984.

[82] J. R. Wilcox and R. W. K. Honeycombe, “Hot ductility of Nb and Al microalloyed steels following high temperature solution treatment”, Met. Technol., pp. 217-225, 1984.

[83] N. Bannenberg, B. Bergmann, H.-A. Jungblut, N. Müller and K. Reich, “Procedures for successful continuous casting of steel microalloyed with Nb, V, Ti and N”, Microalloying 95 conference proceedings, pp. 83-94, 1995.

[84] B. Mintz and J. M. Arrowsmith, “Hot ductility behaviour of C-Mn-Nb-Al steels and its relationship to crack propagation during the straightening of continuously cast strand”, Met. Technol., pp. 24-32, 1979.

[85] Suk-Chun Moon, “The influence of Austenite grain size on hot ductility of steels”, Thesis. University of Wollongong, 2003.

[86] L. H. Chown, “The influence of continuous casting parameters on hot tensile

behaviour in low carbon, niobium and boron steels", PhD thesis, University of Witwatersrand, Johannesburg, 2008.

[87] B. Patrick and V. Ludlow, "Development of Casting Practices to Minimise Transverse Cracking in Microalloyed Steels", Rev. Metall. - CIT, pp. 1081-1089, 1994.

[88] Y. Maehara, K. Yasumoto, H. Tomono, T. Nagamichi and Y. Ohmori, "Overview: Surface cracking mechanism of continuously cast low carbon low alloy steel slabs", Materials science and technology, vol. 6, no. 9, pp. 793-806, 1990.

[89] E. Turkdogan, Steelmaking Conf. Proc., I.S.S., vol. 70, pp. 399-415, 1987.

[90] S. Yue, J. Jonas and B. Mintz, 13th PTD Conf. Proc., pp. 45-52, 1995.

[91] A. Cowley, R. Abushosha and B. Mintz, Mater. Sci. Technol., vol. 14, pp. 1145-1153, 1998.

[92] J. Wilcox and R. Honeycombe, Mater. Sci. Technol., vol. 3, p. 849, 1987.

[93] E. Anelli, A. Mollo and A. Oulhadj, "Surface cracking and hot ductility of low-alloy steel blooms", 34th MWSP conference proceeding, ISS-AIME, pp. 399-407, 1993.

[94] E. Schmidtmam and L. Pleugel, "Influence of C content on high temperature strength and ductility of low alloyed steels after solidification", Arch. Eisenhuttenwes, vol. 51, pp. 49-54, 1980.

[95] G. Bernard, "Le role d la ductilite du metal solide dans la formation des defauts en coulee continue", Revue de Meallurgie-CIT, pp. 307-317, 1980.

[96] Y. Maehara and Y. Ohmori, "The precipitation of AlN and NbC and the hot ductility of low carbon steels", Materials science and engineering, vol. 62, pp. 109-119, 1984.

[97] H. Suzuki, S. Nishimura and S. Yamaguchi, "Physical Simulation of The Continuous Casting of Steels", Proc. Conf. on Physical Simulation Techniques for Welding, Hot forming and Continuous Casting,Canmet, Ottowa, 1988.

[98] B. Mintz and S. Yue, "The Hot Tensile test For Assessing the Likelihood of Transverse Cracking During Continuous Casting of Steel", 34th Mechanical Working and Steel Processing Conference, pp. 391-398, 1992.

[99] Y. Maehara, K. Yasumoto, Y. Sugitani and K. Gunji, Trans. Iron Steel Inst. Jpn., vol. 25, pp. 1045-1052, 1985.

[100] K. Carpenter, "The influence of microalloying elements on the hot ductility of thin slab cast steel", PhD Thesis - University of Wollongong, 2004.

[101] B. Mintz and J.-R. Banerjee, "Influence of C and Mn on hot ductility behaviour of steel and its relationship to transverse cracking in continuous casting", Materials science and technology, 2009.

[102] B. Mintz, R. Abushosha and M. Shaker, "Influence of deformation ferrite, grain boundary sliding and dynamic recrystallisation on hot ductility of 0.1-0.75% C steels", Materials science and technology, vol. 9, no. 10, pp. 907-914, 1993.

[103] D. Crowther and B. Mintz, "Influence of carbon on hot ductility of steels", Materials science and technology, vol. 2, no. 7, pp. 671-676, 1986.

[104] Alberto Espinosa Ruiz, "Prevention of transversal corner cracking in continuous casting of micro-alloyed steels", Thesis - Aolto University, 2014.

[105] B. Mintz, “Influence of nitrogen on hot ductility of steels and its relationship to problem of transverse cracking”, Ironmaking and Steelmaking, vol. 27, no. 5, pp. 343-347, 2000.

[106] D. Karjalainen, H. Kinnunen and H. Porter, “Hot ductility of certain microalloyed steels under simulated continuous casting conditions”, Mater. Sci. Forum Vols, Vols. 284-286, pp. 477-484, 1998.

[107] B. Mintz and J. Arrowsmith, “Influence of Microalloying Additions on Hot Ductility of Steels”, Hot Working and Forming Processes, The Metals Society, pp. 99-103, 1980.

[108] J. Fu, “Hot Ductility of Continuously Cast Microalloyed Steels”, Processing, Microstructure and Properties of High Strength, Low Ally Steels,Pittsburgh, pp. 27-38, 1987.

[109] K. Banks, A. Tuling, C. Klinkenberg and B. Mintz, “Influence of Ti on hot ductility of Nb containing HSLA steels”, Materials science and technology, vol. 27, no. 2, pp. 537-545, 2011.

[110] R. Abushosha, S. Ayyad and B. Mintz, “Influence of cooling rate and MnS inclusions on hot ductility of steels”, Materials Science and Technology, vol. 14, pp. 227-235, 1998.

[111] R. Abushosha, R. Vipond and B. Mintz, “Influence of sulphur and nibium on hot ductility of as cast steels”, Materials science and technology, vol. 7, no. 12, pp. 1101-1107, 1991.

[112] J. Ma, G. Wen, P. Tang, X. Yu, J. Li, G. Xu and F. Mei, “Causes of transverse corner cracks in microalloyed steel in vertical bending continuous slab casters”, Ironmaking & Steelmaking, vol. 37, no. 1, pp. 73-79, 2010.

[113] C.-E. Muller, “Precipitation during continuous casting”, PhD thesis - Technischen Universität Berlin, 2015.

[114] J. Davis and Davis & Associates, Eds, “High-Strength Low-Alloy Steels”, Alloying understanding the basics, ASM International, 1st ed., pp. 121-255, 2001.

[115] Z. Mohamed, “Hot ductility behavior of vanadium containing steels”, Material science and engineering, vol. 326, pp. 255-260, 2002.

[116] R. Lagneborg, T. Siwecki, S. Zajac and B. Hutchinson, “The Role Of Vanadium In Microalloyed Steels,Stockholm, Sweden”, 1999.

[117] B. Patrick, M. Short, R. Walmsley, B. Barber, K. Harste, K.-H. Tacke and I. Steinert, “Crack prevention in continuous casting,Luxembourg”, 1998.

[118] D. Mclean, “Grain boundaries in metals”, Oxford University Press, 1957.

[119] S. Seo, K. Asakura and K. Shibata, Iron Steelmaker, pp. 51-55, 1997.

[120] N. Yoshida, O. Umezawa and K. Nagai, ISIJ Int., vol. 43, no. 3, pp. 348-357, 2003.

[121] B. Mintz and R. Abushosha, “Effectiveness of hot tensile tests in simulating straightening in continuous casting”, Materials science and technology, vol. 8, no. 2, pp. 171-177, 1992.

[122] D. Crowther and B. Mintz, “Influence of grain size on hot ductility of plain CMn steels”, Materials science and technology, vol. 2, no. 9, pp. 951-955, 1986.

[123] V. Kutumba Rao, D. M. R. Taplin and P. Ramo Rao, Metall. Trans., vol. 6A, pp.

77-86, 1975.

[124] J. Fu, C. I. Garcia and S. Pytel, “Processing, microstructure and properties of HSLA steels”, Metallurgical Society of AIME, vol. 27, 1988.

[125] C. Ouchi and K. Matsumoto, Trans. Iron Steel Inst. Jpn, vol. 22, p. 181, 1982.

[126] C. M. Sellars, “Hot working and forming processes”, The Metals Society, vol. 3, 1980.

[127] D. Crowther and B. Mintz, “Influence of grain size and precipitation on hot ductility of microalloyed steels”, Materials science and technology, vol. 2, no. 11, pp. 1099-1105, 1986.

[128] S. Zamberger, M. Pudar, K. Spiradek-Hahn, M. Reischl and E. Kozeschnik, “Numerical simulation of the evolution of primary and secondary Nb(CN), Ti(CN) and AlN in Nb-microalloyed steel during continuous casting”, International Journal of Materials Research, vol. 103, no. 6, pp. 680-687, 2012.

[129] M. Lückl, O. Caliskanoglu, S. Ilie, J. Six and E. Kozeschnik, “Impact of Surface Structure Control Cooling During Continuous Casting on Hot Ductility of Microalloyed Steel”, Steel Research International, vol. 7, pp. 871-879, 2016.

[130] R. Radis and E. Kozeschnik, “Kinetics of AlN precipitation in microalloyed steel”, Modeling and simulation in materials science and engineering, vol. 18, no. 5, 2010.

[131] L. Yang, Y. Li, Z.-l. Xue and C.-g. Cheng, “Influence of Ti(C,N) precipitates on austenite growth of micro-alloyed steel during continuous casting”, Modeling of casting and solidification processes, vol. 14, no. 5, pp. 421-428, 2017.

[132] E. K. Shin, “Hot ductility of TWIP steels”, PhD Thesis - City University London, 2014.

[133] B. Mintz, R. Abushosha and J. Jonas, “Influence of dynamic recrystallization on the tensile ductility of steels in the temperature range 700 to 1150 °C”, ISIJ International, vol. 32, no. 2, pp. 241-249, 1992.

[134] B. Mintz, J. Lewis and J. Jonas, “Importance of deformation induced ferrite and factors which control its formation”, Materials science and technology, vol. 13, no. 4, pp. 379-388, 1997.

[135] J. Lewis, J. Jonas and B. Mintz, “The formation of deformation induced ferrite during mechanical testing”, ISIJ International, vol. 38, no. 3, pp. 300-309, 1998.

[136] W. Irving, “Continuous casting of steel”, I. O. M., pp. 1-120, 1993.

[137] M. Qingshen, J. Zhonghang, L. Wenbin, Y. Xiaoshan, L. Yan and X. Li, “Cause and Measures of Transverse Corner Crack in Hull Structural V-Containing Steel CC Slabs”, International Seminar on Application Technologies of Vanadium in Flat – Rolled Steels, pp. 75-78, 2005.

[138] S. Jansto, “Steelmaking and continuous casting process metallurgy factors incluencing hot ductility behavior of niobium bearing steels”, Brno, Czech Republic, 2013.

[139] R. Abushosha, S. Ayyad and B. Mintz, “Influence of Cooling Rate on Hot Ductility of C-Mn-Al and C-Mn-Nb-Al Steels”, Materials Science and Technology, vol. 14, pp. 346-351, 1998.

[140] R. Abushosha, O. Comineli and B. Mintz, “Influence of Ti on Hot Ductility of C-Mn-Al Steels”, Materials Science and Technology, vol. 15, pp. 278-286, 1999.

[141] R. Abushosha, R. Vipond and B. Mintz, “Influence of titanium on hot ductility of as cast steels”, Materials Science and Technology, vol. 7, pp. 613-621, 1991.

[142] L. Yang, L. Li, Z. Xue and C. Cheng, “Effect of Different Thermal Schedules on Ductility of Microalloyed Steel Slabs during Continuous Casting”, Metals, vol. 9, no. 1, p. 37, 2019.

[143] L. Cepeda, J. Rodriguez-Ibabe, J. Urcola and M. Fuentes, “Influence of dynamic recrystallisation on hot ductility of aluminum killed mild steel”, Materials Science and Technology, vol. 5, pp. 1191-1199, 1989.

[144] Brendan M. Connolly, “The effects of composition and thermal path on hot ductility of forging steels”, PhD Thesis, University of Pittsburgh, 2016.

[145] A. Yamanaka, K. Nakajima and K. Okmura, “Critical strain for internal crack formation in continuous casting”, Ironmaking and steelmaking, 1995.

[146] Y. Li, X. Chen, K. Liu, J. Wang, J. Wen and J. Zhang, “Reasonable Temperature Schedules for Cold or Hot Charging of Continuously Cast Steel Slabs”, METALLURGICAL AND MATERIALS TRANSACTIONS A, vol. 44A, pp. 5354-5364, 2013.

[147] Z. Xia, Z. Cao and D. Luo, J. Iron and steel research, vol. 22, no. 6, pp. 40-45, 2010.

[148] P. Sokolowski and B. Lindsley, Howard I. Sanderow Outstanding Technical Paper, 2009.

[149] T. Digges, C. Irish and N. Carwile, Part of the J. Res. Nat. Bur. Stand., vol. 41, pp. 545-74, 1948.

[150] J. Kirkaldy and D. Doane, “Hardenability Concepts with Applications to Steel”, TMS-AIME, Warrendale, PA, 1977.

[151] B. Bramfitt and J. Speer, Metall. Trans. A, vol. 21A, pp. 817-29, 1990.

[152] M. Schöbel, S. Großeiber, S. Ilie and G. Requena, “Experimental simulation of thermally induced stresses during cooling of continuously cast steel slabs”, Steel research international, vol. 87, no. 10, 2016.

[153] M. Torkar, Mater. Technol., vol. 44, no. 6, p. 327–33, 2010.

[154] C. Tercelli, Metall Plant Technol. Int., vol. 18, no. 1, pp. 69-71, 1995.

[155] A. Carboni, D. Ruzza and S. Feldbauer, Iron Steelmaker, vol. 26, no. 8, pp. 39-42, 1999.

[156] R. Giacomin, B. Webler and H. Yin, “A study on cracking mechanism of 3rd generation of advanced high strength steel slabs”, AISTech conference, Philadelphia, 2018.

[157] D. Stefanescu, Science and engineering of casting solidification, second edition, 2009.

[158] J. Dantzig and M. Rappaz, Solidification. Lausanne: EPFL Press, 2009.

[159] T. Kato, Y. Lto, M. Kawamoto, A. Yamanaka and T. Watanabe, “Prevention of slab surface transverse cracking by microstructure control”, ISIJ Int., vol. 43, no.

11, pp. 1742-1750, 2003.

[160] M. Kurban, U. Erb and K. Aust, “A grain boundary charachterization study of boron segregation and carbide precipitation in alloy 304 austenitic stainless steel”, Scr. Mater., vol. 54, pp. 1053-1058, 2005.

[161] J. Devletian, “Borocarbide precipitation in the HAZ of boron steel welds”, Weld. Res. Suppl., pp. 5-12, 1976.

[162] G. Xia, C. Fürst, J. Six, B. Harrer, A. Samoilov and A. Schiefermüller, “A study about mechanisms of transverse crack formation on continuous casting slab”, AISTech 2016 proc., pp. 2573-2584, 2016.

[163] E. Biro, J. Sengupta, M. Trinh, E. Dillon and D. Colbert, “Mechanism linking austenitic grain size to silver formation on hot rolled coils at arcelormittal dofasco”, Iron Steel Technol., vol. 10, no. 10, pp. 111-120, 2013.

[164] R. Giacomin and B. Webler, “Mechanisms advanced high-strength steel slab embrittlement”, 7th International Congress on Science and Technology of Steelmaking, 2018.

[165] “TA Instruments,” February 2020. [Online]. Available: https://www.tainstruments.com/products/dilatometers/quenching-dilatometers/.

[166] Metallographische Keramographisches Plastographische Ätzen von Günter Petzow, 6. Auflage Ätzmittel Fe m1, 1994, p. 115.

[167] Metallographische Keramographisches Plastographische Ätzen von Günter Petzow, 6. Auflage; Ätzmittel Fe m8, 1994, p. 116.

[168] Abaqus 6.11 documentation, “Getting Started with Abaqus”, Interactive Edition.

[169] C. Ouchi, “Hot ductility in Nb-bearing high strength low alloy steels”, 1981.

[170] Gleeble training book, p. 55.

[171] D. Posalaky and J. Lukacs, “Research of weldability with physical simulation”, Production processes and systems, vol. 5, no. 2, 2012.

[172] C. Pohle, “Zerstörende Werkstoffprüfung in der Schweisstechnik”, Deutscher Verlag für Schweisstechnik DVS-Verlag GmbH, 1990.

[173] S. T. Mandziej, “Physical Simulation of Metallurgical Processes”, Materiali in technologije / Materials and technology 44, pp. 105-119, 2010.

[174] Gleeble Users Training, “Gleeble Systems and Applications”, Dynamic Systems Inc., Poestenkill, New York. 08/07-Rev02, 2011.

[175] J. Li, B. Jiang, C. Zhang, L. Zhou and Y. Liu, “Hot embrittlement and effect of grain size on hot ductility of martensitic heat-resistant steels”, Materials science and engineering A, Vol. 677, pp. 274-280, 2016.

[176] B. Santillana, R. Boom, D. Eskin, H. Mizukami, M. Hanao and M. Kawamoto, “High-Temperature Mechanical Behavior and Fracture Analysis of a Low-Carbon Steel Related to Cracking ”, Metallurgical and Materials Transactions A, Vol. 43A, pp. 5048-5057, 2012.

[177] Y.M. Won, T.J. Yeo, D.J. Seol, and K.H. Oh, Metall. Mater. Trans. B, vol. 4B, 31, pp. 779–94, 2000.

List of figures

Fig. 2.1: Transportation routes of CSG from CS to HSM 13
Fig. 2.2: Broken slab in HSM reheating furnace (Furnace breakdown time: 5.5 h) 15
Fig. 2.3: Broken slab in the HSM stockyard 15
Fig. 2.4: Surface cracking after slab discharge from reheating furnace 17
Fig. 2.5: Surface cracking during roughing rolling 18
Fig. 2.6: Experimental work packages 19
Fig. 3.1: Schematic of steel continuous casting process [16] 20
Fig. 3.2: (a) Photograph of oscillation marks (OM) on the surface of an ultra-low steel Slab, and optical micrographs showing distinctly different features of (b) curved and (c) straight hooks adjacent to OMs [29,31,32] 23
Fig. 3.3: Complex phenomena occurring inside a continuous caster mold (right), influence initial solidification in the meniscus region (left) [29] 24
Fig. 3.4: Surface defects [3,39] 1. Transverse corner cracks; 2. Longitudinal corner cracks; 3. Transverse cracks; 4. Longitudinal cracks (broad face); 5. Star cracks; 6. Deep oscillation marks; 7. Pinholes; 8. Macro inclusions. 25
Fig. 3.5: Internal defects [3,39] 1. Internal corner cracks; 2. Side halfway cracks; 3. Centreline cracks; 4. Centreline segregation; 5. Porosity; 6. Halfway cracks; 7. Non-metallic inclusions, clusters; 8. Sub-surface ghost lines; 9. Shrinkage cavity; 10. Star cracks, diagonal cracks; 11. Pinholes; 12. Semi macrosegregation .. 25
Fig. 3.6: Factors affecting cracks on continuous cast slabs [46] 26
Fig. 3.7: Schematic illustration of types of ductility troughs [3] 28
Fig. 3.8: Schematic illustrations showing intergranular micro-void coalescence by deformation in the low temperature austenite region (a-c) and in the two phase γ-α region (d-f) [88] 31
Fig. 3.9: Schematic models showing formation of wedge cracks by GBS. Arrows indicate sliding boundary and sense of translation [90] 32
Fig. 3.10: Precipitates in SEM micrograph [128] 38
Fig. 4.1: Position of the received material in the slab 45
Fig. 4. 2: Dil805A cylindrical sample 46
Fig. 4.3: Dil805T flat tensile sample 46
Fig. 4.4: Device Dil805A/D/T 48

Fig. 4.5: Cylindrical sample in Dil805A [165] 48
Fig. 4.6: Flat tensile sample in Dil805T [165] 48
Fig. 4. 7: Location of as-cast samples in the received material 52
Fig. 4.8: As-cast microstructure (50X), Location-1, Alloy-1 52
Fig. 4.9: As-cast microstructure (500X), Location-1, Alloy-1 52
Fig. 4.10: As-cast microstructure (50X), Location-2, Alloy-1 53
Fig. 4.11: As-cast microstructure (50X), Location-3, Alloy-1 53
Fig. 4.12: As-cast microstructure 1 (1000X), Location-1, Alloy-1 53
Fig. 4.13: As-cast microstructure 2 (1000X), Location-1, Alloy-1 53
Fig. 4.14: As-cast microstructure, Alloy-1, Point-1 54
Fig. 4.15: EDX spectrum of Point-1 54
Fig. 4.16: As-cast microstructure, Alloy-1, Point-2 54
Fig. 4.17: EDX spectrum of Point-2 54
Fig. 4.18: Cracks in corner regions of the receive material, Alloy-1 54
Fig. 4.19: Corner microstructure in slab corner upper area, inner surface parallel to slab thickness section, Alloy-1 55
Fig. 4.20: Corner microstructure in slab corner central area, inner surface parallel to slab thickness section, Alloy-1 55
Fig. 4.21: As-cast microstructure, Location-1, inner surface parallel to slab thickness section, Alloy-1 56
Fig. 4.22: As-cast microstructure, Location-2, inner surface parallel to slab thickness section, Alloy-1 57
Fig. 4.23: As-cast microstructure, Location-3, inner surface parallel to slab thickness section, Alloy-1 57
Fig. 4.24: As-cast microstructure (50X), Location-1, Alloy-0 58
Fig. 4.25: As-cast microstructure (200X), Location-1, Alloy-0 58
Fig. 4.26: As-cast microstructure (500X), Location-1, Alloy-0 58
Fig. 4.27: As-cast microstructure (1000X), Location-1, Alloy-0 58
Fig. 4.28: Time - Temperature schedule to study austenite to ferrite transformation 59
Fig. 4.29: Austenite to ferrite transformation curve, Alloy-1 60
Fig. 4.30: Scheil solidification model, Alloy-0 60
Fig. 4.31: Scheil solidification model, Alloy-1 61
Fig. 4.32: Time - Temperature evaluation of the NST test, Alloy-1 62
Fig. 4.33: Relation between NST, liquidus and hot tensile test temperatures [171-174] . 63
Fig. 5.1: Temperature profile under ideal/set CC conditions 66
Fig. 5.2: Temperature profile during break-out (1/4) 67
Fig. 5.3: Temperature profile during break-out (2/4) 67
Fig. 5.4: Temperature profile during break-out (3/4) 68
Fig. 5.5: Temperature profile during break-out (4/4) 69

Fig. 5.6: Cycle-1 temperature profile during ideal/set casting conditions 70
Fig. 5.7: Cycle-2 temperature profile for Break-out-4 case..... 70
Fig. 5.8: Hot ductility of ideal casting vs break-out, Alloy-0 73
Fig. 5.9: Fracture surface after Cycle-1, Alloy-0..... 74
Fig. 5.10: Fracture surface after Cycle-2, Alloy-0..... 75
Fig. 5.11: Microstructure at 800 °C after Cycle-1, Alloy-0 76
Fig. 5.12: Microstructure at 800 °C after Cycle-2, Alloy-0 76
Fig. 5.13: Hot ductility of ideal casting vs break-out, Alloy-1 77
Fig. 5.14: Fracture surface after Cycle-1, Alloy-1..... 78
Fig. 5.15: Fracture surface after Cycle-2, Alloy-1..... 79
Fig. 5.16: Comparison of particle size and phase fraction between Model-1 and 2 81
Fig. 5.17: MatCalc Model-1 at 1080 °C, ideal casting, effect on particle size, Alloy-1..... 82
Fig. 5.18: MatCalc Model-1 at 800 °C, effect on particle size, Alloy-1..... 82
Fig. 5.19: MatCalc Model-1 at 700 °C (below Ar_3), effect on particle size, Alloy-1 83
Fig. 5.20: MatCalc Model-2 at 800 °C, effect on particle size, Alloy-1..... 83
Fig. 5.21: Summary of factors affecting hot ductility..... 85
Fig. 5.22: Effect of strain rate on hot ductility at 1080 °C and 800 °C, Alloy-1 86
Fig. 5. 23: Fracture surface at 800 °C, different strain rates, Alloy-1 87
Fig. 5.24: Fracture surface at 1080 °C, different strain rates, Alloy-1 88
Fig. 5.25: Effect of deformation time at 1080 °C on hot ductility at different strain rates, Alloy-1..... 89
Fig. 5.26: Effect of deformation time at 800 °C on hot ductility at different strain rates, Alloy-1 89
Fig. 5.27: Fracture surface at 750 °C, Alloy-1 90
Fig. 5.28: Fracture surfaces at 700 °C, Alloy-1 91
Fig. 5.29: The effect of deformation and cooling rates between 1080 °C and 800 °C, Alloy-1 92
Fig. 5. 30: Effect of cooling rate on phase fraction of TiN and NbC at 800 °C, Alloy-1 ... 93
Fig. 5.31: Comparing the hot ductility of Alloy-0 to Alloy-1 at 800, 700, 600 and 50 °C .. 94
Fig. 5.32: Fracture surface at 700, 600 and 50 °C, Alloy-0 95
Fig. 5.33: Fracture surface at 700, 600 and 50 °C, Alloy-1 96
Fig. 6.1: Temperature distribution in a single slab at time 0, Abaqus FEM model..... 102
Fig. 6.2: Temperature distribution in a single slab after 1 h, Abaqus FEM model 102
Fig. 6.3: Temperature distribution in a single slab after 30 h, Abaqus FEM model 103
Fig. 6.4: Temperature distribution of pile slab 1 after 10 min, Abaqus FEM model 104
Fig. 6.5: Temperature distribution immediately after adding slab 2 to slab 1 after 10 min, Abaqus FEM model..... 104
Fig. 6.6: Temperature distribution of pile slabs 1 and 2 after 20 min, Abaqus FEM model 105

Fig. 6.7: Temperature distribution of pile slabs 1-15, end of piling / start of cooling after 140 min, Abaqus FEM model 105
Fig. 6.8: Temperature distribution of pile slabs 1-15 after 50 h, Abaqus FEM model 106
Fig. 6.9: Temperature distribution of the four slabs pile after 30 h, Abaqus FEM model 106
Fig. 6.10: Four slabs pile for model validation 107
Fig. 6.11: Comparision between the stockyard temperature measurements and the calculated Abaqus FEM cooling profile for single slab cooling 107
Fig. 6.12: Location of temperature profile evaluation - upper slab surface 108
Fig. 6.13: Cooling profiles of single slab at corner, edge and upper surface center 109
Fig. 6.14: Cooling profiles at the upper surface center of pile slabs 7, 14 and 15 109
Fig. 6.15: Cooling profiles at the edge of pile slabs 7, 14 and 15 110
Fig. 6.16: Cooling profiles at the corner of pile slabs 7, 14 and 15 110
Fig. 6.17: Phase transformation curves of single slab at corner, edge and upper surface center, Alloy-1 111
Fig. 6.18: Microstructure of single slab at upper surface center, edge and corner, Alloy-1 112
Fig. 6.19: Phase transformation curves of slab 15 at corner, edge and upper surface center, Alloy-1 113
Fig. 6.20: Phase transformation curves of slab 14 at corner, edge and upper surface center, Alloy-1 113
Fig. 6.21: Microstructure of slabs 14 and 15 at upper surface center, edge and corner, Alloy-1 114
Fig. 6.22: Hardness distribution of single slab upper surface, Alloy-1 115
Fig. 6.23: Hardness distribution of slab 15 upper surface, Alloy-1 116
Fig. 6.24: Hardness distribution of slab 14 upper surface, Alloy-1 116
Fig. 6.25: Cooling profiles of slab 15 surface (upper surface center, edge and corner) and the corresponding mean radius of TiN by MatCalc, Alloy-1 118
Fig. 6.26: Cooling profiles of slab 14 surface (upper surface center, edge and corner) and the corresponding mean radius of TiN by MatCalc, Alloy-1 119
Fig. 6.27: Comparison between the cooling profiles and the corresponding TiN mean radius in the edge regions of slab 14 and 15 surfaces by MatCalc, Alloy-1 120
Fig. 6.28: Particle size analysis, pile slab 15 upper surface center, Alloy-1 120
Fig. 6.29: Transformation curves at the corner of the single slab, pile slabs 14 and 15, Alloy-0 121
Fig. 6.30: Microstructure at the corner of the single slab, pile slabs 14 and 15, Alloy-0 122
Fig. 6.31: Classification of processing situations influencing crack sensitivity, Alloy-1 .. 127

List of tables

Table 2.1: Potential cracking factors 16
Table 4.1: Chemical composition of Alloy-0 and Alloy-1 45
Table 4.2: Device specification of quenching and deformation dilatometer 47
Table 4.3: Ferrite start and end temperatures for Alloy-0 and Alloy-1 59
Table 4.4: Results of the NST experiments, Alloy-1 62
Table 5.1: Comparison between ideal/set and break-out casting conditions 69
Table 5.2: List of the studied effects and testing conditions 72
Table 5.3: Results of Case-1: Ideal casting, Alloy-0 73
Table 5.4: Results of Case-2: Break-out, Alloy-0 73
Table 5.5: Comparison between Cycle-1 & 2 at 800 °C, Alloy-0 75
Table 5.6: Results of Case-1: Ideal casting, Alloy-1 77
Table 5.7: Results of Case-2: Break-out, Alloy-1 77
Table 5.8: Results of MatCalc simulation for Model-1 & 2, Alloy-1 80
Table 5.9: Particle size calculation of break-out slabs 84
Table 5.10: Hot tensile testing results of Cases 3, 4, 5 & 6, Alloy-1 86
Table 5.11: Hot ductility values between 1080 °C and 650 °C, Alloy-1 90
Table 5.12: Hot ductility results at low strain rate and high cooling rate, Alloy-1 91
Table 5. 13: Hot ductility results at high strain rate and low cooling rate, Alloy-1 91
Table 5.14: Effect of cooling/strain rates on precipitation at 800 °C, Alloy-1 92
Table 5.15: Results of Case-8: Low temperature deformation (Alloy-0 & Alloy-1) 93
Table 6.1: FEM temperature model data 101
Table 6.2: Comparision between slab temperature measurements and FEM results at the end of four slab model cooling 108
Table 6.3: Phase transformation results of single slab, Alloy-1 111
Table 6. 4: Phase transformation results of pile slabs 14 and 15, Alloy-1 113
Table 6.5: TiN mean radius and hardness results of pile slabs 14 and 15, Alloy-1 117
Table 6.6: Phase transformation results at corner regions of single slab, pile slabs 14 and 15, Alloy-0 121

Publications and projects

Journal papers, proceedings and conferences

1. H. Ibrahim, H. Palkowski (2020): Influence of casting conditions on crack sensitivity of micro-alloyed steel slabs during continuous casting. TMS2020, San Diego, California, USA.
2. H. Ibrahim, H. Palkowski (2019): Wulste als Ursache für Unplanheiten im Feinblech – Messung und Simulation. Metallurgie Kolloquium, TU Clausthal.
3. H. Ibrahim, H. Palkowski (2019): Effect of cooling strategy on hot ductility of micro-alloyed steels during continuous casting. 4th European Steel Technology and Application Day, Düsseldorf, Germany.
4. H. Ibrahim, H. Palkowski (2018): Einfluss der Gießgeschwindigkeit auf die Duktilität und Ausscheidungskinetik mikrolegierter Stähle beim Stranggießen. CZM Absolventag, TU Clausthal.
5. H. Ibrahim, H. Palkowski (2018): Effect of casting speed on hot ductility of micro-alloyed steels during continuous casting. 7th International Congress of Science and Technology of Steelmaking, Venice, Italy.
6. H. Ibrahim, H. Palkowski (2017): Effect of continuous casting processing parameters on the hot ductility of micro-alloyed Steels. Topical Issues of Rational Use of Natural Resources, Saint-Petersburg Mining University, Russia and TMS 2017, San Diego, California, USA.
7. H. Ibrahim, H. Palkowski (2016): Einfluss der thermo-mechanischen Belastung auf die Bildung von Querrissen bei mikrolegierten Stählen. Metallurgie Kolloquium – TU Clausthal.
8. Soliman M, Ibrahim H, Nofal A, Palkowski H (2016): Thermo-mechanically processed dual matrix ductile iron produced by continuous cooling transformation. Journal of Materials Processing Technology, Vol. 227: 1–10. DOI:10.1016/j.jmatprotec.2015.07.025
9. Soliman M, Ibrahim H, Palkowski H (2016): Ulta-fine Bainite Steel: Influence of Thermomechanical Processing Parameter. AutoMetForm, Wroclaw, Poland.
10. M.Soliman, H. Ibrahim, A. Nofal, H. Palkowski (2015): Effect of Thermo-mechanical Processing Parameters on Phase Transformation and Hardness of Dual Matrix Ductile, Int. J. of Cast Metals Research, 2015, 79-84, doi.org/10.1179/1743133615Y.0000000037
11. Soliman M, Ibrahim H, Nofal A, Palkowski H (2014): Effect of Intercritical Annealing on Phase Transformation and Mechanical Properties of Thermo-Mechanically Processed Dual Matrix Ductile Iron. TMS2014 143rd Annual Meeting & Exhibition, Annual Meeting Supplemental Proceedings. John Wiley & Sons, Inc, Hoboken, S. 959–965.

Projects

1. Experimental study on transverse cracking of micro-alloyed steels
   DFG Project, Start: July 2020

2. Analyse und Modellerstellung für rissgefährdete Stahlsorten
   Duration: 2017-2020, Partner: Salzgitter Flachstahl GmbH

3. Simulationen zu Unplanheiten im Feinblech durch Wulste
   Duration: 2017-2020, Partner: Salzgitter Flachstahl GmbH